CRANFIELD UNIVERSITY

S VELIKOV

Wind Tunnel Modelling of Aerodynamic Baffle Arrays for Aircraft Exhaust Plume Control

SCHOOL OF AEROSPACE, TRANSPORT AND MANUFACTURING

PhD THESIS
Academic Year: 2014-2015

Supervisor: K P Garry
April 2015

CRANFIELD UNIVERSITY

S VELIKOV

Wind Tunnel Modelling of Aerodynamic Baffle Arrays for Aircraft Exhaust Plume Control

SCHOOL OF AEROSPACE, TRANSPORT AND MANUFACTURING

PhD THESIS
Academic Year: 2014-2015

Supervisor: K P Garry
April 2015

CRANFIELD UNIVERSITY

SCHOOL OF AEROSPACE, TRANSPORT AND MANUFACTURING

PhD THESIS

Academic Year: 2014-2015

S VELIKOV

Wind Tunnel Modelling of Aerodynamic Baffle Arrays for Aircraft Exhaust Plume Control

Supervisor: K P Garry

April 2015

This thesis is submitted in partial fulfilment of the requirements for the degree of Doctor of Philosophy.

Abstract

Local air quality is one of the factors constraining the development of airports. In countries of the European Union where new, stricter regulations for emissions of nitrogen oxides (NO_x) have been introduced since 2010, the limits of mean annual concentrations are already exceeded at certain ground monitoring locations of large airports. This research project investigates the possibility of practically abating the aircraft exhaust plume at take-off by placing an array of aerodynamic windbreaks ('baffles') in the runway end safety area close to the aircraft starting position. The thesis investigates whether an array of baffles in the path of the engine exhaust jet at take-off enhances the dispersion of the plume and causes it to separate from the ground.

The undertaken experimental investigation comprised sub-scale wind tunnel tests and full-scale field trials with a BAe 146-301 aircraft, performing take-off and landing cycles at Cranfield Airport. The initial wind tunnel experiments investigated the effect of a solid baffle row, placed in the path of a buoyant nozzle jet, on the development of the plume downstream. Using flow visualisation, the positive effect of the baffle row of promoting buoyant rise of the plume away from the ground was demonstrated successfully without the presence of wind tunnel flow. The investigation highlighted the importance of the distance of the baffles relative to the jet source on their effectiveness. In the presence of wind tunnel flow, the baffles caused an increased vertical spread of the plume downstream, but the plume was not observed to separate from the ground.

In preparation of the field trials, the spatial arrangement of the baffle array was investigated by means of wind tunnel drag measurements, performed with a skin-friction balance. The experiments focused on key parameters such as the baffle slope angle and row spacing, favouring a configuration of three rows of baffles of increasing height. The results were observed to be independent of Reynolds number for Reynolds numbers above 18000, based on the largest baffle height and the exhaust jet velocity. Based on the wind tunnel measurements, full-scale baffle prototypes were designed and manufactured at Cranfield University and were deployed in the field trials.

Lidar and point sampler measurements during the field trials suggested that the plume had risen away from the ground on one occasion when the aircraft was located close to the baffles. A positive effect was shown in terms of reduced concentrations downstream of the baffles. This result was not replicated when the aircraft was further away from the baffles.

The subsequent wind tunnel experiments focused on replicating the field trials at 1:200 scale in Cranfield's Atmospheric Boundary Layer Wind Tunnel. The aircraft was represented at sub scale with a single stationary nozzle while the jet speed and buoyancy were modelled using similarity parameters such as the Froude number and the ratio of ambient and jet density. Mean concentration measurements were performed using a

Flame Ionisation Detector method releasing methane as tracer gas. The effect of the baffles was observed to be mainly local in terms of reduced concentrations close the ground due to their sheltering effect. A more prolonged effect was found to be the increase of the plume's vertical spread resulting in an increase in mean concentrations away from the ground.

Overall, the results of the sub-scale and full-scale experiments were inconclusive with regard to the ability of the baffle array to lift-off the plume. It appears that the parameters, which have a significant effect on the lift-off phenomenon, are the ambient wind speed and the engine starting position. Additional field trials with a sub-scale UAV gas turbine have been proposed to investigate further the differences in the obtained results.

Acknowledgements

It took me quite some time and effort to complete this thesis and I have no doubts that all this would not have been possible without the support I was offered by so many people along the way. Although some of them were not directly involved, they have given me the strength and motivation to carry on until the end.

First and foremost, I would like to thank my academic supervisor Professor Kevin Garry and Dr Michael Bennett from Manchester Metropolitan University for their support, invaluable advice and scientific contribution to my work. I very much appreciate Professor Garry's understanding and patience with me at times when I was struggling to find motivation. Of course, this work would not have been possible without the financial support of EPSRC, for which I will always be grateful.

Thanks also to Jenny Holt, who has always been there to help me with my experiments and has contributed immensely to my work through countless technical discussions and advice offered. Additionally, the wind tunnel work would not have been possible without the assistance of Lynton Banks-Davies, Paul Dancer and John Thrower. I would also like to thank Dr Simon Christie from Manchester Metropolitan University and Barry Walker for the preparation of the field trials and for the occasional friendly conversations, which always raised my spirits and kept me motivated.

I wish to thank my colleagues Klementina Gerova and Apostolos Spanelis for all the work done together and for the shared ups and downs as doctoral students. Thanks also to my colleagues at the University's Sports Department, Roy Chamberlain and Craig Wilde, for giving me the opportunity to financially support my studies at times when I was struggling. My deepest gratitude also goes to Sue Richardson, whose immense efforts and work for the Cranfield Students' Association have been of great help to all of us sports enthusiasts running the student clubs on campus.

Of course, this all would not have been possible without the support of my family back home in Bulgaria, to whom I have never told a single word about my project, but who never stopped asking me how the work was going. I would like to dedicate this thesis to my grandpa, who was so proud of me being enrolled as a doctoral student, but sadly passed away shortly after I started. I promised myself I would finish it one day and here it is. It's been a long wait.

At Cranfield, I have met so many people of different background. It is a unique, very multicultural place where students come and go so fast every year and long-lasting friendships are difficult to maintain. I was very fortunate to meet a few friends, who have left such an incredible mark on my life. I wish to thank Diego Lombetti, Lara Berroth, Giuseppe Trapani and Marta Martínez for being my family in England, Spain and Germany and for never giving up on me. There are no words to express my

gratitude for all the support they have given me. I would also like to thank Michał Orłowski and Giacomo Struzziero for being there for me when I needed them and for all the shared good and bad moments as friends, colleagues and volleyball players on the court, defending the University colours at home and abroad. I have the privilege of being able to call all these amazing people my closest friends.

Special thanks goes to Juanjo Giner Sanz for the countless discussions and training sessions outside in the cold, and for teaching me the true meaning of the words ‘motivation’ and ‘dedication’.

I would also like to thank my house mates and friends Robert Christie, Michele Vianello and Max Starr, who shared with me the small house we called ‘home’ over the past few years. Robbie, Maxi and Miki, your support and advice, both personal and academic, has been invaluable to me and it has been a great pleasure to share a home with you.

Last but not least, I would like thank Eli, Cristina, and Lourdes from the bottom of my heart for making me the person who I am today and for teaching me more about life than they could possibly imagine.

October, 2014
Stefan Velikov

Table of contents

Publications

BENNETT, M., CHRISTIE, S.M., GRAHAM, A., GARRY, K.P., VELIKOV, S., POLL, D.I.A., SMITH, M.G., IQBAL MEAD, M., POPOOLA, O.A.M., STEWART, G., JONES, R.L. (2013). Abatement of an aircraft exhaust plume using aerodynamic baffles. *Environmental Science & Technology*, 47(5), p. 2346-2352.

GEROVA, K., VELIKOV, S., GARRY, K. (2013). The effects of porosity and inclination on the pressure drop across porous screens and honeycombs used for heat exchanger simulations in wind tunnel studies. *SAE International Journal of Passenger Cars – Mechanical Systems*, 6(2), p. 483-494.

List of figures

List of tables

Nomenclature

Acronyms

A/D	Analogue-to-digital
ABL	Atmospheric Boundary Layer
ABLWT	Atmospheric Boundary Layer Wind Tunnel
CFD	Computational Fluid Dynamics
CC	Constant-current
CT	Constant-temperature
DAQ	Data acquisition
ECU	Electronic Control Unit
EPA	United States Environmental Protection Agency
EPSRC	Engineering and Physical Sciences Research Council
ESDU	Engineering Sciences Data Unit
EU	European Union
FAAM	Facility for Airborne Atmospheric Measurements
FDR	Flight Data Recorder
FID	Flame Ionisation Detector
GPRS	General Packet Radio Service
GPS	Global Positioning System
HWA	Hot-Wire Anemometry
IATA	International Air Transport Association
ICAO	International Civil Aviation Organization
ILS	Instrument Landing System
Lidar	Light Detection and Ranging
MNP	Netherlands Environmental Agency (in Dutch: Milieu- en Natuurplanbureau)
Nd:YAG	Neodymium-doped Yttrium Aluminium Garnet
NERC	Natural Environment Research Council
PIV	Particle Image Velocimetry
PM_1	Particulate matter with a diameter of 1 μm or less
$PM_{2.5}$	Particulate matter with a diameter of 2.5 μm or less
PM_{10}	Particulate matter with a diameter of 10 μm or less
ppm	Parts-per-million
RESA	Runway End Safety Area
SFEE	Steady Flow Energy Equation
UAV	Unmanned Aerial Vehicle

Latin symbols

a	Exponential coefficient for velocity profile, see *Equation 3.13*
a_1	Velocity profile constant, see *Equation 3.14*; $a_1 \approx 5.75$
A	Area
A_5	Reference area equal to the sum of the frontal areas of all five rows of baffles, $A_5 = 0.0489$ m^2
b	Spacing between rows or nozzle offset distance in Chapter 2.4, see *Figure 2.9*
B	Proportionality coefficient, see *Equation 4.8*
b_0	Sub-scale distance between nozzle exit and Runway 21 threshold, measured along the runway direction; see *Figure 7.1*
B_1, B_2	Proportionality and exponential coefficients, see *Equation 4.7*
c	Mean concentration, in ppm
c_j	Mole fraction of methane at the nozzle at 1:200 scale, $c_j = 20000$ ppm
c_p	Specific heat capacity at constant pressure, for air $c_p \approx 1005$ J/(kgK)
C	Constant, see *Equation 2.19*
C_1, C_2	Proportionality constants, see *Equation 2.4*
C_b	Balance plate drag-force coefficient, see *Equation 5.2*
C_D	Drag coefficient based on A_5, see *Equation 5.3*
C_{Dn}	Two-dimensional drag coefficient, based on fence height h and freestream dynamic pressure (see *Equation 2.16*), or three-dimensional drag coefficient of a single baffle row, based on projected frontal area ($w \times h$) and freestream dynamic pressure
C_f	Skin-friction coefficient of a two-dimensional wall jet, see Chapter 2.2.1
C_F	Drag coefficient, based on projected frontal area and velocity at top of fence
C_N	Normal force coefficient of a surface-mounted fence, see *Equation D.1*
$C_{N\infty}$	Normal force coefficient of a flat plate, subjected to freestream; see *Equation D.3*
C_T	Total drag-force coefficient, see *Equation 5.1*
d	Nozzle inner diameter or nozzle width, see *Figure 2.2* (two-dimensional wall jet) and *Figure 2.5* (three-dimensional wall jet)
D	non-dimensional deflector position, see *Figure 4.4b* and *Equation 4.4*
f	Mole fraction of helium in the sub-scale jet
f_c	Coriolis parameter, $f_c = 2\omega\sin(\varphi)$
F_0	Specific buoyancy at the jet source
F_b	Measured drag force of the balance plate
F_N	Normal force, at right angles to the baffle surface, see *Figure D.1*

F_M	Momentum flux, see Chapter 2.2.1
Fr	Froude number, see definition in *Equation 1.3*
Fr^*	Modified Froude number, see *Equation 2.13*
F_t	Total take-off thrust
F_T	Measured total drag force
g	Gravitational acceleration, g = 9.80665 m/s
g'	Reduced gravitational acceleration, $g' = g(\rho_\infty - \rho_j)/\rho_\infty$
h	Baffle or fence vertical height, see *Figure 5.1*, or specific enthalpy in *Equation 6.1* and *Equation 6.2*
h'	Baffle slope height, $h' = h/\sin(\alpha)$
H	Plume vertical spread, see *Figure 4.1*
H'	Non-dimensional mean maximum plume vertical spread, see *Equation 4.2*
I_u	turbulence intensity for equilibrium conditions, see *Equation 3.23*
Je	Jensen number, $Je = h/z_0$
k	Proportionality coefficient, see *Equation 4.9*
K_c	Non-dimensional concentration parameter, see *Equation 2.14*
l	Characteristic length or distance
LCV	Lower Calorific Value, for Jet A-1 fuel $LCV \approx 43$ MJ
l_b	Buoyancy length scale, see *Equation 2.13*
l_M	Morton length scale, see *Equation 2.8*
l_P	Length of balance plate
L_p	Lift-off parameter, see *Equation 2.10*
l_{ws}	Blower tunnel working section length, see *Figure 4.14*, l_{ws} = 381 mm
m	Mass
M	Molar mass
M_0	Specific momentum at the jet source
Ma	Mach number, see definition in *Equation 1.2*
$\dot{m}_{air}$	Air mass flow rate through fan
$\dot{m}_f$	Fuel flow rate
n	Number of baffle rows on plate, starting from largest
N	Amount of substance, $N = m/M$
p	Static pressure
p_t	Total pressure
q	Dynamic pressure
Q	Volumetric flow rate
$Q_{1\text{-}2}$	Rate of added heat, see *Equation 6.1* and *Equation 6.3*
r	Spacing of parallel jets (distance between nozzle centre lines, see Chapter 2.5)
R	Specific gas constant; for dry air R = 287 J/(kgK)

R_0	Radius of first row of baffles downstream of nozzle
R^2	Coefficient of determination
R_u	Universal gas constant, R_u = 8.314 J/(molK)
Re	Reynolds number, see definition in *Equation 1.1*
Ri	Richardson number, see *Equation 2.9*
s	Number of baffle rows on plate, starting from smallest
S	Non-dimensional plume area, see *Equation 4.1*
t	Time
t_0	Measurement period of time
T	Absolute temperature
*u**	Friction velocity, see definition in *Equation 2.11*
$u_{z'}(t)$	Fluctuating component of wind speed at height *z'*, see *Equation 3.19* and *Figure 3.7*
U	Velocity
U_∞	Freestream velocity
U_1, U_2	Maximum velocity and half maximum velocity respectively for a two-dimensional wall jet, see *Figure 2.2*
U_{10}	Reference wind speed at 10 m height
U_{40}	Wind tunnel speed measured at 40 mm above the ground
U_j	Exit jet velocity
U_s	Speed of sound, see *Equation 1.2*
U_z	Mean wind speed at height *z*
$U_{z'}$	Mean wind speed at height *z'*
$U_{z'}(t)$	Instantaneous wind speed at any time *t*, measured at a height *z'*, see *Equation 3.19* and *Figure 3.7*
V	Volume
w	Baffle row width
w_n	Individual baffle width
W	Plume lateral spread, see *Figure 4.1*
W'	Non-dimensional mean maximum plume lateral spread, see *Equation 4.3*
$W_{1\text{-}2}$	Rate of work done, see *Equation 6.1*
x	Longitudinal Cartesian coordinate
x'	Non-dimensional longitudinal distance along blower tunnel working section, see *Figure 4.14*
x_s	Longitudinal coordinate relative to a constant freestream
y	Lateral Cartesian coordinate
$y_{0.5}$	Lateral position of the half maximum velocity of a three-dimensional wall jet, see *Figure 2.5*
z	Height above ground

z'	Height above aerodynamic ground surface, see *Figure 3.6*; $z' = z - z_d$
z_0	Roughness length, see *Figure 3.6*
$z_{0.5}$	Vertical position of the half maximum velocity of a three-dimensional wall jet, see *Figure 2.5*
z_d	Zero-surface displacement, see *Figure 3.6*
z_h	Gradient height, see *Figure 3.5*
z_{max}	Vertical position of the maximum velocity U_{max} in the plane of symmetry of a three-dimensional wall jet

Greek symbols

α	baffle slope angle
α_s	Screen angle of inclination, measured to the freestream direction; see *Figure 4.17* and *Figure C.9*
α_v	Screen angle of inclination, measured to the vertical; see *Figure 2.16*
β	Ratio of freestream velocity to exit jet velocity, $\beta = U_\infty / U_j$
γ	Screen porosity, see *Equation 2.15*
δ	Boundary layer thickness or two-dimensional wall jet thickness, see *Figure 2.2*
δ_1, δ_2	Vertical location of the maximum velocity and half the maximum velocity respectively for a two-dimensional wall jet, see *Figure 2.2*
Δp	Pressure drop across a porous screen, see Chapter 2.8
ΔT	Absolute temperature difference, $\Delta T = T_j - T_\infty$
$\Delta \rho$	Density difference, $\Delta \rho = \rho_j - \rho_\infty$
ε	Angle between wind tunnel flow and runway direction at sub scale, see *Figure 7.1*
η	Parameter, see *Equation 3.22*; $\eta = 1 - 6 f_c z'/u^*$
θ_1	Entry angle, measured to the freestream direction; see *Figure 4.18*
θ_2	Upwash angle, measured to the freestream direction; see *Figure 4.17* and *Figure 4.18*
κ	Von Karman constant, $\kappa \approx 0.4$
λ	Scaling, $\lambda = l_M / l_F$
Λ	Aspect ratio
μ	Dynamic viscosity
ρ	Density
σ_u	Standard deviation of the fluctuating component of wind speed in mean wind direction, see *Equation 3.22*
τ_w	Local wall shear stress
ν	Kinematic viscosity, $\nu = \mu / \rho$
φ	Local angle of latitude

ψ	Outflow angle, measured to the freestream direction; see *Figure 2.16*
ψ'	Flow angle at porous screen plane, measured to the freestream direction; see *Figure 2.16*
ω	Angular velocity of the Earth based on a sidereal day, $\omega \approx 7.29\times10^{-5}$ rad/s

Subscript

∞	Freestream
1, 2	Control volume boundaries, see *Figure 6.1*
air	Air
b	Balance plate
e	Edge of boundary layer
F	Full scale
He	Helium
j	Jet (at nozzle exit at sub scale)
M	Model
max	Maximum
mp	Merging point
ref	Reference

"Anybody who has been seriously engaged in scientific work of any kind realises that over the entrance to the gates of the temple of science are written the words: 'Ye must have faith'."

- Max Planck, *Where is Science Going?* (1932)

★ ★ ★ ★

1 Introduction

Aviation has become an integral part of civilisation and human life. Every day approximately one hundred thousand commercial flights take off around the world, carrying millions of passengers and cargo (IATA, 2013). The demand for fast and efficient long-distance transport has made civil aviation a major international business, playing an essential role in the world's commercial infrastructure (Poll, 2009). While safety still remains its primary objective, the immense growth of the civil aviation sector has brought forward other important issues, such as sustainability and environmental impact.

Civil aviation's global mean annual growth rate, in terms of Revenue Passenger-Kilometres[†], is currently predicted between 5% and 6% (ICAO, 2012) and is expected to remain similar within the next 15 years by the world's leading aircraft manufacturers (Airbus, 2007; Boeing, 2008). If correct, such predictions would mean air traffic doubling between 2010 and 2025 (Cheze et al., 2011). Furthermore, a long-term forecast by the International Air Traffic Association (IATA, 2011) predicts an increase of more than six and a half times in 2050, equal to about 16 billion passengers around the world. Such development would similarly increase the environmental impact of air transport and the competition within the airline industry, the former raising a major political concern in recent years. Thus, aviation technology is no longer concentrating on power and size, but has turned its attention to long-term aspects such as sustainability, cost-efficient operation and environmental responsibility. Reduction of

[†]Revenue Passenger-Kilometres (RPK) for a flight is defined as the number of revenue-paying passengers on board multiplied by the distance travelled (in kilometres).

noise and engine exhaust emissions, such as carbon dioxide (CO_2), water vapour and nitrogen oxides (NO_x), has become a priority for civil aviation organisations. For example, IATA, whose airline members carry out more than 90% of the world's scheduled international flights, is committed to stop the growth of emissions of their aircraft by the year 2020 and "to halve emissions by 2050 compared to 2005 levels" (IATA, 2009).

This study is concerned with the environmental impact of aviation. It discusses the possibility of abating an aircraft exhaust plume during take-off and thus promoting its dispersion above the ground. The primary concern would be the short-term emission gases which affect local air quality, i.e. nitrogen dioxide (NO_2) and, to a lesser extend in view of the EU annual limit, nitric oxide (NO). The experimental investigation addresses the aerodynamic behaviour and development of exhaust plumes in a controlled wind tunnel environment and relates this simulation to full-scale field trials with a BAe 146-301 aircraft at Cranfield Airport.

1.1 Aircraft ground-level emissions

Compliance with local air quality regulations is one of the factors constraining the expansion of airports to meet the demands of the growing airline industry. For example, recent environmental reports on air quality at Heathrow (UK Department for Transport, 2006; Heathrow Airport Ltd., 2011) and Frankfurt airports (Fraport AG, 2012) show that the EU limit on mean annual NO_2 concentrations, i.e. 40 $\mu g/m^3$ with 0% margin of tolerance from 1st January 2010 (European Commission, 1999), is already exceeded in some of the monitoring locations around these airports. This could have serious implications on the recently re-proposed plans for construction of a third runway at Heathrow Airport (Heathrow Airport Ltd., 2013), which would increase passenger traffic by 55% to 60% until the year 2025 or 2029 depending on the approved expansion plan. A similar observation by the Netherlands Environmental Agency (MNP, 2011) on the air quality around Schiphol Airport shows that at the predicted traffic growth rates the NO_2 limit would probably be exceeded by the year 2020. The individual contribution of air traffic is estimated by the MNP to be between 15 and 20% of the total NO_2 emissions at Schiphol, including non-airport related traffic. The investigation also identifies similar trends for exceeding the annual limit of particulate matter emissions of 10 μm diameter or less (PM_{10}) by 2020, however, the contribution of airport related traffic is estimated as only a few percent of the total emissions. The reduction of NO_2 emissions resulting from ground-level operations can therefore be considered a primary target for major European airports with regard to meeting EU regulations concerning human health protection.

If we consider only airport related ground-level emissions, aircraft are by far the largest source of pollution. For example, at London Gatwick Airport the NO_2 emissions resulting from aircraft operation are more than 6 times greater than those estimated from airport related traffic on the designated road network and from airside vehicle operation (Gatwick Airport Ltd., 2009). This is attributed primarily to the take-off rolls, e.g. causing 46% and about 40% of the annual NO_2 emissions respectively at Heathrow (Heathrow Airport Ltd., 2009) and Gatwick (Gatwick Airport Ltd., 2009) airports.

In view of this assessment, if the exhaust plume at take-off could be dispersed away from the ground in some way, this would reduce significantly the local NO_2 levels, measured at the monitoring locations at ground level, and thus improve local air quality.

1.2 Baffles concept

A research project, sponsored by the Engineering and Physical Science Research Council (EPSRC, 2009), has been proposed to investigate the possibility of improving local air quality at airports using practical abatement techniques to promote the rise of the aircraft exhaust plume away from the ground during take-off. The concept involves placing an array of windbreaks ('baffles') in the undershoot of the runway to remove sufficient horizontal momentum from the jet, thus allowing for buoyancy effects to become dominant as the jet develops away from the runway (*Figure 1.1*). It primarily targets the use of aerodynamic drag (of the baffles) and the high-temperature jet's natural buoyancy to help the plume physically disperse in the local environment reducing the concentration of exhaust emissions close to the ground. For future reference, the terms 'jet' and 'plume' are used in this work to describe respectively the high-momentum engine exhaust jet close to the nozzle exit, and the developed jet further downstream where horizontal momentum has reduced significantly and the jet's behaviour is dominated by turbulent mixing through entrainment of ambient air.

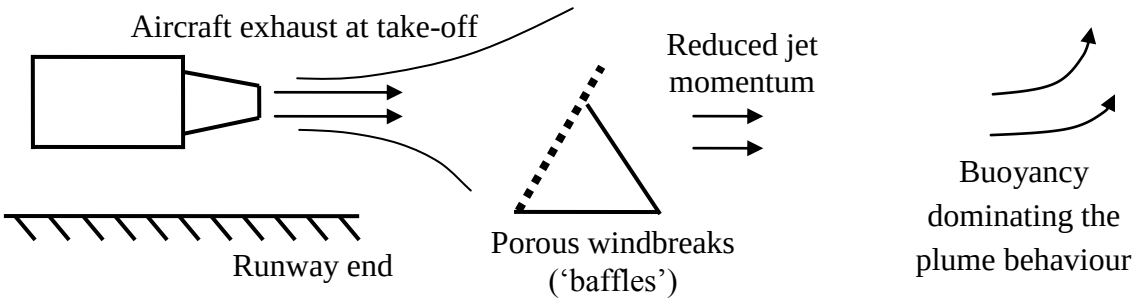

Figure 1.1: Baffle concept for reduction of engine exhaust jet momentum during take-off roll (schematic, side view)

At take-off, the high-momentum exhaust jet is drawn towards the ground by the Coanda effect and stays attached as "the downward momentum flux from the entrainment of air from above tends to keep it there" (Bennett et al., 2013). After a certain travel time the vertical momentum due to buoyancy, counter-acting the Coanda effect, prevails and tends to lift the plume away from the ground. Such plume rise was observed in Lidar (Light Detection and Ranging) studies at Heathrow and Manchester airports (Bennett et al., 2013) and at Denver International Airport (Wayson et al., 2008) during take-off runs of commercial aircraft. Graham et al. (2008) reported that the plume of a modern high-bypass-ratio engine would rise on its own after a travel time of ~80s when its natural buoyancy equalled the horizontal momentum of the jet. As observed by Kaiser (1977) and Meroney (1979) in independent simulations of buoyant gas released into moving air, ground level concentrations under a rising plume are very small with only a small residual part of the plume left behind.

Based on these observations, placing an array of baffles (effectively fences) directly in the path of an engine exhaust jet at take-off, and thus exerting an aerodynamic drag force on the jet, should drain some of its horizontal momentum reducing the time until the plume buoyancy becomes dominant. Such an arrangement would require positioning the baffles in the restricted area downstream of a runway threshold. Taking into consideration the landing angle of approach, restrictions for the height of the baffles as well as frangibility criteria (ICAO, 2006b) would be limiting factors in their structural design. This means that the exhaust jet height would be significantly larger than the baffles, leading to an arrangement of multiple rows of baffles, effectively acting as surface roughness elements.

If successful, the project will not only offer an innovative solution to the growing issue with local air quality at airports and thus have an important scientific contribution to the civil aviation community, but this solution could be of significant practical importance for the following reasons. First, the simplicity of the concept accounts for cost-efficient design, implementation and operation, and second, such system could almost immediately be introduced at airports since it does not require any changes in air traffic operations or aircraft design, e.g. normally design improvements would take years before being introduced into a new generation of engines.

1.3 Scientific motivation

Previously, the baffles concept and its potential practical importance to reducing exhaust emissions at ground level were highlighted. The governing physical phenomena of the baffles concept affecting the jet development are also of considerable scientific interest. The abatement method relies on the temperature and density differences

between the jet and the environment, creating an upward buoyancy force. Due to the entrainment of ambient air, the initial high buoyancy would reduce considerably as the jet travels away, which would consequently reduce the upward force targeted to lift the plume from the ground. The resulting development of the plume is to be investigated – whether a complete lift-off of the plume is possible or individual parts of the plume would separate from the plume.

Of particular interest in this research is whether an object (or an array of objects) in the path of the hightly buoyant jet would positively contribute to overcoming the downward momentum flux caused by the Coanda effect. The Coanda effect contributes to the attachment of jets in ground proximity to the ground surface, which results in a sigficantly greater lateral spread of the plume with distance away from the source. The presence of the object would reduce the jet horizontal momentum through the exerted aerodynamic drag and would deflect the jet exerting an upward momentum flux and aiding the buoyancy forces.

Another scientific interest of high importance would be the effects of ambient flow (wind) on the shear layer interaction and entrainment of ambient air by the jet as it develops downstream of the source.

1.4 Aims and objectives

The proposed project involves researchers from four institutions, i.e. Cranfield University, Manchester Metropolitan University, the University of Cambridge and the University Southampton, collaborating for the planning and execution of field trials with a BAe 146-301 aircraft at Cranfield Airport. The specific area addressed in this study is concerned mostly with the aerodynamic design and wind tunnel modelling of the baffle arrays and the correlation of data from the field trials. The study aims to answer the following research question:

Can an array of windbreaks (baffles) cause the plume of an aircraft at take-off to overcome sooner the Coanda effect and lift-off from the ground, thus enhancing the dispersion of the plume and reducing the exhaust emissions close to the ground?

In order to provide a complete scientific answer to the above research question, the wind tunnel test programme and the field trials were planned according to the following objectives:

1) Conduct preliminary wind tunnel tests to model a nozzle exhaust jet in ground proximity and study the plume behaviour downstream of the nozzle exit; using flow

visualisation, investigate whether a steady 'lift-off' of the plume (i.e. complete physical detachment from the ground surface) can be achieved in a controlled wind tunnel environment.

2) Conduct wind tunnel measurements to investigate the influence of material porosity and angle of inclination to the freestream and Reynolds number on the separation streamline trajectory and shear layer development downstream of obstacles.

3) Establish the mutual interference effects of surface mounted line-like structures embedded within a boundary layer.

4) Plan and conduct full-scale measurements to obtain suitable data for validation of ABLWT measurements.

5) Create a sub-scale model of the BAe 146-301 jet at take-off in Cranfield's 8'×4' ABLWT, accounting for the mass flow of the four turbofan engines and the plume buoyancy. Replicating the test conditions of the field trials in the ABLWT, perform gas concentration measurements to study the jet development. Conduct additional wind tunnel tests to study the velocity distribution in the near and far flow field of the baffles.

6) Establish correlations between model and full scale and identify any occurring differences in the results. Based on the overall results, identify the effects of the baffles on the dispersion characteristics of the plume.

1.5 Key sub-scale modelling issues

In design studies, sub-scale wind tunnel testing offers a significant advantage over full-scale tests in terms of costs and practicality. It enables engineers to experiment with design parameters and obtain important information on the aerodynamic behaviour of the targeted prototype models during every stage of the design process before manufacturing a full-scale product. Alternatively, theoretical and computational methods, the latter widely referred to as Computational Fluid Dynamics (CFD), are successfully used in calculations of well-known flow problems. In particular, the use of CFD in engineering problems has increased immensely over the past few decades with the rapid development of modern technology and increase in computational power. However, in many cases, CFD methods require code validation using experimental data, or are not yet able to calculate accurately complex flow problems, e.g. boundary layer transition, Atmospheric Boundary Layer (ABL) flows (Blocken et al., 2007), unless at

significantly higher cost in terms of computational time, which still remain unrealistic for commercial engineering application (Franke et al., 2004). Similarly, theoretical calculations are usually limited to specific cases of reduced flow variables and yield a simplified solution, strictly applicable in those cases. With this in mind, wind tunnel testing is often the only method capable of providing a complete range of detailed results, especially in the cases of investigating innovative engineering concepts.

The use of geometrically-scaled models requires flow similarity between full-scale and wind tunnel cases. With regard to modelling of aeronautical flows with fixed model geometry, the most important similarity parameters are considered the Reynolds number and Mach number, relating respectively the inertial and viscous forces within a fluid, and the fluid inertia and elastic forces (Garry, 2009a). The Reynolds number *Re*, defined in *Equation 1.1*, is the primary similarity parameter in low speed flows, typically of Mach numbers less than 0.3 (Barlow et al., 1999, p. 11), where compressibility effects are small enough to be neglected. Its significance is mostly for boundary layer flows and viscosity-dominated flow phenomena e.g. flow separation, aerodynamic drag. The dynamic viscosity μ is calculated from the Sutherland's Law, as given by Anderson (2001), p. 723 (see in *Equation A.1* in Appendix A).

$$Re = \frac{\rho U l}{\mu}$$

Equation 1.1

The Mach number *Ma*, defined in *Equation 1.2* where U_s is the speed of sound, is an important similarity parameter for modelling of high speed, compressible flows. In the current case, to assess the importance of the jet Mach number one has to take into account the location of the baffles and the accelerating jet source (engine during take-off run) in the opposite direction of the jet flow. Due to turbulent mixing and the resulting entrainment of ambient air, the jet momentum downstream of the initial engine position would decay significantly before the jet reaches the baffles, i.e. its Mach number would reduce below 0.3. This estimation is based on field trials with a BAe 146-301 aircraft at Cranfield Airport conducted in 2008 and 2009 and described by Graham (2009). In view of this, the jet Mach number is not considered a scaling parameter of primary interest in this research.

$$Ma = \frac{U}{U_s}$$

Equation 1.2

The natural buoyancy of the 'hot' exhaust jet plume within the surrounding ambient air requires further considerations regarding flow similarity between full scale and model. Since Reynolds and Mach number scaling does not take into account the effects of gravitational forces, these need to be accounted for using an additional scaling parameter – the Froude number *Fr*. It is defined as the ratio of inertial and gravitational forces and is the primary similarity parameter for dynamic tests "in which model motion as well as the aerodynamic forces are involved" (Barlow et al., 1999, p. 21). Its most common form used in engineering applications is shown in *Equation 1.3*.

$$Fr = \frac{U}{\sqrt{gl}}$$

Equation 1.3

Wind tunnel modelling of flows, where at full scale the ambient wind close to the ground is playing an important part in the flow development, requires a geometrically scaled model of the Earth's boundary layer (Garry, 2009b). The scale of the experiment is usually reduced considerably according to the wind tunnel arrangement, in order to match accurately the flow properties of the full-scale ABL and the modelled boundary layer in the working section. In practical terms, the vertical distribution of the mean velocity and the intensity and scale of the longitudinal component of turbulence are considered the most important flow parameters to reproduce (Barlow et al., 1999, p. 654). Cranfield's 8'×4' ABLWT facility was used in this study's wind tunnel tests to model the Atmospheric Boundary Layer at 1/200th scale.

Returning to *Equation 1.1*, it is reasonable to assume that the differences in temperature and density of the full-scale and modelled jet would not influence the Reynolds number similarity, as follows. A considerably higher (estimated) full-scale jet exit temperature would increase the jet dynamic viscosity μ, according to Sutherland's law, reducing the full-scale Reynolds number compared to model. At the same time, the lower wind tunnel jet density ρ (reduced deliberately to account for the full-scale jet buoyancy, see Chapter 3.3) would reduce similarly the model Reynolds number. Thus, for a complete Reynolds number similarity the product of jet velocity and characteristic length *Vl* need to be the same at full scale and model. Estimating a factor of U_F / $U_M \approx$ 10 at 1/200th scale (l_F / l_M = 200), the full-scale Reynolds number is larger by three orders of magnitude. As in the course of the project work neither the available equipment nor the scale is likely to change significantly, *Re* scaling issues will remain an important consideration. For the less important Mach number similarity, the factor between full-scale and model Mach number is estimated to be less than 10, since the higher full-scale exhaust temperature would give a higher speed of sound.

At the same time, complete Froude number similarity is possible at such small scale since changes in U and l in *Equation 1.3* have opposite effects on *Fr*. Assuming the same ratios U_F / U_M and l_F / l_M, as shown previously for *Re*, the model Froude number overestimates the full-scale one by a factor of only $\sqrt{2}$.

Apart from flow similarity, the jet modelling requires accurate representation of the take-off run. Due to constraints in the wind tunnel facility, only one nozzle can be used to model the exhaust jets of BAe 146-301's four turbofan engines. Furthermore, the acceleration of the aircraft in opposite direction of the jet flow should be considered. This would require time-dependent measurements, since the jet source would be moving away from its initial position reducing the exhaust gas concentration downstream. At the same time, static measurements can be averaged over a sufficiently long time period. In further view of the planned measurements, at $1/200^{th}$ scale the ambient flow velocity and the jet velocity downstream of the baffles would be very low range (typically < 1 m/s). Additionally, the presence of the modelled highly turbulent ABL is expected to contribute considerably to the unsteady exhaust jet.

To summarise, the highlighted issues with regard to the small scale of the experiments and the wind tunnel restrictions in modelling the take-off run and performing time-dependent measurements require certain simplifications to be made in the adopted test procedure. These will be discussed in detail in Chapter 6.1.

1.6 Thesis structure

The outline of the thesis is presented below including a summary of the contents of each chapter. Starting with a literature review on the subject and a description of the methodology used, the experimental results are then presented in chronological order.

Chapter 2 describes the review of published literature related to the subject of the research. It includes aircraft engine exhaust emissions, turbulent wall jets, buoyant flows, as well as aerodynamic characteristics of windbreaks and flow through porous screens.

Chapter 3 gives an overview of the undertaken steps in the experimental investigation, as well as the measurement equipment and wind tunnel techniques used, including Pitot-static pressure and velocity measurements, flow visualisation, force balance measurements, Flame Ionisation Detector (FID) and Hot-Wire Anemometry (HWA). It also

includes the methods used to model the buoyant exhaust jet and the Atmospheric Boundary Layer.

Chapter 4 describes the wind tunnel tests conducted to study the development of nozzle exhaust jets at sub scale and the possibility of causing the plume to physically detach from the ground surface ('lift-off'). This chapter also includes pressure measurements and smoke visualisation tests used to determine the preliminary design parameters of the baffles.

Chapter 5 presents the force measurements conducted to study the drag of various configurations of baffles, subjected to freestream and nozzle jet, in order to identify a suitable configuration for the full-scale field trials.

Chapter 6 describes the BAe 146-301 exhaust jet sub-scale modelling, using the Steady Flow Energy Equation and similarity parameters in order to match the field trials conditions at 1:200 scale. It includes a detailed description of the ABL and wind tunnel arrangement.

Chapter 7 presents the wind tunnel tests conducted after the field trials, including additional drag measurements, plume concentration measurements and velocity measurements.

Chapter 8 gives an overview on the field trials undertaken with a BAe 146-301 aircraft at Cranfield Airport in September 2011, including the individual baffle design, the test arrangement, and the results of the point-sample concentration and Lidar measurements, as presented in Bennett et al. (2013).

Chapter 9 includes a discussion on the obtained results together with the drawn conclusions and suggestions future work.

Appendix A gives additional equations.

Appendix B includes historical data on NO_x emissions of various airliners.

Appendix C includes additional graphs and images of the initial experiments.

Appendix D includes the preliminary baffle calculations.

Appendix E includes additional graphs and images of the force balance experiments.

Appendix F presents the calculations of the modelled Atmospheric Boundary Layer at sub scale.

Appendix G includes results and additional graph of the ABLWT experiments.

Appendix H includes data, results and images of the field trials.

Appendix I includes supplementary material for the planned UAV field trials.

2 Literature review

With regard to the nature of this study's problem, the review undertaken of published work is concerned primarily with jets in ground proximity ('wall jets'), with a main focus on three-dimensional wall jets, buoyancy effects in fluids and dispersion of exhaust plumes. With regard to the baffles, a summary of the aerodynamic drag of fences and walls is given, as well as a review of flow through porous screens, considered suitable for the surface of the baffles facing the engine exhaust jet. Due to the environmental impact aspect of the project, a brief review of aircraft exhaust emissions is included in the beginning of this chapter.

2.1 Aircraft engine emissions

Concerns about global warming over the past two decades have increased the public awareness of transport related emissions which contribute to the greenhouse effect, i.e. about 13% of all global greenhouse gas emissions (IPCC, 2007). The individual contribution of aviation is estimated to be around 3% of the total radiative forcing by all global human activity (Poll, 2009; IPCC, 2007). Gas turbine engines of commercial aircraft are designed to operate efficiently at cruise conditions throughout the majority of their life cycle. Exhaust emissions, resulting from the fuel combustion process, consist typically of 70% carbon dioxide (CO_2), a little less than 30% water vapour (H_2O), and less than 1% each of nitrogen oxides (NO_x), soot particles, carbon monoxide (CO), volatile organic compounds (VOCs) and sulphur oxides (SO_x) (FAA, 2005). Generally, the first two are recognised to have an impact on global climate, while CO, VOCs and SO_x emissions affect local air quality. NO_x and particulates have both a local and global effect. The nature and impact of the individual emissions is discussed below with an emphasis on NO_x.

2.1.1 Carbon dioxide

Carbon dioxide is an unavoidable end product of the complete combustion of fossil fuels, which forms during the burning process as carbon present in the fuel is oxidised. Released carbon dioxide is long lived – it is absorbed primarily by plants, as well as slowly by the oceans, with a life time between 50 and 200 years, as reported by the United States Environmental Protection Agency (EPA, 2013a). The bulk of aircraft engine emissions, i.e. ~90% (FAA, 2005), occur at high altitudes during cruise and thus

exhaust CO_2 accumulates in the upper troposphere and lower stratosphere. It has a direct impact on climate change since "CO_2 molecules absorb outgoing infrared radiation emitted by the Earth's surface and lower atmosphere" (IPCC, 1999). This is linked to a steady increase in global surface temperature and rising sea levels.

2.1.2 Water vapour

Water vapour is also a product of the complete combustion process and forms as hydrogen present in the fuel is oxidised. H_2O emissions are short lived – residence time in the troposphere is controlled by the hydrological cycle reaching up to several days, while in the stratosphere it is longer, i.e. months to years, due to extreme dryness and slow turnover of air (IPCC, 1999). Therefore, the positive radiative forcing effects of aircraft H_2O emissions on climate change are considered of less importance compared to the forming of contrails in the upper troposphere during flight. Persistent contrails can evolve into cirrus clouds, which contribute to the heating of the Earth's surface through their optical properties – they allow sunlight to pass nearly unhindered while at the same time absorbing and reradiating infrared radiation emitted from the Earth's surface (Lynch, 1996). In the lower stratosphere water vapour emissions are a source of HO_x radicals which directly destroy ozone (O_3) and interact with other chemical families which affect O_3 loss (Tian et al., 2009). Furthermore, H_2O emissions contribute to the formation of polar stratospheric clouds, the particles of which support chemical reactions forming chlorine, which in turn is a catalyst for ozone depletion (WMO, 2002). In both cases, the destruction of the ozone layer leads to enhanced incoming ultraviolet radiation.

2.1.3 NO_x

Nitric oxide (NO) and nitrogen dioxide (NO_2), collectively referred to as NO_x, form as a result of the combustion process, mostly from the oxidation of nitrogen, present in the combustion air, at high temperatures. Small amounts also come from the nitrogen content of the fuel (Rogers et al., 2002). The principal chemical reactions, known as the 'Zeldovich mechanism', take place at temperatures above 1300 °C and lead to the production of NO, a free radical, which is converted into NO_2 when exposed to atmospheric oxygen (EPA, 1999). NO_x emissions depend on the combustion chamber characteristics; typical values are about 14 kg per 1 tonne of burned kerosene in cruse or approximately 0.5% and 1.2% of the carbon dioxide and water vapour emissions respectively (Garry, 2009c). At high power settings, such as during take-off and cruise,

engines operate at high turbine exit temperatures promoting the chemical formation of NO_x emissions. Hence, with regard to local air quality at ground level, they are by far the largest and most important pollutant from aircraft exhausts. Long-term exposure to NO_2 is associated with lung function and respiratory symptoms (WHO, 2003). Furthermore, NO_x emissions are influential in the chemistry of the atmosphere and contribute to the formation of ozone through a photochemical reaction with ambient VOCs (e.g. methane). On ground level, it is one of the air pollutants forming photochemical smog over densely populated cities, which is also associated with respiratory problems. In the troposphere, the production of short-lived ozone (a greenhouse gas) has an impact on global climate change through positive radiative forcing. At the same time, NO_x emissions contribute to negative radiative forcing by decreasing tropospheric methane, which produces long-lived cooling effects of the Earth's surface (Wild et al., 2001). In the stratosphere, nitrogen oxides are known to destroy ozone. However, as reported by Ravishankara et al. (2009), stratospheric NO_x comes primarily from surface emissions of N_2O, which is identified as the single most important ozone-depleting emission and is expected to remain so in the 21st century.

2.1.4 Soot, carbon monoxide, VOCs and SO_x

As a result of the incomplete combustion of fuel, aircraft engine exhausts contain emissions of solid particulate matter, carbon monoxide and VOCs. Particulates consist mainly of unburned carbon, also known as soot, and volatile sulphate aerosols. The latter ones result from the condensation of sulphuric acid, which is formed together with SO_x through oxidation of sulphur, present in trace amounts in aviation fuels (IPCC. 1999). Most of the sulphur in the fuel is emitted in the form of sulphur dioxide (SO_2), which is linked to adverse effects on the respiratory system, as reported by EPA (2013b). Both fine ($PM_{2.5}$) and coarse (PM_{10}) particles, classified as having a diameter of 2.5 μm and 10 μm or less respectively, are strongly associated with mortality due to cardio-pulmonary and lung deceases and cancer (WMO, 2002). They also affect global climate mainly through formation of contrails and cirrus clouds, responsible for warming effects.

Like NO_x, carbon monoxide plays an important role in the production of ozone in the atmosphere. However, since CO emissions from natural sources and non-aircraft anthropogenic activities are substantially larger than analogous NO_x emissions, the role of aircraft CO emissions in ozone photochemistry, compared to NO_x, is considered of significantly less importance (IPCC, 1999). With regard to human health, exposure to carbon monoxide reduces the oxygen supply to the internal body organs with potentially fatal consequences. Like carbon monoxide, aviation related emissions of VOCs come mainly from aircraft exhausts and airport related traffic, i.e. motor vehicles. They

consist of a wide range of hydrocarbon species, mostly non-methane hydrocarbons. Many species are carcinogenic, e.g. formaldehyde, and are therefore considered hazardous air pollutants (Rogers et al., 2002). Unlike all other aircraft engine emissions, only 10% of which are estimated to result from ground level operations, ground level emitted VOCs and CO are significantly higher, i.e. close to 30%, mainly due to the engine combustion inefficiency at low thrust settings during taxiing (FAA, 2005).

2.1.5 Overview

In view of the above, it can be argued that reducing some emissions causes an increase in others and vice versa. In order to improve combustion efficiency and reduce engine size for a given thrust, commercial aircraft engines are designed to have high compressor pressure ratio and high turbine entry temperature. The latter promotes the chemical formation of thermal NO_x, which increases exponentially with increasing flame temperature (Bussman et al., 2003). Similarly, improving engine efficiency also increases contrail formation (Poll, 2009). At the same time, carbon dioxide emissions depend on fuel burn rate and are reduced as engine efficiency increases. Emissions resulting from the incomplete combustion of fuel also reduce as combustion efficiency improves. For this reason, over the last few decades the progress made to reduce emissions of CO and VOCs has been considerably more compared to NO_x (FAA, 2005). This is shown in *Figure 2.1* using data for relative emissions per passenger-mile from the last three decades of the past century. Similar data, presented by Farber et al. (2008), shows that, although aircraft fuel consumption and CO_2 emissions have reduced steadily over the last four decades, NO_x emissions per kilogramme fuel burned have increased. When the same NO_x emissions are considered per seat kilometre, a small improvement is evident due to combinations of both aircraft (airframe) and engine (fuel efficiency) improvements, which is consistent with the trends in *Figure 2.1*. The data is shown in *Figure B.1* and *Figure B.2* in Appendix B.

In conclusion, currently NO_x emissions are of primary concern with regard to the impact of aviation on local air quality. This is because of their chemical formation as a result of high engine exhaust temperatures, as well as their relatively high emission index (produced emission mass per unit mass of fuel burned), compared to other air pollutants from aviation related emissions.

However, with regard to the aerodynamic sub-scale modelling in this work, the chemistry within the plume is not of primary concern, therefore the exhaust gases are not considered individually. They are collectively referred to as a ‘jet’ close to the nozzle exit, where the flow is dominated by the high momentum, and as a ‘plume’ further away from the nozzle, where the flow is dominated by turbulent mixing.

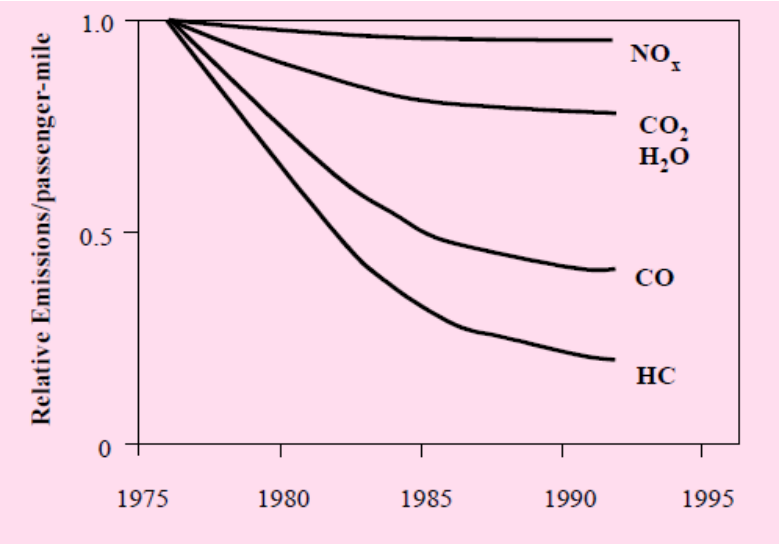

Figure 2.1: Historical overview of the relative reduction of aircraft engine emissions per passenger-mile between 1976 and 1992, based on Boeing data (taken from FAA, 2005)

2.2 Two-dimensional turbulent wall jets

The term ‘wall jet’ was originally introduced by Glauert (1956) to describe the flow case of a jet striking a solid flat surface at right angles and spreading out radially. To differentiate the above case from a flow blowing tangentially to a surface, Glauert further denotes these as ‘radial’ and ‘plane’ wall jets respectively. Typical examples of such flows are engine exhaust plumes at vertical and horizontal aircraft take-off respectively. The latter example represents the main topic of this work, therefore the tangential wall jet, considered of much greater interest here, is referred to from now on simply as a ‘wall jet’.

Depending on the nature of the flow one can generally distinguish two types of wall jets – laminar and turbulent. This is determined by the characteristics of the boundary layer at the flat surface, and the outer edge flow (see *Figure 2.2* in Chapter 2.2.1), which are influenced by the jet’s upstream history and physical properties. By constraining the flow in the spanwise direction one can further divide wall jets into two- and three-dimensional. The former case represents a wall jet of uniform velocity distribution in the spanwise direction. Flow cases include two- and three-dimensional laminar, turbulent (both forced and unforced) and transition wall jets at various nozzle positions with respect to the flat surface, as well as configurations with a perforated flat surface under applied blowing and suction and a flat surface with a pressure gradient.

2.2.1 Two-dimensional turbulent wall jets without an external stream

To introduce the two-dimensional wall jet concept, the elements and the appropriate nomenclature used are described briefly here. *Figure 2.2* shows a schematic two-dimensional wall jet in quiescent surroundings, exiting from a nozzle of characteristic width d, positioned directly on the flat surface. The coordinates x and z are the horizontal distance downstream of the nozzle exit, also referred to as an orifice, and the height above the flat surface respectively. A uniform core of constant jet velocity equal to the mean exit velocity U_j is formed immediately downstream of the nozzle exit, extending to a few lengths d in the x direction. Further downstream the jet velocity decays with distance x as the jet spreads out in z direction. The mean horizontal velocity profile exhibits a local maximum U_1, following the presence of a boundary layer at the surface, after which $U(z)$ decreases to zero (wall jet in quiescent air) defining the jet boundary δ. A common reference point used in velocity profile calculations is the position δ_2 of half the maximum velocity U_2. Myers et al. (1961) describes the imaginary line $\delta_1(x)$, connecting the positions of maximum velocity, as a boundary dividing the wall jet into an 'inner layer', assumed to behave like an ordinary turbulent boundary layer, and an 'outer layer' regarded as free jet. Such a hybrid structure accounts for the retarding of the jet due to frictional resistance near the wall and the entrainment of quiet fluid into the jet near the outer edge (Bakke, 1957).

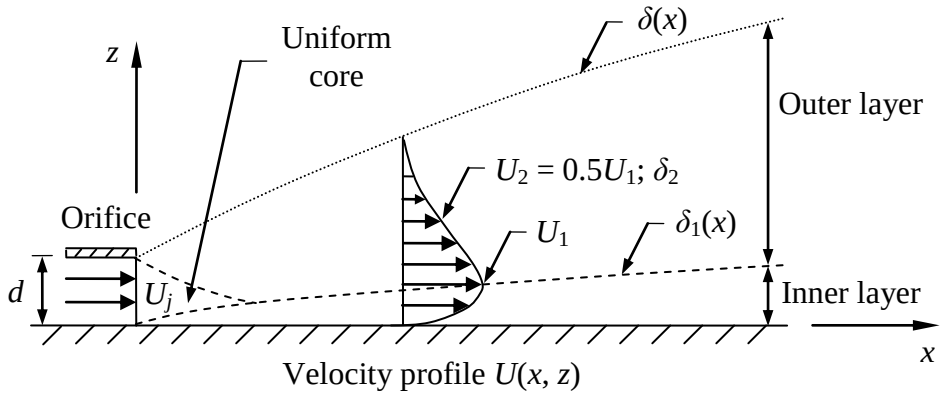

Figure 2.2: Two dimensional wall jet without external stream – features and nomenclature (similar to Figure 1 in Myers et al., 1961)

The case of two-dimensional wall jet was first investigated by Förthmann (1936) using a blown jet exiting from a rectangular slot in a partially open wind tunnel working section layout (flow constrained in lateral direction). He concluded that "the flow follows a simple law of similitude", i.e. all velocity data coincide in one profile over the entire range of x locations tested when plotted in terms of the local maximum velocity

versus the non-dimensional height z/δ_2. The maximum velocity and the wall jet thickness were found to decay with $x^{-0.5}$ and increase proportional to x respectively. Near the wall surface, Förthmann observed a velocity variation with the $1/7^{\text{th}}$ power of the wall distance, which is a commonly used approximation for turbulent boundary layer profiles of flat plates at moderate Reynolds numbers, based on flat plate length and freestream velocity, i.e. between 5×10^5 and 10^7 (Schlichting, 1979, Chapter 21).

Similar cases were investigated analytically by Tetevin (1948) for laminar jets and Glauert (1956) for laminar and turbulent wall jets, and experimentally by Bakke (1957), Sigalla (1958a), Sigalla (1958b) and Rajaratnam (1965) for turbulent wall jets. Other works by Schwarz & Cosart (1960) and Myers et al. (1961) show both analytical and experimental investigations for an extended range of distances and Reynolds numbers of $18 \le x/d \le 66$ and $2.2\times10^4 \le [Re = \rho U_1 \delta/\mu] \le 1.06\times10^5$, and $12 \le x/d \le 180$ and $7.1\times10^3 \le [Re = \rho U_j\, d/\mu] \le 5.65\times10^4$ respectively.

Glauert (1956) divided the flow into inner and outer regions at the velocity maximum location $\delta_1(x)$ and concluded that complete similarity of the flow could not be achieved at all locations downstream. However, when considered separately, the velocity profiles in the outer and inner region are respectively similar. The results of Glauert for maximum velocity decay and length scale variation with x, together with other published results, are listed in *Table 2.1*. For a radial wall jet, Glauert observed the same maximum velocity and wall jet thickness variations to be with $x^{-1.14}$ and $x^{1.02}$ respectively. They are in very good agreement with Bakke's experimental results for a turbulent radial wall jet impinging and spreading out on a smooth flat surface, where these variations were determined to be with $x^{-1.12}$ and $x^{0.94}$ respectively.

Table 2.1: Comparison of published results for maximum velocity decay and thickness growth of two-dimensional wall jets

Reference	*Decay of maximum velocity with*	*Wall jet characteristic length scale*
Förthmann (1936)	$x^{-0.5}$	$\delta \sim x$
Tetevin (1948)	$x^{-0.5}$ (laminar wall jet)	$x^{0.75}$ (laminar wall jet)
Glauert (1956)	x^i, $-0.45 \le i \le -0.6$	$\delta_2 \sim x^j$, $0.9 \le j \le 1.0$
Sigalla (1958b)	$x^{-0.5}$	$\delta_2 \sim x$
Schwarz & Cosart. (1960)	$x^{-0.555}$	$\delta_2 \sim x$
Myers et al. (1961)	$x^{-0.49 \pm 0.03}$	$\delta \sim x^{0.95 \pm 0.03}$
Rajaratnam (1965)	$x^{-0.5}$	$\delta_2 \sim x$
Newman (1969)	$x^{-0.5}$	$(\delta_2 - \delta_1) \sim x$

It is evident that the length scale used to characterise the wall jet varies depending on the study undertaken. The reference length and velocity used to calculate Reynolds numbers also vary. Local *Re* are calculated with U_1 and δ or $(\delta_2 - \delta_1)$, rather than the more common use of U_j and d to account for the conditions at the jet source. It can be concluded that regardless of the turbulent wall jet type (radial or plane), its characteristic length scale is proportional to the distance downstream. In the laminar case of Tetevin (1948) the jet width increases with $x^{0.75}$, thus the growth rate is slower.

Myers et al. (1961) and Bradshaw & Gee (1962) concluded that the maximum velocity decay for a wall jet was the same as the one for a free jet (i.e. no surface present), thus highlighting the importance of the outer layer in the flow development. Experimental velocity data by Sigalla (1958b) between 12 and 65 nozzle widths downstream, and Reynolds numbers between $3.5\times10^4 \leq [Re = \rho U_1(\delta_2 - \delta_1)/\mu] \leq 7.5\times10^4$, suggested the relationship $U_1 / U_j = 3.45(x/d)^{-0.5}$, also stated by Rajaratnam (1965). A similar data fit was calculated by Myers et al. (1961) with an exponent of –0.49. A more recent publication by Shabayek (2011) states a proportionality factor of 3.50 (see *Equation 2.1*) and suggests that the velocity decay is independent of Froude number *Fr*, based on experimental results at low speeds in the range $3 \leq Fr \leq 8$.

$$\frac{U_1}{U_j} = 3.50\left(\frac{x}{d}\right)^{-0.5}$$

Equation 2.1

Sigalla (1958b) showed the skin friction coefficient C_f, defined as the ratio of measured shear stress to exit jet dynamic pressure, to be a function of Reynolds number from 15 nozzle widths onwards, as follows: $C_f = 0.0565(\rho U_1 \delta_1 / \mu)^{0.25}$. Glauert (1956) used a similar formula near the wall with a proportionality factor of 0.045, based on empirical results of flow through a pipe, which underpredicted C_f compared to Sigalla's 0.0565. Bradshaw & Gee (1962) also measured shear stress and found the relationship $C_f = 0.0315(Re^{-0.182})$ for $3.0\times10^3 \leq [Re = \rho U_1 \delta_1 / \mu] \leq 1.5\times10^4$. Schwarz & Cosart (1960) calculated the skin fiction as 0.01109 and observed it to be independent of downstream location, varying only slightly within their Reynolds number range of $2.2\times10^4 \leq Re \leq 1.06\times10^5$. They concluded that 'the law of the wall' method did not apply in the same manner for a wall jet as for a turbulent boundary layer, which contradicted the assumptions stated by Glauert and Sigalla. Similarly, Myers et al. (1961) observed that "the flat plate 'law of the wall' holds for the wall jet for y^+ up to 30 but does not represent the wall jet over the extended y^+ range (up to 1000)", where y^+ is the dimensionless wall distance, defined as

$$y^+ = \sqrt{\frac{u * y}{\nu}}$$

Equation 2.2

In *Equation 2.2*, $u*$ is the friction velocity and ν is the kinematic viscosity. Their shear stress measurements indicated 15% higher results compared to Sigalla (1958b), but 40% lower than those of Schwarz & Cosart (1960).

Both Schwarz & Cosart (1960) and Myers et al. (1961) concluded that the wall jet inner layer velocity profile is not described accurately by the commonly used $1/7^{th}$ power law, adopted by Förthmann (1936), Glauert (1956) and Sigalla (1958a). Measurements in the inner layer showed the velocity varying with the $1/14^{th}$ power of the wall distance. Schwarz & Cosart (1960) suggested that this is due to the presence of the outer layer, modifying the flow structure of the inner layer. This was confirmed in more recent experiments by Hsiao & Sheu (1994) and Scarano et al. (1999), using Hot-Wire Anemometry and Particle Image Velocimetry techniques respectively. They observed a double row vortical structure, shown schematically in *Figure 2.3* (only two pairs of vortices), consisting of a primary vortex in the outer layer coupled with an induced secondary (counter-rotating) vortex in the inner layer with a phase shift.

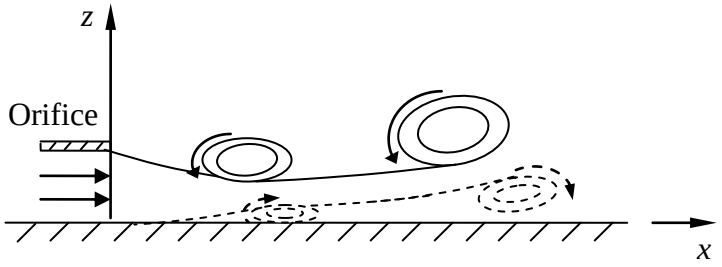

Figure 2.3: Schematic illustration of double-row vortical structure in the near field of a two-dimensional wall jet, observed by Hsiao & Sheu (1994)

Rajaratnam (1965) found that the velocity profiles scaled with U_1 and δ_2 at any location $x/d \geq 15$ where the flow was fully established, and stated the approximate relationships $\delta_1 \approx 0.16\delta_2$ and $\delta \approx 2.25\delta_2$ for the extent of the inner and outer layer respectively. He also investigated turbulent wall jets on rough surfaces, varying the height of the roughness elements up to $0.126d$ for Re_j between 1.91×10^4 and 1.02×10^5, based on U_j and d. He found that increasing the surface roughness accelerated the decay of maximum velocity but did not affect the flow in the outer layer in terms of its length scale variation, which remained the same. This was also observed in recent investigations by Smith (2008) and Tachie et al. (2004). Similarly, Rostamy et al. (2011) reported that surface roughness did not affect the spread of the jet.

Using experimental data, Lauder & Rodi (1981) calculated the outer layer growth rate of a two-dimensional wall jet in terms of δ_2 (see *Equation 2.3*), and reported that its variation with Reynolds number was negligible.

$$\frac{d\delta_2}{dx} = 0.073 \pm 0.002$$

Equation 2.3

Lauder & Rodi (1983) stated that the growth rate of *Equation 2.3* is 30% smaller than the growth rate of a two-dimensional free jet, arguing that the difference is due to "damping of turbulent velocity fluctuations in the direction normal to the wall". The same difference was observed by Rajaratnam & Subramanya (1967).

Narasimha et al. (1973) proposed using the jet momentum flux F_{Mj} (rather than U_j and d separately), equal to $U_j{}^2 d$ for a uniform exhaust jet, and the kinematic viscosity v to scale the mean flow parameters for distances $x/d \geq 30$, described as the fully developed flow region. They argued that the initial conditions are eventually 'forgotten' by the flow, while the momentum flux remains constant with x/d. This statement was not supported by George et al. (2000), arguing that the effects of the slot conditions can persist far downstream. The momentum scaling method was applied by Wygnanski et al. (1992), Abrahamsson et al. (1994), George et al. (2000), Tachie et al. (2004) and Rostamy et al. (2011). They calculated the maximum velocity decay and jet growth rate as a function of the non-dimensional parameter (xF_{Mj}/v^2), obtaining similar results. Furthermore, Abrahamsson et al. (1994) found that, using momentum scaling, the results for maximum velocity decay and half-width growth become independent of Reynolds number Re_j between 10^4 and 2×10^4, based on U_j and d. This was also observed by Wygnanski et al. (1992) for $5\times10^3 \leq Re_j \leq 1.9\times10^4$ and by Tachie et al. (2004) for $5.9\times10^3 \leq Re_j \leq 1.25\times10^4$. Their results experienced a considerable variation with Re when scaled with U_j and d.

Other experimental investigations by Schneider & Goldstein (1994) and Eriksson et al. (1998) showed that the mean flow characteristics scaled well with U_j and d, and observed consistent flow similarity for distances between $45 \leq x/d \leq 90$ and $40 \leq x/d \leq 150$ respectively. No conclusions on the Reynolds number dependency of their results were reported.

Recently, Barenblatt et al. (2005) proposed that the outer and inner layers are separated by a third (mixing) layer, where the velocity is close to the maximum. They concluded that the scaling laws for the inner and outer layer are different and are strongly influenced by the width of the slot d. The maximum velocity decay was found to be $U_1 \sim x^{0.6}$. The three-layer structure and incomplete similarity of the flow do not

agree with the findings of previous authors and have since been dismissed in a numerical investigation by Azim (2013), who observed a two-layer structure throughout the entire flow field with gradually decaying inner layer with x.

2.2.2 Two-dimensional turbulent wall jets in an external stream

This section presents a review of previous work on two-dimensional wall jets in a uniform external stream, moving in the jet direction. Compared to the case of a wall jet in quiescent air, here the velocity does not decay to zero at the jet boundary away from the wall, but has the freestream velocity value U_∞.

Bradshaw & Gee (1962) and Verhoff (1963) investigated turbulent wall jets with and without external flow. In their experiments, Bradshaw & Gee (1962) observed that the wall jet mixed slower with an external stream than with quiescent air due to slower entrainment of ambient fluid into the jet. They found the skin friction coefficient to be $0.026(Re)^{-0.18}$ for $Re = \rho U_1 \delta_1 / \mu$ for $1 < U_j / U_\infty < 2$. These values are lower compared to the still air case where they reported the relationship $0.0315(Re)^{-0.182}$. Verhoff (1963) presented both experimental and analytical results, highlighting the importance of the ratio of jet exit velocity to freestream velocity $\beta = U_\infty / U_j$ in the flow development. He introduced similarity functions to develop empirical solutions for the velocity profile downstream, restricted to $U_\infty / U_1 \leq 0.4$. The results agreed well with experimental data for U_j / U_∞ of 0.082 and 0.19, and $Re_j = 8.9 \times 10^3$ based U_j on and d, showing high accuracy up to a minimum of 400 slot heights downstream.

Kruka & Eskinazi (1964) conducted a theoretical analysis by dividing the flow into an inner (wall) region and an outer (free-mixing) region. They performed experiments with freestream-to-jet-velocity ratios β between 0.055 and 0.485 up to 275 slot widths downstream, varying $Re = \rho U_1 \delta_1 / \mu$ between 3750 and 26270. Results showed that flow similarity existed separately in both regions for mean as well as turbulence quantities. However, the same scales did not apply to both regions. The drag coefficient C_f was found to decrease with Re and β, consistent with the results of Bradshaw and Gee (1962). For the length scales, the data for all values of β was found to fall under the relationships $\delta_1 = 0.0109x$ and $(\delta - \delta_1) = 0.0601x_s$, where x_s is the longitudinal distance relative to the constant freestream. The maximum velocity u_1 and the maximum excess velocity $(U_1 - U_\infty)$ varied with x and x_s respectively, raised to a power which in terms varied with β.

Harris (1965) used a similar approach, simplifying the expressions for the conservation of mass, momentum and energy and solving them with the aid of a digital

computer. An important assumption in his theoretical analysis was the ignored existence of an upstream boundary layer caused by the freestream at the wall, thus the freestream was assumed to have an inviscid flow velocity over the surface. The results were validated with experimental data over a range of jet Reynolds numbers $Re_j = \rho U_j d / \mu$ between 5.9×10^3 and 8.7×10^3, and distances x / d between 100 and 900. The non-dimensional inner layer thickness δ_1 / d was reported to increase proportionally with x / d, having a constant of proportionality which varied with Re_j. Similarly for the outer layer thickness, the relationship $(\delta_2 - \delta_1) / d \sim \beta$ was found, for which two constants of proportionality were used, which varied with Re_j, and x / d and β, respectively. For the velocity decay, the relationship shown in *Equation 2.4* was found, which is similar to a wall jet in quiescent air with an added term accounting for β. The constants of proportionality C_1 and C_2 were calculated as functions of Re_j and x / d respectively, with C_1 varying between 3.6 and 4.0 for $10^3 \leq Re_j \leq 10^5$.

$$\frac{U_1}{U_j} = C_1\left(\frac{x}{d}\right)^{-0.5} + C_2\beta$$

Equation 2.4

Other works by Kacker & Whitelaw (1968), Newman (1969) and Kacker & Whitelaw (1971) have investigated the wall jet in a moving stream with regard to boundary layer control. Newman (1969) reported that the calculations to prevent separation on a trailing edge flap, using a tangentially blown jet, are considerably affected by the upstream boundary layer caused by the freestream, thus disagreeing with the assumptions made by Harris (1965). He observed that results for different slot widths d collapsed on the same curve when scaled using an excess momentum coefficient, defined as $\rho U_j(U_j - U_\infty)d / (0.5\rho U_\infty{}^2 l)$. The characteristic length l for the case of boundary layer control on a trailing edge flap would be the aerofoil chord length.

Kacker & Whitelaw (1968) carried out experiments on mean flow properties and turbulence characteristics for values of β between 0.37 and 1.33 up to 150 slot heights downstream. They found a significant increase in static pressure near the nozzle exit followed by a steady decrease up to 100 slot heights downstream. Thus, the assumption of zero normal pressure gradient, applied for boundary layers, introduces a certain error for a wall jet beneath a moving steam close to the nozzle exit, which decreased with x. For $\beta > 1$ (wakelike flow), the total kinetic energy decreased with x near the nozzle exit and began to increase further downstream (150 slot heights) resembling a zero pressure gradient boundary layer. In the case of $\beta < 1$ (jetlike flow) between 50 and 150 slot heights the total kinetic energy was found to be approximately constant.

2.3 Three-dimensional turbulent wall jets

A three-dimensional wall jet is a jet which exits from a nozzle of finite length and flows tangentially to a surface. The flow is therefore only restricted in the direction of the surface, and the jet is free to spread in the lateral direction. A characteristic feature of a three-dimensional wall jet is the significantly larger spread parallel to the surface in the lateral direction compared to the spread in the vertical direction. This is shown in *Figure 2.4a* and *Figure 2.4b* using flow visualisation images of exhaust jets at different exit Reynolds numbers Re_j. As observed by Liepmann & Gharib (1992) for a free jet, a potential core region is present close to the orifice where one can identify the formation of streamwise vortices, growing in size as they travel downstream and entrain ambient fluid (see *Figure 2.4c*). The vortices merge to form a large single vortex, which would break down abruptly shortly after into smaller structures. Similar flow mechanisms can be assumed at the free end of a three-dimensional wall jet, very close the nozzle.

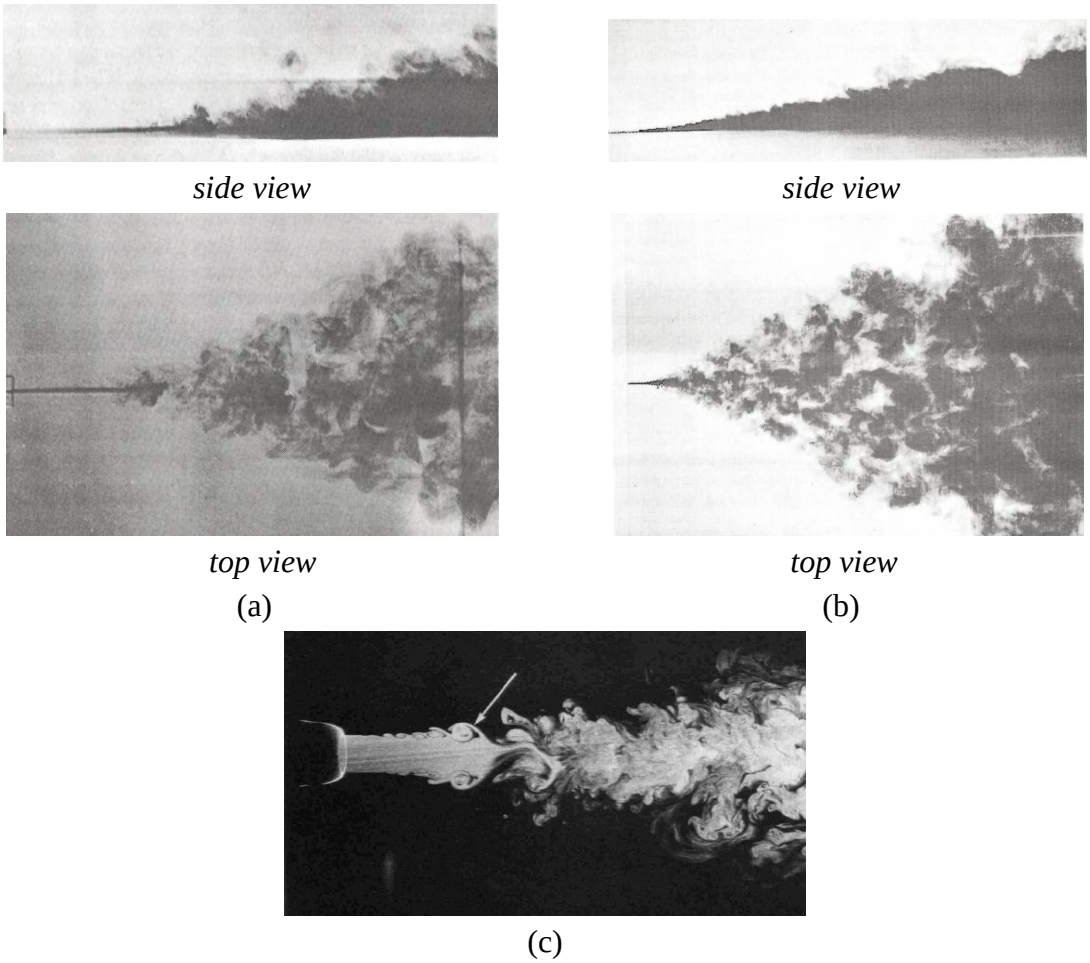

Figure 2.4: Flow visualisation of three-dimensional exhaust jets in quiescent air: (a) turbulent wall jet at Re_j = 1100, (b) turbulent wall jet at Re_j = 4000, (c) circular free jet at Re_j =5500 (images (a) and (b) taken from Launder & Rodi, 1983; (c) taken from Liepmann & Gharib, 1992, arrow indicates a streamwise vortex at 3.5 nozzle diameters downstream)

The notation used for a three-dimensional wall jet in quiescent air is presented in *Figure 2.5* with a rectangular-shaped orifice of width *d* and length *l*, and a schematic jet velocity distribution in the transverse and vertical directions at an arbitrary location downstream of the nozzle exit (only one side of the symmetry plane *xz* shown). For the case of a circular orifice, *d* is used to denote the orifice diameter. The vertical and transverse coordinates, where the wall jet velocity is half the maximum value U_{max}, are denoted with $z_{0.5}$ and $y_{0.5}$ respectively. The velocity U_{max} refers to the local maximum mean velocity in the *xz* plane. Sforza & Herbst (1967) observed that the actual maximum velocity at any position *x* did not necessarily occur on the *xz* plane, and suggested that it was caused by a system of vortex rings, present in the outer layer, which induced additional velocities in planes parallel to the wall surface. The strength of the vortices was observed to decrease with distance *x* and eventually they merged and diffused completely due to viscosity and turbulence effects.

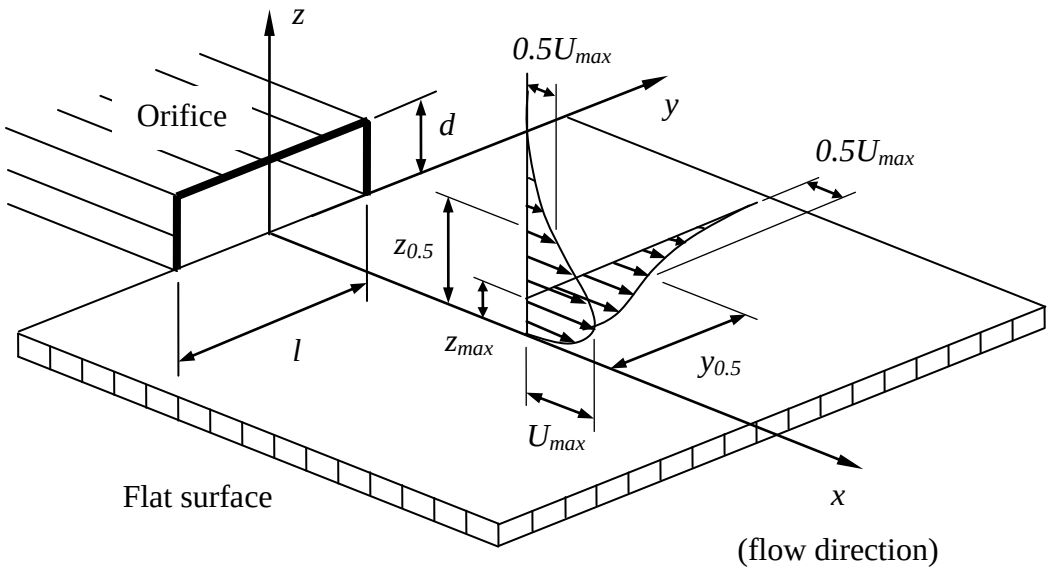

Figure 2.5: Three-dimensional wall jet without external stream – features and nomenclature (similar to Figure 1 in Sforza & Herbst, 1967)

2.3.1 Mean flow characteristics

Küchemann (1949) conducted experiments of a round wall jet of exit diameter *d* beneath an external stream for freestream-to-jet-exit velocity ratio $\beta = U_\infty / U_j$ of 0, 0.25 and 0.5. He observed that the horizontal jet spread decreased with increasing β. For a high freestream velocity, the peak in the velocity distribution is displaced in the positive *z* direction (away from the wall). The opposite effect was observed for a jet in still air – peak moving slightly towards the wall.

Sforza & Herbst (1967) experimentally investigated the mean properties of turbulent, three-dimensional, incompressible wall jets in quiescent air for rectangular orifices of variable width-to-length ratios d/l, also referred to as eccentricity, keeping the orifice area constant. With regard to the velocity decay with distance downstream of the orifice, three characteristic regions of flow development were observed:

1) *potential core* region with a uniform velocity distribution of magnitude close to the mean jet exit velocity.

2) *characteristic decay* region, where the turbulent mixing from the lateral (far) jet boundaries has not yet permeated the entire flow field. For low d/l of 0.025 and 0.05 the maximum velocity decay was found to be proportional to $x^{-0.41}$ and to $x^{-0.44}$ respectively, which is in good agreement with the results of Sigalla (1958) and Bradshaw & Gee (1962).

3) *axisymmetric decay* region, where the turbulent mixing is complete from all sides and the flow field is independent of the orifice geometry. The decay of U_{max} was found to be proportional to $x^{-1.10}$, which is characteristic for the two-dimensional radial wall jet investigated in Bakke (1957). For a square orifice ($d/l = 1$), the wall jet was observed to transition to a radial type already at $5d$ downstream, showing an absence of a characteristic decay region.

The extent of the first two regions, as well as the velocity decay in the characteristic decay region, was observed to depend significantly on the orifice geometry. Padmanabham & Lakshmana Gowda (1991a) reached similar conclusions for orifices having the shapes of various segments of a circle. They found the potential core and characteristic decay regions to extend up to $5 \le x/d \le 6$ and $20 \le x/d \le 40$ respectively, where d is the width of the circle segment of diameter l (analogous to the rectangular shape shown in *Figure 2.5*)

The proposed three-region flow structure is qualitatively similar to the structure observed by Trentacoste & Sforza (1966) for free jets in a similar experimental investigation. They reported a decay of $U_{max} \sim x^{-1}$ in the axisymmetric region, which is similar to the wall jet case of $U_{max} \sim x^{-1.10}$. These are shown in *Figure 2.6*, where the axisymmetric decay for both starts at $x \approx 30d$ (corresponding to $x \approx 10$ inches in *Figure 2.6*). This similarity is an indication that the retarding effect is caused primarily by the free shear due to mixing rather than the wall shear stress. The presence of the wall constrains the flow and results in a smaller rate of spread normal to the surface for a wall jet compared to a free jet, causing the flow to expand at a greater rate in lateral direction. Sforza & Herbst (1967) also observed flow similarity both normal and parallel to the wall in the axisymmetric decay region using the half maximum velocity coordinates $z_{0.5}$ and $y_{0.5}$ respectively. The growth rate $dz_{0.5}/dx$ was found to be virtually the same for the conventional orifice cases of $0.025 \le d/l \le 1$, while $dy_{0.5}/dx$ was found to be dependent on d/l until the axisymmetric decay region.

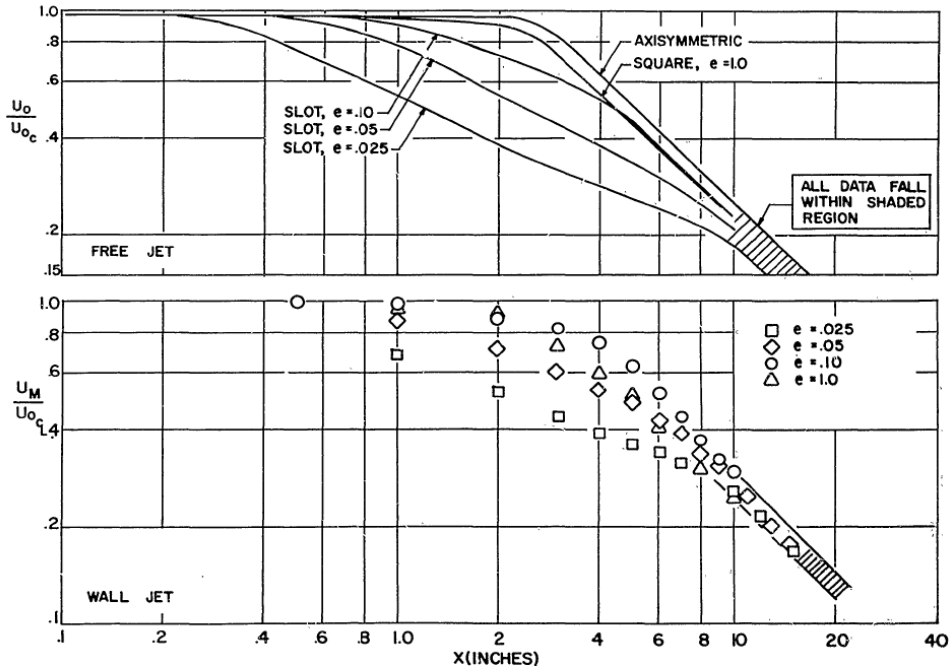

Figure 2.6: Maximum velocity decay in the symmetry plane for free jets and wall jets exiting from rectangular orifices of various eccentricity d / l (denoted with e) (taken from Sforza & Herbst, 1967)

Horizontal axis shows the longitudinal distance from the orifice x (in inches; 1 inch = 25.4 mm); a multiplication factor of (3.16 / inches) would convert x into x / d, where d would be the width of a square-shaped orifice area of 0.100 sq. inches (d / l = 1), kept constant for all orifice shapes; Vertical axis gives the ratio of local maximum velocity to jet exit velocity at the plane xz

The velocity decay and growth rates of three-dimensional jets have been reported by other authors, whose results are presented in *Table 2.2*. Most velocity decay results agree well with the exponent of –1.1 suggested by Sforza & Herbst (1967). Velocity data for different orifice shapes was found to collapse reasonably well on the same curve when plotted versus $x/A^{0.5}$, where A is the orifice area (Rajaratnam & Pani, 1974; Narain, 1975; Padmanabam & Lakshmana Gowda, 1991a; Hall & Ewing, 2007a). Most authors reported complete flow similarity, scaling the vertical and lateral velocity profiles with U_{max} and $z_{0.5}$ and $y_{0.5}$ respectively. The results for the lateral and vertical growth rates vary considerably between authors. It can be concluded that the wall jet grows approximately 4 to 5 times faster in lateral direction, although higher values have been reported, i.e. 9 times by Davis & Winarto (1980). The vertical length scale $z_{0.5}$ increases linearly with distance from the orifice x, while the variation of the lateral length scale $y_{0.5}$ with x is observed to be non-linear close to the orifice and linear further downstream. The start of the linear region has been reported to be $25d < x < 50d$.

The expected Reynolds number range in this work at 1:200 scale would be between 5000 and 9000 for a circular jet, similar to the data by Newman et al. (1972).

Table 2.2: Experimental results for velocity decay and growth rate of three-dimensional wall jets

Reference	*Orifice shape*	$Re_j = \rho U_j d / \mu$ *range*	*Vertical length scale* $z_{0.5}$	*Lateral length scale* $y_{0.5}$	*Velocity* U_{max} *(characteristic decay reg.)*
Sforza & Herbst (1967)	rectangular	5400 to 10800 (est. with U_j and d)	non-linear	non-linear	$U_{max} \sim x^{-1.10}$
Newman et al. (1972)	circular	2800 to 16400	$dz_{0.5} / dx = 0.050$	$dy_{0.5} / dx = 0.278$	$1 / U_{max} \sim x / d$
Rajaratnam & Pani (1974)	various	59500 to 102000	$z_{0.5} / d = 0.045x / d + 0.90$	$y_{0.5} / l = 0.20x / l - 1.25$ $x / l > 10$	$1 / U_{max} \sim x / d$
Narain (1975)	various	59500 to 102000	$dz_{0.5} / dx = 0.045$ (est. from data)	$y_{0.5} / d \sim (x / d)^{1.46}$	$U_{max} / U_j \sim (x / d)^{-1.06}$
Davis & Winarto (1980)	circular	170000 (est. with U_j and d)	$dz_{0.5} / dx = 0.037$ for $x / d \geq 40$	$dy_{0.5} / dx = 0.32$ for $x / d \geq 40$	$U_j / U_{max} = 0.15(x / d - 5.6)$
Koso & Ohashi (1982)	semi-circular	66200	$z_{0.5} / d \sim (x / d)^{0.8 \pm 0.05}$	$y_{0.5} / d \sim (x / d)^{1.61 \pm 0.02}$	$U_{max} / U_j \sim (x / d)^{-1.27 \pm 0.02}$
Launder & Rodi (1983)	–	–	$dz_{0.5} / dx = 0.048$	$dy_{0.5} / dx = 0.26$	–
Padmanabham & Lakshmana Gowda (1991a)	segments of a circle	95400	$0.067 \leq dz_{0.5} / dx \leq 0.04$	$0.216 \leq dy_{0.5} / dx \leq 0.25$	$U_{max} / U_j \sim (x / d)^{-1.15 \pm 0.02}$
Abrahamsson et al. (1996)	circular	80000 (est. with U_j and d)	$dz_{0.5} / dx = 0.065$	$dy_{0.5} / dx = 0.32$	$U_{max} / U_j \sim (x / d)^{-1.29}$
Law & Herlina (2002)	circular	5500 to 13700	$z_{0.5} / d = 0.042x / d + 0.60$ for $x / d > 20$	$y_{0.5} / d = 0.21x / d - 1.91$ for $x / d > 25$	$U_{max} / U_j = 9.23(x / d)^{-1.066}$ for $x / d \geq 20$
Sun & Ewing (2002)	circular	108000	$dz_{0.5} / dx = 0.045$ for $20 \leq x / d \leq 40$	$dy_{0.5} / dx \approx 0.24$ (est. for $30 \leq x / d \leq 40$)	$U_{max} / U_j \sim (x / d)^{-1.2}$ (est. for $30 \leq x / d \leq 40$)
Hall & Ewing (2007a)	rectangular	89600	$dz_{0.5} / dx = 0.052$ (est. for $20 \leq x / d \leq 60$)	non-linear for $x / d \leq 60$; vary with d / l	$U_{max} / U_j \sim (x / A^{0.5})^{-0.162}$ for $x / A^{0.5} \geq 20$
Agelin-Chaab & Tachie (2011a)	circular	5000 to 20000	$dz_{0.5} / dx = 0.054$ for $52 \leq x / d \leq 100$	$dy_{0.5} / dx = 0.255$ for $50 \leq x / d \leq 70$	$U_{max} / U_j \sim (x / d)^{-1.15}$ for $52 \leq x / d \leq 100$

Law & Herlina (2002) also obtained data on gas concentration of neutrally buoyant wall jets using laser-induced-fluorescence flow visualisation and calculated a mathematical relationship for the decay of maximum concentration along the x axis for $x/d > 20$, shown in *Equation 2.5*. By calculating the concentration half-width length scale in the lateral and vertical directions, similar to $y_{0.5}$ and $z_{0.5}$ respectively, they observed that in each direction the concentration expanded approximately 1.5 times faster than the velocity. The ratio of lateral to vertical concentration growth rate was consequently the same as the ratio of $(dy_{0.5}/dx)$ to $(dz_{0.5}/dx)$, equal to 5.0.

$$\frac{c_{max}}{c_j} = 6.97\left(\frac{x}{d}\right)^{-1}$$

Equation 2.5

Reynolds number dependency studies for a defined jet Reynolds number of $Re_j = \rho U_j d/\mu$ were performed by Newman et al. (1972), Law & Herlina (2002) and Agelin-Chaab & Tachie (2011a) for circular nozzles, Launder & Rodi (1983) for a square nozzle, and by Rajaratnam & Pani (1974) for circular, rectangular, square, triangular and elliptic nozzles. Newman et al. (1972) reported no variation with Re_j for $2.8\times10^3 \leq Re_j \leq 1.64\times10^4$, which can also similarly be concluded from the data of Rajaratnam & Pani (1974) for $5.95\times10^4 \leq Re_j \leq 1.02\times10^5$ and Law & Herlina (2002) for $5.5\times10^3 \leq Re_j \leq 1.37\times10^4$. At the same time, a recent investigation by Agelin-Chaab & Tachie (2011a) for $5\times10^3 \leq Re_j \leq 2\times10^4$ suggests a significant dependency of the flow development on Reynolds number up to $50d$ for the decay of U_{max} and the jet growth rates $dz_{0.5}/dx$ and $dy_{0.5}/dx$, and up to $20d$ for the velocity profile similarity.

At the same, Launder & Rodi (1983) reported significant Reynolds number dependence of the jet growth rate for lower Re_j of 1.1×10^3 and 4.0×10^3 (see *Figure 2.4a* and *Figure 2.4b* for flow visualisation images). For these Re_j the lateral growth was observed to be twice and more than three times the vertical growth rate respectively.

2.3.2 Turbulence characteristics and flow structure

Turbulence measurements indicate that, with regard to streamwise turbulence intensity, flow similarity occurs at a certain distance downstream of the orifice. This distance was observed to be $x/d \geq 110$ by Newman et al. (1972), $x/h \geq 60$ by Padmanabam & Lakshmana Gowda (1991b), $x/d \geq 40$ by Agelin-Chaab & Tachie (2011a), and $x/A^{0.5} \geq 30$ by Hall & Ewing (2007a). The values of $x/d = 110$, $x/d = 60$ and $x/d = 40$ correspond to $x/A^{0.5} \approx 124$, $37 \leq x/A^{0.5} \leq 67$ and $x/A^{0.5} \approx 45$ respectively, calculated by taking into account the corresponding orifice areas used. These

differences highlight the influence of the orifice on the flow characteristics. The streamwise turbulence for a three-dimensional circular wall jet was reported by Newman et al. (1972) to be significantly higher (~ 50%) compared to a two-dimensional wall jet, a statement also supported by Abrahamsson et al. (1996).

Using flow visualisation, Newman et al. (1972) observed a strong divergence of the jet pathlines at the wall surface away from the plane of symmetry (see *Figure 2.7*). Similarly, based on velocity correlation measurements, Davis & Winarto (1980) concluded that the presence of the wall caused an interaction between its surface and the normal component motions towards the surface, which produced "strong out-flow motions along the plane in a symmetrical manner about the plane of symmetry". They reported the existence of a large-scale motion in a plane perpendicular to the jet flow, indicated by higher levels of measured momentum transport in the lateral direction than in the vertical direction. This motion provides a physical mechanism for the increased mixing parallel to the surface and the resulting high lateral growth rate.

Reviewing the results of Newman et al. (1972) and Davis & Winarto (1980), Launder & Rodi (1983) emphasised the "substantial and sustained streamwise vorticity" created in a three-dimensional wall jet and recognised its importance in the jet's anisotropic growth pattern. They identified the anisotropy of the Reynolds stresses in the plane at right angles to the flow as one of the potential source of the induced streamwise vorticity. The validity of this statement was confirmed in a computational investigation by Craft & Launder (2001), who attributed the large lateral growth rate entirely to the induced streamwise vorticity.

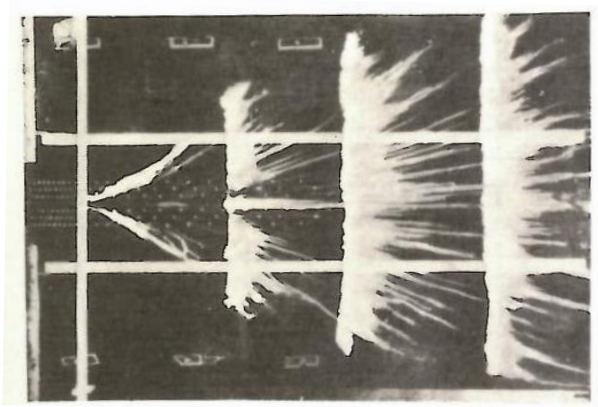

Figure 2.7: Flow visualisation of the surface pathline pattern of a circular three-dimensional wall jet (by Newman et al., 1972)

An experimental investigation by Iida & Matsuda (1988) also shows evidence of secondary flows, identified by the presence of two pairs of streamwise vortices located in a symmetrical arrangement with respect to the *xz* plane near the wall ($z < z_{max}$) and in

the mixing region ($z > z_{max}$) respectively (see small image in *Figure 2.8a*, where the vertical and lateral axes are Y and Z respectively, and z_{max} is denoted as Y_m). The formation mechanism of these vortices was further investigated by Matsuda et al. (1990) for $Re_j = 1.6\times10^5$ and by Ewing & Pollard (1997) for $Re_j = 2.5\times10^4$, using Hot-Wire Anemometry. They found the presence of a large-scale structure very much resembling a horseshoe vortex, which stretched and inclined progressively in the direction of the flow near the surface as it moved downstream (see *Figure 2.8a*). As a consequence of the inclination, the legs of the horseshoe vortex form counter-rotating quasi-streamwise vortices in the mixing region, identified by Matsuda et al. (1990) as the primary cause of the high lateral growth rate.

Ewing & Pollard (1997) modified the model suggesting that the structures shed by the circular jet were ring-like vortices which interacted with the wall, resulting in the centre of their base being raised off the surface while the outer edges of the base moved closer to the surface. This phenomenon resulted in the formation of two horseshoe vortices, one large near the jet edges and one smaller near the jet centre line, shown with solid and dashed contours respectively in *Figure 2.8a*. Such modification predicts both pairs of streamwise vortices observed by Iida & Matsuda (1988). Hall & Ewing (2007b) observed a similar pattern of a large horseshoe vortex, associated with the outer shear layers, and a smaller independent structure near the wall.

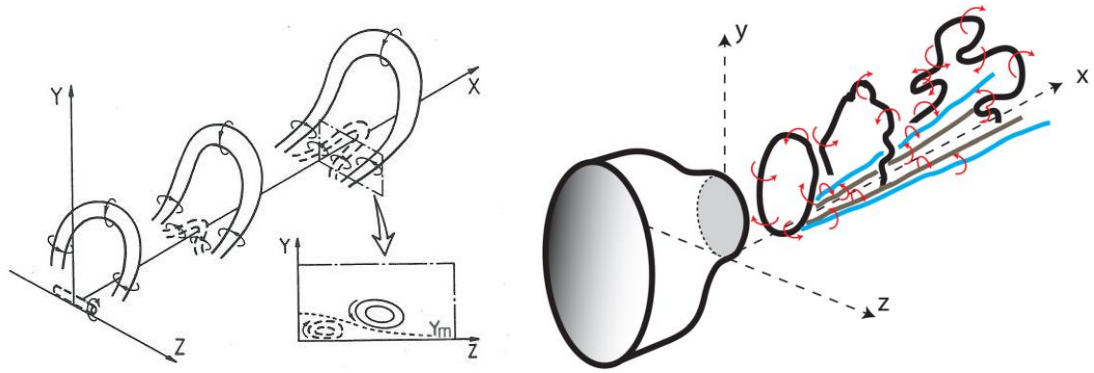

(a) (b)

Figure 2.8: Proposed models of vortex structures in near-field region of a three-dimensional wall jet according to (a) Matsuda el al., 1990 and (b) Namgyal & Hall, 2013

Y and Z in (a) and y and z in (b) denote the vertical and transverse axes respectively, differing from the notation shown in Figure 2.5

A recent investigation by Hall & Ewing (2010) for square wall jets of $Re_j = 9\times10^4$ showed that the large coherent structures were asymmetric with respect to the jet centre line. Their passage was associated with lateral sweeps of fluid across the entire span of the jet, causing the characteristic large lateral spread.

Namgyal & Hall (2013) investigated a round wall jet of $Re_j = 1.2\times10^5$ at $x/d = 5$ using Particle Image Velocimetry attempting to link the formation of mean streamwise vorticity (secondary flow) and the unsteady vorticity of the coherent structures in the near field. They proposed a flow model, shown in *Figure 2.8b*, which predicts the development of instabilities within the large coherent vortex rings as they travel downstream, which would eventually form into coherent streamwise vortex structures away from the surface, similarly to a free jet. The smaller structures also form streamwise vortex pairs, bound close to the wall, which are not related to the vortices away from the wall, as observed by Hall & Ewing (2007b). Namgyal & Hall (2013) concluded that the coherent vortex structures, formed in the outer shear layers in the near-field region, did not contribute directly to the secondary flow in the plane at right angles to the flow.

2.4 Offset jets

The term 'offset jet' describes a jet originating from an orifice, located at an offset distance of a few orifice diameters *d* above a flat surface. The features and characteristic regions are shown schematically in *Figure 2.9* for a two-dimensional offset jet exiting from an orifice in a vertical wall (offset distance is denoted with *b*). Because of the offset, the jet travels a certain distance downstream before attaching to the surface. As it travels further, it would eventually acquire the flow characteristics of a wall jet, defining the longitudinal span of the *attachment* region, also called *impingement* region, and the start of the *wall jet* region. The region upstream of the attachment point is characterised by reverse flow. Compared to a free jet, the offset jet is drawn towards the surface by the Coanda effect, causing a downwards jet trajectory as illustrated in *Figure 2.9*. The Coanda effect is described by Giles (1977) as follows. Due to the presence of the wall surface, less fluid is available for entrainment on the surface side compared to the free side as the jet expands. This causes a partial vacuum or low pressure area between the surface and the jet, which tends to attract the jet towards the surface.

Rajaratnam & Subramanya (1969) and Pelfrey & Liburdy (1986) reported that downstream of a small developing sub-region within the wall jet region, the flow becomes independent of the offset distance. Both observed velocity profile similarity at a distance from the nozzle of $x/d \approx 20d$. For an offset of $7d$ and Re_j of 1.5×10^4, Pelfrey & Liburdy (1986) reported that the jet attached at $x/d = 13$. In a similar investigation for an offset of $3d$ and Re_j of 1.78×10^4, Miller & Comings (1960) observed attachment at $x/d = 7$. In comparison, a turbulent free jet would have a half-width of $3d$ at $x/d \approx 12$ and $7d$ at $x/d \approx 30$, calculated with a half-width spread angle of approximately 12 degrees, given by Tollmien (1945). This difference can be attributed to the Coanda

effect and the associated downwards trajectory of the jet, causing the jet to attach earlier. Hoch & Jiji (1981) obtained results for the offset jet trajectory in a parallel freestream, varying the orifice offset at 3*d*, 5.7*d* and 8.7*d* and the ratio of ambient velocity to exit jet velocity β between 0 and 0.25. It is evident that up to 5.7*d* the attachment point is not influenced by the freestream velocity for the range of β tested, while at 8.7*d* the attachment is delayed further downstream.

More recent investigations on two-dimensional offset jets have been conducted by Nasr & Lai (1998) and Gao & Ewing (2008). Results by Nasr & Lai (1998) showed that the static pressure variation on the wall surface is independent of Reynolds number for $Re_j > 1.0\times10^4$. They also obtained a relationship for the attachment distance variation with offset ratio, shown in *Equation 2.6* where the nomenclature of *Figure 2.9* is used.

$$\frac{x_r}{d} = 2.63\left(\frac{b}{d}\right)^{0.855}, \text{ for } b/d \leq 20$$

Equation 2.6

Gao & Ewing (2008) concluded that, based on the variation of jet half-width and maximum velocity, five regions in the flow development could be distinguished for small offsets ($\leq 1.7d$) – three within the attachment process ($x/d \leq 6$), and two describing the development towards a wall jet. The developed wall jet region was observed to be at $x/d \geq 10$.

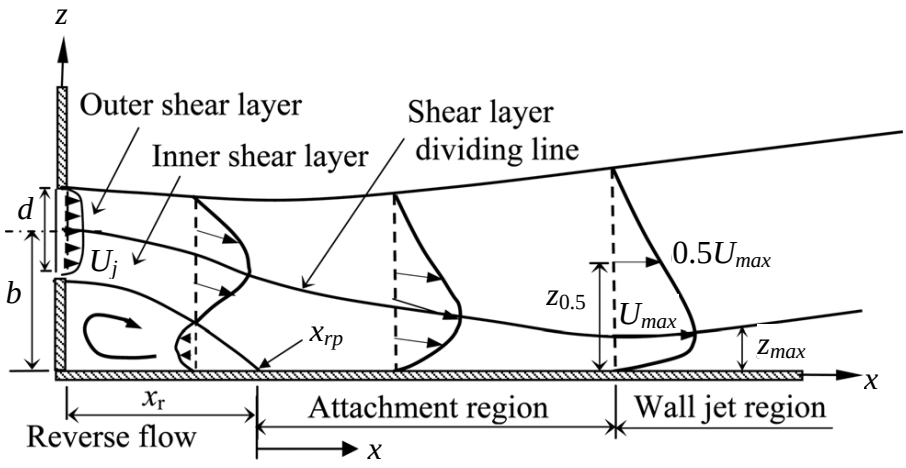

Figure 2.9: Offset jet features and nomenclature, adapted from Agelin-Chaab & Tachie (2011b)

Considerably less research has been done on three-dimensional offset jets. McLean and Herring (1976) conducted experiments for a single circular jet at a surface offset of 3*d* and an array of eleven jets, placed uniformly in lateral direction at spacings

of 35*d*. They used a high exit jet Mach number of 0.89 at $Re_j \approx 4.3\times10^4$ and reported that the compressibility effects were limited primarily to the potential core region. For a single jet, the maximum velocity decay was observed to be $U_{max} \sim x^{-1.23}$ between $100 \leq x/d \leq 200$. The measured entrainment rate up to $x/d \leq 150$ agreed well with results for a free jet, implying that the wall had very little effect on the total entrainment. For the array of jets, the entrainment rate was reported to fall below the values for a free jet as soon as adjacent jets began to merge, i.e. $x/d \leq 20$. Two-dimensionality of the array of jets, in terms of mean flow characteristics, was observed at $x/d \geq 30$.

Nozaki (1983) investigated the effects of nozzle shape and Reynolds number on the attachment of an offset jet for rectangular nozzles of aspect ratio between 1 and 8. Within the range $9.5\times10^4 \leq Re_j \leq 1.02\times10^5$, he observed no Reynolds number influence on the attachment flow for aspect ratios larger than 2. Furthermore, the flow behaviour of offset jets of nozzle aspect ratio larger than 3 was shown to be approx. two-dimensional. For smaller aspect ratios, Nozaki (1983) proposed correction factors for calculation of the attachment distance downstream of the nozzle as a function of the offset distance, nozzle aspect ratio and Re_j.

Davis and Winarto (1980) and Agelin-Chaab & Tachie (2011b) performed similar experiments with a circular nozzle at offsets between 0.5*d* and 4*d*. For $Re_j \approx 1.7\times10^5$, Davis and Winarto (1980) observed both the lateral and vertical growth rates to decrease and increase with increasing offset respectively. The values varied between $0.32 \leq dy_{0.5}/dx \leq 0.23$ and $0.037 \leq dz_{0.5}/dx \leq 0.046$ for $0.5 \leq b/d \leq 4$. Agelin-Chaab & Tachie (2011b) obtained the growth rates $dz_{0.5}/dx = 0.055 \pm 0.001$ and $dy_{0.5}/dx = 0.250 \pm 0.005$ for a Reynolds number range of $1.0\times10^4 \leq Re_j \leq 2.0\times10^4$. Both investigations confirmed only small differences in the growth rates up to $b/d = 2$, and reported a similar decay of maximum velocity: $U_{max} \sim x^{-1.15}$ by Davies and Winarto (1980) and $U_{max} \sim x^{-1.18 \pm 0.03}$ by Agelin-Chaab & Tachie (2011b). The latter ones also observed the growth rates and maximum velocity decay to be nearly independent of Re_j for $x/d \geq 73$ and $b/d \leq 2$. For $b/d = 1$, 2 and 4, Agelin-Chaab & Tachie (2011b) reported the attachment distance downstream from the nozzle to be $x_r/d = 1.5$, 3.2 and 6.4 respectively, increasing linearly with b/d and remaining nearly constant within the Reynolds number range tested. These values are larger compared to the two-dimensional offset jet values, calculated from *Equation 2.6*.

2.5 Jet interaction

The multiple-engine exhaust jets of an aircraft taking off merge rapidly into a single jet as they travel downstream, as observed in Lidar measurements by Bennett et

al., 2010. Single take-off plumes are also evident in the Lidar data of Wayson et al. (2008). Following this assessment, it would reasonable to assume that the merged exhaust jet could be modelled with a single nozzle at sub scale. The interaction of parallel jets is discussed briefly in this section.

First, it is useful to define a criterion for the merging of multiple jets. With regard to concentration and velocity distribution, "the merger point is taken to be the shortest distance from the nozzles that the velocity profile has a single as opposed to double peak" (Baratian-Ghorghi et al., 2012, p. 258). This point indicates the beginning of the 'combined jet' region, where the flow has the characteristics of a single jet.

Miller & Comings (1960) investigated the interaction between two parallel two-dimensional jets, separated by an offset r (distance between the nozzle centre lines, see *Figure 2.10* where it is denoted with $2b$) of $6d$ at $Re_j = 1.78\times10^4$. It was found that the jets merged at $x/d = 12$ downstream, forming a single jet which exhibited all mean flow characteristics of a single-jet flow. The jet convergence was caused by a sub-atmospheric static pressure region between the individual jets at distances x close to the orifices.

Tanaka (1970) conducted experiments of two parallel two-dimensional jets at Re_j between 4.29×10^3 and 8.75×10^3 and nozzle spacing r between $8.5d$ and $26.3d$. He found the non-dimensional distance of the merging point x_{mp}/d (see *Figure 2.10*) to vary with r/d as follows: $x_{mp}/d = 5.06(r/d)^{0.27}$ for $r/d < 16$ and $x_{mp}/d = 0.667(r/d)$ for $r/d > 16$. In a subsequent report, Tanaka (1974) showed that a single jet with one distinct velocity maximum formed downstream between $19d$ and $30d$, or approximately $2.24r$ and $1.14r$ respectively, for the range of r/d tested. He also observed no Reynolds number dependence on the maximum velocity decay with x within the range Re_j of tested.

Lin & Sheu (1991) investigated parallel two-dimensional jets at large spacings r between 30 and $40d$ and reported the same distance for the start of the combined region of $1.3r$. Similar experimental investigations by Nasr & Lai (1997) for $r = 4.25d$ and $Re_j = 1.1\times10^4$, and Fujisawa et al. (2004) for $r = 3d$ and $Re_j = 1.1\times10^3$, showed a combined region starting at $x/d \geq 8$ and $x/d \geq 6$ respectively (both at approximately $x/r > 2$). Recently, Durve et al. (2012) reported $x/r \approx 3$ for the start of the combined region.

It should be noted that the above results were reported for free jets. As discussed in Chapter 2.3, wall jets have a greater lateral spread compared to free jets, thus the merging would occur at a shorter distance from the jet exit plane. Based on the results for free jets, it would be safe to assume that the start of the combined region would be at $x < 2r$.

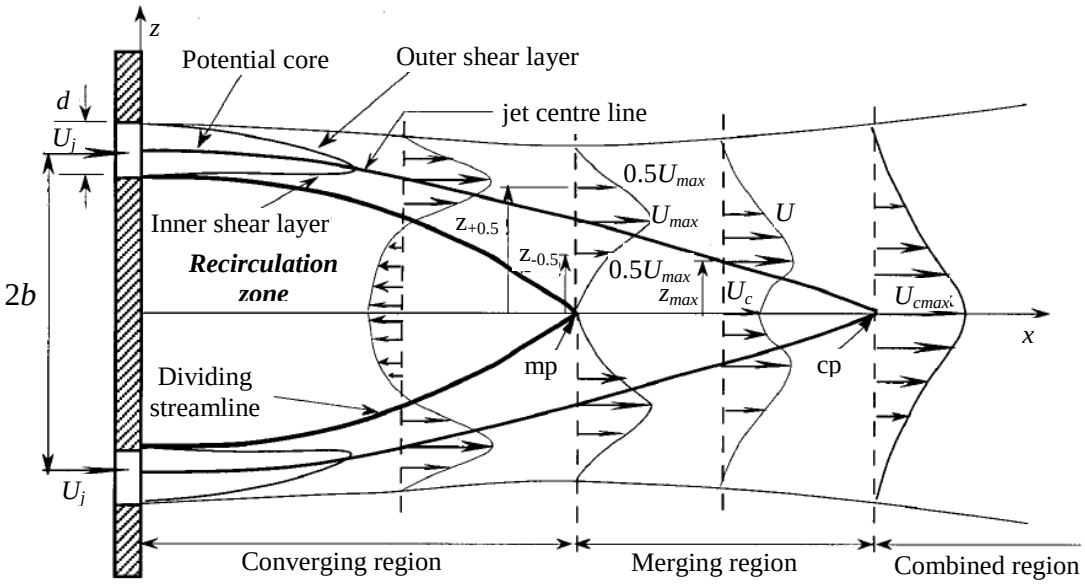

Figure 2.10: Schematic diagram of the merging of two parallel two-dimensional jets (adapted from Nasr & Lai, 1997)

Nomenclature used: 'c' at centre line (along x axis); 'mp' plane where jets merge, 'cp' plane where jets form a single jet of one velocity maximum at centre line; b denotes offset distance of wall from nozzle centre line for a single offset jet case (2b = 4.25d)

2.6 Buoyant flows

The ability of an aircraft engine exhaust to rise in the surrounding air due to its natural buoyancy is the fundamental principle in the proposed baffles concept. Therefore a literature review on buoyant flows and their characteristics is presented in this section.

In general terms, buoyancy can be described as the capacity of an object to stay afloat or rise when submerged in a fluid. Examples in engineering include ships, submarines, hot air balloons, as well as buoyant exhaust plumes from chimneys, exhaust pipes etc. In the latter cases of heterogeneous flows, i.e. gases, or in general fluids, of different density, the plume tends to rise with a surrounding denser gas. The force exerted by gravity on each element of fluid is ρg per unit volume, where ρ is the local fluid density and g is the acceleration due to gravity, thus the buoyancy effects result from the variation of ρ from point to point in the fluid (Turner, 1973, p. 3).

Morton (1959) described the two limiting cases of a forced flow as 'plume' and 'jet', referring respectively to the flow from a source of buoyancy and from a source of momentum only. A buoyant flow exiting a stationary source would have jet

characteristics close to the source, and plume characteristics further downstream as its buoyancy starts dominating the flow behaviour. Shabbir & George (1994) described the distance x (or height z for vertical plumes), over which the buoyancy overcame the initial momentum at the source, in terms of the Morton length scale l_M, defined as

$$l_M = \frac{M_0^{3/4}}{F_0^{1/2}}$$

Equation 2.7

where M_0 and F_0 are the specific momentum and specific buoyancy at the source.
Their analysis shows plume-like behaviour of a vertical forced jet at $z / l_M > 5$. Dai et al. (1994) and Sangras & Faeth (1999) gave a relationship for l_M, shown in *Equation 2.8*, for a uniform round jet, exiting with a velocity U_j from a source of diameter d, and an absolute difference between jet and ambient fluid density $\Delta\rho = |\rho_j - \rho_\infty|$.

$$l_M = d\left(\frac{\pi}{4}\right)^{0.25}\sqrt{\frac{\rho_\infty U_j^{\,2}}{\Delta\rho g d}}$$

Equation 2.8

2.6.1 Governing similarity parameters

Modelling of buoyant flows at reduced scale requires accurate scaling of the governing flow parameters such as buoyancy and flow induced pressures. Using dimensional analysis, Poreh & Hassid (1982) obtained similarity parameters in a theoretical investigation on ventilation and air exchange in buildings. With regard to buoyancy and momentum driven flow motion at low and moderate Mach numbers, these include the excess temperature ratio $\Delta T / T_\infty$, the ratio $U_j^{\,2} / gl$, which is the squared Froude number $Fr^{\,2}$ (see *Equation 1.3*), as well as Reynolds number *Re* and Prandtl number. The Prandtl number gives the ratio of momentum to thermal diffusivity independent of a length scale, thus it would have the same value in full-scale and model testing in air. Its effects were considered negligible Poreh & Hassid (1982).

With regard to buoyancy, two similarity parameters are used universally in flow modelling and are considered or primary importance in buoyancy-driven plume dispersion (Zhu et al., 1998). These are:

- *Froude number Fr*, used primarily to describe the initial conditions of an exhaust jet at the source. Examples include the works of Sharp & Vyas (1977), Meroney (1979), Chen (1991), Dai et al. (1994), Hanna et al. (1998) and Kanda et al. (2006).

- *Richardson number Ri*, which represents the ratio of buoyancy to inertia terms (Turner, 1973, p. 12). It is used in studies of vertical exhaust jets and buoyant plumes (e.g. Miles, 1961; Subbarao, 1989; Wang & Law, 2002; Kaminski et al., 2005), as well as in atmospheric stability studies (e.g. Carlson & Foster, 1986; Yang et al., 2007).

The general form of the Richardson number is shown in *Equation 2.9*, where l is a characteristic length scale and U is the relevant velocity scale (usually U_j in buoyant jet studies). Local Richardson number can be calculated with the local vertical velocity and a vertical (e.g. Miles, 1961) or radial (e.g. Kaminski et al., 2005) length scale. Miles (1961) described the Richardson number as the principal measure of stability when buoyancy forces dominated inertia forces ($Ri > 1$).

$$Ri = \frac{gl}{U^2}$$

Equation 2.9

Generally, the Froude and Richardson numbers are related by $Ri = 1/Fr^2$, since in both similarity parameters a velocity scale and a length scale is used. In buoyant flows where density differences are small, it is common to apply what is known as the Boussinesq approximation – density differences are considered negligible on the inertia forces and are accounted for only in the buoyancy term (Spiegel & Veronis, 1960), using the reduced gravitational acceleration $g' = g(\rho_\infty - \rho_j)/\rho_\infty$. This is referred to as 'densimetric' Froude or Richardson number. For small temperature differences, Poreh & Hassid (1982) and Gerz & Ehret (1997) use the ratio $\Delta T/T_\infty$ to calculate g' instead of the excess density ratio $(\rho_\infty - \rho_j)/\rho_\infty$. In this case, ΔT is the difference between jet and ambient absolute temperatures, and T_∞ is the ambient absolute temperature.

Poreh & Hassid (1982) and Pournazeri et al. (2012) reported that after a certain minimum Reynolds number *Re*, the primary large scale characteristics of turbulent flows are similar and become independent of *Re*. This was also observed by Turner for buoyant flows at large values of *Re*, stating that the Reynolds number cannot "enter directly into the determination of the overall properties of a turbulent plume" (Turner, 1973, p. 168). For non-buoyant external flows around bluff bodies, Reynolds number independence occurs for $Re > 1.1\times10^4$ (Cermak, 1975), based on a characteristic length scale of the body, while for turbulent buoyant flows this is expected to start at even lower values of *Re* (Schlichting, 1979, cited in Poreh & Hassid, 1982, p. 562).

For a buoyant jet in a freestream, Subbarao (1989), Sinclair et al. (1990) and Ramsdale & Tickle (2001) highlighted the importance of the co-flow-to-jet-velocity

ratio $\beta = U_\infty / U_j$ on the flow development and on the ability of a buoyant wall jet to detach from the wall surface ('lift-off'). Hoult et al. (1969) identified the densimetric exit jet Froude number, calculated with the reduced gravitational acceleration, and the ratio of ambient wind velocity to exit jet velocity as the two primary scaling parameters in wind tunnel modelling of buoyant plume dispersion. They also reported that the Reynolds number could be neglected in comparisons of model and theory.

2.6.2 Buoyant wall jets and lift-off

The case of buoyant jet near a surface has been investigated predominantly for environmental purposes, to study the dispersion of waste disposal and the released of pollutants by human industrial activity into the atmosphere and hydrosphere. Compared to non-buoyant wall jets, significantly less information has been reported on buoyant wall jets. Experimental studies have been performed mostly in water tanks (e.g. Sharp & Vyas, 1977; Wiuff, 1977; Sinclair et al., 1990; Chen, 1991), and in wind tunnels using buoyant gases (e.g. Meroney, 1979; Poreh & Cermak, 1988). Other studies by Briggs (1973) and Hanna et al. (1998) show a theoretical approach to parameterise the plume lift-off.

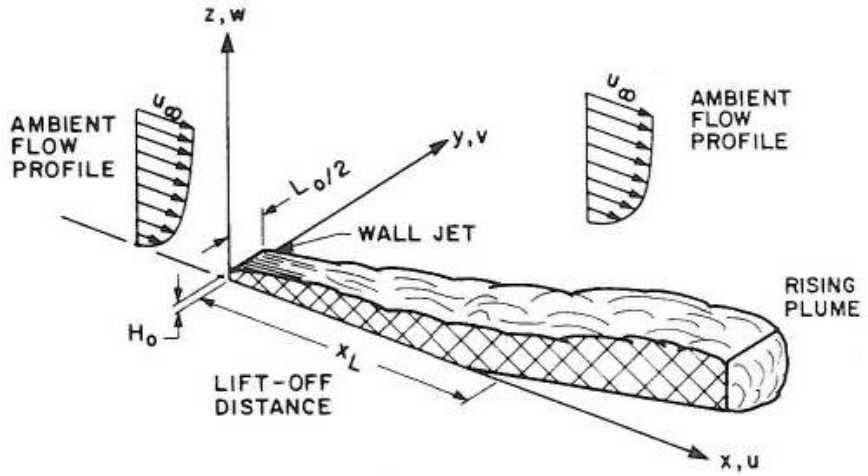

Figure 2.11: Schematic illustration of a buoyant wall jet in an ambient co-flow (taken from Sinclair et al., 1990)

The flow development of a buoyant wall jet in ambient co-flow is illustrated in *Figure 2.11*. If the initial jet buoyancy is relatively small, the jet would stay attached to the ground and diffuse like a non-buoyant wall jet. As its initial buoyancy is gradually increased, the jet tends to transport upward with enhanced vertical dispersion, compared to a non-buoyant jet, without a complete physical detachment from the surface (Sharp &

Vyas, 1977; Meroney, 1979; Hanna et al., 1998). Whether a buoyant jet would lift itself off the ground depends on the interaction between the vertical forces due to buoyancy and the pressures induced by the ambient flow velocities which keep the jet attached to the surface. This may be expected to happen at high source buoyancy and low ambient velocities (Meroney, 1979; Sinclair et al., 1990).

Buoyant wall jet lift-off is affected by various flow parameters. Sinclair et al. (1990) highlighted the influence of jet temperature, ambient and jet velocity, and source orifice shape. Briggs (1973) obtained a single lift-off parameter L_p, defined in *Equation 2.10*, where l is the vertical length scale of the jet and u^* is the friction velocity, defined in *Equation 2.11* with the local wall shear stress τ_w and the fluid density ρ. A common approximation for estimating the friction velocity was given by Hanna et al. (1998): $U/u^* = 10$. Due to lack of measurements, Briggs (1973) reported high uncertainty in calculating an accurate critical value of L_p for which lift-off occurs. Measurements by Meroney (1979) showed this to be $9 \leq L_p \leq 27$ for point source jets, while Hanna et al. (1998) stated values of $L_p \geq 20$.

$$L_p = \frac{(\rho_\infty - \rho) g l}{\rho_\infty u^{*2}}$$

Equation 2.10

$$u^* = \sqrt{\frac{\tau_w}{\rho}}$$

Equation 2.11

Meroney (1979) conducted experiments with helium wall jets from line, area and point sources in a 1:375 scale neutral Atmospheric Boundary Layer (no thermal processes), developed over a roughness length $z_0 \approx 4.6 \times 10^{-3}$ m. His results showed that increased ambient wind velocity delayed lift-off. The ambient velocity U_{ref} was measured at a reference height from the surface of 20 nozzle diameters, corresponding to 0.25 m. As depicted in *Figure 2.12a*, at $\beta = U_{ref} / U_j \approx 0.14$, corresponding to $U_{ref} =$ 0.76 m/s, the helium jet detaches completely from the surface, leaving behind only small traces of low-concentration gas. This is not the case for $\beta \approx 0.33$ or $U_{ref} = 1.83$ m/s (see *Figure 2.12b*), where no lift-off from the surface is visible within the shown distance downstream. It should be noted that although there is coherent plume lift-off, individual buoyant eddies are able to propagate upwards.

Measuring the lift-off distance for various ambient velocities and jet volumetric flow rates, Meroney (1979) obtained the relationship

$$\frac{x}{l_b} \geq 0.24(Fr*)^{1.5}$$

Equation 2.12

where $Fr*$ is the modified Froude number and x / l_b is the non-dimensional lift-off distance, defined as the ratio of the measured longitudinal distance to lift-off x to the buoyancy length scale l_b. The definitions of l_b and $Fr*$ are shown *Equation 2.13*, where Q_j is the source volumetric flow rate and l_{ref} is a characteristic source width (i.e. 0.03 m for the point source arrangement). The empirical relationship of *Equation 2.12* suggests that a buoyant jet would always eventually lift off, and the distance to lift-off downstream of the source increases with $Fr*$.

$$l_b = \frac{Q_j g(\rho_\infty - \rho_j)}{\rho_\infty U_{ref}{}^3} \qquad Fr* = \frac{\rho_\infty U_{ref}{}^3 l_{ref}}{Q_j g(\rho_\infty - \rho_j)}$$

Equation 2.13

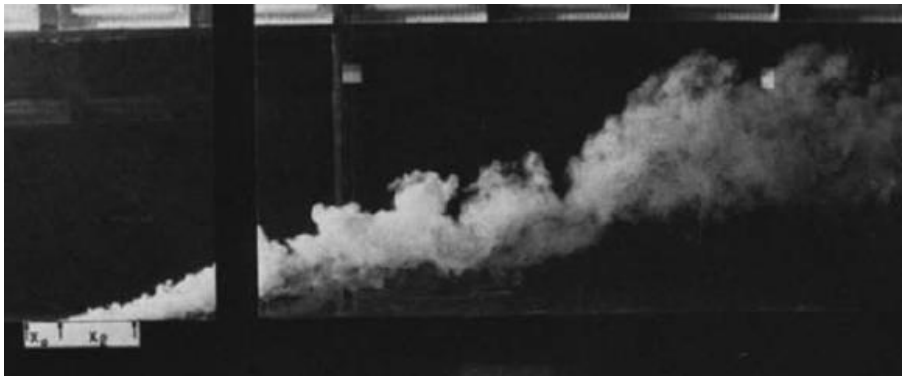

(a)

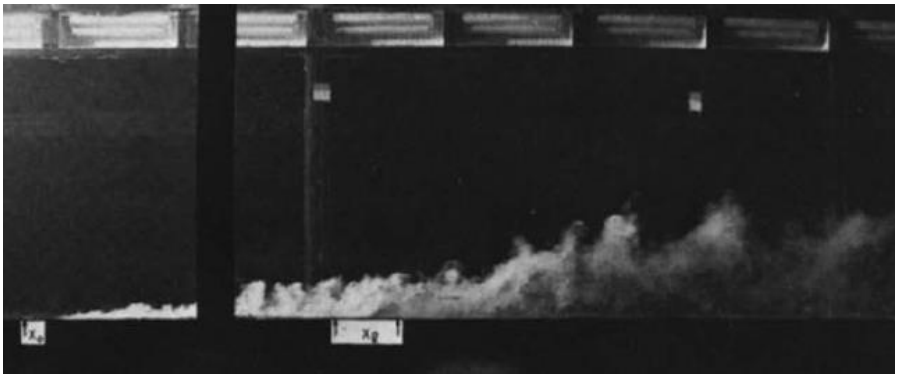

(b)

Figure 2.12: Side view images of a buoyant wall jet of helium and smoke exiting from a point source in a scaled neutral Atmospheric Boundary Layer (Meroney, 1979)
Co-flow velocity U_{ref} of (a) 0.76 m/s and (b) 1.83 m/s (no lift-off), measured at a reference distance of 25 cm ($y / d \approx 20$) above the wall surface

Sinclair et al. (1990) performed experiments of buoyant wall jets from a line source in a co-flowing turbulent boundary layer. They highlighted the important role of the wall jet's streamwise vorticity on the entrainment of ambient fluid near the wall, suppressing lift-off from the surface. The lift-off distance was measured for velocity ratios $\beta = U_{ref} / U_j$ between 0.1 and 0.5 at a constant ambient reference velocity $U_{ref} \approx$ 4.7 m/s, averaged over the height of the jet of 0.03 m. It was found that decreasing β increased the lift-off distance for low-aspect-ratio slot jets (also observed by Ramsdale & Tickle, 2001), which contradicts the results of Meroney (1979), who varied U_{ref} at constant values of U_j. It can be concluded that while the velocity ratio β is important in modelling the flow, it is not sufficient to characterise the jet lift-off.

Hanna et al. (1998) proposed using the local non-dimensional buoyancy flux to analyse lift-off. This is defined as $g\pi H(\rho_\infty - \rho) / (U_{ref}{}^2 \rho_\infty)$, where H is the local plume height and U_{ref} is the effective wind speed over the plume. Such 'local' parameters enable the analysis of flows which experience changes in buoyancy (e.g. due to chemical reactions) as they move downstream of the source. The model of Hanna et al. (1998) was validated using measurements by Hall & Waters (1986) of buoyant flows exiting from buildings. It predicts ground-level concentrations at the centre line of a buoyant plume, initially from a source on the ground, as a function of the non-dimensional buoyancy flux.

Recently, Aloysius & Wrobel (2009a) investigated numerically the dispersion characteristics of buoyant free jets and wall jets in a co-flow of 2.5 m/s (β = 0.031). The wall jet was found to rise from the surface at 55 nozzle diameters downstream. In a further numerical simulation, Aloysius & Wrobel (2009b) investigated the exhaust jet dispersion of an aircraft exhaust jet at take-off (headwind of 2.5 m/s) with a complete model of a Boeing 737 and a simplified model, consisting of two engines only. They reported that in the far field the flow was governed by counter-rotating streamwise vortices which created sinusoidal instabilities leading to break-ups of the plume and thus to its greater dispersion. The presence of the full aircraft geometry, compared to the simplified double-engine model, was found to enhance the effect of the streamwise vortices, also leading to greater plume dispersion. For the simplified model the plume was reported to lift-off from the ground at 363 engine diameters downstream of the engines, while for the complete model no lift-off was observed.

2.6.3 Plume rise, entrainment and concentration

Plume dispersion has been studied mainly for environmental purposes to predict the concentration of pollutants from industrial and domestic chimneys, pool fires,

accidental releases of hazardous materials, etc. As reported by Bennett et al. (1992b), the rate of plume rise is determined by: the buoyancy and momentum of the emissions, the ambient stability and the ambient wind velocity at the plume height. Models and theories of the buoyant plume rise have been developed most notably by Morton et al. (1956), Hoult et al. (1969) and Briggs (1975). Assuming self-similarity within the plume and a 'top-hat' distribution, i.e. constant buoyancy force and velocity across the plume and zero outside of it, Morton et al. (1956) proposed that the entrainment velocity was proportional to a characteristic velocity at the height in question, usually the vertical velocity. This was adopted by Hoult et al. (1969), who reported the existence of two additive entrainment mechanisms for rising plumes: one due to the difference between plume velocity and the ambient wind velocity component parallel to the plume, and the other due to the ambient wind velocity component normal to the plume. They concluded that the resulting two entrainment parameters were universal constants. Recent investigations on the entrainment parameters have been done by Wang & Law (2002) and Kaminski et al. (2005). The latter ones reported that the entrainment of ambient air was larger in plumes than in jets, as a result of buoyancy-induced turbulence.

For a neutrally stable laminar atmosphere, Briggs (1975) showed that the plume rise varied proportional to $x^{2/3}$, also known as the '$x^{2/3}$ law', where x is the downstream distance from the plume source in the direction of the ambient wind. A relationship for the vertical plume trajectory, taken from Hanna et al. (1982) is shown in *Equation A.2* in Appendix A. Modifications of Briggs's model have been proposed for example by Netterville (1990), to account for atmospheric turbulence effects, and by Bennett et al. (1992a) in an experimental investigation using Lidar measurements. Other mathematical models have been developed by Schatzmann (1979) for round buoyant jets in a stratified, flowing ambient fluid and Janicke & Janicke (2001) for dry and wet plumes in arbitrary wind fields.

The spatial distribution of exhaust gas concentration downstream of a plume or jet source is commonly modelled using Gaussian profiles (e.g. Hanna et al., 1982; Huber, 1991; Bächlin et al., 1992). Such modelling accounts for the characteristic 'bell-shaped' lateral profiles in planes at right angles to the flow (see *Figure 2.13* for an example of Gaussian data curve fit). In the absence of crosswinds, the profiles are symmetrical with respect to the flow centre line, where the maximum concentration occurs. Gaussian models are restricted to cases of flat, unobstructed terrain, uniform wind velocity and homogenous turbulence distribution, which do not usually occur within the Atmospheric Boundary Layer (Bächlin et al., 1992). Adjustments to the shape of the profiles can be made by modifying empirically the plume vertical and horizontal spread parameters to account for discrepancies in the above conditions. An example of a

Gaussian equation, as given by Bächlin et al., 1992, is presented in *Equation A.3* in Appendix A.

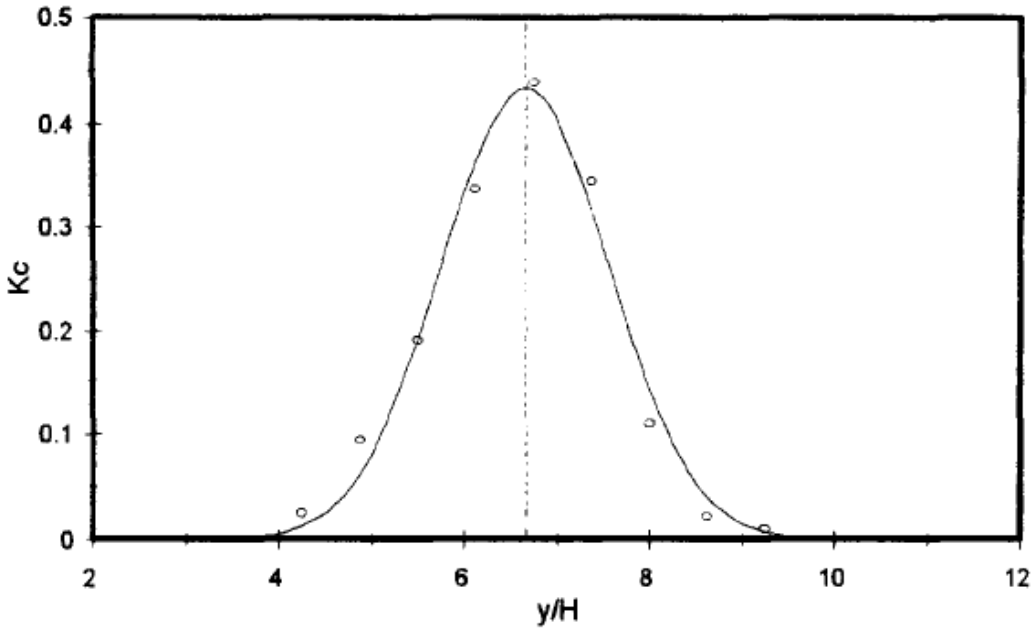

Figure 2.13: Example of a Gaussian curve fit for a lateral concentration profile of a plume in open terrain, measured by McDonald et al. (1997)

Vertical axis shows the non-dimensional concentration parameter K_c (see Equation 2.14); horizontal axis shows the non-dimensional lateral distance y/H; the choice of H in this case is a building height since the concentration measurements were performed in the presence of buildings as well as in open terrain; flow centre line is marked with a dashed line

In plume concentration analyses, it is common to normalise the measured mean values of concentration by the emission mass flow rate at the plume source (e.g. Hanna et al., 1982; Huber, 1991). In studies of plume dispersion in the presence of obstacles and buildings, similar data reduction has been used (e.g. Robins & Castro, 1977; McDonald et al., 1997; Mavroidis & Griffiths, 2001), obtaining a non-dimensional concentration parameter K_c. Its definition is shown in *Equation 2.14* where c is the measured mean concentration, usually in parts-per-million (ppm), l is a characteristic length scale, usually the obstacle or building height, U is the measured velocity at the height l, and Q_j is the source volumetric flow rate.

$$K_c = \frac{cUl^2}{Q_j}$$

Equation 2.14

2.6.4 Plume dispersion through obstacles

In view of the proposed baffles concept, the dispersion of plumes in the presence of obstacles and buildings is of particular interest. Experimental investigations have been carried out on plumes in the near field of single objects (e.g. Robins & Castro, 1977; Mavroidis et al., 2003) and arrays of obstacles and building models (see *Figure 2.14b*) of various spacing (e.g. Bächlin et al., 1992; Davidson et al. 1996; MacDonald et al., 1997).

Robins & Castro (1977) performed a wind tunnel investigation the plume dispersion around single cubes and highlighted the importance of modelling accurately the approach flow characteristics on the flow development. They concluded that the maximum concentration is relatively insensitive to the ratio of obstacle height to boundary layer thickness. The obstacle height and boundary layer thickness were identified as the dominant flow length scales in the vicinity of the obstacle and far downstream respectively. Combining field trials and 1:100 scale wind tunnel tests (see *Figure 2.14a* for an example flow visualisation), Mavroidis et al. (2003) reported that the near-ground concentrations in the wake of an object were lower compared to open terrain and showed that they decreased with increasing height of the obstacle. They observed greater lateral dispersion rates in the field compared to the wind tunnel, which was also reported in a similar investigation by Higson et al. (1994). As a result, the obtained mean concentrations in the wind tunnel were larger by a factor between 1 and 3. These discrepancies were attributed to the higher levels of large scale turbulence in the field.

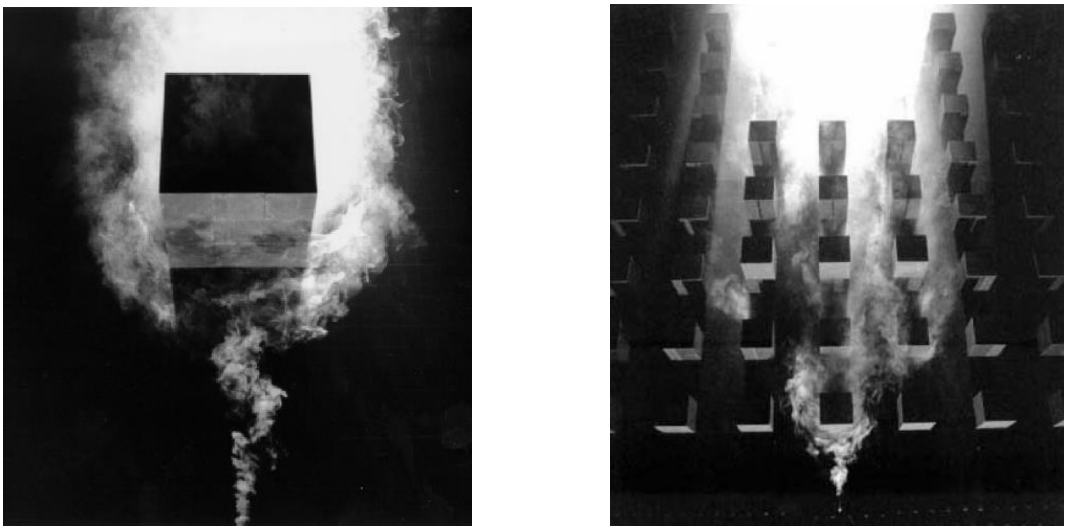

(a) (b)

Figure 2.14: Flow visualisation of plume dispersion in the near field of (a) a single cube (Mavroidis et al., 2003) and (b) an array of cubes (Mavroidis & Griffiths, 2001) (top view)

Bächlin et al. (1992) compared wind tunnel measurements of gas dispersion around different building patterns with simple Gaussian models (see *Equation A.3*). They concluded that the Gaussian models did not accurately reproduce the lateral displacement of the plume when the wind was at an angle to the building pattern.

Field measurements by Davidson et al. (1995) highlighted the importance of the plume size relative to the overall size of the obstacle array. They reported no significant changes in the mean concentration if the plume was large relative to the array, although changes in the plume structure and the concentration fluctuations were observed. For relatively small plumes, the decay of mean concentration along the centre line and the plume's lateral spread did not change significantly, while the vertical extend of the plume was observed to increase by 40-50% due to upward motion resulting from the reduction in mean velocity. These conclusions were shown to apply only if a significant amount of the plume was deflected above the array. The study was extended by Davidson et al. (1996) to 1:20 and 1:200 scales with similar results. They identified two mechanisms which determined the behaviour of the plume as it passed through the array: the divergence and convergence of streamlines as the flow moved around the obstacles and the changes in turbulence structure due to vortex shedding by the obstacles. They also highlighted that the effective lateral gap between the obstacles was inversely correlated with the plume's increase in vertical height due to its influence on the streamlines divergence.

Enhanced vertical mixing was similarly observed by MacDonald et al. (1997) and Mavroidis & Griffiths (2001). MacDonald et al. (1997) described it as a deflection of the mean streamlines over the array, which lifted the plume centre of mass upwards. They also reported only similar mean centre line concentrations compared to a plume in open terrain and concluded that this is due to the enhanced vertical mixing and the reduction of mean velocity counteracting one another. Both MacDonald et al. (1997) and Mavroidis & Griffiths (2001) observed an increased lateral dispersion of the plume within the array, which decreased with distance downstream.

Lin et al. (2006) investigated the dispersion of odour from livestock through windbreaks. In contrast to the cases of building arrays, they also investigated the far-field downstream, within approx. 60 windbreak heights, and the effects of windbreak porosity (see *Equation 2.15* for definition of porosity). The windbreaks were found to enhance odour dispersion. Their effectiveness was increased when more dense (lower porosity) and when located closer to the odour source. The characteristics of windbreaks are discussed in the following section.

2.7 Aerodynamic characteristics of windbreaks

The physical principle of the baffles concept is that of reducing the exhaust jet momentum through aerodynamic drag, thus the baffles are effectively acting as windbreaks to the approaching exhaust jet. For this reason, a review of windbreaks and their characteristics is presented in this section.

The term 'windbreaks' refers to man-made structures, or very often plantations of trees and shrubs, used mainly for agricultural purposes in open areas where protection from the ambient wind is necessary (van Eimern et al., 1964). The sheltered zone behind the windbreak affects the microclimate and soil erosion, as well as plants and animals. Recently, the use of man-made windbreaks on bridges connecting open roads has been investigated as a method of reducing aerodynamic side forces on passing Heavy Goods Vehicles (Chu et al., 2013).

The velocity reduction by a windbreak is proportional to its vertical height h and, at the same time, the percentage reduction is, with small exceptions, independent of the ambient wind velocity (van Eimern et al., 1964). An important parameter of the shelter characteristics of windbreaks is their porosity, also historically referred to as 'permeability' and 'density' by various authors (see definition in *Equation 2.15*).

$$\gamma = \frac{perforated\ (open)\ frontal\ area\ perpendicular\ to\ the\ flow}{total\ \ frontal\ area}$$

Equation 2.15

Figure 2.15 presents a schematic illustration of the flow field around a solid (A) and a porous (B) windbreak, subjected to ambient wind. A solid windbreak causes a significant upward deflection of the flow and creates a large area of separated flow ('recirculation bubble') downstream, extending to a horizontal length of 5h to 6h to the flow reattachment point and characterised by high turbulence intensity (Guyot, 1995). As the windbreak porosity is increased, the 'bleed flow' through the windbreak surface increases, preventing the vortex formation. The resulting wind reduction is less and extends further downstream, compared to the case of a solid windbreak. Perera (1981) and Heisler & Dewalle (1988) observed the recirculation bubble to detach from the windbreak and move downstream for $\gamma \geq \sim 0.3$. Lee & Kim (1998) reported the absence of recirculation flow downstream of a vertical, porous fence when $\gamma \geq 0.4$ Guyot (1995) distinguished between 'impermeable' and 'permeable' windbreaks, having porosities of $\gamma \leq 0.25$ and $\gamma \geq 0.25$ respectively. He reported the respective extent of the shelter zone to be in the order of 12h and 20h.

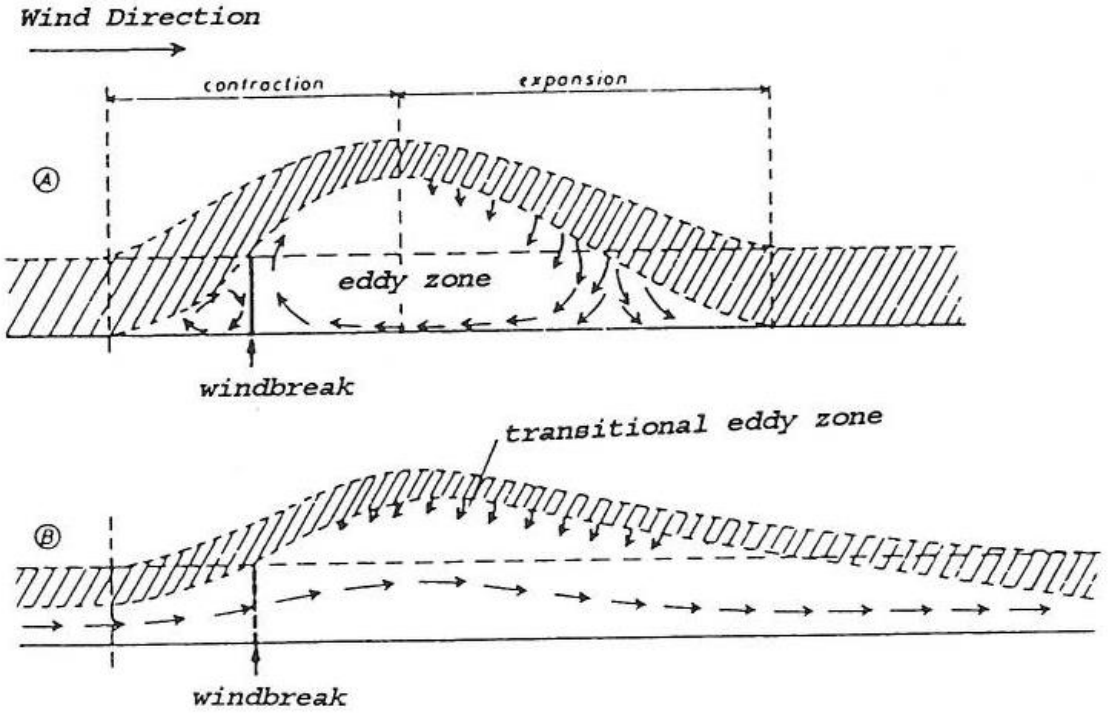

Figure 2.15: Flow field around (A) impermeable windbreak (B) permeable windbreak (taken from Guyot, 1995)

Historically, the case of a single flat plate mounted perpendicularly on a surface and subjected to a turbulent boundary layer has been investigated experimentally for different purposes. Wieghardt (1953) carried out experiments on small two-dimensional plates of various thicknesses to study their effect on the surface roughness in terms of additional drag of the plate measured with a drag balance. The two-dimensional drag coefficient C_{Dn}, based on the fence height h and the dynamic pressure of the flow over the fence height, was found to vary between 1.0 and 1.3 for fence thickness-to-height ratios < 1. Experimental results, summarised by Hoerner (1965, p. 5-7), give a similar drag coefficient of 1.25 for a two-dimensional small fence-type protuberance of zero thickness, and 1.20 for a body of square frontal area and thickness smaller than its height. Plate (1964) did further analysis of the data of Wieghardt (1953) and concluded that the body geometry alone is not sufficient to determine the value of C_{Dn}. He found the drag coefficient to be dependent on the ratio of plate height to boundary layer thickness, h / δ, and proposed the empirical relationship:

$$C_{Dn} = 1.05\left(\frac{h}{\delta}\right)^{\frac{2}{7}}$$

Equation 2.16

Similar experimental investigations on single two-dimensional fences were reported by Good & Joubert (1968), Raju et al. (1976), Ranga Raju (1983) and Ranga Raju & Sharma (1997). Good & Joubert (1968) obtained correlations for the variation of drag with h in a smooth-wall boundary layer and found the flow-reattachment distance downstream of the fence to be 13h to 14h. Ranga Raju et al. (1976) recognised h / z_0, the ratio of fence height to roughness length (z_0 is defined by ESDU, 1982, see Chapter 3.4) also referred to as Jensen number, as a dominant parameter for the scaling of wind tunnel results in Atmospheric Boundary Layer (ABL) modelling. They defined a drag coefficient C_D*, based on the skin-friction velocity, for which an empirical relationship as a function of only C_n and Jensen number was derived. C_n was observed to be independent of Jensen number within the range tested. Ranga Raju & Sharma (1997) extended this study to disturbed boundary layers where the disturbance was achieved with a second fence put upstream of the primary one and the distance between both as well as their heights ratio was varied. A separate investigation by Ranga Raju (1983), including two- and three-dimensional blocks of various thickness, concluded that the two-dimensional drag coefficient was independent of the block thickness for thickness-to-height ratios between 0 and 2.

Three-dimensional single fences of various aspect ratios, defined as the width-to-height ratio, were investigated by Sakamoto and Arie (1983). They found the drag coefficient, based on the panel area $w \times h$, to be minimum at an aspect ratio $w / h = 5$. This result was confirmed in separately conducted experiments by Holmes (1986) and Letchford (1986). For a single panel of $w / h > 10$, ESDU (1989) gives an area-averaged mean drag coefficient $C_F = 1.15$, based on the hourly-mean wind speed at the top of the panel and the panel area $w \times h$. Cook (1990) reported a similar drag coefficient of 1.2 for surface-mounted rectangular plates of $w / h \geq 2$.

Raine & Stevenson (1977) investigated the flow around windbreaks of porosity γ (see *Equation 2.15* for definition) between 0 and 0.5 and found that porosity of 0.2 gave the best overall reduction in mean leeward velocity. Guyot (1995), Santiago et al. (2007) and Dong et al. (2007) suggested an optimum porosity of 0.4, 0.35 and 0.2-0.3 respectively, in terms of maximising the combination of wind reduction and extend of the shelter zone. In a more recent investigation, Dong et al. (2010) found the shelter efficiency to be related to the turbulent intensity of the flow in terms of sediment transport near the ground surface and observed that for $\gamma > 0.2$ the turbulence intensity and the vertical component of the leeward velocity are greatly reduced.

Chu et al. (2013) conducted a combined experimental and numerical investigation on the sheltering effects of porous windbreaks, mounted on both sides of road bridges, on passing Heavy Goods Vehicles. They found the influence on the side force

coefficient of the vehicle due to windbreak porosity to be negligible compared to the influence of the windbreak height.

Guan et al. (2003) proposed the use of 'aerodynamic porosity' γ_a, defined as the ratio of the approaching velocity to the velocity immediately downstream of the windbreak surface, for which the relationship $\gamma_a = \gamma^{0.4}$ was derived for $\gamma \leq 0.4$. They obtained a relationship for the windbreak drag coefficient, shown in *Equation 2.17*, based on the approaching velocity at the height h of the windbreak and the windbreak frontal area $w \times h$. Guan et al. (2003) concluded that for narrow windbreaks the use of aerodynamic porosity was more appropriate compared to the optical porosity γ.

$$C_F = 1.08\left(1-\gamma_a^{1.8}\right)$$

Equation 2.17

The shelter effects of an array of multiple rows of windbreaks – similar to the planned baffle arrangement – have been investigated mainly for protection of crops. A summary by van Eimern et al. (1964) of experimental data suggest spacings between 20h and 30h to be favourable for efficient wind reduction and identifies the importance of factors such as windbreak shape and porosity, and prevailing wind direction and strength, on the choice of spacing The protective effect is reported to practically disappear for spacings below 10h. Data by Naegeli (1965) for rows of windbreaks of γ = 0.5 show that reducing the rows spacing from 20h to 15h gives a reduction in mean velocity of 14%, while from 15h to 10h the reduction is only 7%.

Letchford & Holmes (1994) investigated the shielding effects occurring for a configuration of two identical walls placed at various distances parallel to each other. They observed a reverse direction of the wind loading on the main wall when the second wall is at a distance of less than 5h upstream. Robertson et al. (1996) reported lack of scientific data on the shelter of rows of walls of different height. Shelter factors for estimating net pressure coefficients have been published by the British Standards Institution (BSI, 1997). These are applicable for walls of equal height and in cases when the upwind wall is taller than the sheltered wall.

In the present investigation the baffles are subjected to a flow governed primarily by a wall jet of rapidly-decaying momentum downstream of its source due to entrainment of ambient air. This differs from the cases described above, where the ambient wind velocity does not decay naturally. For an efficient arrangement of several rows of baffles it is therefore necessary to increase the height and width of each row with distance away from the jet source.

2.8 Flow through porous screens

The initial experimental phase of this work included pressure drop measurements and visualisation of the flow in the near field of porous screens to determine the baffles preliminary design parameters and investigate the possibility of using a porous windbreak surface in the planned field trials. A short review of previous work on the subject is therefore included in this section, including mainly results on pressure distribution and observations of the flow behaviour around porous screens and gauzes of negligible thickness at various angles of inclination and porosity. The review, together with the pressure drop measurements was published as Gerova et al. (2013).

Taylor (1944) and Taylor & Davies (1944) conducted theoretical and experimental studies of the relationship between pressure drop coefficient $\Delta p / q_\infty$ (ratio of pressure drop across the screen to freestream dynamic pressure) and drag coefficient C_{Dn}, based on screen height and freestream velocity, for two-dimensional porous sheets and wire gauzes. They proposed the relationship

$$C_{Dn} = \frac{\Delta p / q_\infty}{\left(1 + 0.25 \Delta p / q_\infty\right)^2}$$

Equation 2.18

The product γRe was used as similarity parameter and observed no Reynolds number dependency of the measured drag coefficients for $\gamma Re \geq 1000$. In this case, the screen Reynolds number Re is based on the freestream velocity U_∞ and the mean wire or hole diameter of the screen, and γ is the screen porosity, as defined in *Equation 2.15*.

Koo & James (1973) proposed a mathematical model for a two-dimensional steady flow, replacing the porous screen with a distribution of sources, and modified the relationship of *Equation 2.18*, reported by Taylor and Davies (1944). Their experimental and numerical data showed good agreement up to pressure drop coefficients of 10.

Schubauer et al. (1950) measured the pressure drop across screens of porosity $0.2 \leq \gamma \leq 0.8$ for angles of inclination α between 0 and 45 degrees, defined as the angle between the flow direction and the direction normal to the screen (see *Figure 2.16*). They found that $\Delta p / q_\infty$ was a function only of γ and the velocity component normal to the screen, equal to $U_\infty \cos\alpha$. Results for screens of $\gamma \geq 0.4$ showed to be independent of Reynolds number for $Re\cos\alpha > 150$.

Annand (1953) correlated available experimental results, including those of Taylor & Davies (1944) and Schubauer et al. (1950), and obtained a relationship

between pressure coefficient and porosity for $0.2 < \gamma < 0.8$ and $\alpha = 0$ degrees, shown in *Equation 2.19*. The dynamic pressure q is calculated with the flow velocity component $U_\infty \cos\alpha$ perpendicular to the screen, and the coefficient C is a function of Reynolds number, asymptotically approaching the value of 0.56 for $Re \geq 400$. A similar value of 0.54 was reported by Pinker & Herbert (1967) for $Re \geq 800$. The corresponding pressure drop coefficient for an inclined flow, based on the freestream dynamic pressure q_∞, is given by $(\Delta p / q_\infty) = (\Delta p / q)\cos^2\alpha$. *Equation 2.19* was further adapted by Brundrett (1993) for very low Reynolds numbers, i.e. < 1, and for screens in a boundary layer.

$$\frac{\Delta p}{q} = \left(\frac{1-\gamma^2}{\gamma^2} \right) C$$

Equation 2.19

In a review of experimental data, similar that of Annand (1952), Carrothers & Baines (1965) obtained the relationship $(\Delta p / q) = 1.26\gamma / (1 - \gamma)$, where the pressure drop coefficient was taken to be independent of *Re*. Other reports by Laws & Livesey (1978) and Su & Huang (1991) also suggested negligible Reynolds number effects on the pressure drop coefficient for $Re > 250$ and $Re > 1000$ respectively. This is also evident from the data of Ito & Garry (1998) at $Re > 400$ for a mesh of $\gamma = 0.37$. Teitel et al. (2009) also highlighted that inertia forces became dominant at $Re > 150$ resulting in negligible viscosity effects. In general, for screens of lower porosity the threshold *Re*, after which $\Delta p / q$ becomes independent of *Re*, is greater. The differences in the results can also be attributed to the mesh geometry and the experimental arrangement.

Reynolds (1969) developed a theoretical model to predict the deflection of duct flow passing through a gauze screen at an angle of inclination α_v, measured to the vertical (see *Figure 2.16*). For screens of $\gamma < 0.5$, he proposed the relationship $\psi' = 0.5\psi$ for $\psi' < \psi < \alpha_v$, where ψ and ψ' are the angles in the outflow and at the plane of the screen respectively, of the mean velocity vector to the freestream direction. For $\gamma > 0.5$, Reynolds suggested that the outflow angle and the angle at the screen are the same, $\psi' = \psi$.

Ito & Garry (1998) studied the flow pattern through a screen of $\gamma = 0.37$ for various angles of inclination and Reynolds numbers between 36 and 409, based on mesh monofilament diameter. Using smoke visualisation, they observed a uniform expansion of the flow downstream of the screen. They also obtained results for lift and drag coefficients using force measurements and integration of pressure distribution measurements, which were reported to be in very good agreement. The lift coefficient was observed to have a maximum value at $\alpha_v = 45^o$, i.e. 0.55, which was more than half

of the lift coefficient value calculated from pressure distribution measurements on a solid flat plate at the same angle of inclination.

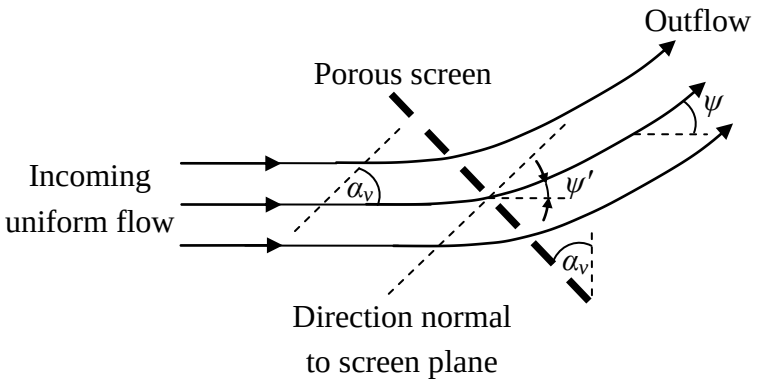

Figure 2.16: Schematic illustration of flow deflection when passing through an inclined porous screen

Miguel (1998) and Valera et al. (2005) obtained relationships between permeability and porosity for two-dimensional thin porous screens of various mesh geometry. The permeability is a measure of the ability of the material to allow fluid through its porous surface and relates the velocity normal to the screen and the pressure drop across the screen. Based on the results obtained for screens of both regular and irregular mesh geometry, Miguel (1998) concluded that the shape of the yarns and the mesh geometry had a negligible influence on the characteristics of the flow. His results do not seem to agree with those of Valera et al. (2005), who proposed a governing equation to calculate the pressure drop from the screen porosity and Reynolds number.

2.9 Conclusions

The following conclusions were drawn from the literature review with regard to this study:

- The mean flow characteristics of two and three-dimensional wall jets were reviewed in terms of jet growth rate, velocity decay and skin-friction coefficient. There seems to be some discrepancies in the experimental results reported for velocity decay and lateral and vertical growth rate of three-dimensional wall jets, as well as for the occurring vortex structures in the near field. This is mainly attributed to the different test conditions.

- Significantly more research has been done on wall jets in quiescent air compared to wall jets in an external stream (co-flow). There is lack of data on wall jets submerged in an Atmospheric Boundary Layer.

- Offset jets exhibit wall jet characteristics after a certain (short) distance downstream, which is a function of the offset distance. Parallel jets tend to merge as they expand, forming one single (wider) jet, which justifies the use of a simplified model of a BAe 146-301 exhaust jet at take-off, consisting of a single nozzle only.

- The Froude number and the ratio of ambient wind velocity to exit jet velocity have been identified as the most important scaling parameters in sub-scale modelling of buoyant wall jets in a co-flow. The importance of the Reynolds number on the flow development reduces significantly if the tests are performed above a certain critical value, typically 11000 for buildings, based on the building height.

- It has been suggested (Meroney, 1979) that a buoyant wall jet would always eventually rise from the ground surface, with its lift-off distance being a function of the flow Froude number (*Equation 2.12*). Attempts to define a universal lift-off parameter (*Equation 2.10*) have shown considerable discrepancies in the results for a critical value beyond which lift-off would occur. The effect of ambient wind is to delay the plume rise. No quantitative results on the effect of the ratio of ambient wind velocity to exit jet velocity have been reported.

- Buoyant plume dispersion is enhanced within an array of obstacles. However, studies have been performed only in the near field at low flow velocities. The effects of the obstacles in the far field downstream have not been reported.

- Studies on solid and porous windbreaks and configurations of multiple rows of windbreaks have suggested values for optimum porosity (i.e. 0.3) and spacing (i.e. 20-30*h*) in terms of wind protection and extend of the shelter zone. Results of drag coefficient have been obtained for windbreaks submerged in turbulent boundary layer flows and Atmospheric Boundary Layer flows of constant freestream velocity. A major difference to this study is the naturally decaying velocity of the exhaust jet to which the baffles would be subjected. This would require baffle rows of increasing height *h* and optimum spacing to maximise their effectiveness.

- Results for screens and meshes of different mesh pattern indicate little dependency of the pressure drop coefficient on the pattern, as long as it is homogenous and evenly spread on the surface. There is lack of results on the effects of screen porosity and angle of inclination on the flow deflection downstream of the screens.

3 Experimental methodology

In this study, an entirely experimental approach was adopted to support the BAe 146-301 field trials at Cranfield Airport. The wind tunnel experiments were conducted in two stages, before and after the field trials respectively: 1) baffle arrangement and design of field trials experiment, and 2) replication of the field trials at sub scale and correlation of wind tunnel and full-scale results. This chapter presents a summary of the steps undertaken during the experimental investigation, the wind tunnel test techniques used and the methods of modelling the engine exhaust buoyancy and the Atmospheric Boundary Layer (ABL).

3.1 Experimental approach

The steps in the experimental approach were indentified in order to provide a complete answer of the research question of the thesis. These defined the following experimental test programme, consisting of five phases of separate experiments.

Phase I: Plume behaviour and lift-off

The initial phase consisted of 1:200 scale tests with an exhaust jet from a stationary nozzle, investigating the plume development downstream and the effects of jet buoyancy at the nozzle, wind tunnel flow (ambient wind), boundary layer characteristics and distance of the baffles (single row) to the nozzle. Additionally, the tests targeted to explore the possibility of the ground-based plume to overcome the Coanda effect and detach from the ground surface ('lift-off'), investigating the factors constraining this phenomenon.

Phase II: Flow through porous materials

The original concept of the baffles included the possibility of using catalythic converters to reduce the pollution from the exhaust emissions. For this reason, the surface of the baffles facing the jet would have to be porous in order to allow some of the flow to pass through. The experiments of Phase II aimed to explore the aerodynamic properties of porous screens to be used for the baffles, investigating the effects of screen porosity and angle of inclination on the upwash angle of the flow downstream of the

screen. Since the baffles are acting effectively as windbreaks, the wake is characterised by periodically shed vortices (von Karman vortex street). In addition, the use of porous baffle surface aimed to reduce the structural load on the baffles due to the vortex shedding.

Phase III: Force balance tests on baffle array configurations

Next, the experimental programme continued by expanding the initial single baffle rown with configurations of multiple rows of increasing height with distance from the nozzle. The effects of the baffle array on the reduction in jet horizontal momentum were investigated in terms of measured total drag of the array. Configurations of baffles of three angles of inclination were tested varying the spacing between the rows, the number of rows and the row lateral shape.

Phase IV: 1:200 scale experiment of a real engine with a modelled Atmospheric Boundary Layer

The last step of the sub-scale experimental investigation involved modelling the take-off exhaust jet of a real engine in order to represent accurately the ambient wind effects and real atmospheric conditions. The purpose of the experiments was to identify the behaviour and development of the plume with and without the array of baffles in terms of local plume concentration and loca flow velocity, measured using Flame Ionisation Detector (FID) and Hot-Wire Anemometry (HWA) respectively. The representation was of an ALF502R-5 turbofan engine, powering the BAe 146-301 aircraft, which was used to perform the full-scale tests of *Phase V*. The atmospheric conditions and ABL of the full-scale tests were modelled.

Phase V: Full-scale field trials

The final step of the investigation consisted of full-scale field trials with a BAe 146-301 performing take-off and landing cycles at Cranfield Airport. The tests were performed to obtain data of real take-off runs and correlate the results with the sub-scale results, thus providing a complete answer to the proposed scientific question and completing the targeted research.

3.2 Experimental methods

3.2.1 Pressure, temperature and velocity measurements

Pressure measurements are essential for monitoring and assessment at a controlled flow environment in the wind tunnel working section during tests. A common method of determining the freestream velocity U_∞ is by measuring the total and static pressures of the freestream with a Pitot-static tube. The velocity is then calculated with

$$U_\infty = \sqrt{\frac{2(p_t - p_\infty)}{\rho_\infty}}$$

Equation 3.1

where the freestream density ρ_∞ is calculated from the Ideal Gas Law (see *Equation 3.4* in Chapter 3.3), using ambient temperature and barometric pressure readings.

The above described calculation method was used predominantly in this study's wind tunnel tests to calculate freestream velocity. The Pitot-static tube was connected to a Furness FC016 digital manometer, operating at a range of ±199.9 mmH_2O (±1960.4 Pa) with an accuracy of ±1% of reading. Atmospheric pressure was measured with a Druck DPI 141 resonant sensor barometer with a range of 800 to 1150 hPa absolute pressure and an accuracy of ±0.15 hPa. Temperature readings were taken from a RS-2130WC digital thermometer with an accuracy of ±1 ºC.

Other pressure measurements were conducted to study the flow across porous screens (see Chapter 4.3.1). These measurements were made using working section wall mounted static pressure tappings, connected through external tubing to Omega PX139 pressure transducers. As specified by the manufacturer, the repeatability of the measurements was ±0.3% of their full range of 0.3 psi (2068.4 Pa), giving a measurement error of ±0.0009 psi (±6.2 Pa).

Modelling dispersion of the exhaust plume with the Atmospheric Boundary Layer (ABL) at sub scale required matching the full-scale ratio of jet exit velocity to ambient wind velocity and thus operating the wind tunnel at very low velocities in the working section (i.e. U_∞ < 1 m/s). At such velocities the Pitot-static tube did not provide the required accuracy, therefore velocity in the working section was measured with a Schiltknecht MiniAir6 Mini vane anemometer of a measurement range between 0.4 and 20 m/s. Its accuracy is specified by the manufacturer as the greater of ±1.5% of reading or ±1.0% of the full range (i.e. ±0.2 m/s).

3.2.2 Exhaust plume visualisation

The initial experiments included using a laser light sheet flow visualisation method to study the behaviour of a buoyant exhaust plume from a single nozzle in ground proximity. The wind tunnel working section arrangement is shown schematically in *Figure 3.1* and in *Figure C.1* and *Figure C.2* in Appendix C. The air flow was supplied to the nozzle from an external compressor and was mixed with smoke, which was chemically generated from burning oil and delivered through an electrically powered fan. A diverging laser beam ('laser sheet'), reflected back from the smoke particles in the flow, was used to illuminate the plume in various planes perpendicular to the flow direction. Video images of the visualised flow were recorded with a digital camcorder, positioned sufficiently far downstream of the nozzle exit, in order not to interfere with the flow upstream. A Class IV Argon ion laser was used to deliver a beam of 514 nm wavelength (green light) through an optical fibre cable to a cylindrical plano-concave lens, which generated the light sheet.

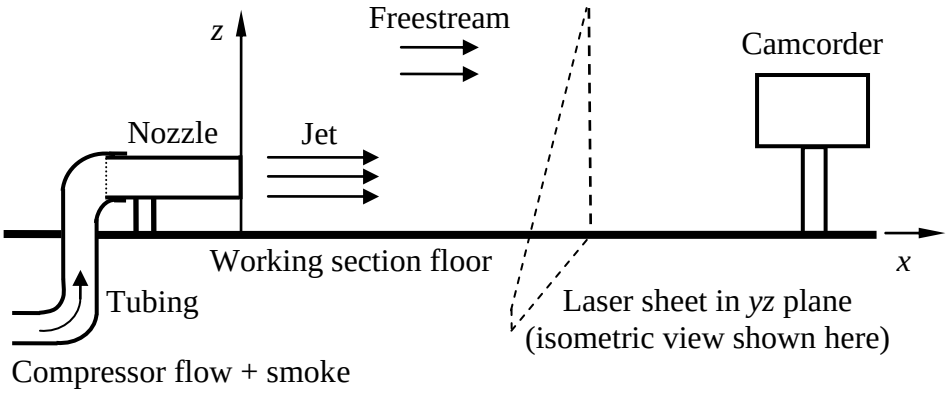

Figure 3.1: Schematic illustration of the basic experimental arrangement for the plume visualisation tests (side view; not to scale)

The post-processing method consisted of dividing the recorded videos into individual frames, which were then passed through image-analysis software (i.e. Pixcavator IA v4.2) to separate digitally the plume from the background. The primary function of Pixcavator is to detect and capture objects by applying a threshold for different levels of grey to convert a grey scale image to a binary scale image (INPERC, 2013). Objects are picked up using size and contrast criteria (threshold values) which are manually set by the user. Such analysis enabled quantitative data to be obtained on the plume area and its maximum vertical (height) and lateral (width) spread in terms of image pixels (see *Figure 4.1* in Chapter 4.1).

The analysis of a sequence of video images involved counting the number of pixels (output from Pixacavator) within the plume area for each extracted individual frame of the video and calculating an arithmetic mean value for all frames. Similarly, using the jet area boundaries defined by Pixcavator, the maximum plume height and width could be obtained. The contrast threshold was kept constant for all frames where possible and the size threshold was adjusted according to the local spread of the plume. The method of averaging made the results dependent on the number of frames per video used, especially at large distances downstream (> 65 nozzle diameters) where occurring unsteady phenomena within the jet caused the plume shape to change significantly from frame to frame (minimum time interval between frames being of 0.04 seconds). Therefore the influence of the number of frames per video used on the averaged results was further investigated at 129 diameters downstream (the largest distance from the nozzle exit where the laser sheet was positioned during the plume visualisation tests). Results for plume height, width and area were obtained for 30, 60 and 120 frames and showed a maximum relative difference of only 3.8% between 30 and 120. Therefore, averaging over 30 frames was considered sufficiently accurate for the purpose of the experiment and was used in all data analysis.

3.2.3 Smoke tunnel flow visualisation

As part of the study on porous screens, two-dimensional flow visualisation tests were conducted at Cranfield University's smoke wind tunnel. The working section arrangement is described in detail in Chapter 4.3.2 (see *Figure 4.17* for a schematic illustration). The flow visualisation method consisted of injecting small quantities of smoke into the freestream at several uniformly-distributed vertical locations as it entered the wind tunnel working section, thus creating visible pathlines. The working section was illuminated with a lamp, allowing photographs of the observed flow patterns to be taken and analysed.

3.2.4 Skin-friction balance

Drag measurements were conducted using a one-component force balance modified at Cranfield University from an existing custom-built design, intended for direct skin-friction measurements. It consisted of a rectangular plate, 1060 mm long, 700 mm wide, inset flush with the working section floor. The plate is connected to a floating platform element, supported by strain gauged flexures, arranged in a standard Wheatstone bridge electrical circuit. A similar design was described by Winter &

Gaudet (1973). Loads applied on the plate results in a bridge output which is sampled at 0.5 kHz by a PC driven data acquisition system. The output of the balance consists of mean values taken for a period of 10 seconds. A prior calibration of the balance established the measurement precision to be within ±0.01 N.

3.2.5 Flame Ionisation Detector

Plume concentration measurements were performed using a flame ionisation method of detection, described by Halasz & Schneider (1961) and Littlebury (1981). It is a standard gas chromatography technique utilising a sensor, i.e. Flame Ionisation Detector, to detect a tracer gas in the plume. A schematic illustration of the basic FID measurement principle is shown in *Figure 3.2*. The sample gas flow from the measurement probe is delivered continuously to a flame inside the FID, sustained by separate regulated flows of fuel gas (hydrogen or a mix of hydrogen and helium) and oxidising gas (air). During the combustion process, any hydrocarbon components present in the sample would undergo a complex ionisation process forming ions and free electrons (Littlebury, 1981). The ions are attracted by the electrodes of a metal collector, causing electric current to flow across the collector plate. This current is proportional to the rate of ionisation and thus to the concentration of hydrocarbons in the sample flow. Typically, the sample gas consists of an inert carrier gas (e.g. nitrogen or helium) and a hydrocarbon gas used as tracer (e.g. methane). The FID calibration is performed with samples of known tracer gas concentration.

In this study, the FID used was a Signal Instruments 3000HM hydrocarbon analyser, measuring the concentration of organic molecules with a carbon-hydrogen bond present in the sample gas (Signal Instruments, 2014) in volume per volume parts per million (ppm). The flame was fuelled with a gas mixture of 60% helium and 40% hydrogen, while a mixture of 98% nitrogen and 2% methane, equal to a mole fraction of 20000 ppm, provided the carrier and tracer gas respectively. The 3000HM model operates at measurement ranges between 0-4 ppm and 0-10000 ppm with a response time of less than 2 s at a sample flow rate of 2 l/min. The total response time of the FID measurement system, from the start of a measurement to the display of the sample reading, depends significantly on the tubing length used to connect the FID and the sampling probe in the wind tunnel working section. The accuracy of the FID, as specified by the manufacturer, is within ±1% of the used measurement range or within ±0.2 ppm, whichever value is greater. During tests, the measurement range of the FID was alternated between 0-1000 ppm and 0-4000 ppm depending on the value of the obtained readings. The accuracy of the measurements was thus within ±10 ppm and ±40 ppm respectively.

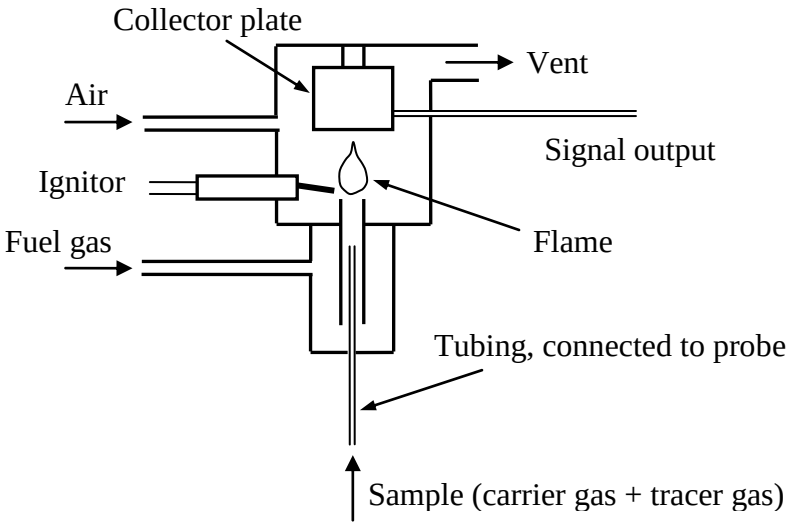

Figure 3.2: Schematic illustration of a Flame Ionisation Detector, used in gas chromatography (not to scale)

3.2.6 Hot-Wire Anemometry

Hot-Wire Anemometry is a measurement method involving an electrically-heated wire or film element, placed in the fluid flow of interest. Any changes in the flow conditions would change the element's convective heat transfer and thus its electrical resistance, which in turn can be related to, for example the flow velocity. HWA is the principle research tool in most studies of turbulent gas flows, offering cost-efficient measurement of one, two or three components of the velocity vector at high accuracy (i.e. < 1%) and excellent spatial resolution due to the small size of the hot-wire sensor (Bruun, 1995, p. 1). The high frequency response of modern hot-wire anemometers makes them suitable for velocity measurements in flows of low to moderate turbulence intensity (~ 25 %).

The basic HWA instrumentation consists of a hot-wire sensor, a probe tube, including its support and cabling, an anemometer and an analogue-to-digital (A/D) converter connected to a computer, controlling the HWA operation. HWA sensors are typically tungsten wires of 5 μm diameter, welded to the prongs of the probe (see *Figure 3.4a* and *Figure 3.4b* for schematic examples). There are two main operating modes of hot-wire anemometers: at constant current (CC), where the electrical current across the wire is kept constant while the wire temperate varies, or at constant temperature (CT), where the wire's electrical resistance and temperature are kept constant by varying the current. CT anemometers have more complex electrical circuit, but are much simpler to use than CC anemometers, therefore they are usually the

preferred anemometer type for velocity measurements (Bruun, 1995, p.37). The operating principle of a CT anemometer is shown in *Figure 3.3*. The hot-wire is placed in a Wheatstone bridge opposite to a resistor of variable electrical resistance, which defines the operating resistance of the wire and thereby its operating temperature. An increase in the flow velocity would reduce the wire temperature and resistance, causing a change in the voltage output across the bridge. This voltage output is used by a servo amplifier to control the system voltage supply such that the original values of hot-wire temperature and resistance are maintained constant. The amplifier output is thus a function of the flow velocity.

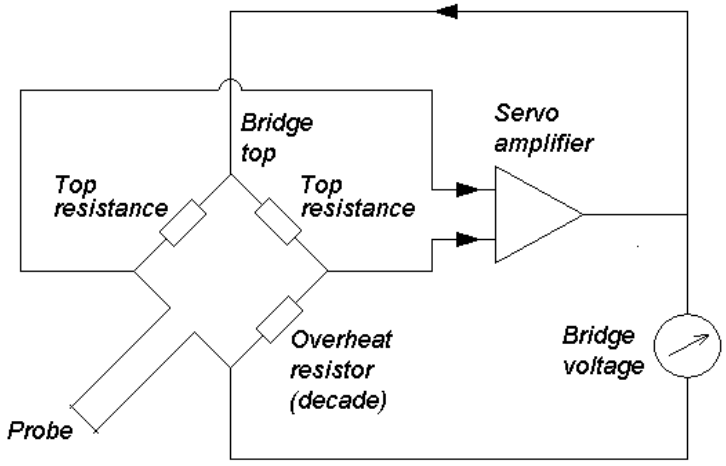

Figure 3.3: Principle diagram of a constant-temperature (CT) anemometer (taken from Dantec Dynamics, 2002)

In this study, constant-temperature HWA with a single-sensor probe was used for two different purposes: 1) to measure the vertical profiles of mean velocity and turbulence intensity of the modelled Atmospheric Boundary Layer (ABL) at sub scale; 2) for one-component velocity measurements of the flow field downstream of a buoyant nozzle jet at 1:200 scale with and without baffles.

A Dantec 55P14 hot-wire sensor (*Figure 3.4a*), oriented horizontally and at right angles to the flow, was used for the boundary layer measurements, while the velocity measurements of 2) were performed with a 55P13 sensor (*Figure 3.4b*), oriented vertically. In both cases, the probe was mounted on a three-dimensional traverse in the working section of the 8'×4' Atmospheric Boundary Layer Wind Tunnel (ABLWT), which allowed accurate, computer-controlled movement of the probe to the desired measurement locations.

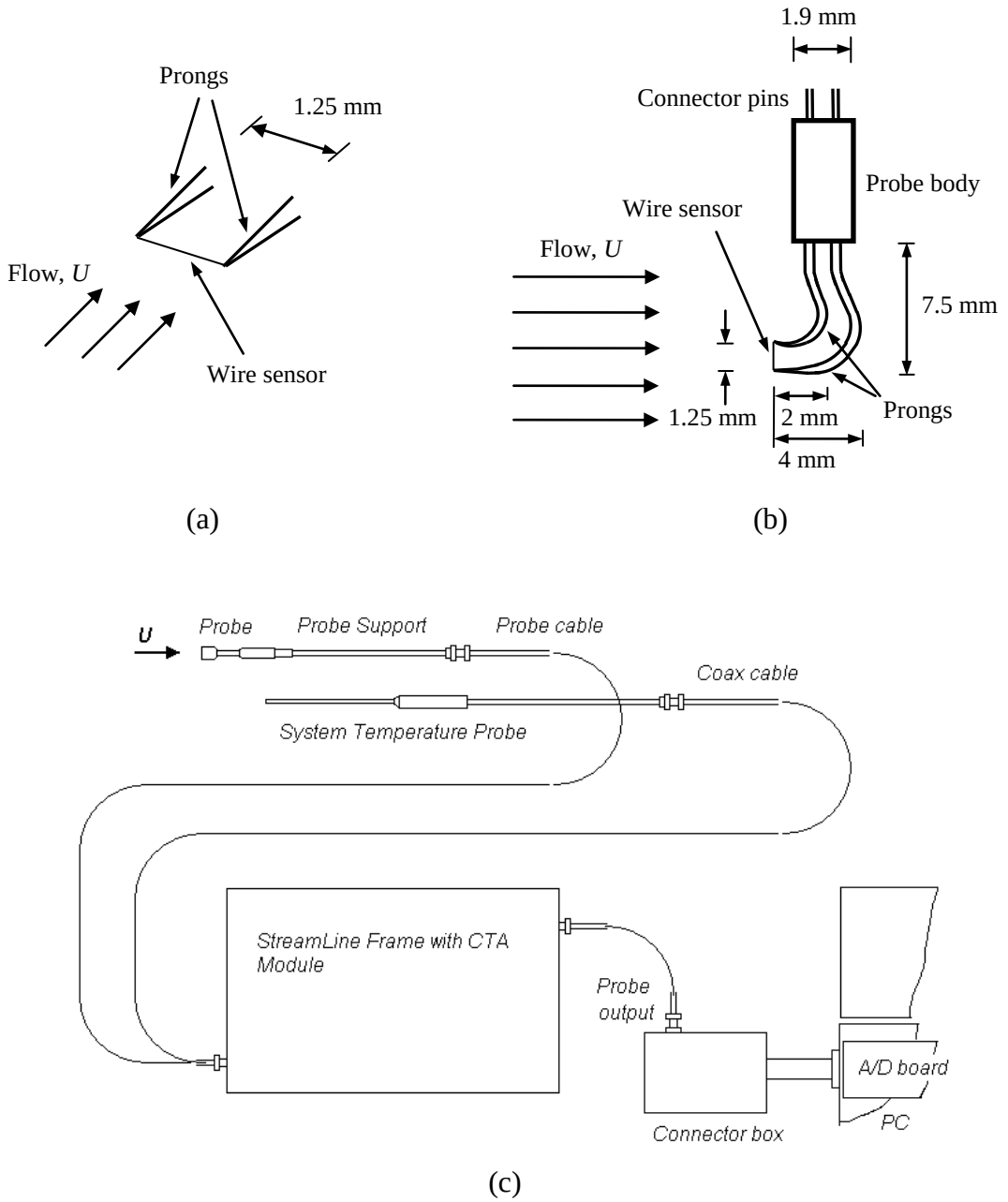

Figure 3.4: Schematic illustration of (a) Dantec 55P14 miniature hot-wire probe for boundary layer measurements (isometric view, sensor and prongs only); (b) Dantec 55P13 miniature hot-wire probe (not to scale); (c) Hot-Wire Anemometry (HWA) arrangement for velocity measurements (taken from Dantec Dynamics, 2002)

The measurements were performed at a sampling frequency of 1 kHz and a sampling period of 5 seconds, using a standard CT anemometry arrangement (*Figure 3.4c*). More details on the operation and data analysis can be found in Dantec Dynamics (2002). The hot-wire probe was connected to a Dantec Dynamics StreamLine CT anemometer with a built-in signal conditioner for amplification and filtering of the CTA

signal, which was located in the wind tunnel control room. The output signal from the anemometer was passed through an A/D converter and connected to a computer, where the HWA operation was controlled using the StreamWare application software. Temperature in the working section was measured with a Dantec 55P32 Thermistor probe, connected to the CT anemometer. This allowed corrections for temperature variation to be performed in situ during data reduction, within the software.

At the beginning of each test day, the CT anemometer voltage output was calibrated versus freestream velocity by applying polynomial curve fitting. The freestream velocity was measured with a Schiltknecht MiniAir6 Mini vane anemometer approximately at the working section centre line for a range typically between 0.18 and 13 m/s. Calibration tests were repeated during the course of the day, if the temperature in the working section varied considerably (i.e. $\geq$ 5 ºC) from the temperature at the initial calibration. Calibration errors of the polynomial curve fitting method varied typically between 0 and ± 3%.

Regarding the accuracy of the HWA measurements, it should be noted that the tests at 1:200 scale were performed with an exhaust gas mixture of nitrogen, helium and methane and a freestream of air, to account for the full-scale jet buoyancy and the ambient wind respectively, while the calibration was performed in a freestream of air only. This issue are discussed in more detail in Chapter 7.2.2.

3.3 Exhaust jet buoyancy modelling

At take-off, aircraft engines operate at the highest turbine entry temperature of the flight cycle. For a turbofan engine, the high temperature exhaust jet of the core flow and the ‘colder’ fan bypass flow mix as they travel downstream. This mixing is mostly influenced by the nozzle design and the engine bypass ratio, defined as the ratio of bypass mass flow to core mass flow. Enhanced mixing is a desired feature of modern turbofan nozzle designs as it has been reported to increase specific thrust, and reduce specific fuel consumption and noise (Sangai & Lakshmanan 2001; MacManus, 2009). Common nozzle designs include angled bypass flow, chevron nozzles and mixer devices for generating streamwise vortices (e.g. Cullom & Johnsen, 1977; DeBonis, 2008). An example of enhanced mixing is shown in a numerical investigation by DeBonis (2008), who reported uniform velocity distribution across the mixed jet at distances greater than 7 fan diameters downstream of the nozzle exit.

In view of the above assessment, it is reasonable to assume that the core and bypass flow would mix quickly as they travel downstream. This would allow for an approximation of constant density and temperature within the mixed jet.

The discussion in Chapter 2.6.1 on similarity parameters highlighted the importance of the Froude number *Fr* and the ratio of jet velocity to ambient wind velocity β for accurate sub-scale modelling of a buoyant jet or plume. To account for the buoyancy forces, arising from the differences at full scale between the high exit jet temperature and the ambient air temperature, *Fr* is usually calculated with the reduced gravitational acceleration $g' = g(\rho_j - \rho_\infty)/\rho_\infty$. This calculation in terms of the difference between jet and ambient density is convenient for wind tunnel testing, where it is common to use a less dense gas (e.g. helium) to represent the sub-scale jet instead of a high-temperature gas. In this study, the modelling method reported by Littlebury (1981) and Garry (1989) is used, where the density ratio (ρ_j / ρ_∞) is considered a separate similarity parameter, together with *Fr* of *Equation 1.3* and β. While *Fr* and β are used to scale the flow velocity and nozzle mass flow rate (see Chapter 6.1), the mass fraction of helium in the sub-scale jet is determined from the density ratio only, using the following calculation method:

1) The primary modelling requirement is equality of the density ratio ρ_j / ρ_∞ at full scale and in the wind tunnel, denoted with subscripts '*F*' and '*M*' respectively.

$$\left(\frac{\rho_j}{\rho_\infty}\right)_M = \left(\frac{\rho_j}{\rho_\infty}\right)_F$$

Equation 3.2

In further analysis, the jet and ambient conditions are denoted with the subscripts '*j*' and '∞' respectively. At full scale, '*j*' refers to the mixed jet conditions downstream of the engine, while for the wind tunnel model '*j*' refers to the nozzle exhaust conditions.

2) The full-scale exhaust jet and ambient air are assumed to obey the Ideal Gas Law

$$pV = NR_uT$$

Equation 3.3

where p is the gas absolute pressure, V is the gas volume, N is the amount of substance of gas, R_u is the universal gas constant, and T is the gas absolute temperature. With $N = m / M$, $R = R_u / M$ and $m = \rho V$, where m is the gas mass, M is the gas molar mass and R is the specific gas constant, *Equation 3.3* can be written as

$$p = \rho RT$$

Equation 3.4

For dry air at standard conditions, R is equal to 287 J/(kgK) (Anderson, 2001, p. 440). The properties of the full-scale exhaust jet are very similar to that of air, thus $R_j \approx R_\infty$, which is a reasonable assumption for the mixed exhaust jet of a high-bypass-ratio engine.

3) To calculate the full-scale density ratio, the full-scale exhaust jet is assumed to have ambient static pressure p_∞ after a certain travel distance downstream of the engine. Hence, from *Equation 3.4*, the following relationship is valid for $p_{\infty F} = p_{j\,F}$:

$$\rho_{\infty F} T_{\infty F} = \rho_{jF} T_{jF}$$

Equation 3.5

Solving for the density ratio, yields

$$\left(\frac{\rho_j}{\rho_\infty}\right)_F = \left(\frac{T_\infty}{T_j}\right)_F$$

Equation 3.6

The assumption $p_j = p_\infty$, referred to as 'ideal expansion' (see for example MacManus, 2009), is used in simplified performance analysis of civil subsonic aircraft engines. It is a desirable condition in engine design in order to minimise thrust losses. Engines are designed to operate close to this condition during cruise, while at take-off the exhaust jet would be 'under-expanded' at the nozzle exit, i.e. $p_j > p_\infty$.

4) From *Equation 3.3*, with $N = m/M$, $R = R_u/M$ and $m = \rho V$, the density ratio of nozzle jet and ambient air in the wind tunnel can be expressed as follows:

$$\left(\frac{\rho_j}{\rho_\infty}\right)_M = \left(\frac{(p_j M_j)/(R_u T_j)}{(p_\infty M_{air})/(R_u T_\infty)}\right)_M$$

Equation 3.7

where $M_{air} \approx 28.96$ g/mol is the molar mass of air and M_j is the average molar mass of the mixed nozzle jet. The nozzle jet would have approximately ambient temperature and static pressure, therefore the density ratio can be expressed as the ratio of the molar masses:

$$\left(\frac{\rho_j}{\rho_\infty}\right)_M = \left(\frac{M_j}{M_{air}}\right)_M$$

Equation 3.8

For a mole fraction of helium f in the mixed jet, consisting of helium and air, M_j is calculated with the molar mass of helium $M_{He} \approx 4$ g/mol as follows:

$$M_j = M_{He} f + M_{air}(1 - f)$$

Equation 3.9

Combining *Equation 3.8* and *Equation 3.9* yields

$$\left(\frac{\rho_j}{\rho_\infty}\right)_M = \left(\frac{M_{He} f + M_{air}(1 - f)}{M_{air}}\right)_M$$

Equation 3.10

Thus, from *Equation 3.2*, *Equation 3.6*, and *Equation 3.10*, the mole fraction of helium is given by

$$f = \frac{1 - (\rho_j / \rho_\infty)_M}{1 - (M_{He} / M_{air})} = \frac{1 - (T_\infty / T_j)_F}{1 - (M_{He} / M_{air})}$$

Equation 3.11

For an ideal gas, mole fraction and volume fraction are identical (Reible, 1998, p. 97), thus the volumetric flow rate of helium Q_{He} can be calculated from the total nozzle volumetric flow rate Q_{jM} as

$$Q_{He} = Q_{jM} f$$

Equation 3.12

To conclude, the above method allows for modelling the buoyancy of a high-temperature jet with a jet of approximately ambient temperature, which is a mixture of air and a less dense gas (helium) to account for the buoyancy forces due to jet temperature difference. The sub-scale jet buoyancy modelling is based on equality of the ratio of jet and ambient density at full scale and model. In order to calculate the full-scale jet density, two important assumptions are made: 1) the exhaust jet and ambient static pressures are equal at a certain distance downstream of the engine and 2) at that distance, the core and bypass flows are fully mixed, forming one jet of temperature T_{jF}. For known ambient conditions and mixed jet temperature T_{jF}, the mole fraction of helium f in the modelled sub-scale jet can be obtained from the above calculation sequence, assuming all gases used have ideal-gas properties.

3.4 ABL modelling

3.4.1 Mean wind speed profile and turbulence intensity

Ambient winds are movements of air masses caused by differences in atmospheric pressure, occurring due to uneven heating of the Earth's surface by the sun. Close to the surface, the wind characteristics are influenced greatly by the local landscape and the presence of obstacles such as trees, buildings etc., which exert a drag force on the airflow and generate turbulence. Additionally, the Earth's surface absorbs solar radiation and re-radiates it in heat form to the surrounding atmosphere, resulting in a thermal surface-air interaction. Both effects are diffused through turbulent mixing as the vertical distance z from the surface increases. As a result, the wind velocity increases gradually with z until the surface effects become negligible at z_h, called the 'gradient height' (see *Figure 3.5*), which defines the edge of the Atmospheric Boundary Layer (ABL). Modelling of the ABL is essential in civil engineering, where accurate calculations of the wind loads are required in structural analysis and building design. The ABL is commonly divided into an inner (surface) layer, starting from the surface and extending to nominally 10-20% of the ABL thickness, and an outer layer, extending to z_h. Within the surface layer, the flow is dominated by friction forces and the Coriolis effect[§] on the wind, caused by the rotation of the Earth, is not considered important.

The vertical extent of the ABL depends on the surface terrain and the wind speed. *Figure 3.5* shows schematic examples of ABL mean wind speed profiles for urban (high surface roughness), suburban and level country terrain (low surface roughness), where the gradient height z_h reduces with reducing surface roughness. For strong winds, defined as $U_{10} > 10$ m/s (U_{10} is a common reference velocity, measured at $z = 10$ m), the gradient height is typically between 500 and 3000 m (ESDU, 1982). For $U_{10} > 10$ m/s, the thermal effects can be neglected due to the dominance of mechanically-generated turbulence within the ABL (Cook, 1978; ESDU, 1982). This is referred to as 'adiabatic' or 'neutral' Atmospheric Boundary Layer. The mean vertical wind speed profile of a neutral ABL can be expressed mathematically using a power law (Barlow et al., 2009, p. 654; Lubitz & White, 2004, p 2), as shown in *Equation 3.13*, where the reference velocity U_{ref} is usually taken to be U_{10} at $z_{ref} = 10$ m and the power-law exponent a depends on the surface roughness (see *Figure 3.5*).

[§] The Coriolis effect is the apparent deflection of a moving object when viewed from a rotating frame of reference, such as the constantly rotating Earth. It is commonly described as a fictitious force, acting perpendicular to the axis of rotation and the direction of movement of the object.

$$\frac{U_z}{U_{ref}} = \left(\frac{z}{z_{ref}} \right)^{\frac{1}{a}}$$

Equation 3.13

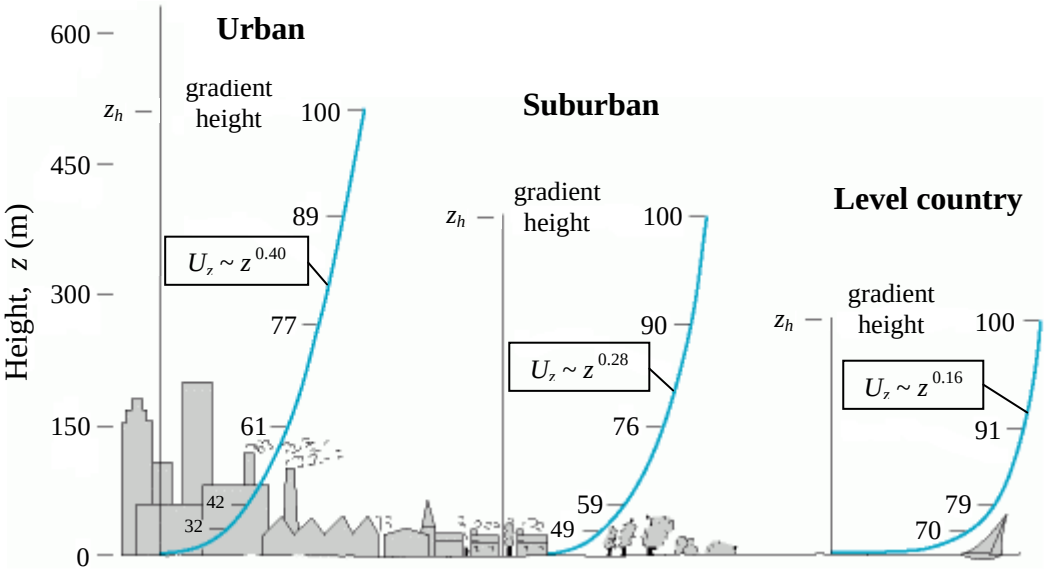

Figure 3.5: Atmospheric Boundary Layer profiles for different terrain, adapted from Plate (1971) Numbers represent velocity in percentage of the gradient wind velocity, shown as 100

A more common mathematical representation of the mean ABL wind speed profile is the logarithmic law. ESDU (1982) gives a method of estimating hourly-mean wind speeds in a neutral ABL (i.e. U_{10} > 10 m/s) by taking into account the height above the surface, the local terrain roughness, as well as changes in the terrain roughness upwind of the site of interest and probability of exceeding the wind speed. The method introduces two modelling parameters – the zero-plane displacement and the surface roughness parameter, illustrated in *Figure 3.6*:

- The *zero-plane displacement* (z_d) defines the boundary, called the 'aerodynamic ground plane', between the resolved part of the flow and the region of unresolved flow near the ground. The region of unresolved flow is typically within areas of buildings or dense vegetation, such as forests, where the flow is complicated and predictions of wind speed cannot be made with a sufficient degree of certainty. The zero-plane displacement is usually smaller than the average local obstacle height. ESDU (1982) gives only nominal values of z_d, for example, $0 \leq z_d \leq 2$ for a wide range of terrain types from ice and calm open sea to open terrain of isolated trees and hedges.
- The *surface roughness parameter* (z_0) is a mathematical parameter in the logarithmic-law model of the ABL, which accounts for the retarding effect of the surface terrain on the wind speed near the ground. It is also a measure of the eddy size

at the ground (Simiu & Scanlan, 1978, p. 46). Within the logarithmic-law model the velocity becomes theoretically zero at z_0, as can be seen from *Equation 3.16*. In practice, below z_0 the wind speed profile does not follow the logarithm function.

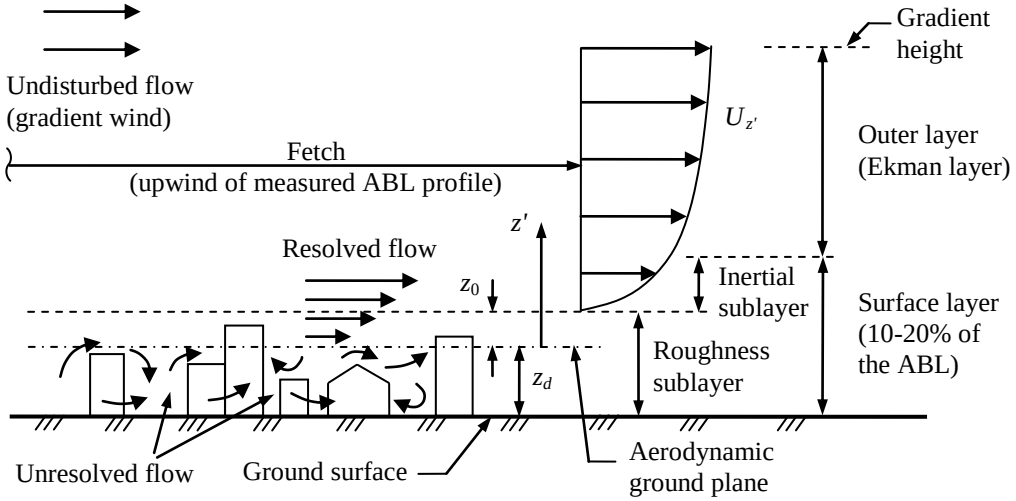

Figure 3.6: Representation of the Atmospheric Boundary Layer (not to scale)

The physical height above surface z is commonly expressed as $z = (z_d + z')$, where z' is the height above the aerodynamic ground plane (see *Figure 3.6*). It should be noted that the notation used here differs from the one used by ESDU (1982), where only the height above the aerodynamic ground plane, denoted with z, is considered. It will be argued later in Chapter 6.2 that in an open terrain the zero-plane displacement can be considered to be approximately zero and thus $z \approx z'$.

The structure of the surface layer can further be divided into a roughness sublayer, extending from the ground to $z' = z_0$, and an inertial sublayer. Merlot (2010) summarised the flow characteristics of the surface layer as follows. Within the roughness sublayer the flow turbulence is affected predominantly by the structure of the roughness elements, making z_0 the governing length scale. Turbulence is generated by both shear production and by the wake regions behind the roughness elements. Within the inertial sublayer ($z' > z_0$), the shear production is considered negligible and the dominant turbulent process is the convection of large-scale eddies.

The method for determining the mean vertical wind speed profile, given in ESDU (1982), starts with assuming a wind speed $U_{z'\,ref}$ at a reference height z', usually at $z' = 10$ m, for a known location close to the location of interest. Examples of reference hourly-mean wind speeds over a return period of fifty years in the UK are given in Figure 1 in ESDU (1982) for uniform open terrain ($z_0 = 0.03$ m). The method then follows a sequence of calculations of correction factors using graphs developed from

experimental measurements for an ABL in equilibrium. An ABL is defined to be in equilibrium with the underlying surface when the wind speed profile does not vary with increasing fetch upwind, shown in *Figure 3.6*. In practice, this is achieved when the ABL is developed over a fetch of at least 100 km of approximately uniform terrain (ESDU, 1982, p. 7). The factors in the ESDU method account for step changes in the terrain roughness along the fetch, probability of exceeding the wind velocity magnitude and direction, and changes in the local topography. In the current study, the local site of the field trials, i.e. Cranfield Airport, which is to be modelled at sub scale, is surrounded by open country terrain of approximately even distribution from all sides, with little changes in terrain roughness in the prevailing direction of the mean wind velocity. Therefore, no correction factors were considered and a simplified model of the wind speed profile, based on data by Harris & Deaves (1981) and described in Appendix A of ESDU (1982), was adopted in this study. It is given by

$$U_{z'} = \frac{u^*}{\kappa}\left[\ln\left(\frac{z'}{z_0}\right) + a_1\left(\frac{z'}{z_h}\right) + \left(1 - \frac{a_1}{2}\right)\left(\frac{z'}{z_h}\right)^2 - \frac{4}{3}\left(\frac{z'}{z_h}\right)^3 + \frac{1}{4}\left(\frac{z'}{z_h}\right)^4\right]$$

Equation 3.14

where the following parameters are introduced:

- mean wind speed at a height z'
- gradient height $z_h = u^*/(6f_c)$
- Coriolis parameter $f_c = 2\omega\sin(\varphi)$, accounting for the wind deflection due to the Coriolis effect; f_c depends on the local latitude angle φ and the angular velocity of the Earth, based on a sidereal day, $\omega \approx 7.29\times10^{-5}$ rad/s
- friction velocity u^*, defined in *Equation 2.11*
- von Karman constant $\kappa \approx 0.4$
- empirical constant $a_1 \approx 5.75$

Equation 3.14 is an empirical model of the full ABL wind speed profile up to the gradient height. With respect to the planned measurements of this study, modelling the ABL at such heights is of little practical significance. For heights below 300 m, the second-order terms can be neglected, reducing *Equation 3.14* to

$$U_{z'} = \frac{u^*}{\kappa}\left[\ln\left(\frac{z'}{z_0}\right) + 34.5\frac{f_c z'}{u^*}\right]$$

Equation 3.15

This can be further simplified for heights $z' < 30$ m, where the Coriolis effect on the wind speed can be neglected:

$$U_{z'} = \frac{u*}{\kappa} \ln\left(\frac{z'}{z_0}\right)$$

Equation 3.16

With regard to the current study, a height of 30 m would equal to 150 mm at 1:200 scale, which is beyond the vertical height limit of the planned measurements at sub scale. Also, the largest row of baffles are planned to extend to a height of 2 m above the surface, as will be discussed in detail in Chapter 8.1, which equals to 10 mm at 1:200 scale and is well inside the 150 mm model boundary of the vertical wind speed profile.

At $z' = 10$ m, *Equation 3.16* is written as

$$U_{10} = \frac{u*}{\kappa} \ln\left(\frac{10}{z_0}\right)$$

Equation 3.17

where z_0 is given in metres. Solving *Equation 3.16* and *Equation 3.17* for the velocity ratio $U_{z'}/U_{10}$ yields:

$$\frac{U_{z'}}{U_{10}} = \frac{\ln(z'/z_0)}{\ln(10/z_0)}$$

Equation 3.18

The obtained relationship gives a non-dimensional wind speed profile with height z', based on a reference wind speed at $z' = 10$ m, which is only a function of the surface roughness parameter z_0.

As discussed in Chapter 1.5, the second important parameter in ABL modelling is the turbulence intensity of the flow. It is a measure of the wind speed fluctuations due to particle movement and the resulting high momentum convection within the ABL flow, leading to generation of turbulence. Theoretically, the velocity fluctuations would occur in all three dimensions within the flow, however, in practice only the component in the mean flow direction I_u is considered important. As shown in *Figure 3.7*, at a height z' the instantaneous wind speed in mean flow direction $U_{z'}(t)$ can be represented by the sum of a mean wind speed component $U_{z'}$ and a fluctuating component $u_{z'}(t)$:

$$U_{z'}(t) = U_{z'} + u_{z'}(t)$$

Equation 3.19

The mean wind speed component $U_{z'}$ is averaged over a certain period of time t_0, usually taken to be one hour in meteorological studies. With $U_{z'}$, the turbulence intensity I_u is defined as

$$I_u = \frac{\sigma_u}{U_{z'}}$$

Equation 3.20

where the standard deviation σ_u is obtained by integrating the fluctuating component $u_{z'}(t)$ over the interval t_0 as follows:

$$\sigma_u{}^2 = \frac{1}{t_0}\int_0^{t_0} [u_{z'}(t)]^2 \, \mathrm{d}\, x$$

Equation 3.21

ESDU (1983) gives the following relationship, based on data by Harris & Deaves (1981) for an ABL in equilibrium

$$\frac{\sigma_u}{u*} = \frac{7.5\eta\left[0.538 + 0.09\ln(z'/z_0)\right]^{\eta^{16}}}{1 + 0.156\ln\left[u*/(f_c z_0)\right]}$$

Equation 3.22

where $\eta = 1 - (6f_c z'/u*)$. From *Equation 3.20*, the turbulence intensity can be expressed the product of two ratios

$$I_u = \frac{\sigma_u}{U_{z'}} = \frac{\sigma_u}{u*}\frac{u*}{U_{z'}}$$

Equation 3.23

where $\sigma_u / u*$ is given in *Equation 3.23* and $u* / U_{z'}$ is obtained from *Equation 3.16*. The calculations of the modelled ABL at sub scale for the FID and HWA experiments are presented in detail in Chapter 6.2.

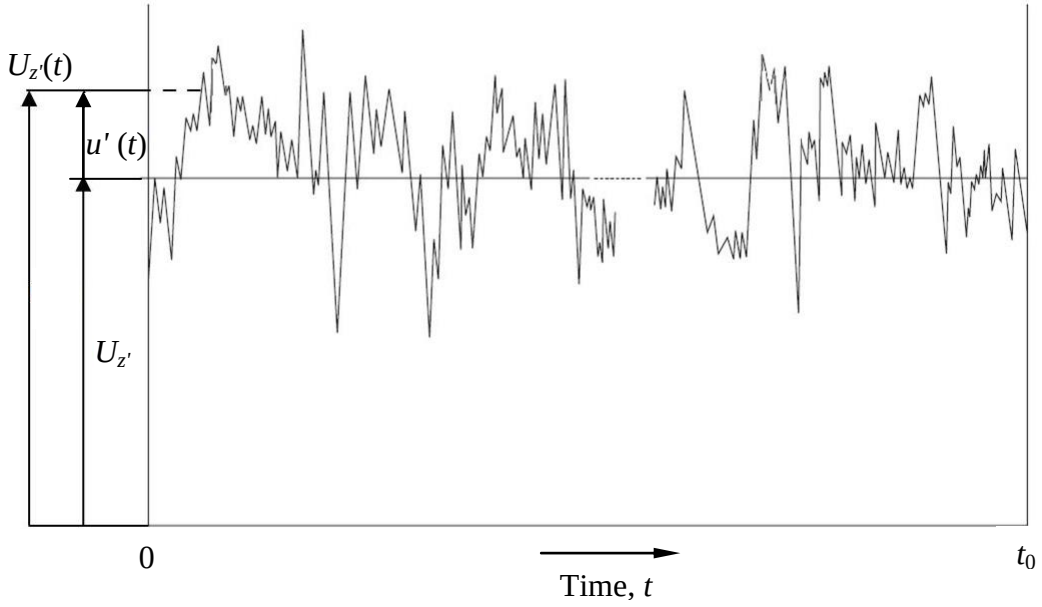

Figure 3.7: Definitions of instantaneous wind speed, mean wind speed component and fluctuating component (adapted from Merlot, 2010)

To conclude, the above ABL modelling method is based on the empirical equations given in ESDU (1982) for the mean wind speed profile and ESDU (1983) for the turbulence intensity profile. It assumes a neutral ABL in equilibrium with the underlying local surface. The mean wind speed profile is assumed to follow a logarithmic law, which is restricted to heights up to 30 m, where the Coriolis effect on the mean wind speed is negligible.

3.4.2 Sub-scale modelling devices

Modelling the Atmospheric Boundary Layer in sub-scale tests requires preconditioning the flow upstream of the wind tunnel working section in order to generate the desired geometrically-scaled velocity profile and high level of turbulence. The type of wind tunnel facility used for ABL modelling, called Atmospheric Boundary Layer Wind Tunnel (ABLWT), includes a flow development section between the settling chamber and the working section. Ideally, the sub-scale boundary layer should grow naturally over a long rough wall in order to give good match to the full-scale ABL in terms of mean and turbulent flow characteristics (Cook, 1978). In practice, the fetch required for such natural development is usually too long and cannot be provided by the test facility, requiring the use of ‘artificial’ methods. These are a combination of an

initial generation of turbulence through mixing devices and an intermediate fetch of roughened wall over which the boundary layer develops.

The arrangement of the flow development section consists commonly of a system of barriers and vortex generators, located at the start of the section, and roughness elements, distributed in a certain pattern on the remainder of the section floor. Examples of vortex generators and tripping rods are shown in *Figure 3.8*. The elliptic vortex generators, similar to the ones of *Figure 3.8a*, were first proposed by Counihan (1969) as an alternative to the triangular vortex generators, which had a tendency for an excessive momentum loss in the boundary layer region close to the wall and insufficient momentum loss in the region away from the wall. Elliptic vortex generators are commonly used in ABL modelling studies in Cranfield University's 8'×4' ABLWT.

The roughness elements are typically solid blocks of the same size (see *Figure 3.9a*), which varies depending on the turbulence length scale of the modelled ABL. Armitt & Counihan (1968) and Counihan (1969) used standard LEGO® base boards with LEGO® bricks to create the roughed floor of the flow development section. LEGO® bricks have the advantage of being relatively small, thus fine adjustments can be made to the floor roughness and larger bricks can be created, if necessary, by building up on the existing pattern.

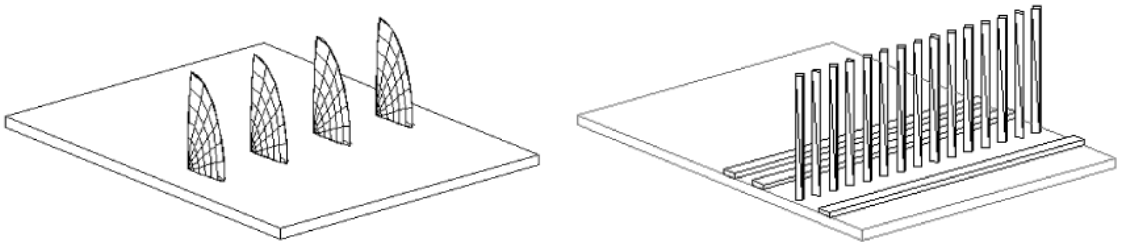

(a) (b)

Figure 3.8: Examples of Atmospheric Boundary Layer (ABL) modelling devices (flow direction is from bottom right): (a) elliptic vortex generators; (b) rods and tripping bars (taken from Barbosa et al., 2002)

The distribution pattern and size of the roughness elements and the arrangement of the system of barriers and vortex generators varies depending on the wind tunnel facility used and on the flow characteristics of the full-scale ABL to be modelled. As described by Cook (1978), the choice of arrangement is largely made on the basis of intuition and experience from trial-and-error. While the components vary in shape and size between different methods of ABL simulation, their roles remain effectively the same. The barrier is used to provide initial momentum deficit and increase the depth of the boundary layer, while the vortex generators, located at a close distance downstream

of the barrier, increase the flow turbulence and thus provide the necessary mixing within the boundary layer. A coarse turbulence grid upstream of the barrier can also be used to generate additional turbulence. Examples of flow development section arrangements are shown in *Figure 3.9a* (without vortex generators) and *Figure 3.9b* (with triangular vortex generators).

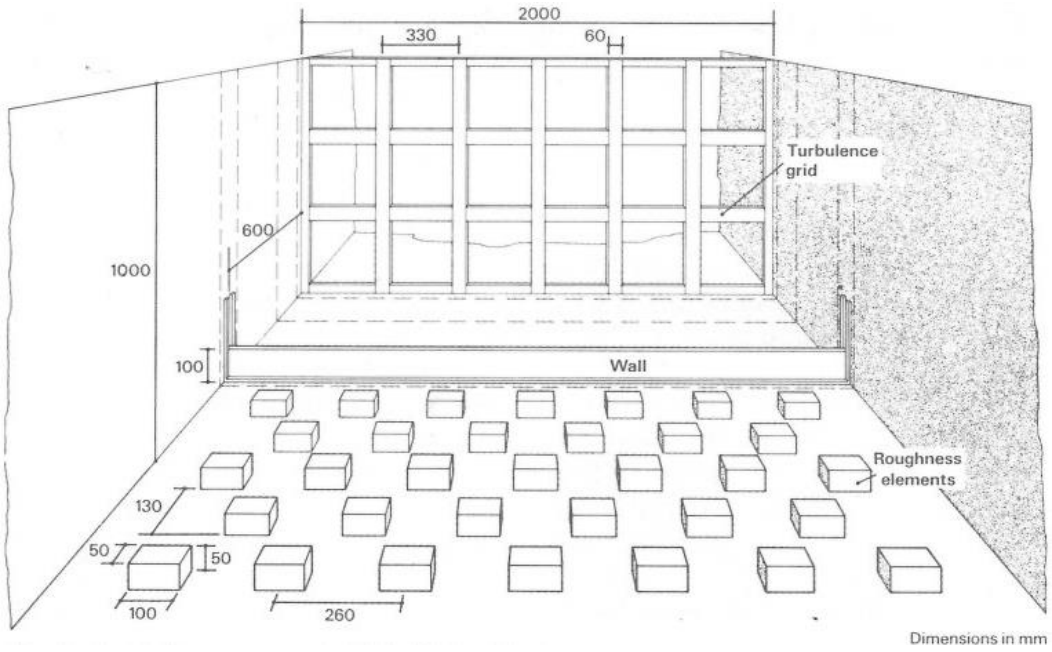

(a)

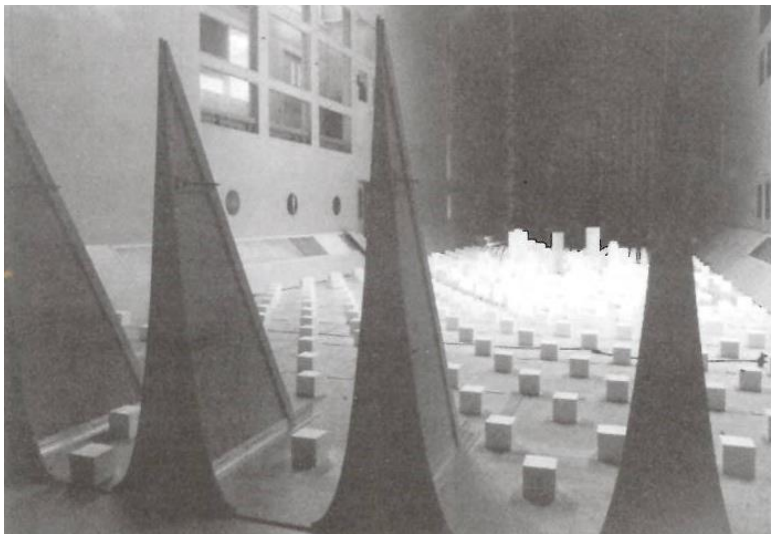

(b)

Figure 3.9: Examples of development sections of Atmospheric Boundary Layer Wind Tunnels (ABLWT) by: (a) Cook (1978), including a barrier and a turbulence grid (flow direction is from top to bottom); (b) Barlow et al. (1999), including vortex generators (flow direction is from bottom left)

3.4.3 8'×4' ABLWT

Cranfield University's low speed 8'×4' ABLWT, depicted schematically in *Figure 3.10*, was used for the majority of the sub-scale tests conducted in this study. It has an open return circuit layout with a flow development section of 15 m length and a closed working section of 8 ft (2.4 m) nominal length and cross section of 8 ft by 4 ft (2.4 m by 1.2 m). Tests can be conducted for freestream speeds between 0.5 and 16 m/s with and without a simulated boundary layer. In the latter case the freestream turbulence intensity in the working section is nominally less than 0.1%. The working section has a 360º floor-mounted rotating turntable, which allows models to be turned relative to the flow direction in crosswind simulations, and a computer-controlled three-axis traverse system for automatic three-dimensional movement of measurement probes. A separate high pressure system can be used to deliver suction or blowing, e.g. an exhaust jet, in the working section. The test capabilities of the 8'×4' ABLWT include measurement outputs such as pressure, velocity, forces and moments, gas concentration of a tracer gas using FID, as well as flow visualisation.

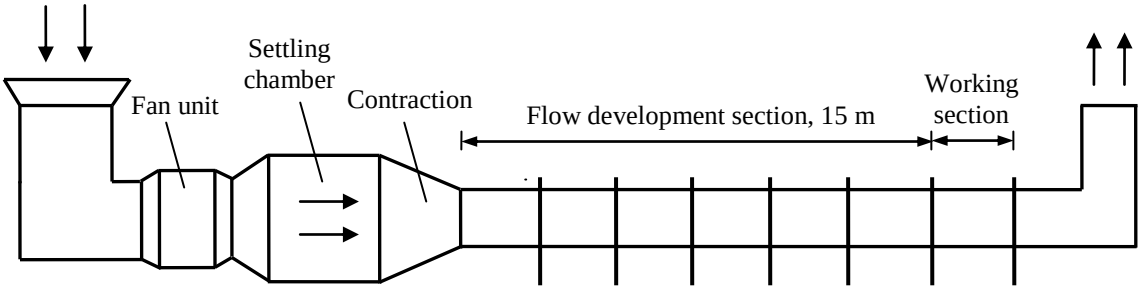

Figure 3.10: Schematic illustration of Cranfield University's 8'×4' low speed Atmospheric Boundary Layer Wind Tunnel (ABLWT) (side view; not to scale)

In the course of this study, various experimental techniques were applied within the 8'×4' ABLWT. The measurement principles of these techniques were discussed in Chapter 3.2. The individual arrangement for each test is described in detail at the start of the corresponding chapter presenting the test results.

4 Initial experiments

The initial wind tunnel tests consisted of several sets of experiments designed to study the behaviour of an exhaust jet in a controlled wind tunnel environment, and the flow field in the near and far field of porous screens of different porosity and orientation to the flow direction.

4.1 Exhaust plume visualisation

The flow development of an exhaust jet in ground proximity was first studied using flow visualisation. The experiments aimed

- to visualise the exhaust jet plume beneath an external stream and identify any occurring trends in its behaviour, and

- to determine whether steady 'lift-off' of an exhaust plume in ground proximity can be achieved in a wind tunnel environment. This was defined as the physical separation of the coherent plume from the ground (visible gap between plume and wind tunnel floor), resulting in changes in the vertical plume trajectory.

All plume visualisation experiments were conducted in Cranfield University's 8'×4' Atmospheric Boundary Layer Wind Tunnel (ABLWT) using the flow visualisation method described in Chapter 3.2.2 (see *Figure 3.1* for working section arrangement). The Atmospheric Boundary Layer (ABL) was not modelled at this stage of the experiments. Boundary layer velocity profile measurements of the clean working section were performed at a later stage of this study during the force balance experiments and are described in Chapter 5.3. A circular nozzle of inner diameter d = 6.2 mm was chosen to represent the mean exhaust jet diameter of a CFM56-family engine at 1:200 scale. This value has been reported by Cini (2008) as part of a literature survey on Boeing 737 and Airbus A320 aircraft. The nozzle was fixed at 12.5 mm above the working section floor, measured to the nozzle centre line, which is the mean engine height above the ground up to the fan axis of rotation of a BAe 146-301 aircraft at 1:200 scale. Nozzle flow rate measurements were taken with flow meters connected to the tubing. The digital camcorder was positioned at x = 1250 mm and 30 mm ground clearance to its lens centre line. The exhaust jet was illuminated with a laser sheet at various x locations (yz planes) between 3.2d and 129d. Images of the 8'×4' ABLWT working section are shown in *Figure C.1* and *Figure C.2* in Appendix C.

The arrangement of the tubing connection to the nozzle in the working section (see *Figure 3.1* in Chapter 3.2 and *Figure 4.4b*) raised concerns about possible stem vortex interference effects on the exhaust plume. As a result of the finite span of the tube, the wind tunnel flow would form a three-dimensional horseshoe vortex downstream. Consequently, the wake would be governed by a pair of counter-rotating streamwise vortices creating a downwash effect, i.e. inducing a downward velocity component, when interacting with the nozzle jet. Such interference effects would counter-act the upward buoyancy component, which is fundamental to the baffles concept. Considerations were made to maintain a sufficient horizontal length of the tube connecting to the nozzle (see *Figure 4.4a*) in order to allow for the flow to reattach. Close to the ground, the vortex effects would dissipate due to the retarding effect of the wind tunnel floor surface. At the nozzle exit, the interference effects were assumed to be small due to the high momentum of the jet. Further downstream where the jet momentum is reduced signifcantly, the vortices are decayed and their influence on the jet development is considered negligible.

Tests were performed with a nozzle volumetric flow rate of 34 l/min (litres per minute), the maximum achievable flow rate with the available test equipment, which gave a mean exit jet velocity U_j = 18.8 m/s. The freestream velocity in the working section was U_∞ = 5 m/s, giving a ratio of freestream velocity to exit jet velocity β = 0.266. Two cases of exhaust jet were investigated: a 'COLD' case where a mixture of air at ambient temperature and smoke was used, and a 'HOT' case where helium was added to the mixture to simulate the buoyancy of an exhaust jet at high temperature. A full-scale exhaust jet density of ρ_{jF} = 1 kg/m^3 was assumed at this initial stage of the investigation, which at standard pressure (i.e. 101325 Pa) gives an exhaust jet temperature of 353 K. The mole fraction of helium was then calculated from *Equation 3.11* as f = 0.19, giving a volumetric rate of helium Q_{He} = 6.5 l/min. The jet Reynolds number, calculated with d and U_j, was $Re_j \approx 5580$ in the HOT case and $Re_j \approx 7680$ in the COLD case. In all above calculations the smoke flow in the jet was neglected, as it was considered small compared to the flow rates of helium and air.

The post-processing method of the results, discussed in Chapter 3.2.2, is illustrated in *Figure 4.1*. Results (in pixels) for plume area in the laser sheet plane and for maximum spread in lateral (W) and vertical (H) direction were obtained each video recording analysed and averaged over 30 frames per video. The jet area and diameter, observed at x / d = 3.2, were considered to be approximately equal to the nozzle exit area and diameter respectively, and were used to obtain non-dimensional results for plume area S, width W' and height H', as follows:

$$S = \frac{Plume\ area\ inside\ boundaries}{Plume\ area\ at\ x/d = 3.2}$$

Equation 4.1

$$H' = \frac{Plume\ mean\ maximum\ height}{Jet\ diameter\ at\ x/d = 3.2}$$

Equation 4.2

$$W' = \frac{Plume\ mean\ maximum\ width}{Jet\ diameter\ at\ x/d = 3.2}$$

Equation 4.3

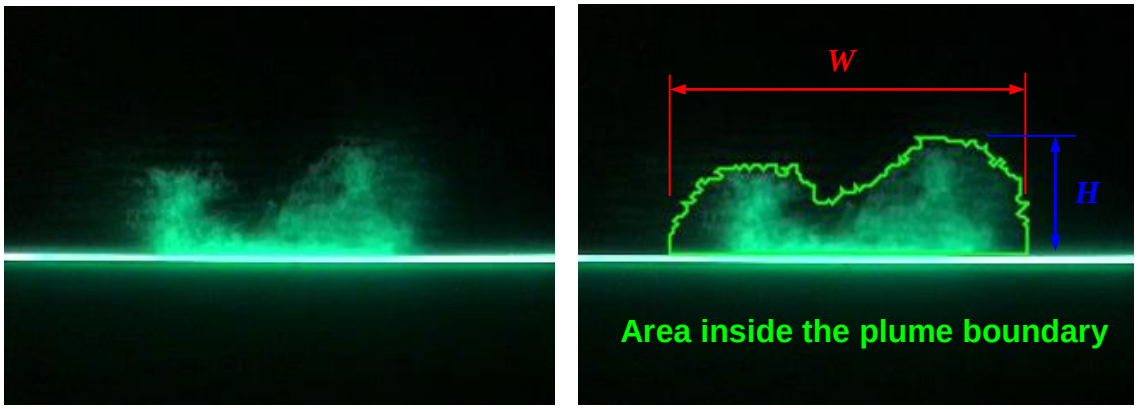

Figure 4.1: Flow visualisation post-processing method (example of an individual frame)

The results for non-dimensional plume area S are shown in *Figure 4.2*. No differences between COLD and HOT case were observed for $x/d \leq 50$. For greater distances downstream the plume of the HOT case becomes progressively larger compared to the COLD case. It appears that initially S varies linearly with distance downstream until $x/d \approx 50$. For $50 \leq x/d \leq 129d$, S increases with $(x/d)^2$ reaching 173 and 185 for the COLD and HOT case respectively. To estimate the precision of the results, a short statistical analysis was conducted at $x/d = 97$ and $x/d = 129$, taking several sets of 30 frames from the recorded videos and comparing the results. A maximum variation of approximately 10% (indicated by the error bars in *Figure 4.2*) was estimated at $x/d = 129$, where the largest plume spread was observed and thus the uncertainty in defining the plume boundaries was the highest. Such error analysis leads to the conclusion that although the HOT gas case appears to achieve greater plume area as d increases, the calculated values lie within or very close to the estimated error range. Thus, no buoyancy effects could be definitely demonstrated when modelling the exhaust jet with a mole fraction of helium $f = 0.19$.

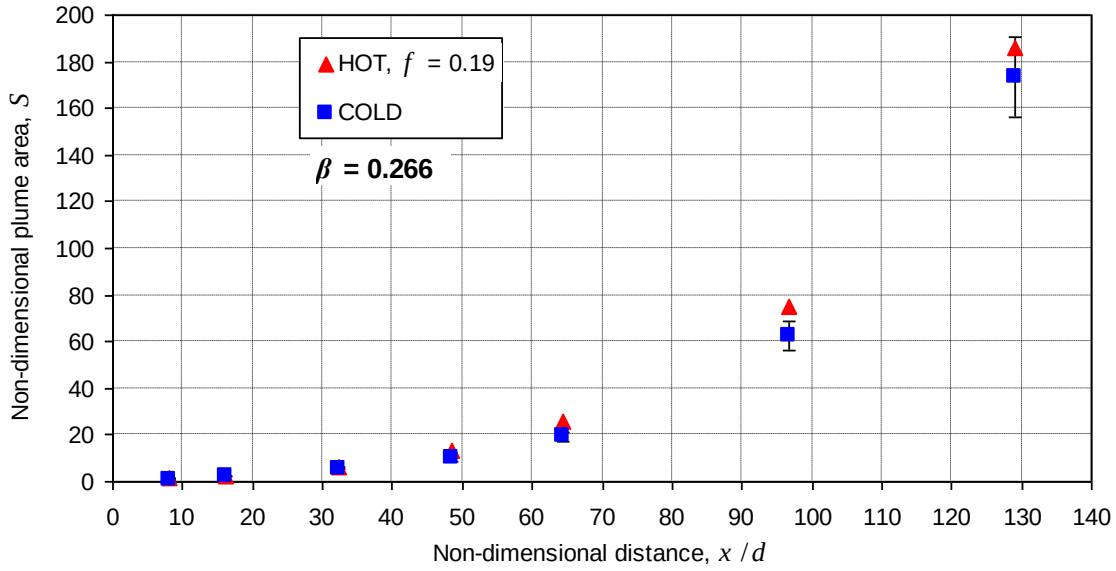

Figure 4.2: Variation of non-dimensional plume area with longitudinal distance downstream of nozzle exit for β = 0.266

The results for the variation of H' and W' with x/d, shown in *Figure 4.3*, agree qualitatively with other results reported in the literature and discussed in Chapter 2.3. The jet growth rate parallel to the wall is considerably greater than its growth rate perpendicular to the wall. For both length scales the obtained results are greater in the HOT case. It appears that the growth rates upstream and downstream of $x/d = 50$ can reasonably well be approximated by linear relationships. In *Figure 4.3*, a comparison is made with data from Davis & Winarto (1980) for ground clearance of the nozzle centre line of $2d$ and downstream distances as far as $x/d = 65$. The results compare well for both jet length scales albeit the results of Davis & Winarto (1980) have been carried out in quiescent air. The secondary (freestream) flow is expected to restrict the jet spread as the downstream distance from the nozzle exit increases and the wind tunnel velocity becomes greater than the local jet velocity. However, a quantitative comparison of growth rates downstream of $x/d = 48$ shows that these agree very well for W' (slope is approximately 0.240), whereas for H' the growth rate reported by Davis & Winarto (1980) is less than half the value obtained here. The error introduced from the choice of post-processing method for the characteristic jet scales was estimated similarly to the one of the plume area, obtaining an approximate value of ± 5 pixels at $d = 129$. This gives 6.7% relative error in H' and 2.8% in W'. Likewise the error bars indicate that the observed differences between HOT and COLD case cannot be strictly attributed to buoyancy effects.

A plot of the variation of plume aspect ratio with x/d, defined as $\lambda = W'/H'$, is included in *Figure C.3* in Appendix C. It appears that in both cases λ reaches a

maximum at $x/d \approx 100d$, downstream of which the relative growth rate of the jet in vertical direction becomes greater. This could be an indication of the jet buoyancy characteristics, starting to affect its distribution in space. However, since this maximum was determined essentially by the results at $x/d = 129$, more data further downstream is required to validate this statement. The error analysis performed combining the errors of H' and W' confirms previous conclusions regarding the differences between COLD and HOT case.

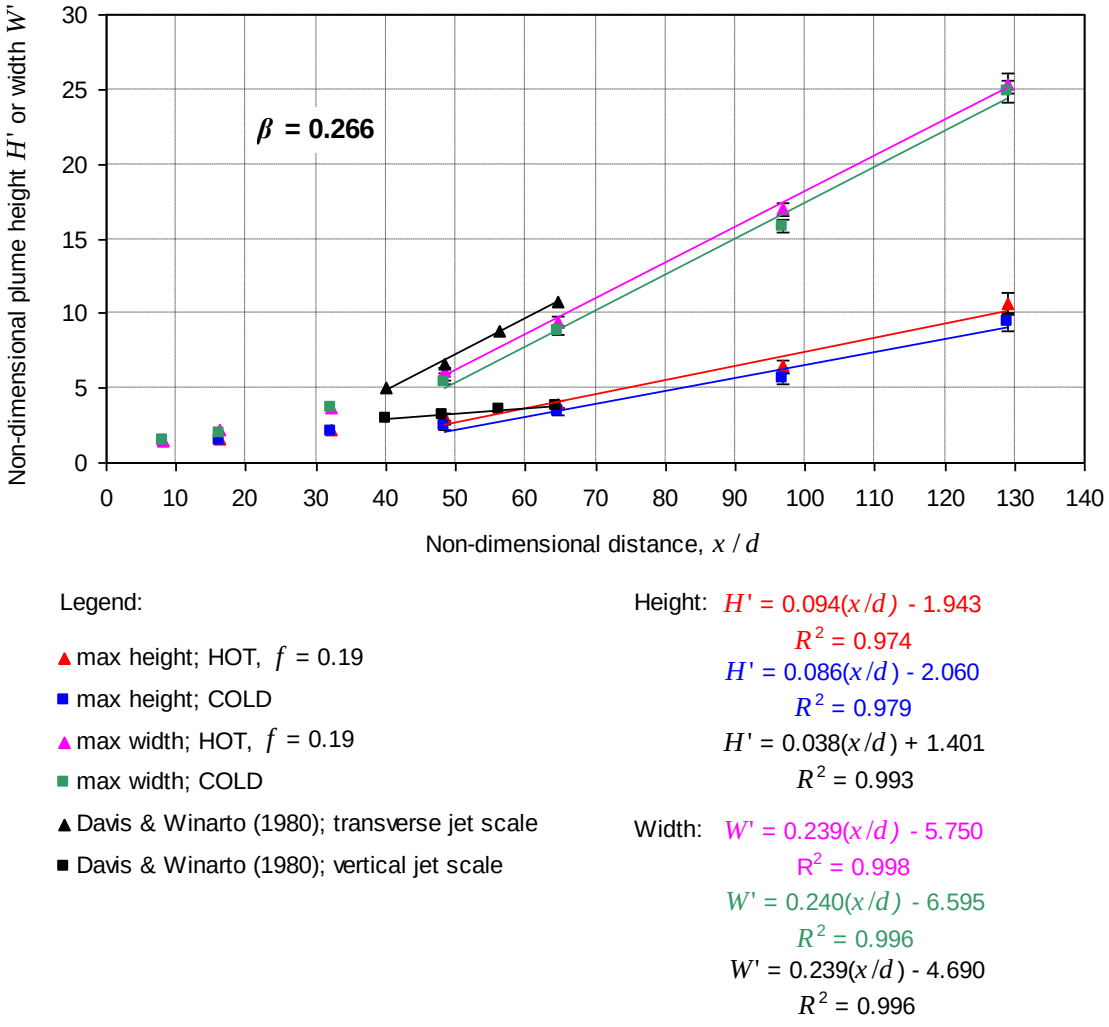

Figure 4.3: Variation of plume mean maximum width and height with distance downstream of nozzle exit for β = 0.266

Both the post-processing tools used and the choice of flow visualisation method show several disadvantages which have to be considered when discussing the accuracy of the obtained results. First, as was evident that during some of the tests the smoke flow rate reduced occasionally causing the visualised plume area to appear smaller than

in reality. Such time periods of the video footage were omitted during the post-processing of the results. The choice of flow visualisation method also created difficulties as the laser beam pixels had to be digitally "removed" from each frame. Second and most important, defining the plume area boundary further downstream of the nozzle exit proved to be subjective even with an increased contrast level, thus all results for x / d = 129 should be considered with a tolerance of nominally 10%. With decreasing distance to the nozzle, this tolerance becomes of considerably smaller magnitude. Additionally, the available version of Pixcavator automatically applied a shrink factor of 2, blurring the plume boundaries and reducing the quality of the images. Finally, the method of averaging raises the question of how many frames from each recorded video are sufficient to obtain a representative result. However, compared to the tolerances discussed above, the error introduced by this method can be considered of small significance.

4.2 Plume 'lift-off' visualisation

In the second stage of the exhaust plume visualisation tests, attempts were made to cause coherent plume lift-off by increasing the jet buoyancy and varying the wind tunnel speed. These experiments were conducted with thinner tubing to reduce the wake induced from the wind tunnel flow. As a consequence, the maximum achievable flow rate was 27 l/min, giving a mean exit jet velocity of 14.9 m/s and an exit jet Reynolds number of 6100 for the COLD case. The arrangement in the working section (*Figure 4.4*) was modified by adding a wooden prism-shaped 'deflector' in the path of the jet, fixed to the working section floor so that it was symmetrically positioned in lateral direction with respect to the nozzle.

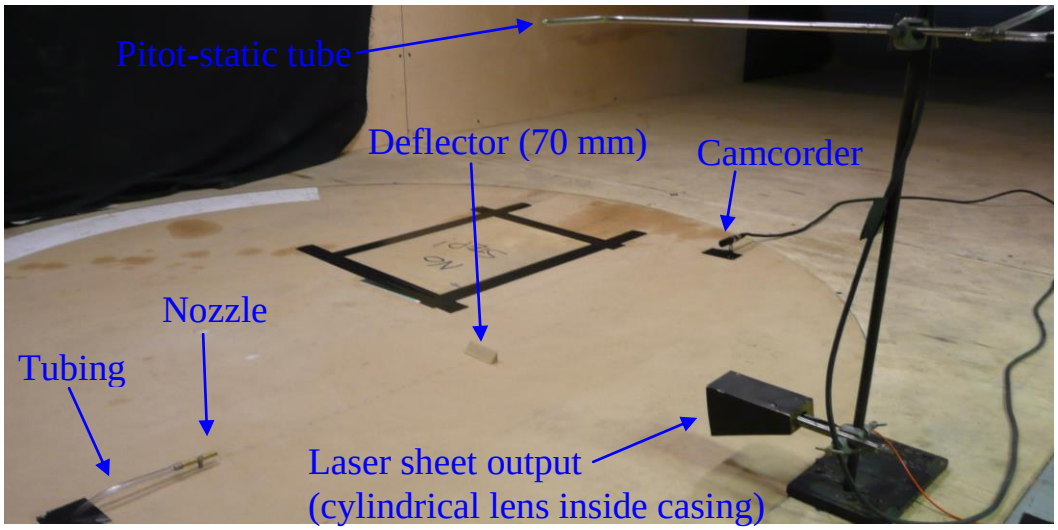

(a)

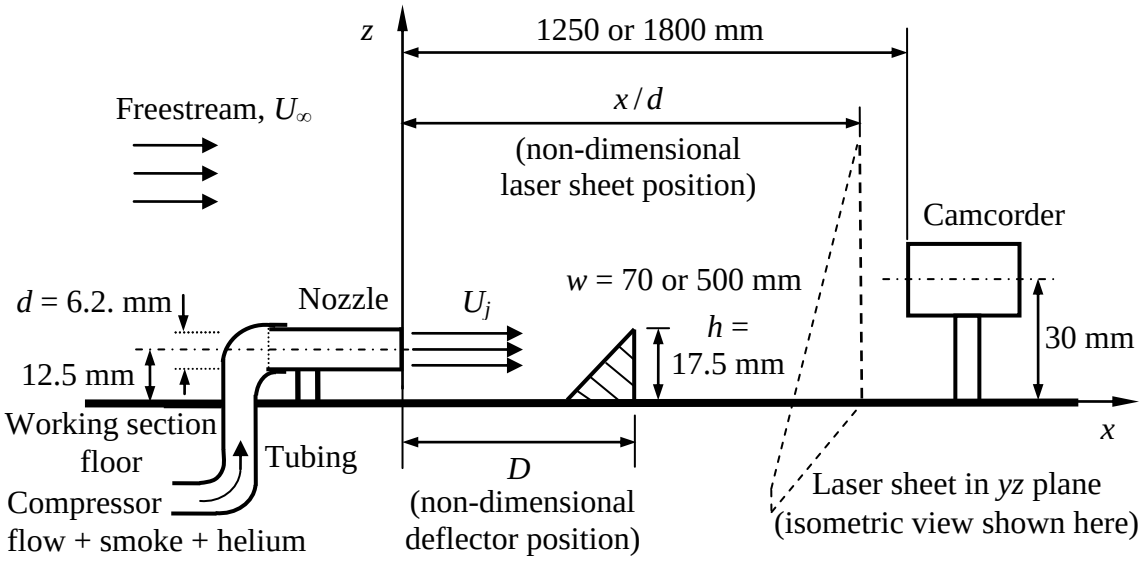

(b)

Figure 4.4: 8'×4' ABLWT arrangement for lift-off flow visualisation tests: (a) working section image (isometric view); (b) schematic illustration of working section (side view, not to scale)

Deflectors of two different widths (70 mm and 500 mm), both of the same height (12.5 mm) and slope angle (45º), were tested. In full-scale this would yield a height of 2.5 m, widths of 14 m and 100 m respectively, and total inclined areas of 49.5 m^2 and 353.6 m^2 respectively. The deflectors are referred to using their width in terms of the nozzle diameter, w / d = 11.3 and w / d = 80.6, respectively. The non-dimensional deflector position D, used in the results analysis, is defined as follows:

$$D = \frac{Deflector\ position\ along\ x\ axis}{Nozzle\ diameter}$$

Equation 4.4

In the first stage of the lift-off experiments, tests were conducted only with the short deflector (w = 70 mm). The lift-off criterion by Meroney (1979), presented in *Equation 2.12* in Chapter 2.6.2, was applied to estimate the lift-off distance. The buoyancy length scale l_b and the modified Froude number Fr^* were calculated from *Equation 2.13* using a reference length l_{ref} = 0.015 m and the freestream velocity U_∞ as reference velocity. These parameters were estimated from Meroney's experiments, where a characteristic source width of 0.03 m for l_{ref}, equal to approximately 2.4 times the nozzle diameter, and the ambient wind tunnel speed were used. The conducted tests are described below.

1) Air and smoke only ($Fr^* = \infty$, since $\rho_j = \rho_\infty$), $w/d = 11.3$, D varied between $32 \leq D \leq 97$, constant freestream velocity $U_\infty = 5$ m/s

The purpose of this initial test was to investigate solely the effect of placing a deflector in the path of a neutrally-buoyant jet. The laser sheet was moved in small increments of 4 nozzle diameters upstream and downstream of the deflector. Compared to a plain wall jet without deflector, no apparent differences in the vertical jet trajectory were observed. It appears that the entire plume is drawn in the deflector wake. Images for D = 64.5 are shown in *Figure C.4* in Appendix C. A possible cause for such jet behaviour is the presence of a horseshoe vortex due to the finite span of the deflector.

2) Air and smoke only ($Fr^* = \infty$); no deflector; freestream velocity varied between $0 \leq U_\infty \leq 5$ m/s

As concluded from the literature review in Chapter 2.9, the presence of a secondary flow is considered to have a significant role on the possible plume lift-off at large distances downstream where the jet velocity is reduced. Therefore, the test under *1)* was repeated without a deflector at lower wind tunnel speeds. Up to x/d = 16, the secondary flow effects of constraining the plume spread appear to be insignificant for all wind tunnel speeds tested. Downstream of x/d = 60, differences in the spread could be observed only between 0 and 3 m/s. If no secondary flow is present, the jet spreads in lateral direction at a considerably higher rate and stays attached to the surface, keeping approximately the same maximum height. This trend was observed up to the furthest distance tested, x/d = 129. Random frames from the recorded video footage, showing the plume at x/d = 64.5 for wind tunnel speeds of 0, 2 and 5 m/s, are presented in *Figure C.5* in Appendix C.

3) No deflector; wind tunnel off ($Fr^* = 0$, since $U_{ref} = 0$); helium flow rate Q_{He} increased up to 9 l/min

The effects of increasing the natural buoyancy of the jet were investigated by gradually adding more helium in a still air environment. The flow rate of air and smoke was reduced accordingly in order to keep the overall flow rate 27 l/min. The observed jet behaviour was similar to the one stated under *2)*. No lift-off occurred within the tested distances $x/d \leq 129$. At large distances downstream the maximum jet height appeared to increase as Q_{He} increased, most certainly due to buoyancy starting to prevail as the jet momentum reduces.

4) HOT ($Q_{He} = 9$ l/min, $f = 0.33$, $Fr^* \approx 95$) and COLD (air and smoke, $Fr^* = \infty$); $w/d = 11.3$, D varied between $32 \leq D \leq 97$; constant freestream velocity $U_\infty = 2$ m/s

As no changes in the vertical trajectory of the jet could be observed during the tests of *1), 2)* and *3)*, a configuration of a buoyant jet and a deflector was tested. The

freestream velocity in the working was reduced to 2 m/s to compromise between the constraining effects at higher speeds and the jet aptitude to attach to the surface and spread in lateral direction when no secondary flow is present. Quantitative data were obtained from the recorded videos (*Figure 4.5*) by means of the Pixcavator post-processing method used in Chapter 4.1. Using simple statistical analysis on 15 random frames of the video recording at the furtherst location x/d tested, the uncertainty of the obtained values for the mean maximum plume height and width was estimated to be approximately 6.5% and 4% respectively (see error bars in *Figure 4.5*). It appears that the differences in mean maximum height H' between the HOT and COLD case are very small and are within the estimated error bars. Downstream of $x/d = 60$, the lateral spread of the COLD case becomes greater compared to the HOT case (*Figure 4.5b*), with the observed differences exceeding the error range. It is also evident that moving the deflector closer to the nozzle exit increases the spread of the plume downstream in both vertical and lateral direction.

Calculations of the modified Froude number $Fr^* \approx 95$ and buoyancy length scale $l_b \approx 1.6\times10^{-4}$ give a lift-off distance of approximately 35 mm according to the criterion by Meroney (1979). Further analysis of the calculations shows that if the helium flow rate were reduced to $Q_{He} = 2$ l/min (more than 4 times) and the remaining flow parameters were kept the same, the lift-off distance should increase only by a factor of approximately 2, according to *Equation 2.12* and *Equation 2.13*. During the experiments of *3)*, where Q_{He} was varied from 0 to 9 l/min, the plume was observed to be completely attached to the ground at such small distances downstream of the nozzle.

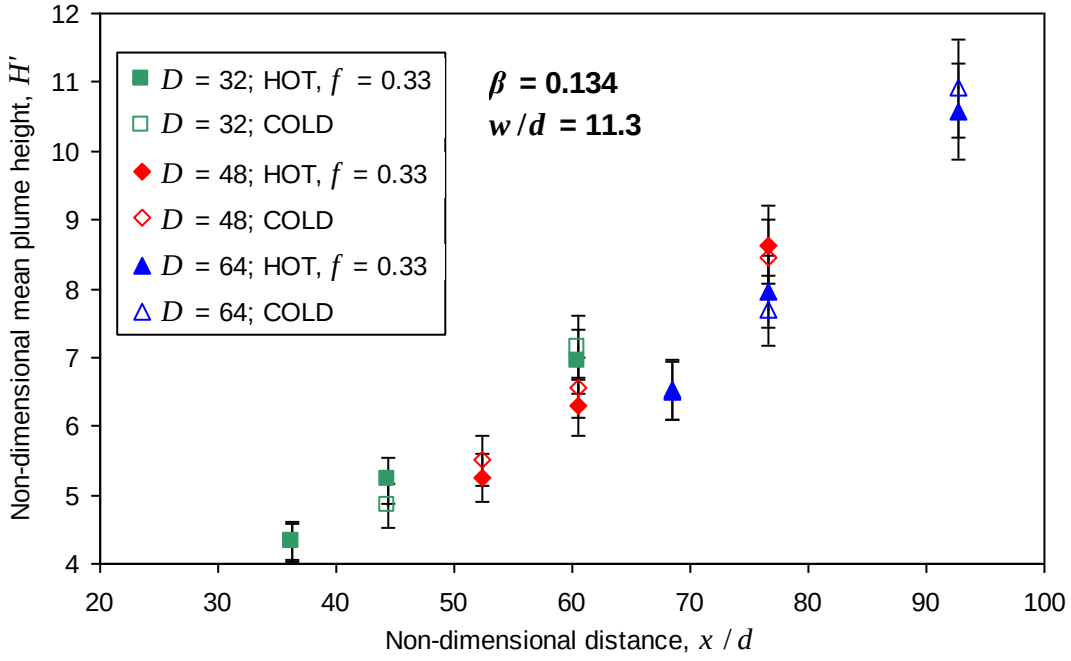

(a)

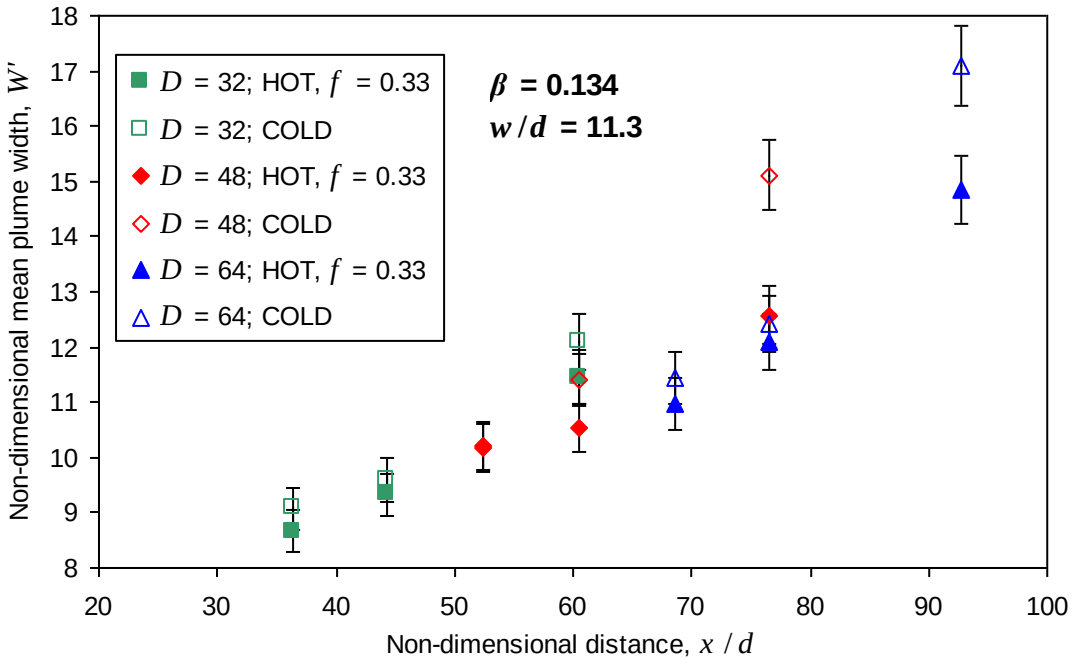

(b)

Figure 4.5: Comparison of HOT (f = 0.33) and COLD case with a deflector (w / d = 11.3) at β = 0.134 (U_∞ = 2 m/s): (a) non-dimensional mean plume height; (b) non-dimensional plume width

5) *Q_{He} = 9 l/min (f = 0.33); w / d = 11.3, D varied between 32 ≤ D ≤ 64; freestream velocity varied between 1 ≤ U_∞ ≤ 5 m/s (12 ≤ Fr* ≤ 1478); Atmospheric Boundary Layer modelled at 1:200 scale*

A further flow visualisation study of the exhaust plume was conducted in a simulated Atmospheric Boundary Layer at 1:200 scale, representing the suburban area of a major city. The ABL was modelled by placing 21 rows of roughness elements (100×100×50 mm) in the flow development section, placed 450 mm apart in a diamond-shaped orientation (similar to *Figure 3.9a* in Chapter 3.4.2) starting approximately 2 m upstream of the nozzle exit position. The arrangement included a set of elliptic vortex generators, a castellated barrier and a turbulence grid, placed upstream of the roughness elements. Such arrangement is commonly used in Cranfield University's 8'×4' ABLWT to model ABL at sub scale, for example in studies by Cini (2008) and Stein (2009) where more information can be found on the mean velocity and turbulence intensity profiles in the working section. Comparing the results for H' and W' (*Figure 4.6*) with the results of *4)*, shows a significant increase of the plume spread in both vertical and lateral direction as a consequence of the higher turbulence intensity of the boundary layer flow, however, again no lift-off was observed for $x / d \leq 129$. With increasing freestream velocity and thus increasing β, the mean plume width W' reduces, while the mean plume height H' remains approximately the same (*Figure 4.7*), thus the freestream

flow constrains primarily the lateral spread of the plume within the range of β tested. For $12 \leq Fr^* \leq 1478$, the lift-off distances would be between 12 mm and 138 mm, according to the criterion by Meroney (1979). Again, no lift-off was observed.

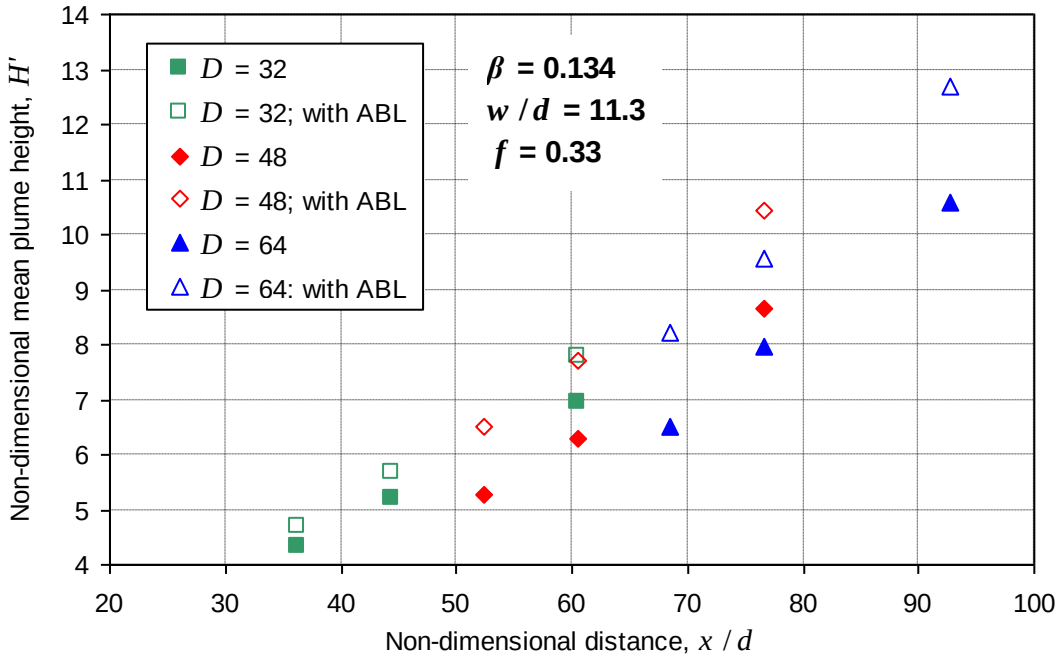

(a)

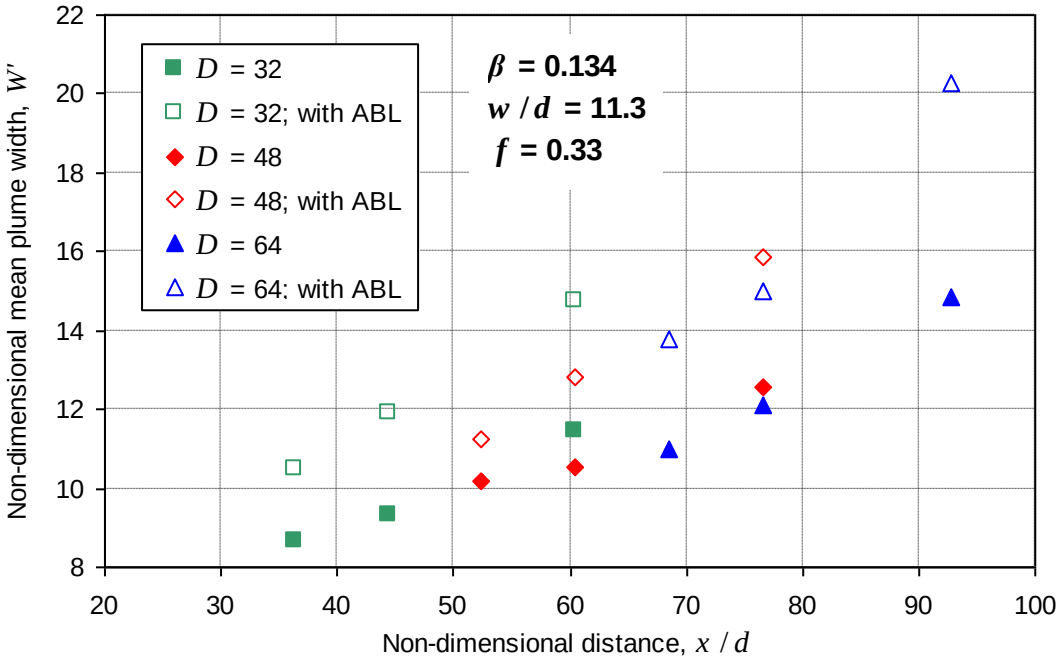

(b)

Figure 4.6: Plume development downstream of a deflector (w/d = 11.3) in an Atmospheric Boundary Layer at β = 0.134 (U_∞ = 2 m/s): (a) plume height H'; (b) plume width W'

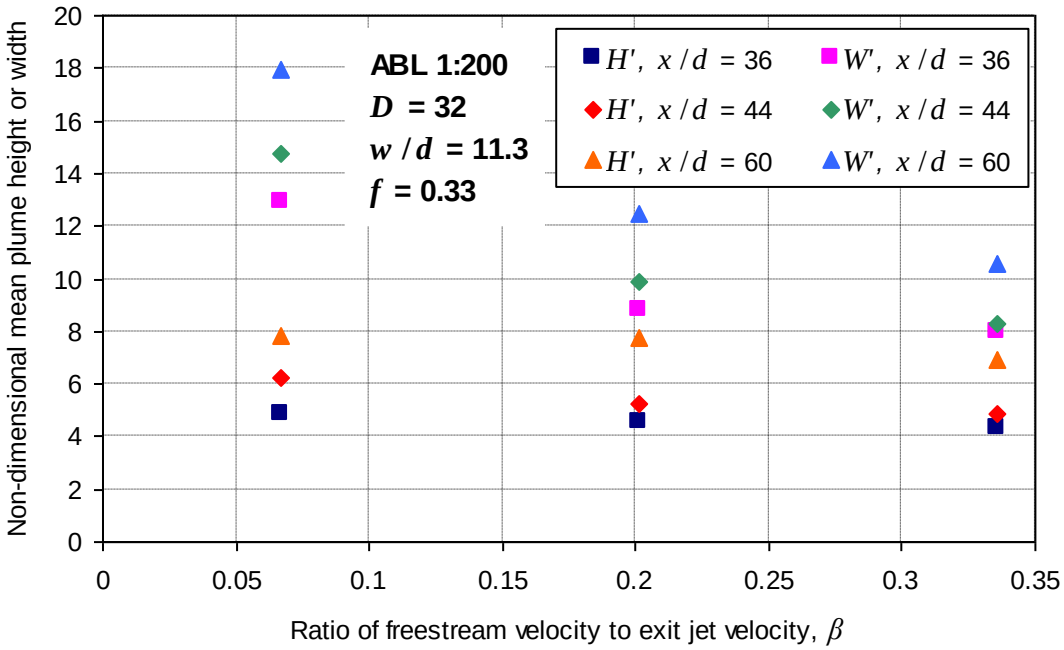

Figure 4.7: Variation of non-dimensional plume height H' and width W' with velocity ratio β downstream of a deflector (w / d = 11.3) in an Atmospheric Boundary Layer

From the first stage of the 'lift-off' experiments several important conclusions were drawn regarding the influence of the test parameters on the plume development:

- First and most important, it appears that, even reduced to 1 m/s, the freestream velocity is too high, constraining the plume and not allowing its buoyancy to become dominant within the range of distances x / d tested. For a clean boundary layer in the working section (no ABL modelled), U_∞ = 1 m/s gives a velocity U_{ref} = 0.94 m/s at a reference height of 0.125 m from the ground, which is equivalent to 25 m at full scale. For the same ratio U_{ref} / U_j at full scale, the full-scale wind speed is estimated to be 22 m/s, assuming a full-scale exit jet velocity of 345 m/s, reported by Cini (2008) in a review on CFM56 engines models. From meteorological data, published by the UK Department of Energy and Climate Change (DECC, 2014), the annual mean wind speed at Cranfield Airport (and UK Midlands) can roughly be estimated to be between 5 and 7 m/s, measured at 25 m above the surface – more than 3 times the equivalent wind speed of the one tested at sub scale.

- For a helium flow rate of 9 l/min and no external stream, the plume does not keep its integrity downstream. Small parts were observed to separate from the top of the plume in a slow upward motion, indicating buoyancy dominance away from the wind tunnel floor. However, close to the surface the flow remained attached, thus no

coherent plume lift-off was observed. This suggests that lift-off possibly occurred further downstream of the range x/d tested.

- Differences in the plume dimensions were observed when varying the deflector position downstream of the nozzle exit. Generally, when the deflector was positioned closed to the nozzle the plume downstream appeared to be larger. Relevant parameters in this case are the deflector position with respect to the jet velocity, and the deflector size relative to the plume size.

- The lift-off criterion (*Equation 2.12*) by Meroney (1979) doesn't seem to agree with the obtained results. For the test flow parameters, the lift-off criterion seems to predict lift-off distances very close to the nozzle, at which the plume was observed to be completely attached to the surface. An alternative theoretical method of predicting lift-off would be to use the lift-off parameter (*Equation 2.10*) suggested by Briggs (1973), which would require measurements of shear stress at the surface to calculate the friction velocity.

Based on these results, additional experiments were performed with the wider deflector of 500 mm width (w/d = 80.6). Videos were recorded at various x/d for two deflector positions D = 32 and D = 64 and two freestream velocities U_∞ = 0.6 m/s (β = 0.04) and U_∞ = 1.8 m/s (β = 0.12). The total and helium nozzle flow rates were kept the same, at 27 and 9 l/min respectively. The camcorder was moved to 1800 mm (290d) to increase the tests range of distances downstream of the nozzle ($x/d \leq 226$).

As with previous tests, no lift-off of the plume was observed in the working section. The wider deflector (w/d = 80.6) was estimated to have a width equal 11.7 and 3.6 times the local jet plume width at D = 32 and D = 64 respectively; while for the narrower deflector (w/d = 11.3) these values were 1.6 and 0.5 respectively. When comparing both deflector cases for the same D and x/d (*Figure 4.8*), it is evident that the wider deflector produces a larger plume downstream, which is possibly related to a greater loss of jet momentum, resulting in increased entrainment of ambient air into the turbulent jet. Within the scope of the experiment, this effect is considerably greater when the deflector is further away from the nozzle (D = 64), while for D = 32 only small differences in the plume size far downstream of both deflectors (x/d = 161) can be observed. These trends are consistent with the results obtained during the first tests with regard to the deflector position relative to the nozzle exit and highlight the importance of the deflector size relative to the plume dimensions. The effect of reducing the freestream velocity on the size of the plume downstream of the deflector appears to be greater when the deflector is further away from the nozzle (D = 64). Again at large distances, the coherent plume stays attached to the ground with small parts separating

from the top of the plume possibly due to buoyancy effects, but no lift-off from the ground was observed within the range of distance tested.

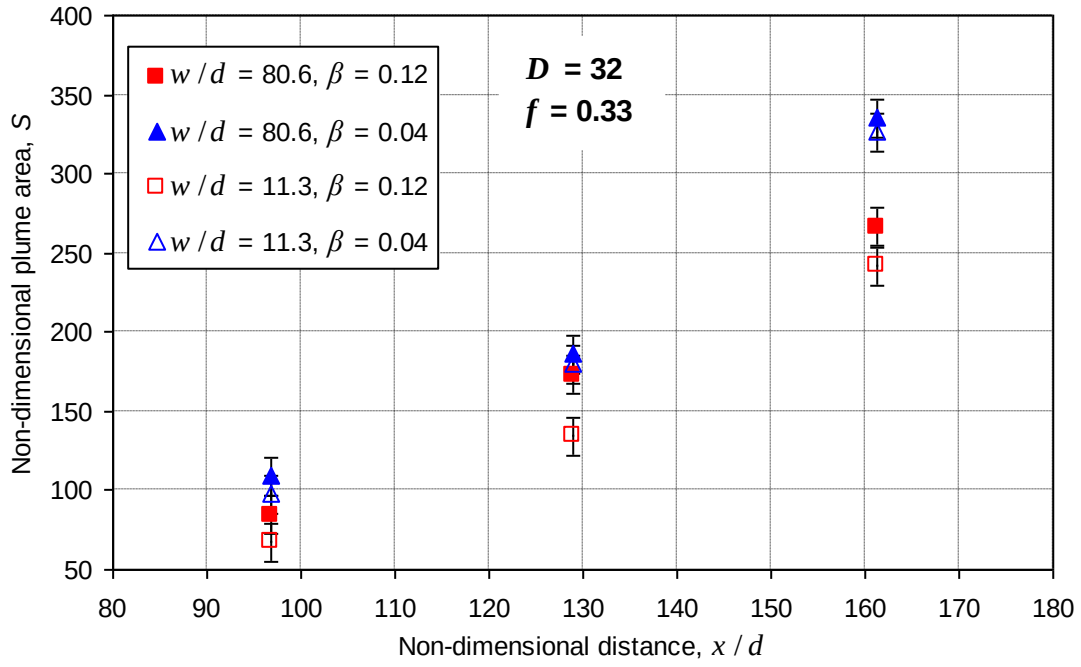

(a)

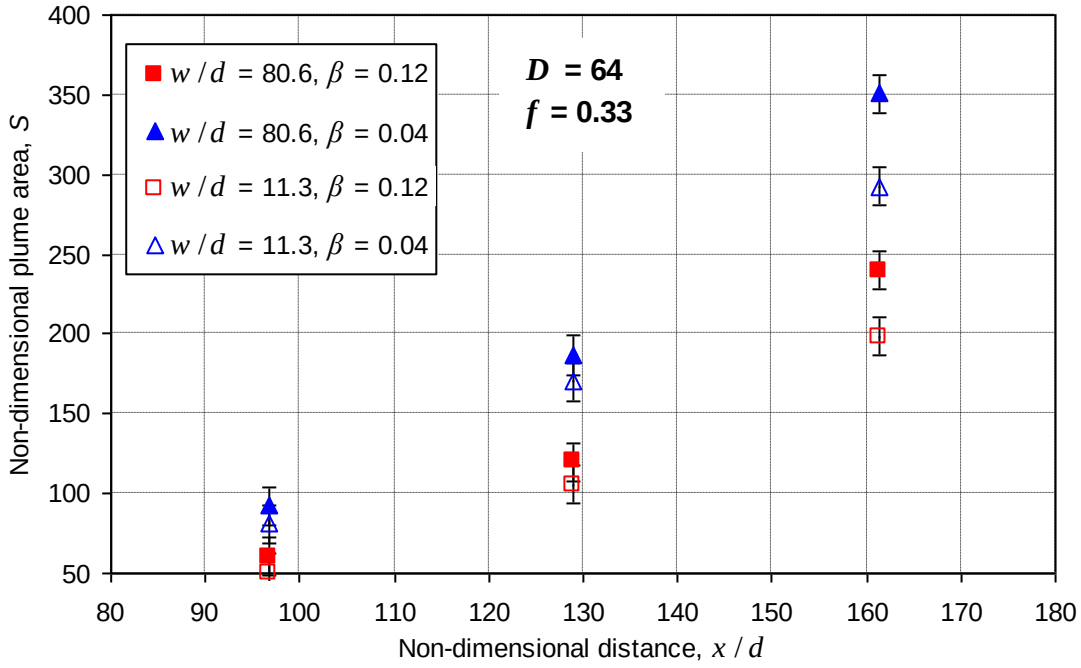

(b)

Figure 4.8: Comparison of non-dimensional plume area S downstream of a single deflector of width w / d = 80.6 or w / d = 11.3 at fan speeds of 50 and 100 rpm for: (a) D = 32; (b) D = 64

It is evident that even at low wind tunnel velocities the plume spread seems to be restricted as the secondary flow becomes more dominant with downstream distance from the nozzle. For this reason, subsequent tests were performed with no wind tunnel flow. It should be noted that this configuration was not tested previously as the 'wind tunnel off" tests were not extended further than a simple nozzle jet configuration without a deflector after the results of *3)*. When no deflector was present, no lift-off was observed between x/d = 129 and x/d = 177. Images of the plume at these distances are shown in *Figure C.6a* and *Figure C.7a* in Appendix C respectively. At x/d = 177, the coherent plume is still attached to the surface with small individual parts separating at the top. These are not entirely visible in *Figure C.7a* since they are above the laser sheet.

If a deflector is placed in the path of the jet, the plume eventually separates from the surface within the tested range of x/d. Images showing the plume development for a deflector positions D = 32 are shown in *Figure 4.9* and *Figure 4.10* (two images for each x/d). At x/d = 129, the plume downstream of the narrower deflector (w/d = 11.3) is still attached (*Figure 4.9a*), whereas in the case of the wider deflector (w/d = 80.6) it has just about separated from the surface (*Figure 4.10a*). At x/d = 177, the plume downstream of the narrower deflector also lifts off (*Figure 4.9b)*, while the plume downstream of the wider deflector now 'sits' in the air above the laser sheet upper boundary and is not visible within the illuminated laser sheet plane. This occurs already at x/d = 145 (*Figure 4.10b*). Placing the deflector further downstream increases the plume lift-off distance. Images of the plumes downstream of both deflectors, positioned at D = 64, are shown in *Figure C.6* and *Figure C.7* in Appendix C. At x/d = 177, the plume downstream of the narrower deflector (w/d = 11.3) does not lift off unlike when the deflector is positioned at D = 32. The behaviour of the upper part of the plume seems to be dominated by buoyancy, increasing the overall height of the plume and causing some parts of it to separate, but the coherent plume is still attached to the surface (*Figure C.7b*). For the wider deflector (w/d = 80.6), the plume has just about separated at x/d = 177 and is still visible within the laser sheet plane (*Figure C.7c*).

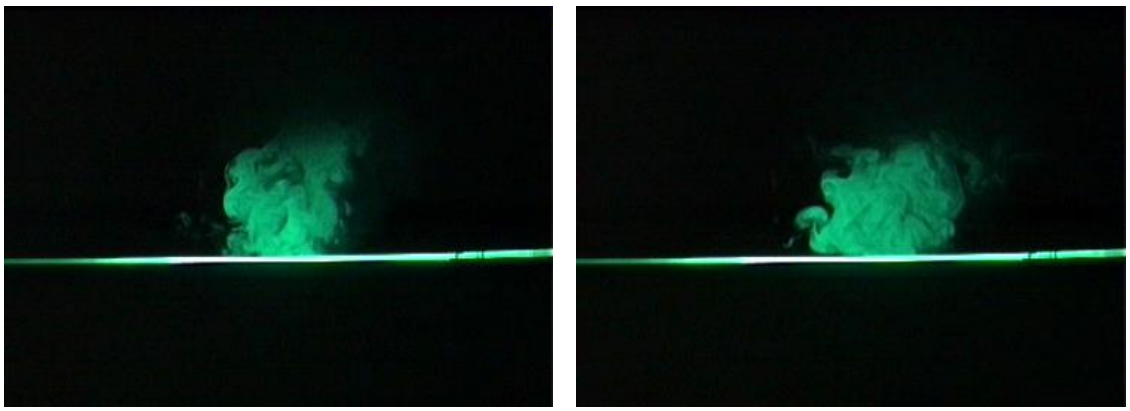

(a) x/d = 129

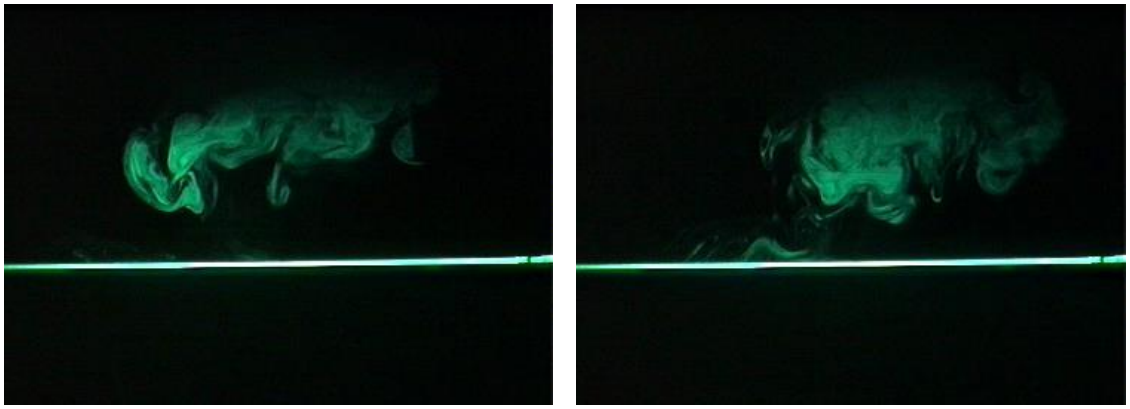

(b) $x/d = 177$

Figure 4.9: Plume 'lift-off' downstream of a deflector of width w / d = 11.3 at D = 32 without freestream (U_∞ = 0 m/s)

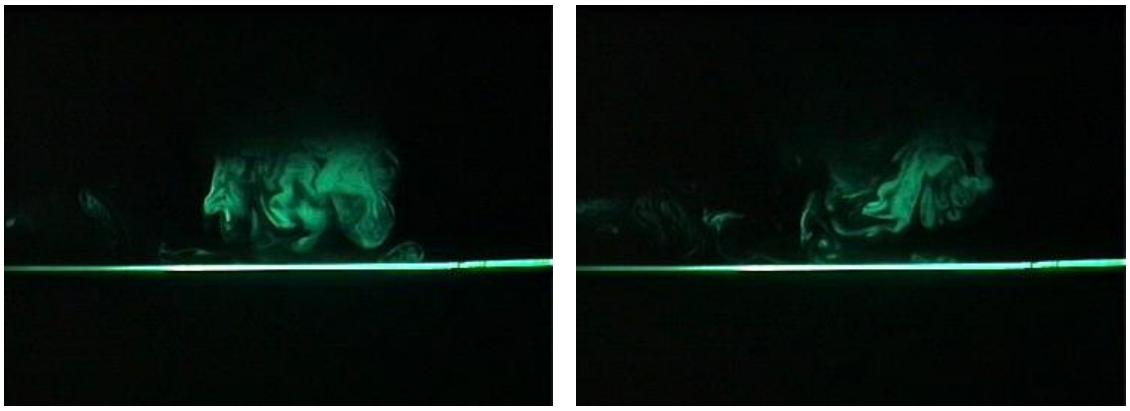

a) $x/d = 129$

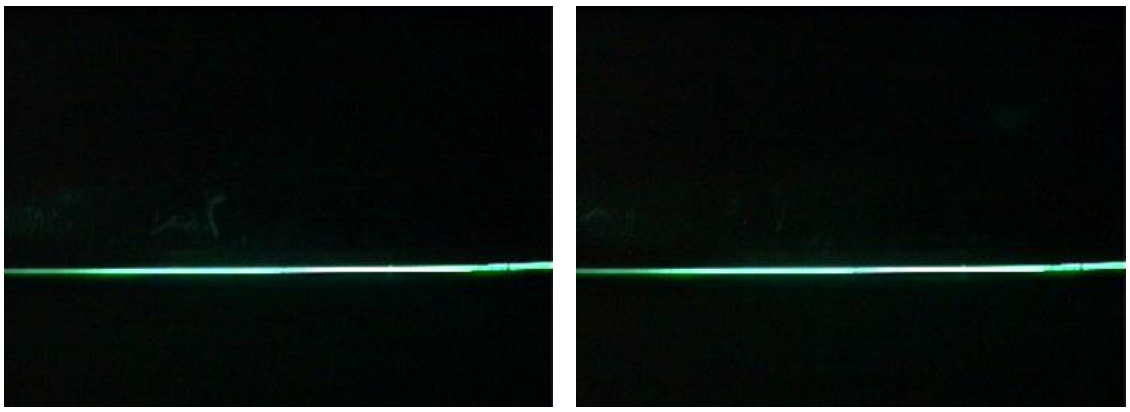

b) $x/d = 145$

Figure 4.10: Plume 'lift-off' downstream of a deflector of width w / d = 80.6 at D = 32 without freestream (U_∞ = 0 m/s)

An additional test was conducted for a configuration of two deflectors of 12.5 and 17.5 mm height and each of 500 mm width, positioned parallel and downstream of each other at a front-to-front spacing of 12.5 mm. The first (smaller) deflector was positioned at D = 64. Such configuration was expected to give less aerodynamic drag due to the sheltering effect of the smaller deflector positioned upstream, which in turn was expected to delay lift-off. As can be seen in *Figure 4.11*, where the plume development is shown at four locations downstream, lift-off does not occur until approximately x/d = 226. This is considerably further downstream compared to the separation point for the single deflector (w/d = 80.6) case of D = 64. These results, together with the lack of separation observed within the distances tested in the case where no deflector was present (*Figure C.6a* and *Figure C.7a*), show that drag exerted on a buoyant wall jet promotes its lift-off from the surface and confirms the physical principle of the baffles concept at sub scale.

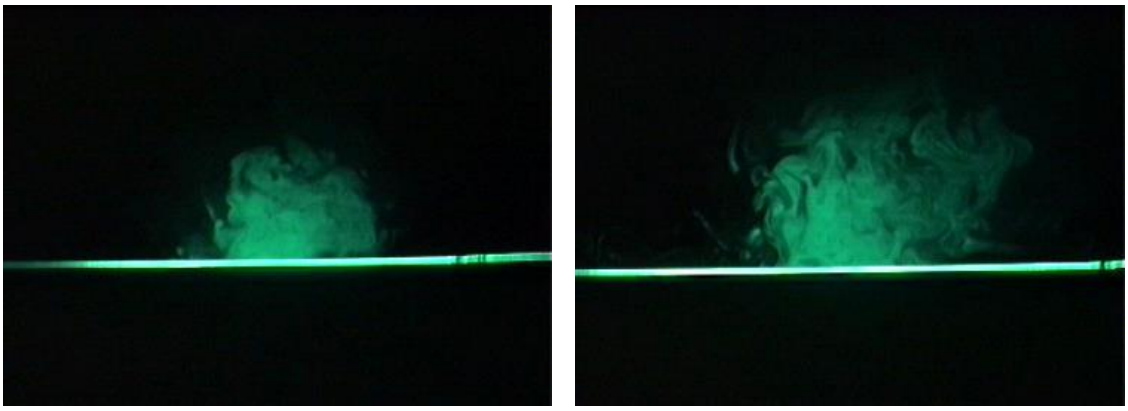

(a) x/d = 129 (b) x/d = 177

(c) x/d = 193 (d) x/d = 226

Figure 4.11: Plume 'lift off' downstream of a configuration of two deflectors of the same width (w/d = 80.6) in succession, first at D = 64; U_∞ = 0 m/s

Repeatability runs were conducted to study any variations in the location of plume lift-off. On a few occasions the plume was observed to lift off, then re-attach and lift off again within a single test, as follows. The chaotic movement of flow segments within the turbulent plume causes an accidental contact of a small flow segment with the surface, which draws the coherent plume downward re-attaching it to the surface. It stays attached for an indefinite time period until separation occurs again. The repeatability of this process doesn't seem to follow any regularity as generally the plume would remain detached. Within the time periods when the plume remained attached within the laser sheet plane, it was observed to lift off further downstream (without laser illumination), thus the separation point shifted backwards and forwards within the process of lift-off and re-attachment. This phenomenon is shown in *Figure C.8* in Appendix C by means of several images representing a video footage time period of 17 seconds. It was recorded at $x/d = 65$ for a single deflector of width $w/d = 80.6$, positioned at $D = 32$. Previously, for this configuration the plume separation occurred at $x/d \approx 129$ (see *Figure 4.10a*).

In conclusion, coherent plume lift-off was observed within the distances x/d tested only when no freestream was present; even a freestream velocity of 0.6 m/s ($\beta = 0.04$) seemed to prevent the buoyant plume from lifting off. However, small flow parts were observed to detach from the plume as it progressed with distance downstream of the nozzle, indicating that lift-off possibly occurred further downstream of the range of x/d tested. During tests without freestream it was observed that, when reaching the ceiling of the working section, the separated plume started moving upstream causing flow re-circulation, depicted schematically in *Figure 4.12*. A possible cause for this phenomenon is the constraining effect of the working section walls, trapping buoyant gas masses inside without the presence of wind tunnel flow.

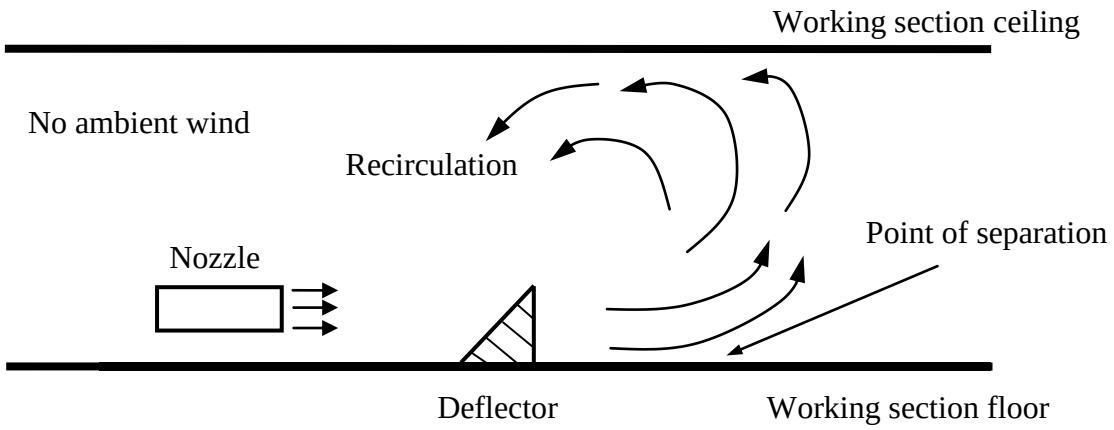

Figure 4.12: Schematic illustration of the time dependency of a jet plume 'lift-off'; flow recirculation in the working section (side view; not to scale)

4.3 Measurements of flow through porous screens

The second part of the initial experiments was concerned with porous materials and their possible use as surface material for the baffles. The tests were conducted to investigate the two-dimensional flow in the near field of porous screens in order to determine preliminary design parameters such as slope angle of the baffles towards the jet and surface porosity of the baffles. The experimental test programme was divided into quantitative pressure measurements and qualitative flow visualisation tests in the near field of porous screens.

4.3.1 Pressure drop measurements

The pressure drop across a porous screen is a measure of its aerodynamic drag, which in view of the baffles concept was a primary design parameter for the field trials arrangement. Porous screens are also used in sub-scale wind tunnel testing to represent the pressure drop across a heat exchanger in automotive aerodynamics. The obtained pressure measurements, combined with experimental data for honeycombs of various thicknesses, were published as Gerova et al. (2013).

The purpose of the pressure measurements was to obtain pressure drop data across screens of various porosities and at different inclination relative to the freestream. This was achieved by adapting an existing blower wind tunnel such that a porous screen could be mounted in the blown duct covering its entire cross section area. An image of the blower tunnel showing its main components is presented in *Figure 4.13*. A detailed schematic illustration, showing the pressure tappings arrangement, is presented in *Figure C.9* of Appendix C. Sections 1 and 4 are fixed while 2 and 3 (the working section) are variable, depending on the angle of inclination of the screen relative to the freestream direction, denoted with α_s. The arrangement of sections 2 and 3 for all angles tested is presented in Appendix C in *Figure C.10* and *Figure C.11*, while the individual cross sections in the plane of the screen are shown in *Figure C.12*.

All pressures were taken as differential pressure readings, referenced to a pressure p_{ref}, which was measured just upstream of the contraction as a pneumatic average pressure of a ring of static pressure tappings. Static pressure measurements were carried out at various positions both upstream and downstream of the screen. These tappings are aligned with the lateral centre line of the working section. At $\alpha_s = 90^o$, the readings were pneumatically averaged values from the wind tunnel top and bottom tappings, while at all other angles individual top and bottom readings were taken. The freestream dynamic pressure was measured with a Pitot-static tube mounted on the working section

centre line upstream of the screen (see *Figure C.9*). The pressure tubes from the static, Pitot-static and reference ring pressure tappings were connected to Omega PX139 pressure transducers, which were in turn connected to the input channels of a data acquisition (DAQ) hardware. Data was recorded on a computer using National Instruments *LabView* software and a custom DAQ programme written for the tests.

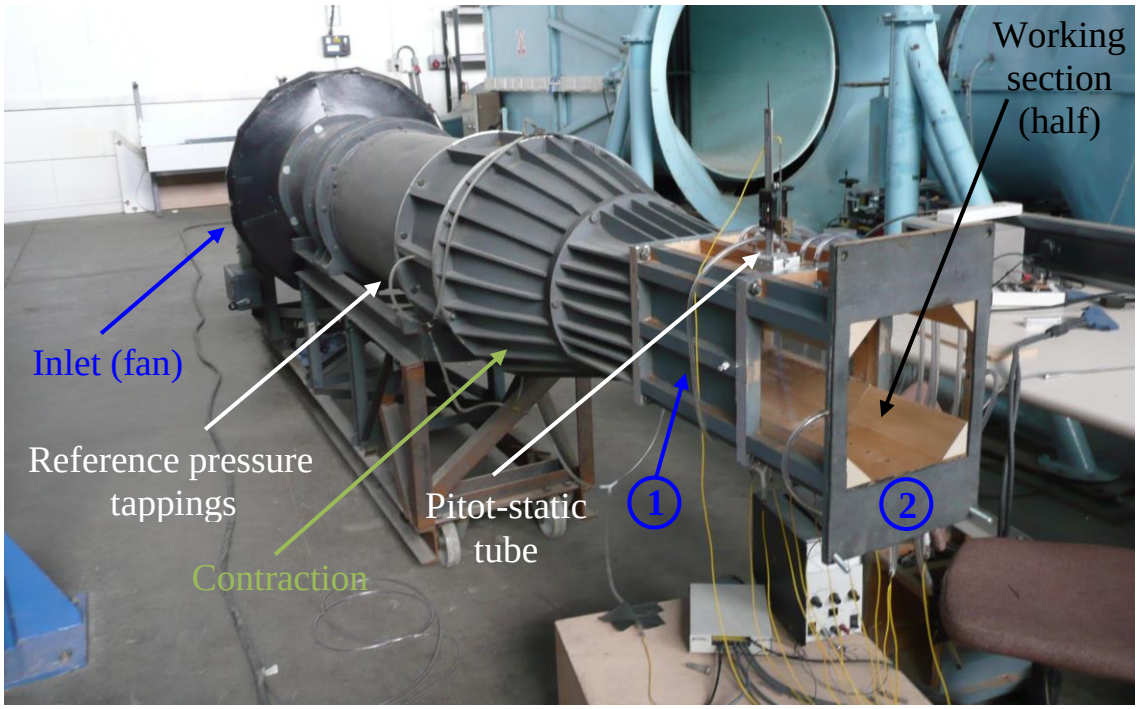

Figure 4.13: Open circuit layout blower tunnel, half of working section (α_s = 90º) removed

The measurements were conducted with screens inclined at 90º, 75º, 60º and 45º to the freestream. The wind tunnel speed U_∞ was varied between 3 and 31 m/s. Within this range the velocity profile of the empty working section (no screen mounted) was measured at the lateral centre line and was found to be uniform (within ±1% of the mean value) for 90% of the working section height. Five different materials with porosity γ, defined in *Equation 2.15* in Chapter 2.7, between 0.76 and 0.41 were tested. Most of the materials used had manufacturer data for their porosity. If this data was not available, the porosity was calculated either by measuring samples with a microscope or by taking photographic images of the screens against a single-colour background and using pixel-counting software, i.e. Pixcavator IA 4.2, to measure the ratio of mesh (material) pixels to background pixels. On these measured porosity values the tolerance was statistically estimated to be nominally ±0.03.

The results for the longitudinal pressure distribution along the duct show a consistent trend which is qualitatively similar for all screens tested. Data for a screen of

porosity γ = 0.64 inclined at 90º and 45º are shown in *Figure 4.14a* and *Figure 4.14b* respectively, where the non-dimensional coordinate x' is used to describe the longitudinal distance x from the start of section 2 of the working section relative to its total length l_{ws}. More example results are included Appendix C in *Figure C.13* for γ = 0.64 and angles of 75º and 60º, and *Figure C.14* and *Figure C.15* for γ = 0.41. The pressure drop across the screen increases with increasing wind tunnel velocity U_∞. This is shown as variation with Reynolds number *Re* in *Figure 4.14*, where *Re* is defined in *Equation 4.5*. The average screen thickness, equal to 1 mm, was used as l_{ref} to calculate *Re*.

$$Re = \frac{\rho_\infty U_\infty l_{ref}}{\mu_\infty}$$

Equation 4.5

Downstream of the screen, the newly established lower static pressure remains constant until the end of the working section (x' = 1) and then slowly increases with distance. The same trend is observed upstream of the screen. These changes in static pressure away outside of the working section are due to the variable cross section of the duct sections 1 and 4, which have corner fillets of longitudinally decreasing (with distance from the working section) cross section area.

As a result of the duct-type working section arrangement, when the screen is inclined, differences in the top and bottom pressure distribution occur in close proximity to the screen. These differences become greater with increasing wind tunnel speed and screen angle of inclination. This occurs possibly due to a difference in the effective screen angle relative to the incoming flow (streamlines are aligned with the duct walls) between top and bottom of the working section. For all angles of inclination tested lower than 90º, the screen at the top is inclined with the flow direction and at the bottom it is inclined against the flow direction. This results in a noticeably greater pressure drop across the screen at the bottom (x' = 0.8) compared to the one at the top (x' = 0.2), as can be seen in *Figure 4.14b*. However, sufficiently far away from the screen (upstream of x' ≈ 0.1 and downstream of x' ≈ 1) the pressures on top and bottom even out as the flow symmetry in vertical direction within the duct is restored, as evident from the data for angles of 75º, 60º and 45º, shown in *Figure 4.14b* as well as in *Figure C.13*, *Figure C.14* and *Figure C.15* of Appendix C.

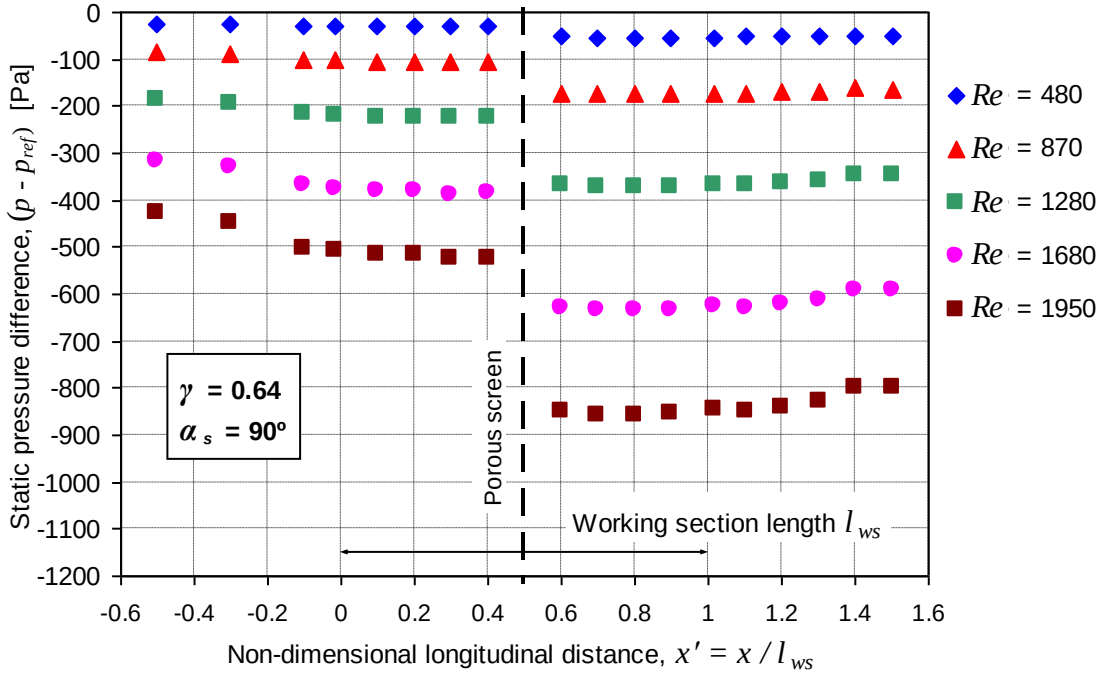

(a)

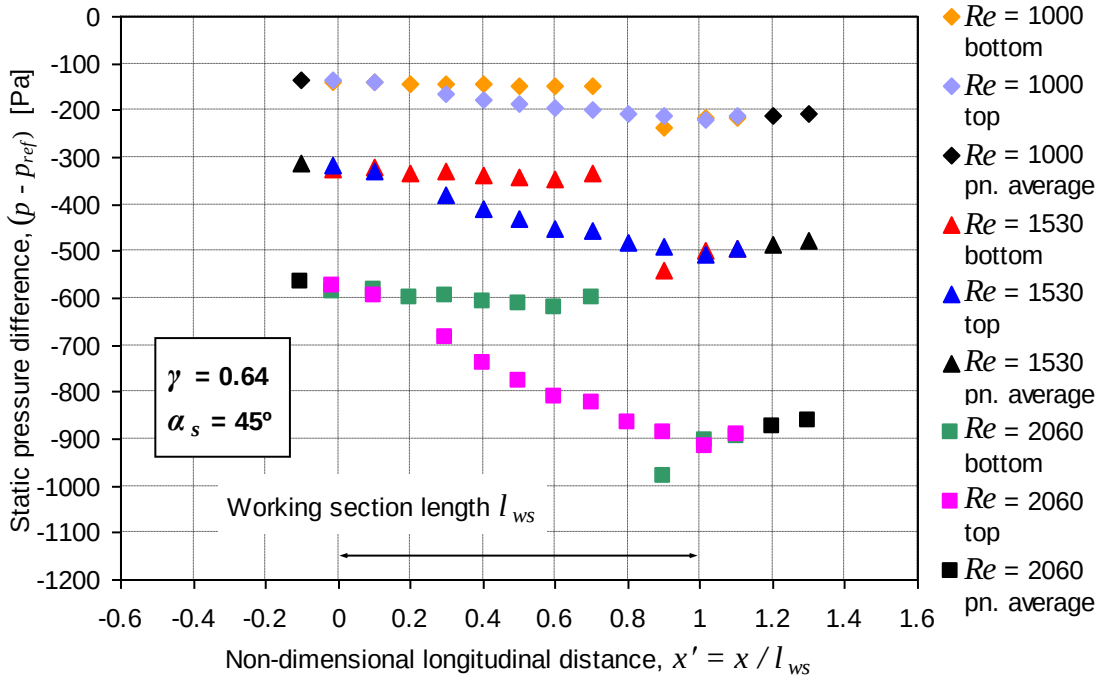

(b)

Figure 4.14: Longitudinal static pressure distribution in the working section across a screen of 0.64 porosity at an angle of inclination of: (a) 90º and (b) 45º

x-axis shows longitudinal distance along the wind tunnel centre line, non-dimensionalised by the working section length; the working section starts at x' = 0 and ends at x' = 1; y-axis shows the

pressure difference between the local static pressures (upstream and downstream of the screens) and the reference ring static pressure in the contraction.

To evaluate the variation of pressure drop Δp with porosity at all four screen angles of inclination tested, Δp was calculated with measured static pressure values p at both ends of the working section (see *Equation 4.6*). This was sufficiently away from the screen to eliminate the previously-described effects on the pressure distribution at the top and bottom of the wind tunnel, caused by inclining the screen. For the purpose of non-dimensionalising the data obtained, a pressure drop coefficient $\Delta p / q_\infty$ was introduced as follows:

$$\frac{\Delta p}{q_\infty} = \frac{\left(p - p_{ref}\right)_{x'\approx 0} - \left(p - p_{ref}\right)_{x'\approx 1}}{q_\infty}$$

Equation 4.6

Idelchik (1994) describes the pressure drop coefficient of barriers distributed uniformly over tube or duct cross sections to be dependent on their porosity, shape (holes arrangement) and Reynolds number. Data presented by Idelchik (1994) for screens of various shape and porosity, suggest that $\Delta p / q_\infty$ becomes independent of Reynolds number (based on freestream velocity and screen thickness) for $Re > 500$. For the screens tested in the current experiments, the Reynolds number range was between nominally 200 and 2100.

The variation of $\Delta p / q_\infty$ with Reynolds number for all screen angles of inclination tested is shown in *Figure 4.15*. It is evident that for materials with porosity greater than 0.50, $\Delta p / q_\infty$ becomes virtually independent of Reynolds number for $Re \geq 500$ ($U_\infty \approx 8$ m/s) regardless of the mesh inclination, which is in good agreement with Idelchik (1994). The pressure drop coefficient variation for $\gamma = 0.41$ shows tendency to become constant at higher speeds outside the tested range. For a given porosity, $\Delta p / q_\infty$ reduces with angle of inclination, thus inclining the screen would reduce its aerodynamic loading, i.e. its aerodynamic drag. As evident from *Figure 4.15*, the drag-reduction effect of inclining the screen to the flow decreases as the screen porosity increases. For example, at $Re \approx 1280$ ($U_\infty = 19$ m/s) the pressure drop coefficient for $\gamma = 0.41$ is reduced by approximately 29% between 90º and 45º, while for $\gamma = 0.70$ this reduction is only 13%. Generally, screens of high porosity ($\gamma \geq 0.64$) show only small differences in their pressure drop coefficient variation with freestream speed and screen angle of inclination. Changes in α_s have a considerably smaller effect on $\Delta p / q_\infty$ compared to screens of 0.50 and 0.41 porosity.

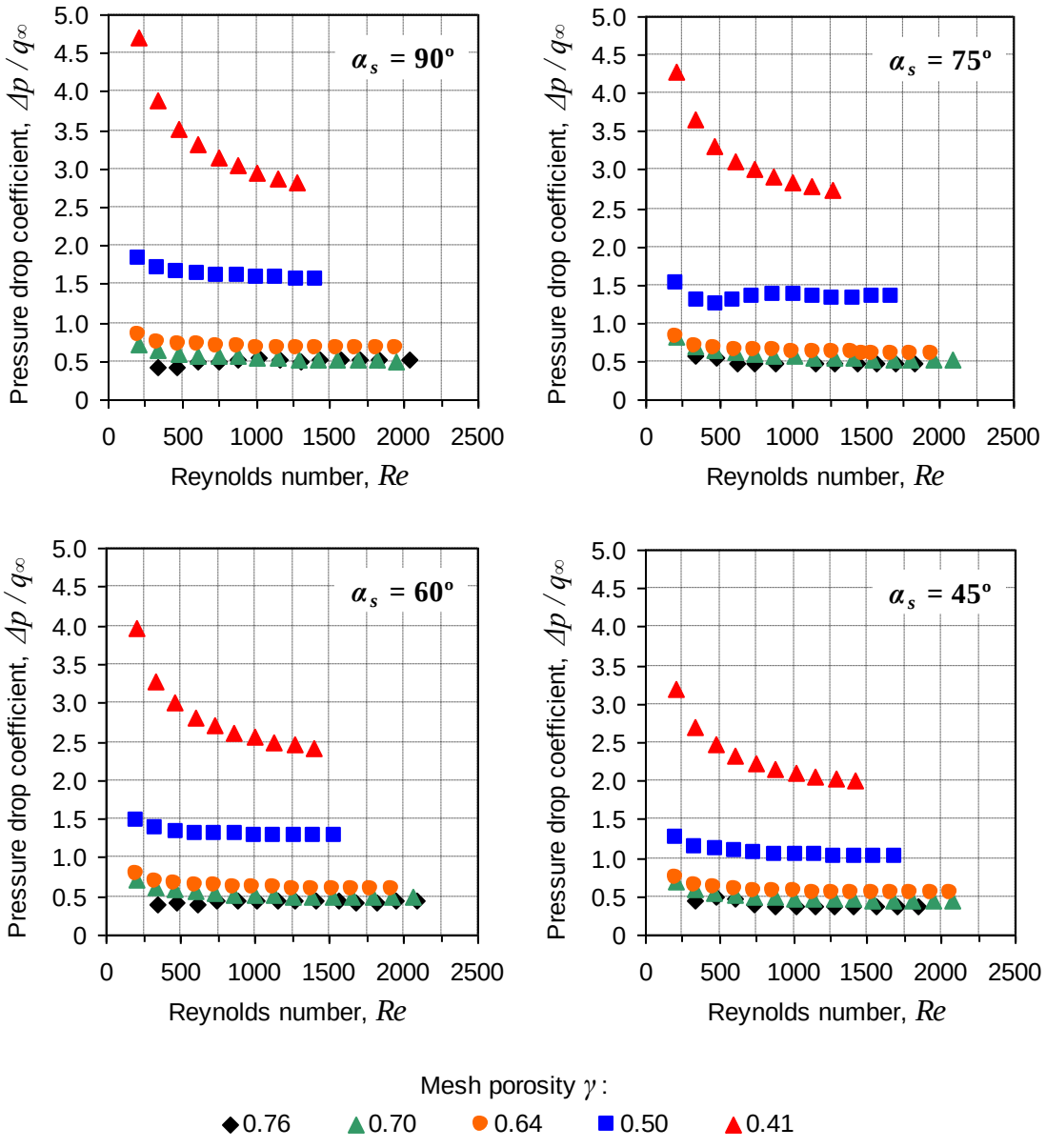

Figure 4.15: Variation of pressure drop coefficient with Reynolds number for mesh angles of inclination of 90º, 75º, 60º and 45º

The measured variation of pressure drop coefficient with porosity for each screen angle of inclination is shown in *Figure 4.16*. For $Re > 450$ and porosity values of $0.41 \leq \gamma \leq 0.76$, the pressure drop coefficient was found to vary with the power of the screen porosity as follows

$$\frac{\Delta p}{q_\infty} = B_1 \gamma^{B_2}$$

Equation 4.7

where the proportionality constant B_1 and the exponent B_2 vary with α_s and were obtained using exponential curve fitting of the form of *Equation 4.7* and are given in *Table 4.1* for all angles α_s tested. The complete equations and their corresponding coefficients of determination R^2 are shown in *Figure 4.16*.

Table 4.1: Proportionality and exponential coefficients for the variation of pressure drop coefficient with porosity

α_s (°)	α_s (rad)	B_1	B_2
0	0	0.192	-3.048
15	0.262	0.193	-2.902
30	0.524	0.182	-2.912
45	0.785	0.177	-2.699

It should be noted that at the lower end of the screen porosity range ($\gamma \approx 0.40$), the pressure drop coefficient does not become completely independent of Reynolds number within the range tested. Consequently the accuracy of *Equation 4.7* decreases for screens of such porosity. Additionally, it is evident that the mathematical relationships identified are not representative towards the high ($\gamma = 0$) and low ($\gamma = 1$) ends of the porosity range. In the latter case, where no screen material is present, the pressure drop should be theoretically zero, yet they yield a small positive value for $\Delta p / q_\infty$, equal to B_1.

Idelchik (1994) and Hou et al. (2009) show two different empirical relationships for describing the variation of $\Delta p / q_\infty$, denoted as 'resistance coefficient', with porosity for screens placed normal to the flow within a duct. Comparing experimental and numerical data on a perforated plate, Hou et al. (2009) use the following equation

$$\frac{\Delta p}{q_\infty} = \frac{1}{B^2 \gamma^2} - 1$$

Equation 4.8

where the coefficient B varies with the porous material's open area arrangement shape (holes distribution). For a circular holes arrangement, Hou et al. (2009) use $B = 0.85$. Although showing a qualitatively similar variation, *Equation 4.8* overestimates the current experimental data at $\alpha_s = 90^o$ (*Figure 4.16a*) mainly due to the choice of B. For $B = 1.17$, *Equation 4.8* shows very good agreement with the results for $\alpha_s = 90^o$.

Idelchik (1994) suggests the following empirical equation based on data obtained for circular metal wire screens with square-shaped holes

$$\frac{\Delta p}{q_\infty} = k(1-\gamma) + \left(\frac{1}{\gamma} - 1\right)^2$$

Equation 4.9

where k = 1.3 for Reynolds numbers $Re \geq 500$ based on freestream velocity and wire thickness. This is the case in the current experimental data for velocities $U_\infty > 8$ m/s ($Re \approx 550$). *Equation 4.9* is in an excellent agreement with the experimental data at $\alpha_s = 90^o$ (*Figure 4.16a*). Furthermore, by reducing the value of k appropriately (*Figure 4.16b*, *Figure 4.16c* and *Figure 4.16d*), *Equation 4.9* also shows similar agreement to the experimental data for the inclined screens at 75º, 60º and 45º.

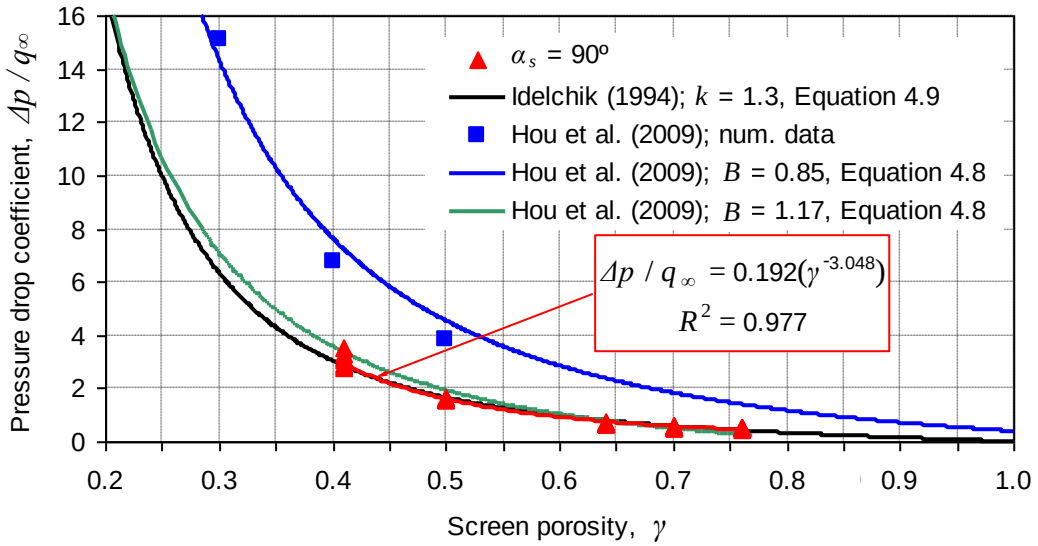

(a)

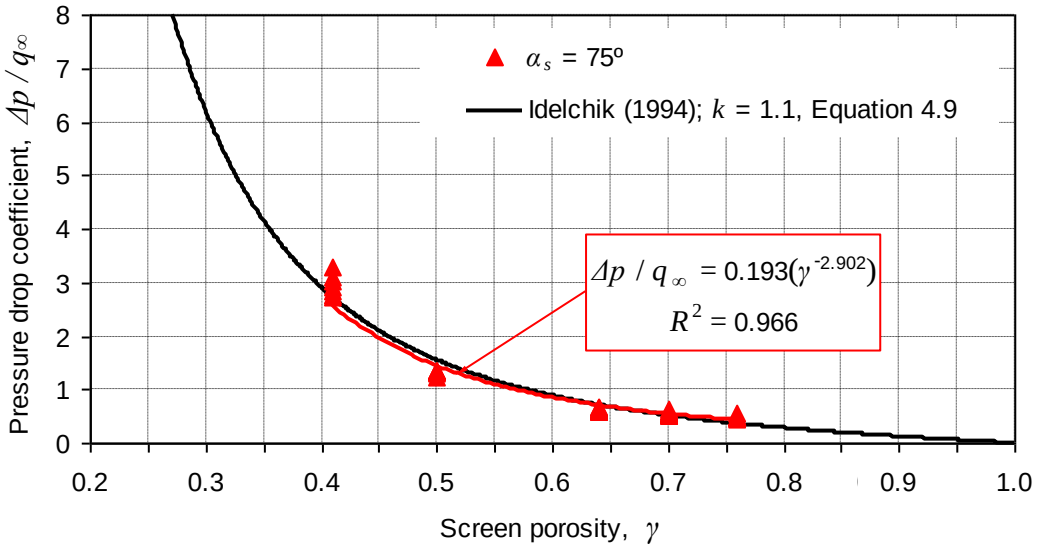

(b)

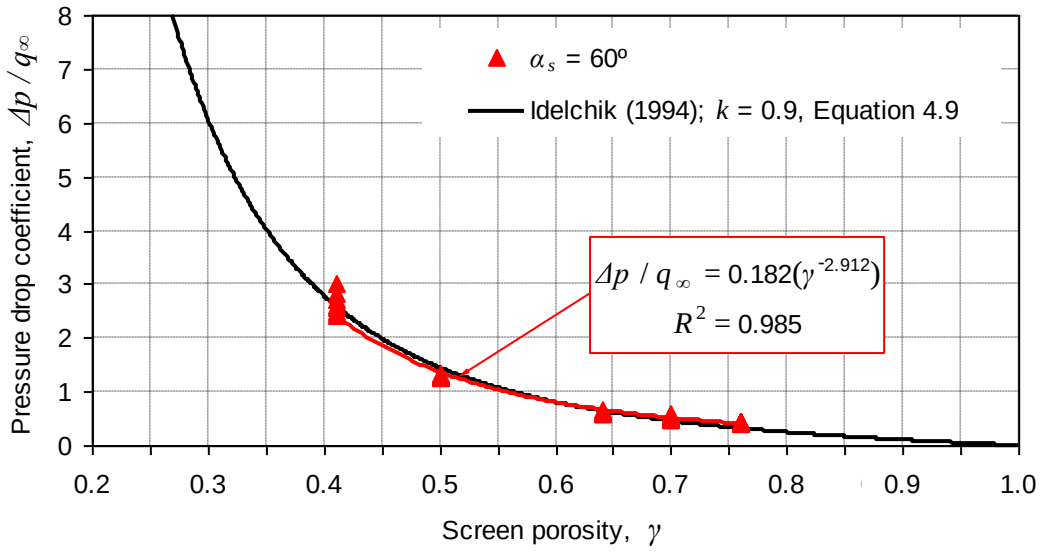

(c)

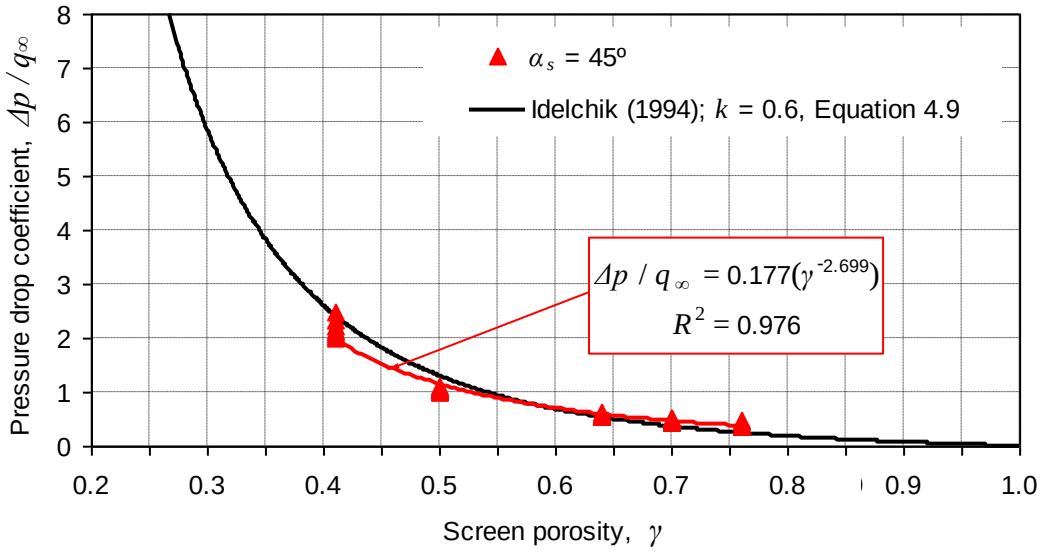

(d)

Figure 4.16: Variation of pressure drop coefficient with mesh porosity for mesh angles of inclination of (a) 90º, (b) 75º, (c) 60º and (d) 45º

4.3.2 Smoke visualisation

In addition to the measurements of pressure drop across screens located in a duct, the two-dimensional flow in the near field of 'free' screens, i.e. no duct present (see *Figure 4.17*), was investigated using the flow visualisation method outlined in Chapter

3.2.3. The arrangement of the 1500 mm long, 1100 mm high and 100 mm wide smoke tunnel working section is shown in *Figure 4.17*. The flow was restricted only to the working section *xz* plane of symmetry to create a two-dimensional flow field. The screens were fixed on two cylindrical struts of 13 mm diameter each positioned 300 mm apart on a removable turntable. The wind tunnel speed in the working section was measured with a Pitot-static tube, positioned well above the screens. Side-view images of the flow pathlines, illuminated by the working section lights, were taken with a digital camera, positioned at approximately half the working section height.

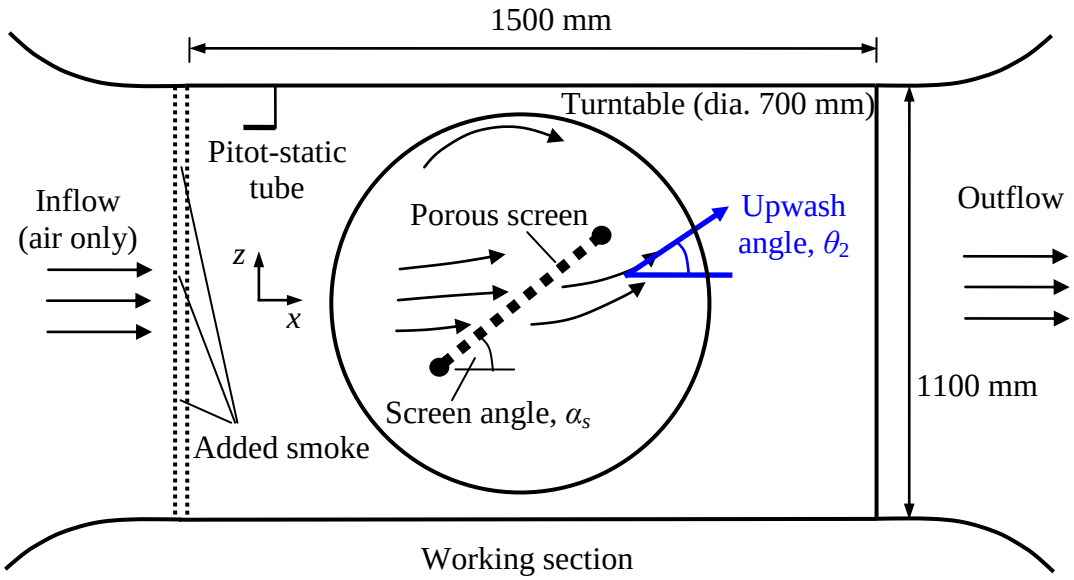

Figure 4.17: Schematic illustration of the smoke wind tunnel working section (side view, not to scale)

Screens of porosity γ = 0.80, 0.41, 0.35, 0.20, 0.15 and 0.10 were tested at freestream speeds U_∞ = 3, 5 and 7 m/s, corresponding to Reynolds numbers *Re*, based on U_∞ and l_{ref} = 300 mm, of 60000, 100000 and 140000. The screen chord length was used as reference length as it is the relevant scale in an external flow around flat plates and windbreaks (see Chapter 2.7). Ito & Garry (1998) used the same *Re* analysis and observed only small Reynolds number influence on the screen pressure distribution for *Re* > 163000. The screen angle of inclination was varied between 90º (perpendicular to the flow direction) and 0º in steps of 10º.

The analysis of the taken images investigated the orientation of the central pathline upstream and downstream of the screen relative to the freestream direction, denoted respectively as 'entry angle θ_1 and 'upwash angle' θ_2. These concepts are elaborated graphically in *Figure 4.18*. The upwash angle is in the opposite direction of the flow deflection reported by Reynolds (1969), where the duct flow passing through

the screen is turned in the direction of inclination of the screen (see *Figure 2.16* in Chapter 2.8). In the current case, the upwash resulted from the deflected flow around the screen, unrestricted in the absence of a duct, and was thought to be a measure of the vertical force, generated by the screen on the flow. The post-processing method consisted of measuring entry and upwash angles with a protractor on printouts of the taken images or in some cases digitally on a computer screen, using drawn lines and calculating the angle, when the quality of the printouts was not sufficient for accurate measurement. Another method, using pixel-counting software, was considered, however, it could not be applied consistently due to variation of the quality of the taken images. The measurement errors were estimated as ±0.5 deg for the screen inclination due to possible misalignment of the turntable during tests and an average of ±3 deg for the deflection angles. The latter one was based on statistical estimation from several repeated measurements. Screen porosity was measured using the method described in Chapter 4.3.1, with an estimated tolerance of ±0.03.

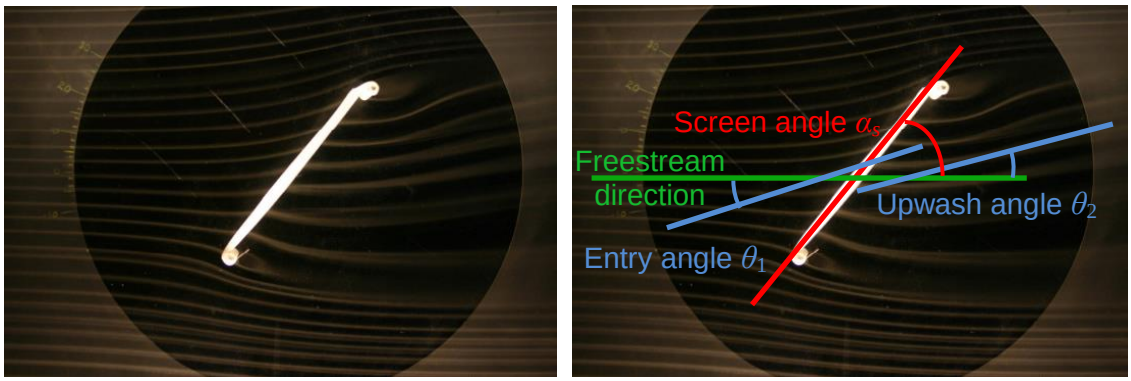

Figure 4.18: Smoke visualisation post-processing method; image of flow through a screen of 0.35 porosity and 50º angle of inclination (flow direction from left to right)

Examples of flow visualisation images are shown in *Figure 4.19* for various porosity and angles of inclination. The presence of the support struts affected the flow at both ends of the screen, displacing the nearby pathlines (*Figure 4.19b*). The central pathline, used to determine the entry and upwash angles, didn't not seem to be affected by the struts, except at very low angles of incidence. For the screen of γ = 0.80, only small changes in the pathline orientation compared to the freestream were observed (*Figure 4.19a*) at all screen angles tested, thus the flow appears to be virtually independent of the angle of incidence. The entry and upwash angles at all α_s for this screen were taken as 0. The screens of γ = 0.15 and γ = 0.10 were observed to behave similarly to a solid plate. In this case the majority of the airflow was deflected around the mesh, creating unsteady vortex shedding downstream similar to a von Karman vortex street. This resulted in a high oscillation of the entry flow pathlines, which

occurred at an increased frequency at higher wind tunnel speeds. Such unsteady phenomena would considerably increase the aerodynamic loading on the screen. In the taken flow visualisation images, the pathlines downstream of the screen were not visible as a result the shed vortices (*Figure 4.19d*).

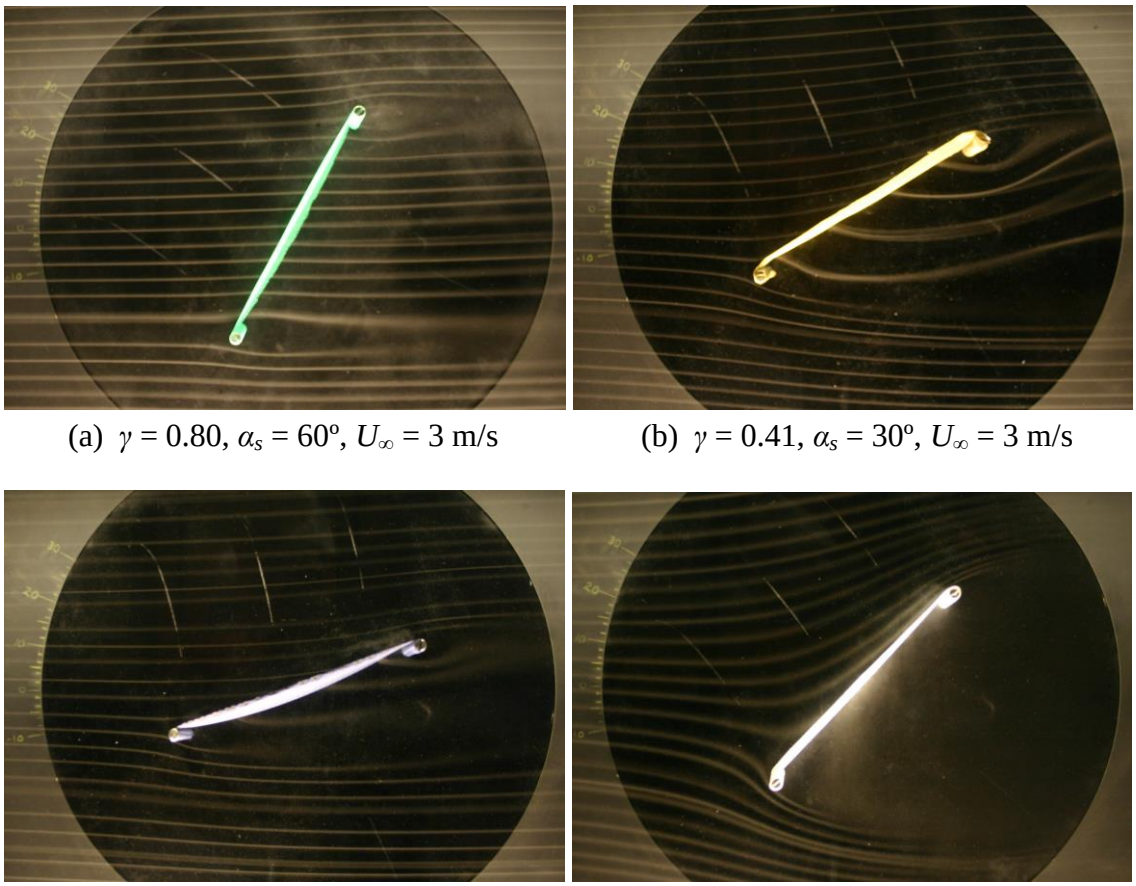

(a) γ = 0.80, α_s = 60º, U_∞ = 3 m/s (b) γ = 0.41, α_s = 30º, U_∞ = 3 m/s

(c) γ = 0.20, α_s = 20º, U_∞ = 7 m/s (d) γ = 0.10, α_s = 45º, U_∞ = 5 m/s

Figure 4.19: Examples of visualised flow pathlines for screens of various porosity and angle of inclination (flow direction from left to right)

Results for upwash angle variation with screen incidence for 0.41, 0.35 and 0.20 porosity are plotted in *Figure 4.20*. It appears that the upwash angle θ_2 reaches a maximum between 30º < α_s < 50º, depending on the tested screen. At α_s = 90º, all screens show only small changes in the orientation of the pathlines with respect to the freestream. The values for θ_2 at α_s = 0º were taken to be 0 in all cases. Generally, increasing the wind tunnel speed, and thus the flow Reynolds number, reduces the upwash angle. Plots of θ_2 versus screen porosity (*Figure 4.21*) show that θ_2 increases logarithmically with increasing porosity. The increase in upwash angle occurs possibly due to the deflection of the pathlines above and below the screen with increasing restriction of the flow through the screen.

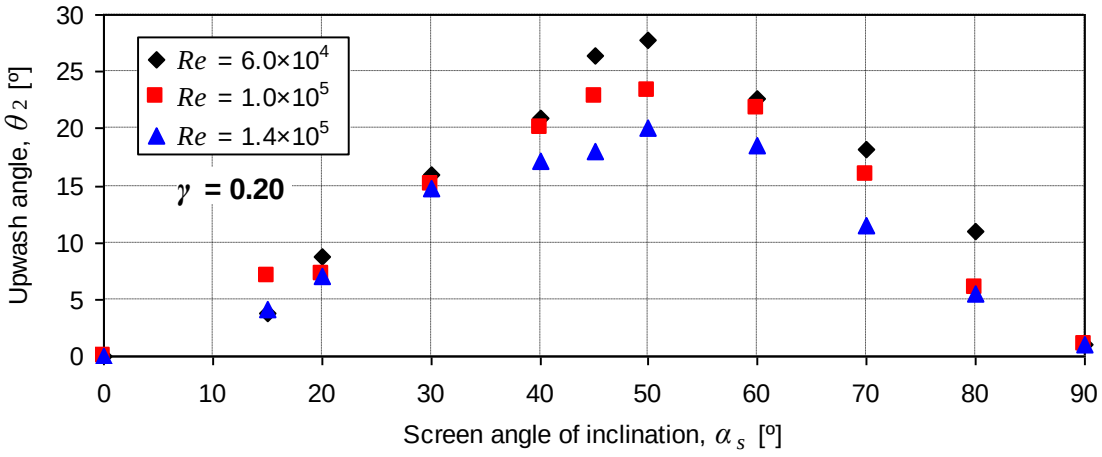

(a)

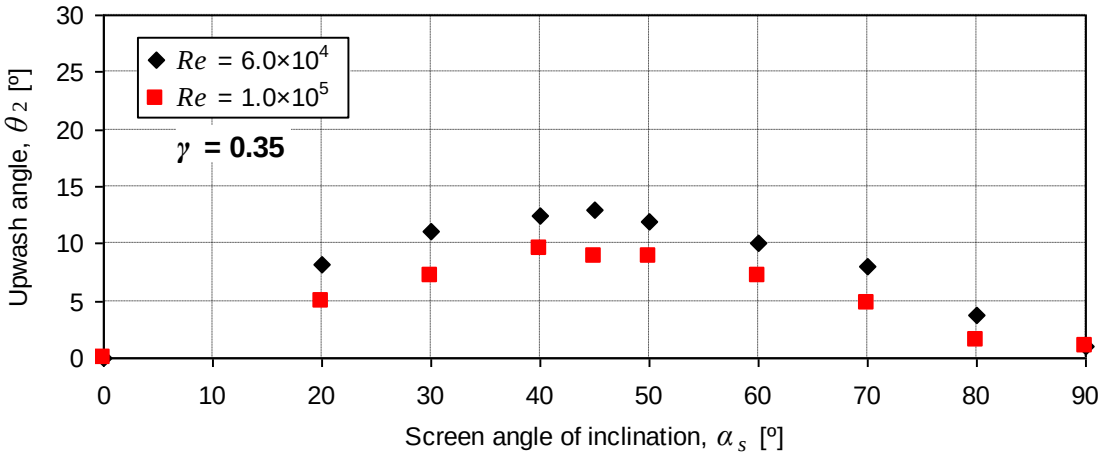

(b)

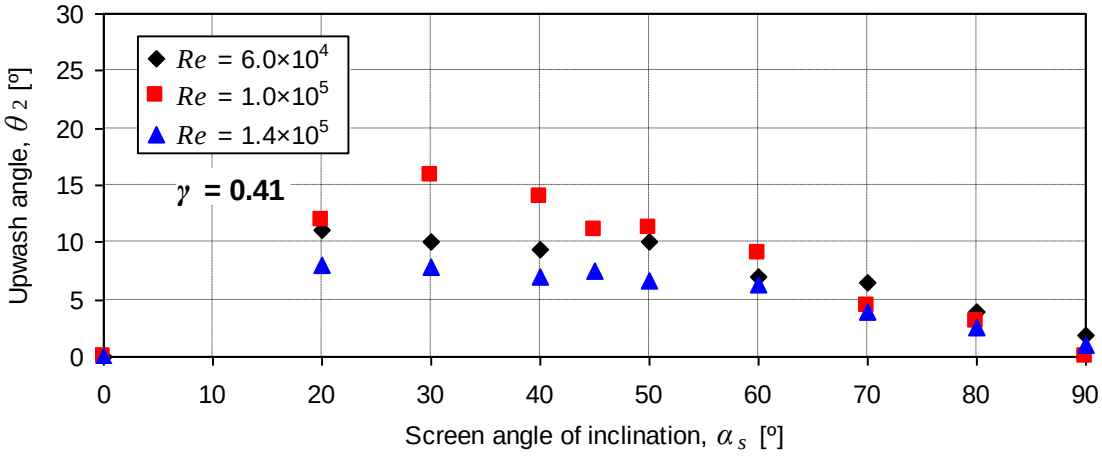

(c)

Figure 4.20: Variation of upwash angle (in degrees) with angle of inclination (in degrees) for screen porosity of: (a) 0.20, (b) 0.35 and (c) 0.41

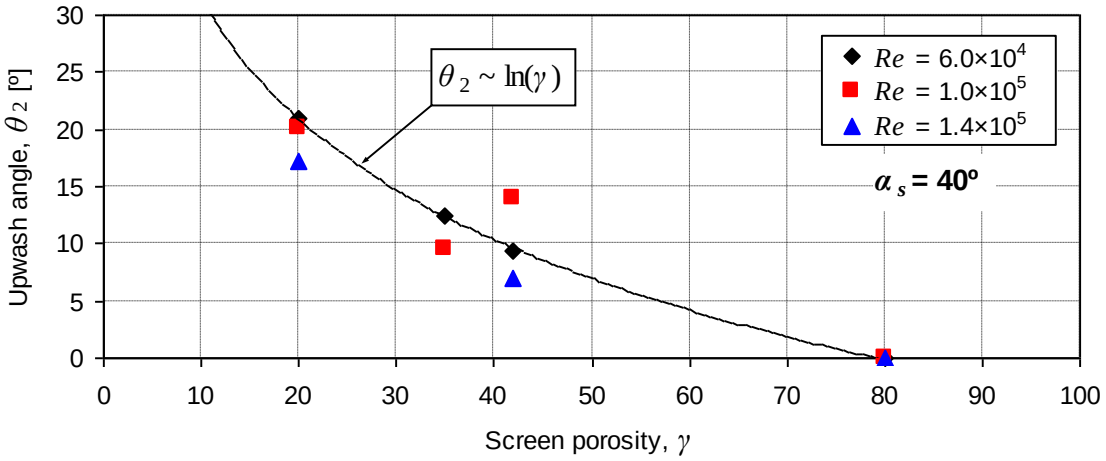

(a)

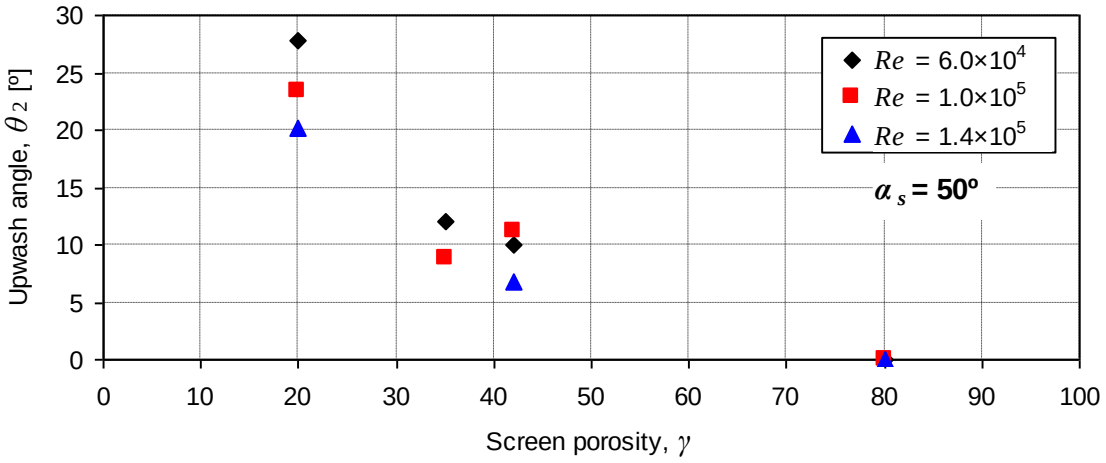

(b)

Figure 4.21: Variation of upwash angle (in degrees) with screen porosity for screen angles of inclination of: (a) 40º and (b) 50º

The maximum entry angle in all cases occurred between 40º < α_s < 50º (*Figure C.16* in Appendix C), which is in agreement with the results for the measured upwash angle. For all porosities other than γ = 0.80, as the screen angle of inclination increases from 0º, the entry flow aligns itself with the screen (entry angle θ_1 increases). With decreasing screen porosity, and thus increasing restriction of the flow through the screen, only a few pathlines pass through the screen at low angles of inclination ($\alpha_s \leq$ 20º), while the rest are deflected above or below the screen (*Figure 4.19c*).

4.4 Discussion

During the initial experiments of the research, the wind tunnel tests were conducted in two main directions: 1) to understand the behaviour of a sub-scale three-dimensional buoyant jet in ground proximity, representing a full-scale engine exhaust at take-off, and to investigate the possibility of a lift-off of the coherent plume downstream where its natural buoyancy becomes dominant over its horizontal momentum; 2) to study the flow in the near field of porous screens of various porosity and angle of inclination to the freestream. The results of 2) were used to determine the preliminary design parameters of the baffles, such as porosity and slope angle, to be further investigated in subsequent tests and in the field trials.

First, a three-dimensional buoyant wall jet from a single nozzle was investigated at 1:200 scale using laser sheet flow visualisation and modelling the jet buoyancy with the method outlined in Chapter 3.3. The ratio of freestream velocity to exit jet velocity β was varied up to 0.34 and the mole fraction of helium f in the jet up to 0.33, corresponding to a full-scale exhaust jet temperature of 403 K. Both increasing f and reducing β was found to increase the vertical spread of the plume downstream; individual parts of the top of the plume were observed to separate from the main plume body, which stayed attached to the ground within the range of tested longitudinal distances downstream of the nozzle exit. Reducing β also significantly increased the lateral spread of the plume. Modelling the Atmospheric Boundary Layer was also found to increase both the vertical and lateral spread of the plume.

The observations made with regard to plume lift-off are in disagreement with the theoretical method for predicting lift-off distances by Meroney (1979). Within the range of tested longitudinal distances, a coherent plume lift-off was observed only under certain conditions: 1) no freestream and 2) a deflector present in the path of the jet. It was shown that increasing the deflector size (width) relative to the size of the plume reduced the downstream distance to lift-off. The baffles concept of promoting plume lift-off was demonstrated by comparing the plume at the same distance downstream of the nozzle without a defector in the jet path (no lift-off observed) and with a defector (plume separated from the surface). On a few occasions, the location of the point of separation from the surface was found to vary within the running time of the test. It was observed that the re-attachment of the plume was caused by an accidental contact of a part of the plume with the surface due to unsteady meandering in the plane at right angles to the flow. A probable cause of this effect is the constraining effect of the wind tunnel ceiling on the plume, leading to recirculation flow in the working section when no freestream is present. The following important conclusions with regard to the jet sub-scale modelling were drawn:

- The ratio of freestream velocity to jet exit velocity is of high importance for the jet development with distance downstream and possible lift-off. Practically, scaling accurately the ambient wind speed of the field trials at 1:200 would mean operating the wind tunnel at its very low limit of steady freestream speed.

- The position of the deflector relative to the nozzle exit plays a significant role in the plume development in terms of the deflector size compared to the plume size and in terms of the local jet velocity at the position of the deflector. In view of the BAe146-301 exhaust jet modelling, consisting of four individual jets merging as they travel downstream, the width of the baffles should be sufficiently wider than the local jet width. This would reduce the effect of any differences in the lateral spread of the full-scale four-engine jet compared to the sub-scale model where only a single nozzle is to be used.

The experimental results on the flow in the near field of porous screens showed consistent trends as the screen porosity and orientation were varied. The measured pressure drop across various screens, considered to be a measure of the screen drag coefficient, was found to decrease with porosity and angle of incidence. Thus, inclining the screen reduced the imposed aerodynamic loading by the jet. In view of the full-scale baffles, the jet would be unrestricted, i.e. free to flow around the baffles, thus the performed measurements in the duct blower tunnel overestimated the pressure drop. Any structural analysis based on this data would therefore be conservative. More importantly, it was observed that the pressure drop coefficient approached a constant value as the flow Reynolds number *Re* increased, which suggested Reynolds number independency of the results (in this case $Re > 1200$ based on freestream velocity and screen thickness). This is a positive result considering the small scale of the planned experiments, where complete Reynolds number equality with full scale cannot be achieved.

The upwash angle just downstream of an unrestricted screen was considered to be a measure of the vertical force (lift), which the screen exerts on the flow, and thus a desirable feature of the baffles in terms of adding vertical momentum to the exhaust jet buoyancy. Generally, the upwash angle increased with reducing porosity and was observed to reach a maximum value when the screens were inclined between 30º and 50º, depending on the screen porosity. An important observation was the occurring vortex shedding downstream of screens of porosity $\gamma < 0.20$, similar to the flow around a solid flat plate. Considering the tolerance of the calculated screen porosity values, this is in agreement with the critical value of $\gamma = 0.25$, reported by Guoyt (1995) to classify ‘impermeable’ and ‘permeable’ windbreaks (see Chapter 2.7). The value of 0.20 was

also reported by Raine & Stevenson (1977) for optimum reduction of mean leeward wind speed ($\gamma = 0.20$).

In view of the above, a material of 0.20 porosity was chosen for the baffle prototypes to be built for the field trials, aiming to provide the desired deflection of the flow upwards and at the same time reduce the aerodynamic load on the baffles and avoid vortex shedding (i.e. von Karman vortex street). Inclining the baffles was also considered, compromising between reduction in drag (and aerodynamic loading) and increase in lift, since the design of the baffle prototypes required them to have sufficient strength to withstand the strong jet blast and at the same time comply with the frangibility criteria for runway edge lighting, described in Chapter 8.1. The slope angle, together with the arrangement of the baffles in the field trials (i.e. number of rows and row spacing), were investigated in the next stage of the wind tunnel experiments, using force balance measurements.

5 Force balance measurements

Following the initial stage of the experiments, the design of the baffle configuration was approached with the choice of a skin-friction balance as a suitable design tool. This allowed the baffle shape and spatial arrangement to be optimised in terms of aerodynamic drag, which was considered the primary parameter within the mechanism of the baffle concept. The key parameters in the baffle configuration, such as baffle slope angle, number of baffle rows and separation distance between them, were investigated in a series of drag measurements, subject to this chapter.

5.1 Experimental arrangement

In order to demonstrate the effect of the baffles, it was estimated that a momentum reduction, equivalent to about 25% of the total engine thrust, would be sufficient (Bennett, 2012). This was incorporated into a scoping calculation, based on drag coefficients of walls (ESDU, 1989) and inclined flat plates (Cook, 2010), and measurements at Cranfield Airport of the plume spread and velocity decay behind a stationary BAe 146-301 aircraft during engine power-up prior to take-off (Graham, 2009). The calculation sequence is presented in detail in Appendix D1. The resulting initial (estimated) full-scale arrangement of five rows of baffles is shown in *Table 5.1*, where the downstream distance is taken from the piano keys of the runway (assumed aircraft starting position) and the baffles are inclined at a slope angle to the horizontal, α = 45º. The spacing was estimated at 12× the slope height h' of the row upstream, or approximately 17h, ensuring the baffles are located safely below the standard landing approach slope, i.e. 3º.

Given this configuration, the wind tunnel models were manufactured as wooden prisms at 1:50 scale with slope angles α equal to 45º, 60º and 90º, keeping the width and the vertical height constant for the respective row from 1 to 5, as given in *Table 5.1*. The width of each row w corresponds to the estimated width of the jet and results in an aspect ratio w / h of approx. 21 for each row. The dimensions of the models at 1:50 scale are included in *Figure E.1* in Appendix E. During tests the baffle rows were fixed to the balance plate with double-sided tape. It should be noted that the models are not representative for a typical windbreak shape, which is essentially an inclined flat plate or porous screen, due to their upright base. However, the purpose of this investigation was to obtain trends in the drag variation of various baffle configurations, not precise drag coefficients for estimation of drag forces in full scale. Therefore, these simplified models were considered suitable for the purpose of the tests.

Table 5.1: Parameters of the provisional full-scale baffle calculation

Baffle row no.	Distance from engines [m]	Estimated width of jet* [m]	Slope height, h' [m]	Vertical height**, h [m]
1	60.0	14.6	1.00	0.71
2	72.0	17.6	1.20	0.85
3	86.4	21.1	1.44	1.02
4	103.7	25.3	1.73	1.22
5	124.4	30.4	2.07	1.46

* Estimated from Lidar data during field trials at Cranfield (Graham , 2009)

** The vertical height is given for a baffle slope surface inclined at $\alpha = 45^{o}$

The measurements were taken in the 8'×4' Atmospheric Boundary Layer Wind Tunnel (ABLWT). The working section boundary layer (see *Figure 5.4* in Chapter 5.3.1) was that which formed downstream of a clean flow development section, i.e. no roughness elements. The jet flow was simulated with a round nozzle of diameter 20 mm. *Figure 5.1* shows a schematic of the arrangement for each of the cases considered. Images of the baffle models in the working section are shown in *Figure 5.2*. The first set of tests was performed at a freestream velocity of 14 m/s for all three types of baffles, varying the distance between the rows and the number of rows on the balance plate (*Figure 5.1a*). For the second set of tests, the nozzle was positioned at 60 nozzle diameters from the first row of baffles (*Figure 5.1b*). The jet flow of ambient air was supplied by an external compressor connected to the nozzle through plastic tube underneath the working section floor. It had an exit bulk velocity of $U_j \approx 57$ m/s, equivalent to a Reynolds number, based on U_j and nozzle diameter, of nominally 75200. Tests were performed with both ($\beta = U_\infty / U_j = 0.05$) and without freestream ($\beta = 0$) for configurations of three, four and five rows of baffles inclined at $\alpha = 60^{o}$.

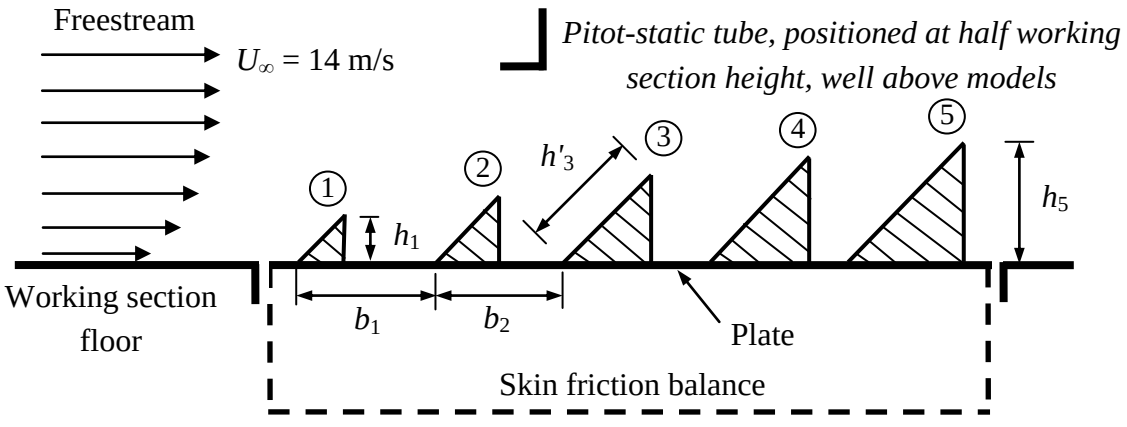

(a)

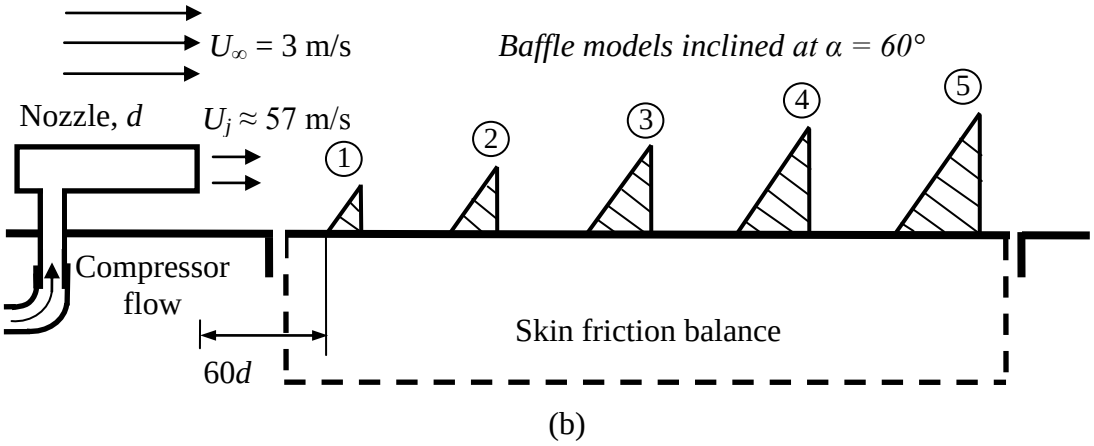

Figure 5.1: Schematic illustration of the 8'×4' ABLWT working section arrangement for force balance measurements of an array of baffles at 1:50 scale, subjected to: (a) freestream, (b) a nozzle jet (side view, not to scale)

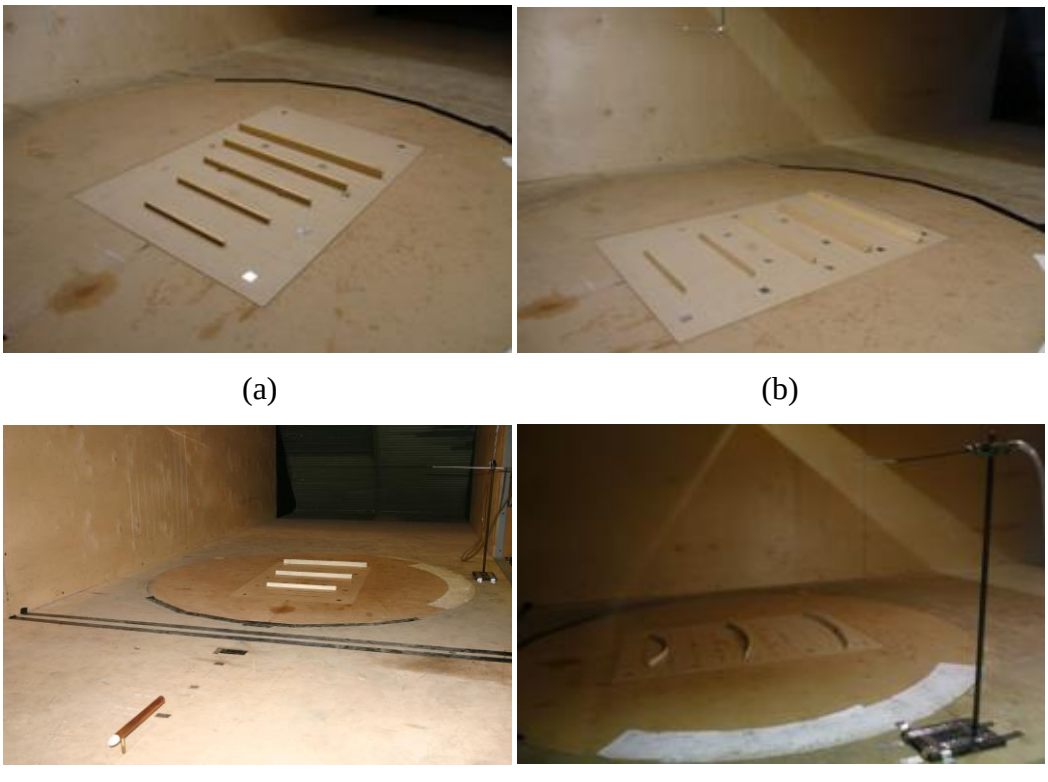

Figure 5.2: Images of the 8'×4' ABLWT working section for force balance measurements (a) freestream α = 90° (flow direction is from bottom left), (b) freestream α = 45° (flow direction is from bottom left), (c) nozzle jet α = 60° straight arrangement (flow direction is from left to right), (d) nozzle jet α = 60° arc-shaped arrangement (flow direction is from bottom to top)

5.2 Post-processing and repeatability

Given that the balance measures the aerodynamic load experienced by both the baffles and the plate on which they are mounted, measurements were also made on the plate in isolation to aid the subsequent data analysis as follows:

1) A total drag-force coefficient C_T is calculated from *Equation 5.1* with the freestream density ρ_∞ determined from the recorded ambient barometric pressure and temperature, and based on a reference area A_{ref} of 0.0489 m^2 (the sum of the projected frontal area of all five rows of baffles, calculated with the models' width w and vertical height h).

$$C_T = \frac{F_T}{0.5\rho_\infty U_\infty{}^2 A_{ref}}$$

Equation 5.1

2) The balance plate drag coefficient C_b, defined in *Equation 5.2*, is calculated. The average value for U_∞ = 14 m/s (or $q_\infty \approx 115$ Pa) is $C_b = 0.04$.

$$C_b = \frac{F_b}{0.5\rho_\infty U_\infty{}^2 A_{ref}}$$

Equation 5.2

3) The drag coefficient of the baffle models C_D is calculated by subtraction:

$$C_D = C_T - C_b$$

Equation 5.3

This data reduction method assumes the same plate tare-drag coefficient C_b irrespective of the number of rows of baffles or their longitudinal position on the plate. It does not take into account the 'loss' of plate area due to being covered by the baffles, nor the changes in the flow structure and boundary layer over the free plate area due to the presence of the baffles. Additional runs were performed to investigate the effect of changing the position of the baffles on the plate for configurations of two, three and four rows. Relative differences in C_D of up to 4% were observed, which were considered insignificant for the purpose of the tests. The differences in drag arise possibly due to the following flow development: a more forward position leaves the majority of free plate area downstream of the models and is therefore within their wake,

governed predominantly by turbulent vortex formations and associated reverse flow; when the models are at the back of the plate, its free frontal area is subjected to a fully-developed turbulent boundary layer. The method was considered sufficiently accurate to obtain trends in the aerodynamic drag behaviour of the baffles.

Repeatability runs for various configurations of five rows of baffles at Reynolds numbers in the nominal range $10000 < Re < 26000$, based on the measured freestream velocity and the vertical height of the largest baffle row h_5, are presented in *Figure 5.3*. C_T appears to approach a constant value as the freestream velocity increases and thus becomes independent of Reynolds number close to the test conditions (U_∞ = 14 m/s corresponding to Re = 26000).

Figure E.2 in Appendix E gives an overview of the repeatability in terms of relative errors in C_F and absolute force errors (in N) for the lowest (6 m/s) and highest (14 m/s) tested freestream velocity. These were calculated from the minimum and maximum measured forces within all runs of the appropriate configuration and freestream velocity. At 14 m/s, the relative errors for most data are within 1%. At 6 m/s the uncertainties increase as most relative errors are within 5%, with one set of data reaching 7.6%. Most absolute errors are within 0.02 N, indicating good repeatability even at low speeds. This is a positive conclusion for the application of the skin-friction balance in the planned nozzle experiments, where the exerted forces on the baffles would be considerably smaller due to the decay of the jet velocity with distance downstream.

The repeatability tests for the balance platform indicate similar absolute errors of up to approximately 0.03 N.

The choice of h_5, equal to 29 mm, as characteristic length in the calculated Reynolds numbers of *Figure 5.3*, is due to its assumed role as a governing length scale in the flow field close to the baffles. It may be argued that the governing length scale would depend on the spacing of the rows. For example, if the rows are positioned close together, the taller rows would be in the wake of the smaller ones, thus the drag of the array would be determined mainly from the height of the first row. By all means, the drag forces on the baffles would be caused primarily by flow separation and the presence of a wake region downstream of each row. Returning to *Figure 5.3*, there seems to be little variation of the results with Reynolds number for $Re > 18000$. In view of the experiments planned at 1:200 scale, the Reynolds number at the nozzle can be assumed to be below 10000, and lower locally at the baffle array. Therefore, a Re dependency at 1:200 scale should be expected. However, the results shown in *Figure 5.3* can surely be regarded as positive, since the quoted Re at 1:200 scale and the observed limit value of Re = 18000 are of the same order of magnitude. In comparison, the Reynolds numbers at full scale and 1:200 scale differ by three orders of magnitude.

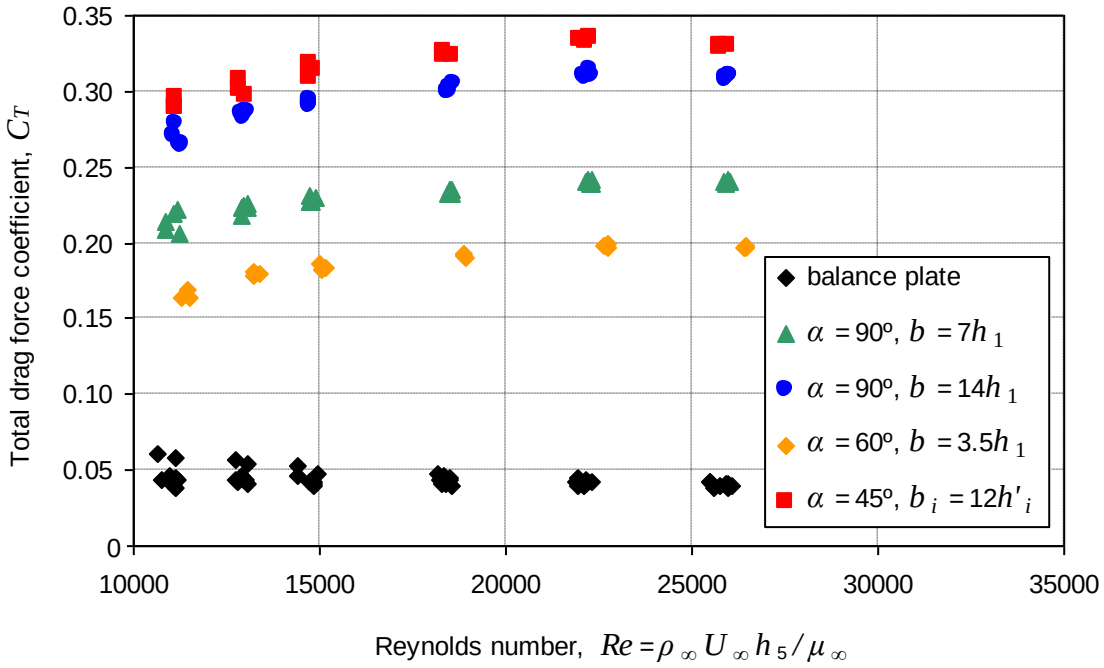

Figure 5.3: Total drag coefficient vs. Reynolds number for repeated runs with various configurations of five baffle rows;

x-axis shows the Reynolds number calculated with the freestream velocity and height h_5 of the largest baffle row; y- axis shows the total force coefficient, calculated from Equation 5.1

5.3 Results

5.3.1 Drag of single baffles beneath freestream

Vertical profiles of the mean velocity in the empty working section were measured to determine the boundary layer development on the balance plate. The measurements were taken at three distances x from the start of the plate along the centre line, equal to $0.095l_P$, $0.5l_P$ and $0.95l_P$, where l_P is the length of the plate equal to 1060 mm. The boundary layer thickness δ was determined by obtaining a numerical approximation of the variation of U with height z close to the measured freestream velocity using the Microsoft Excel function *Trendline*. The data is presented in a logarithmic plot in *Figure 5.4*, showing good linear fit. Using *Trendline* and *Equation 3.13*, included in Chapter 3.4, the power-law exponent a was estimated to be approximately $1/8$, varying slightlty depending on the location on the balance plate where the measurements were taken. It is in good agreement with the theoretical power

exponents of 1/7 and 1/9, used for a fully developed turbulent boundary layer on a flat plate at local Reynolds numbers, based on the freestream velocity and the distance from the plate's leading edge, of $5\times10^5 < Re < 10^7$ and $10^6 < Re < 10^8$ respectively (Garry, 2008). The boundary layer measurements were used to estimate the velocity at the height of the individual baffle rows in the subsequent analysis.

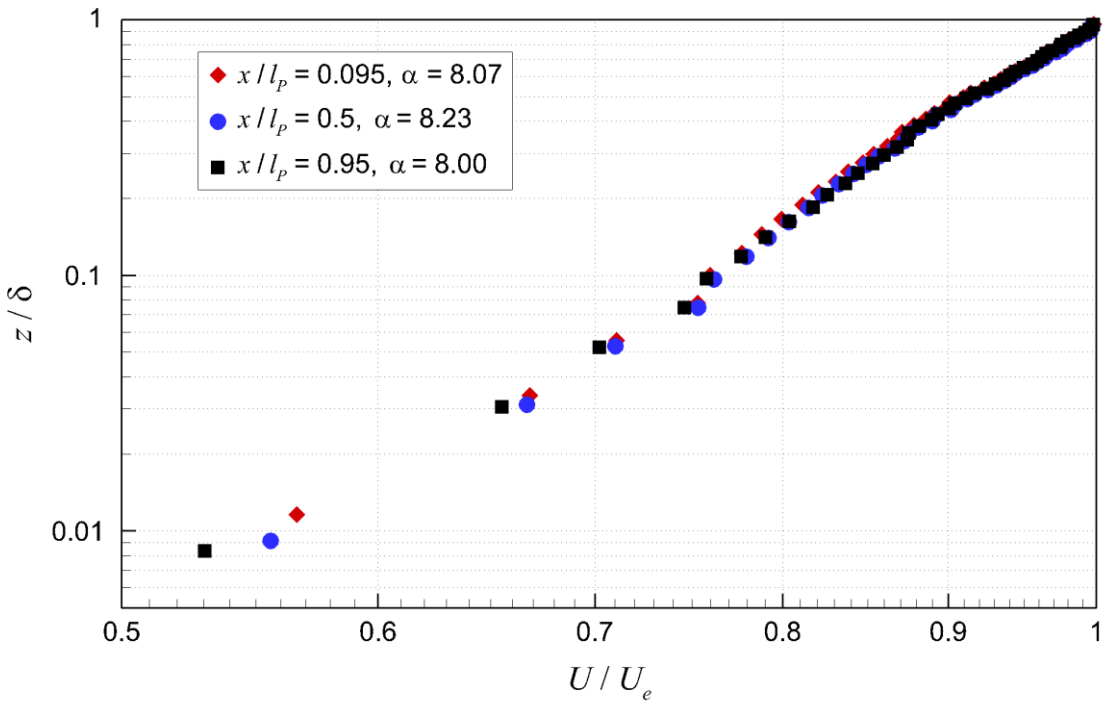

Figure 5.4: Vertical boundary layer velocity profiles measured along the centre line of the empty 8'×4' working section at 0.095l_P, 0.5l_P and 0.95l_P

For a single baffle row, the drag coefficients C_{Dn} and C_F are calculated from *Equation 5.1* to *Equation 5.3*, based on a reference area equal to the corresponding projected baffle frontal area ($w \times h$). To calculate C_F, the drag coefficient C_{Dn} is multiplied with the squared ratio of freestream velocity to velocity at the corresponding baffle height h, taken from the measured velocity profile at $x / l_P = 0.5$. As shown in *Figure 5.5*, the results compare well with the empirical formula of Plate (1964), obtained for $0.09 \leq h / \delta \leq 0.50$, even at lower values of h / δ. The formula is presented in *Equation 2.16* in Chapter 2.7.

The calculated values of C_F for baffles with a slope angle $\alpha = 90^o$ remain approximately constant with h / δ, however they are considerably lower compared to those reported in ESDU (1989) and Cook (2010). The value of 1.20, stated by Cook, is a good approximation for the typical range of Jensen number for fences, i.e. between 10

and 1000. The Jensen number *Je* was defined in Chapter 2.7 as the ratio of fence height h to roughness length z_0. If the boundary layer is developed over a smooth surface, as was the case for the boundary layer measurements, z_0 is practically zero and $Je = \infty$. As shown by Cook (2010) using comprehensive data reported by Ranga Raju et al. (1976), C_F reduces with increasing Jensen number (see *Figure E.5* in Appendix E). Therefore, the lower values, obtained here for a boundary layer developed over a smooth surface, are justified.

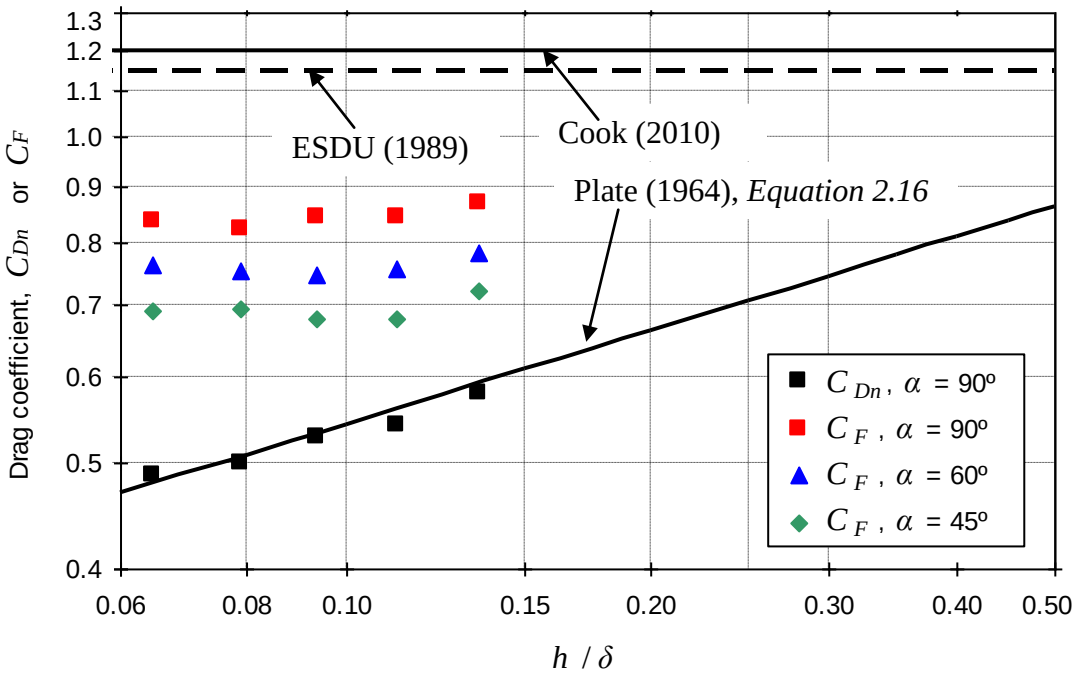

Figure 5.5: Drag coefficient vs. row-height-to-boundary-layer-thickness ratio for a single-row baffle of 90º, 60º and 45º slope angle

5.3.2 Drag of arrays of baffles beneath a freestream

For configurations of multiple rows of baffles the drag coefficient was calculated using the same method of *Equation 5.1* to *Equation 5.3* with a reference area A_{ref} of 0.0489 m^2, equal to the sum of the projected frontal areas of each individual row. The front-to-front spacing between the baffle rows, b, was varied between $3.5h_1$ and $21h_1$ (with each row a constant distance apart). Additional two cases of $b_i = 12h'_i$ and $b_i = 15h'_i$, where the spacing increases progressively from row to row as the slope height h'_i increases, were also tested. For the five-row configurations of the latter two cases and for $b = 21h_1$ the first row had to be positioned upstream of the balance plate due to insufficient plate length. This was accounted for by measuring the drag of the first row individually in separate tests and adding it to the results.

For the five-row configuration, also referred to as 'all 5', the drag coefficient was observed to vary linearly with distance between the rows (see *Figure 5.6*). As b / h_1 increases towards infinity, the influence of the wake, caused by the rows upstream, and thus the interference drag between the rows should reduce to zero and the total drag of the configuration should asymptotically approach a constant value. The C_D values at infinite non-dimensional spacing were obtained by measuring the drag of each row separately, and correspond to the sum of the resulting individual drag coefficients of the baffle rows. *Figure 5.6* shows similar trends of C_D with b / h_1 for all three baffle angles tested. As with single rows (see *Figure 5.5*), inclining the baffle surface facing the flow reduces its drag. This effect is well known for single flat plates of width-to-slope-height ratio larger than 2 in freestream (ESDU, 1970).

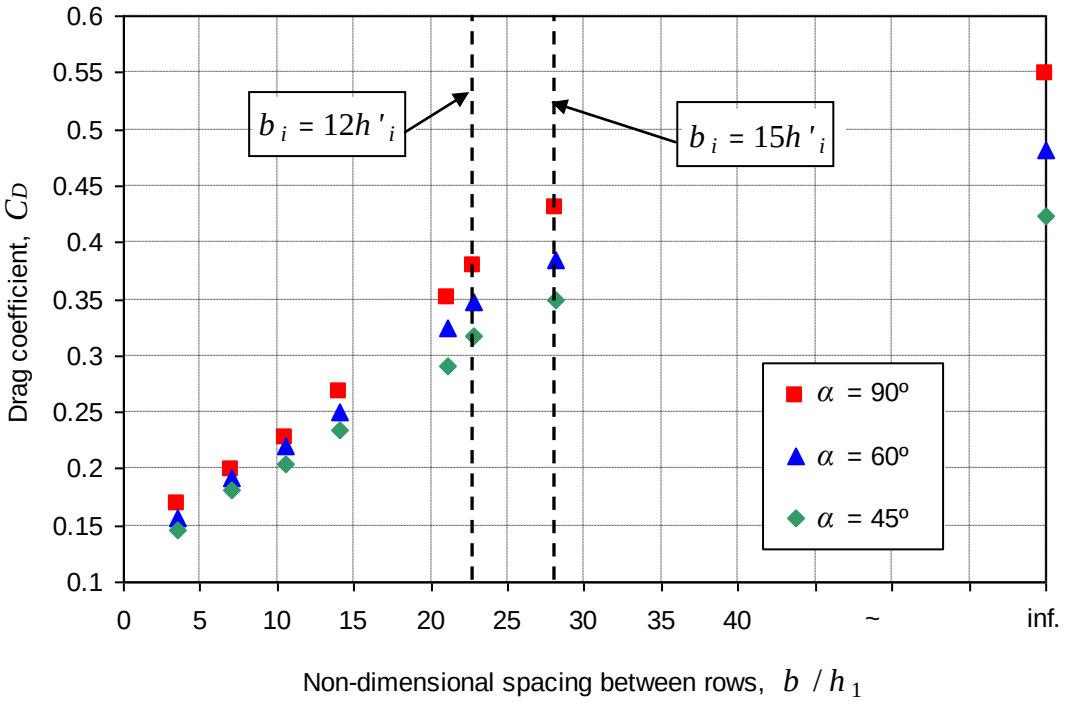

Figure 5.6: Drag coefficient vs. spacing for configurations of five rows of baffles inclined at 90º, 60º and 45º in a freestream

The variation of drag coefficient with number of baffle rows is shown in *Figure 5.7*, where s and n are the number of baffle rows starting from the smallest and the largest respectively. For example, $s = 3$ is a configuration of rows 1, 2 and 3, while $n = 3$ is a configuration of rows 3, 4 and 5. At close distances ($b / h_1 = 3.5$), the drag coefficient reduces as n increases from 1 to 5 due to the sheltering effect produced by the wake of the smaller rows upstream. At $b / h_1 = 7$, C_D remains approximately constant as n is varied, thus the (negative) interference drag of the rows upstream must equal approximately the incremental drag rise due to increase in row size. For greater b / h_1,

C_D increases with n. In both *Figure 5.7a* and *Figure 5.7b*, the infinity values for each number of baffles, both n and s, appear to be closer to the cases of b tested as the angle reduces from 90º to 45º, suggesting that inclining the baffles reduces the influence on the rows downstream by possibly reducing the extent of the wake.

Figure E.3 in Appendix E shows the results plotted as a percentage of the drag coefficient C_D of the corresponding 'all 5' arrangement. The subscript 'red' indicates the reduced number of baffles in the configuration (less than 5). For all baffle angles and spacing between rows of $b/h_1 > 14$, approximately 90% of the observed C_D for the 'all 5' configuration is achieved with rows 3, 4 and 5 only (i.e. $n = 3$). This number is approximately 95% if the four largest rows are present on the balance ($n = 4$). Considering the planning of the field trials, a three-row arrangement offered the most efficient solution when taking into account manufacturing, arrangement and operation. However, as the above measurements were performed under constant freestream flow in the working section, the question remains raised whether the same trends would occur if only a nozzle jet were present upstream. Due to the natural decay of jet momentum with distance, if the rows were too far apart, the large baffle rows downstream may become ineffective as they would be subjected to a lower jet velocity. If too close, they would be 'sheltered' by the smaller rows upstream. This approach suggests that, in terms of maximising the drag of the baffle array, an optimum configuration with defined row spacing and number of baffle rows should exist.

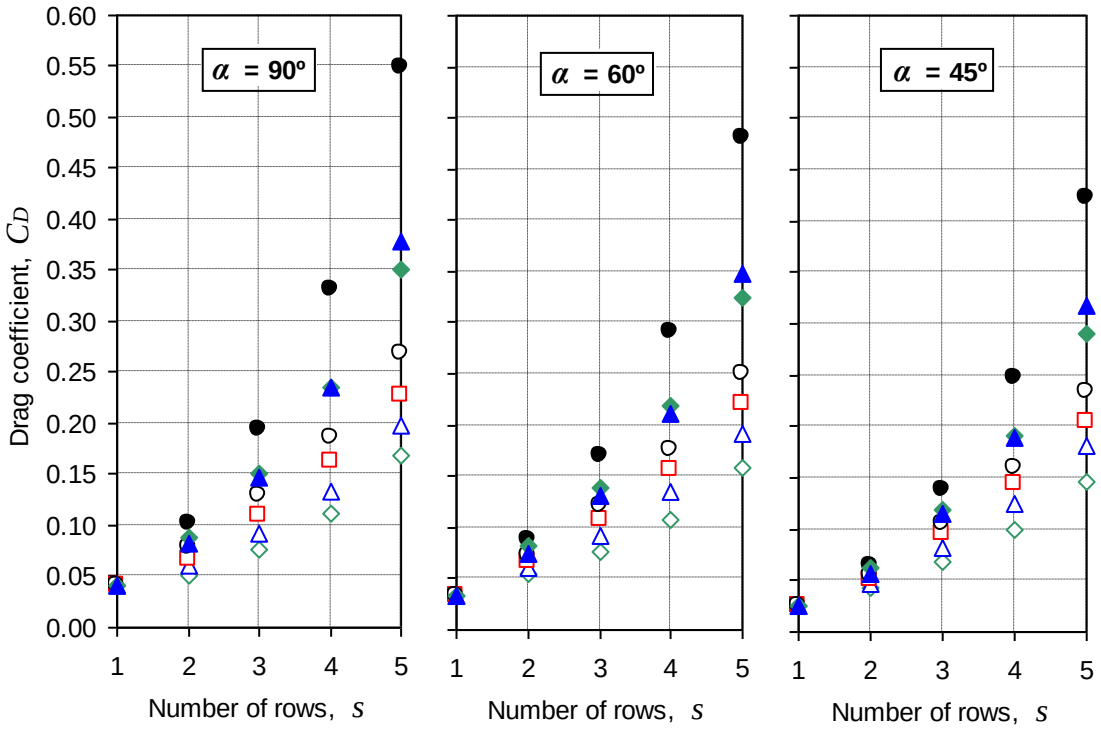

(a)

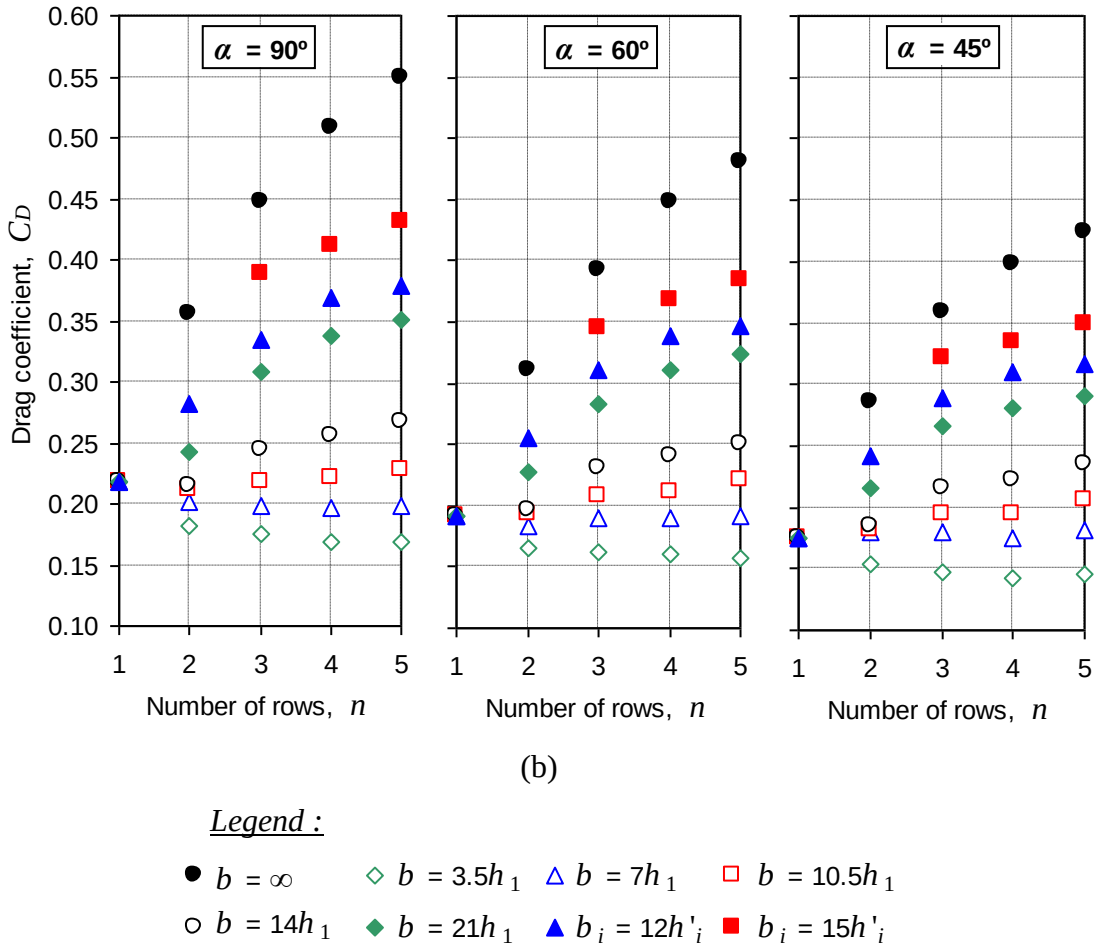

Figure 5.7: Drag coefficient vs. number of baffle rows in a freestream: (a) starting from the smallest adding rows downstream; (b) starting from the largest adding rows upstream

5.3.3 Drag of arrays of baffles beneath an exhaust jet

After the experiments in a freestream, a decision was made to use baffle prototypes of α = 60º in the field trials. A baffle row inclined at 60º would add a vertical component, deflecting the plume upwards, and at the same time would give a greater drag compared to a row inclined at 45º. Furthermore, the possibility of using only three rows of baffles was explored by varying their longitudinal position relative to the nozzle. Therefore, the experiments in a nozzle jet were conducted with baffle models of α = 60º only. The configurations tested are shown schematically in *Figure E.4* in Appendix E. The term 'upstr' denotes configurations where row 1 (2-5 upstr) or row 1 and 2 (3-5 upstr) were removed from the balance and the remaining rows were moved one or two row spacings b upstream respectively, so that the first row in the path of the jet was always at a distance of 60d from the nozzle.

The data for the nozzle jet case were calculated with the dynamic pressure of the jet at the nozzle exit and are shown as C_D multiplied by a factor of 100 in *Figure 5.8*. When no freestream is present, the drag coefficient is seen to be a maximum for a spacing $b / h_1 \approx 20$ when the rows are moved upstream (first row moved to 60*d*) and $b / h_1 \approx 15$ when they are left in their initial position. The four-row 'upstr' configuration yields the largest drag coefficient. It appears that the larger rows further downstream become ineffective as the jet momentum decays naturally with distance due to ambient air entrainment and the presence of the baffles upstream. This is not the case when a freestream is present. Generally, under a combination of a freestream and jet the five-row arrangement yields the largest drag coefficient. The effect of the freestream is to constrain the plume and reduce the entrainment of ambient air which in turn slows down the rate of decay of momentum of the jet with distance downstream. However, its direct contribution to the increase in the drag coefficients is relatively small. This conclusion was reached following separate drag measurements in the presence of freestream only, which was found to produce ~1/20th of the total drag coefficient of the freestream and jet combination (the actual value varies depending on the number of baffles and their configuration).

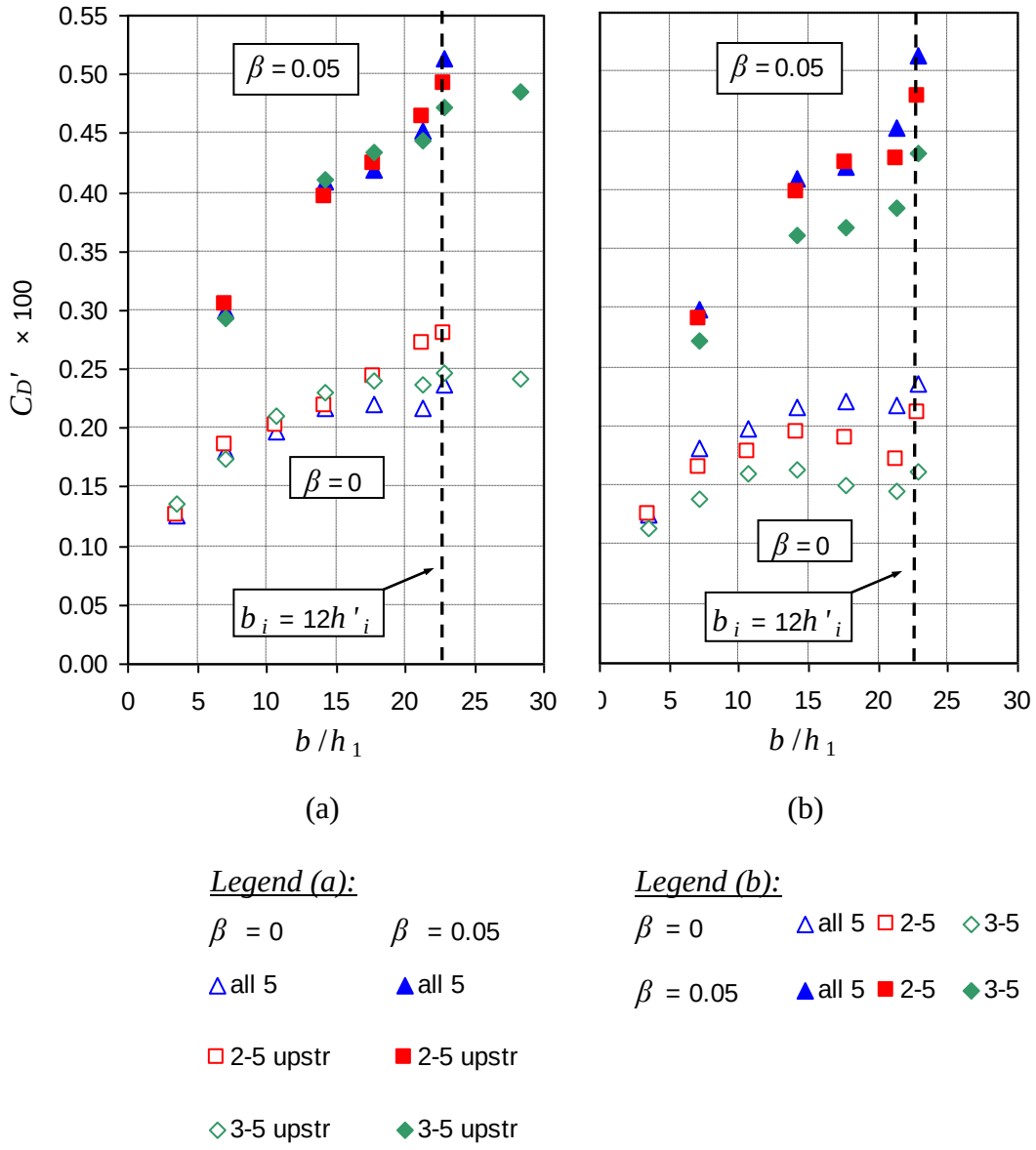

Figure 5.8: Drag coefficient vs. spacing for straight rows of baffles inclined at 60º, in a nozzle jet (a) configurations of baffle rows moved upstream, (b) configurations of first and second row of baffles removed

C_D is calculated with A_{ref} and the nozzle exit velocity, and multiplied by a factor of 100 upstr' denotes the cases when all rows present are moved upstream so that the distance from the first row (row no. 2 in '2-5 upstr' and row no. 3 in '3-5 upstr') to the nozzle at the centre line remains constant at 60 nozzle diameters, see Figure E.4 in Appendix E

5.3.4 Arc-shaped arrays of baffles

Finally, a configuration of arc-shaped rows was investigated further for three rows of baffles (i.e. n = 3) of α = 60º to identify any effects on the drag coefficient. Two different radii R_0 were tested in addition to the straight rows, considered effectively as arcs of infinite radius. The radius R_0 was defined as the radius of the first row downstream of the nozzle exit. All subsequent rows were arranged as concentric arcs to the first row with a spacing distance b. For a '3-5 upstr' configuration, R_0 was the radius of row 3; for a '3-5' configuration, it was the radius of row 1 (not present on the balance). The latter case is shown schematically in *Figure 5.9*; row 1 and 2 are not on the balance and are therefore depicted with dashed lines.

The results obtained generally show a small reduction in drag coefficient as R_0 reduces (see *Figure 5.10*), thus the straight rows appeared to be more efficient for the purpose of the field trials. However, from a practical viewpoint, a concentric arc arrangement was easier to map on the grass of the runway end safety area and – more importantly – due to the finite width of the rows, an arc shape gave a better chance of capturing the plume in case of strong crosswinds. This is due to the natural decay of jet momentum causing the jet to drift in a curved path sideways in the direction of the wind as it travels away from the engine.

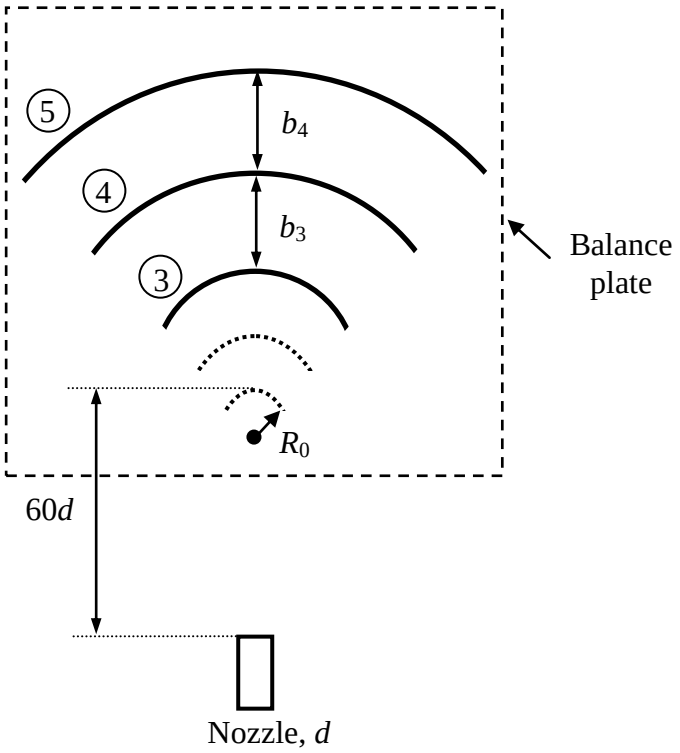

Figure 5.9: Schematic of the circular baffle arrangement in the 8'x4' working section; top view (not to scale)

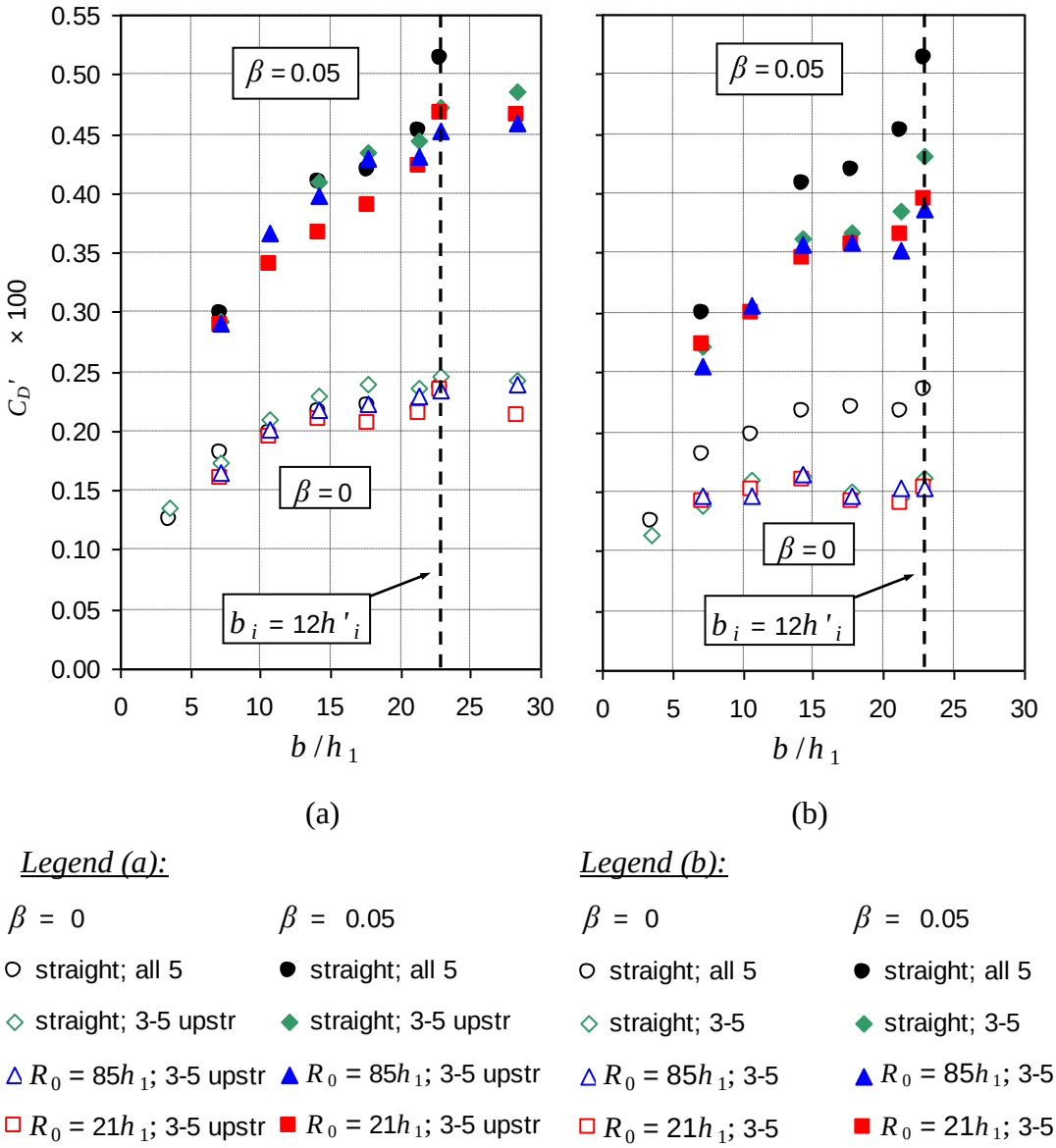

Figure 5.10: Drag coefficient vs. spacing for curved rows of baffles inclined at 60º in a nozzle jet (a) configurations of baffle rows moved upstream, (b) configurations of first and second row of baffles removed

C_D is calculated with A_{ref} and the nozzle exit velocity, and multiplied by a factor of 100 upstr' denotes the cases when all rows present are moved upstream so that the distance from the first row (row no. 2 in '2-5 upstr' and row no. 3 in '3-5 upstr') to the nozzle at the centre line remains constant at 60 nozzle diameters, see Figure E.4 in Appendix E

5.4 Summary

The aerodynamic drag of arrays of surface-mounted rows of triangular-prism shaped baffles with 90º, 60º and 45º slope angle, subjected to a nozzle jet and freestream was measured at 1:50 scale using a skin-friction balance. Data were obtained by subtracting the drag of the skin-friction balance plate from the total drag measured, which showed excellent repeatability. This was found to be a sufficiently accurate method to investigate the variation of drag coefficient with number of baffle rows, their spacing and shape in terms of slope angle. Drag coefficients obtained for a single baffle of 90º slope angle were found to agree with trends suggested by previous investigations of fences.

When subjected to a freestream in isolation, similar trends in drag coefficient were observed for all three baffle slope angles. Reducing the angle was found to reduce the wake of the rows resulting in smaller downstream interference effects. Strong sheltering effects were observed for non-dimensional row spacings of $b/h_1 \leq 7$ when additional rows of baffles were placed upstream. Configurations of three and four of the largest baffle rows were found to give ~90% and ~95% respectively of the drag of the five-row configuration. At the test freestream velocity of 14 m/s, the results were observed to be practically independent of Reynolds number.

Under a combination of a freestream and nozzle jet, the three-row arrangement was also found to deliver the same results when both were located at the same distance from the nozzle. If located sufficiently downstream of the nozzle, the baffles experienced a maximum drag, thus at large spacing the large rows of baffles become inefficient as they are subjected to lower local velocity. The primary effect of the freestream was observed to reduce the entrainment of ambient air thus conserving the decaying jet momentum over a longer distance downstream of the nozzle.

An arc-shaped arrangement reduces the overall drag. It appeared, however, to be a better practical solution when considering the field trials arrangement. After taking into account the wind tunnel results, the final arrangement to be used in the sub-scale ABLWT experiments and full-scale field trials was changed to a three-row arrangement comprising rows 3, 4 and 5. While the aerodynamic efficiency of the baffles in terms of drag did not appear to be reduced greatly, a changing from a five-row to a three-row configuration would give a significant reduction in costs and time for manufacturing, transportation and operation during the field trials.

With regard to the subsequent ABLWT experiments, the observed Reynolds number independence of the obtained drag results for $Re > 18000$, based on the baffe row height h_5, is of significant importance. It suggests that wind tunnel modelling of the

effects of the baffles does not require a complete Reynolds number equality in sub scale and full scale. Compared to the initial expectations of a significant Reynolds number difference, i.e. approximately three orders of magnitude, the results of the drag measurements show that experiments could successfully be perfomed at lower Reynolds numbers. The observed critical value of 18000 is in the same order of magnitude as the expected Reynolds numbers at 1:200 scale, which is a positive result with regard to achieving flow similarity with the adopted wind tunnel modelling techniques. At the same time, a complete Froude number equality between sub scale and full scale can be achieved.

Following this conclusion, the final stage of the sub-scale experimental research was conducted. In order to be able to obtain a good correlation between sub scale and full scale, a more accurate model of the exhaust jet was needed, taking into account the BAe 146 engine characteristics at take-off.

6 Sub-scale field trials model

The initial sub-scale plume visualisation tests (Chapter 4.2) highlighted the importance of the position of the baffle array relative to the jet source and the influence of the secondary flow (ambient wind) on the plume development and dispersion. Therefore, for an accurate representation of the field trials at sub scale, the following aspects need to be considered carefully:

- Exhaust jet model
- Representation of the ambient conditions of the field trials in the wind tunnel
- Atmospheric Boundary Layer (ABL) model.

This chapter describes the modelling issues, practical considerations and steps undertaken to obtain the exhaust jet and ABL models of the 8'×4' wind tunnel tests, in addition to the full-scale field trials. Chronologically, the field trials were conducted before the 8'×4' experiments, therefore the recorded full-scale parameters were used to create sufficiently accurate models in order to obtain a valid representation at sub scale.

6.1 Exhaust jet model

Generally, a full-scale exhaust jet at take-off is characterised by high momentum and temperature at the engine nozzle exit, which reduce as the jet progresses away from the source and entrains ambient air. The BAe 146-301 would initially produce four individual jets which would rapidly merge into a single jet before reaching the baffles. This can be observed from the Lidar data at 0.7º elevation (see *Figure H.6a*, *Figure H.7a*, *Figure H.8a* and *Figure H.9a* in Appendix F), obtained during the full-scale field trials, which are subject to Chapter 8. As suggested by Graham et al. (2008), the initial four jets would interact and merge as they travel about a wing span distance downstream, forming a coherent plume. Bennett et al. (2010) also observed this during Lidar studies of multiple take-off runs, performed by commercial aircraft of various sizes and engine configurations. With regard to the sub-scale modelling of the BAe 146-301 field trials, for practical reasons, only one nozzle can be used in the 8'×4' ABLWT arrangement. Following the above considerations and the observations on the merging of multiple jets in close proximity, discussed in Chapter 2.5, the choice of a single nozzle to represent the BAe 146-301 exhaust jet is justified.

Another important aspect of the sub-scale modelling of the take-off run is whether to use a stationary or moving nozzle. Ideally, an accelerated source should be used in

order to represent realistically the full-scale take-off run of a conventional civil aircraft. This would require instantaneous measurements to be taken in order to capture the starting plume. During the BAe 146-301 field trials, the take-off run was executed with a static burn of approximately ten seconds before the brakes were released and the aircraft was accelerated on Runway 21. Thus, the Lidar data showed the development of a jet from a stationary source. Furthermore, accelerating a sub-scale nozzle, positioned at an offset from the working section floor and connected to external tubing, would require additional practical considerations and equipment. In view of the above, a stationary nozzle was chosen as a source of the sub-scale jet. This is a key aspect of the field trials modelling in the 8'×4' ABLWT, described in this chapter. Further considerations of a possible moving source model are discussed in Chapter 6.1.4.

In addition to the jet source, the presence of the aircraft was also considered in the sub-scale model. During a static burn, the interaction between the wingtip vortices, formed normally as a result of the wing-generated lift, and the exhaust jet would be negligible. The wingtip vortices in this case would be generated by the ambient wind. Furthermore, the influence of the wake behind the streamlined aircraft body, as a result of the ambient wind, on the development of the high-momentum exhaust jet was also considered small. Therefore, a geometrically scaled model of the aircraft was not included in the 8'×4' ABLWT wind tunnel tests. For the proposed model of a single stationary source, the following key parameters were considered:

- Jet momentum
- Jet buoyancy
- Nozzle position with respect to the baffles
- Nozzle ground clearance

The jet momentum and buoyancy are modelled in terms of the exit jet velocity and density respectively. As discussed previously in Chapter 3.3, the high exhaust jet temperature at full scale is modelled with a less dense gas in the wind tunnel. While the starting position of the aircraft engines for each sortie and their ground clearance are known, only limited information on the full-scale exhaust jet characteristics was recorded during the BAe 146-301 field trials. The method of obtaining the mean flow characteristics of the full-scale jet is described in the following section.

6.1.1 Full-scale mixed jet parameters

The wind tunnel investigation focused on modelling the exhaust jet during the static burn, performed by the BAe 146-301 at the start of each sortie. The aircraft's Flight Data Recorder (FDR) provided only information on the engines' fuel flow rates

in addition to the known maximum thrust of each engine at full power, i.e. 31 kN (see *Table 8.1* in Chapter 8.2). Therefore, the necessary full-scale flow parameters, such as jet exit speed and temperature, were calculated analytically and were then used to model the jet momentum and buoyancy respectively.

A suitable analytical method is to calculate the full-scale exit jet parameters from an energy balance across a control volume in the near field of a single engine (see *Figure 6.1*). The control volume is taken between two imaginary vertical planes '1' and '2', where freestream (denoted with subscript '∞') and fully-mixed jet conditions (denoted with subscript '*j*') are present, respectively. It should be noted that the subscript '*j*' is also used to describe the sub-scale jet characteristics at the nozzle exit, as in the model they are representative for the mixed jet conditions at full scale. This analytical method assumes that the speed and the temperature of the single jet are the same as those of the mixed jet of all four engines. More importantly, it assumes that the bypass and core flows are fully mixed at '2'. This was discussed in Chapter 3.3 as a reasonable assumption on the basis of recent examples of enhanced mixing through the application of mixing devices.

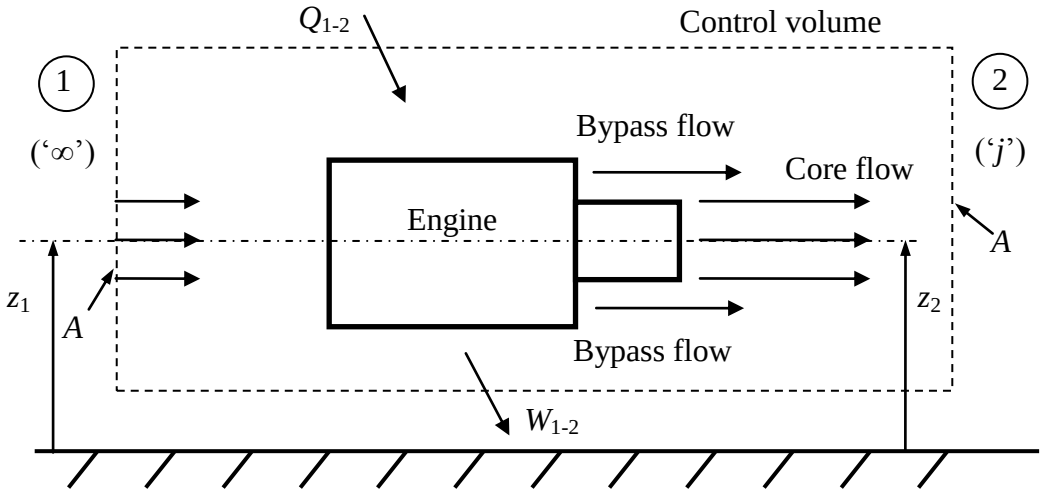

Figure 6.1: Schematic illustration of the control volume principle over an engine, used to estimate the fully-mixed exhaust jet properties

The energy balance across the control volume is taken using the Steady Flow Energy Equation (SFEE). Apart from the fully-mixed core and bypass flows at '2', the following assumptions are made:

1) The jet is assumed to obey the Ideal Gas Law.

2) The jet static pressure at '2' is equal to the ambient static pressure ($p_j = p_\infty$).

3) The jet specific heat capacity at constant pressure $c_p \approx 1005$ J/(kgK) is assumed to be constant, i.e. independent of the jet temperature.

Across the control volume between '1' and '2', the SFEE can be written in the form

$$Q_{1-2} - W_{1-2} = \dot{m}_{air}\left[h_2 - h_1 + \frac{U_2{}^2 - U_1{}^2}{2} + g(z_2 - z_1)\right]$$

Equation 6.1

where $Q_{1\text{-}2}$ is the rate of energy transferred to the system as heat, $W_{1\text{-}2}$ is the rate of work done by the system, $\dot{m}_{air}$ is the total air mass flow rate through the fan, h is the specific enthalpy, U is the flow velocity and z is the vertical coordinate. In *Equation 6.1*, the fuel mass flow rate $\dot{m}_f$ is neglected since it is considered small compared to $\dot{m}_{air}$. The nominal values of $\dot{m}_{air}$ and $\dot{m}_f$ for a single BAe 146-301 engine, operating at maximum thrust, are 87 kg/s (taken from IHS, 2011) and 0.378 kg/s (average value, recorded by the FDR) respectively, see *Table 8.1*.

Equation 6.1 can be simplified further with $z_1 = z_2$ (no movement in vertical direction, this no change in potential energy), $W_{1\text{-}2} = 0$ (no work done by the jet on the environment), and the following expressions for the specific enthalpy and the rate of transferred energy:

$$h_2 - h_1 = c_p(T_2 - T_1)$$

Equation 6.2

$$Q_{1-2} = \dot{m}_f LCV$$

Equation 6.3

where *LCV* is the Lower Calorific Value of the Jet A-1 fuel, equal to nominally 43 MJ.

The mixed jet velocity U_2 can be calculated from the following Thrust Equation, obtained from a momentum balance over the control volume:

$$F_t = U_2(\dot{m}_{air} + \dot{m}_f) - U_1\dot{m}_{air} + (p_2 - p_1)A$$

Equation 6.4

where p_1 and p_2 are the ambient static pressure p_∞ and the static pressure of the fully-mixed jet p_j respectively, and A is the control volume area at both '1' and '2'. During the static burn, the velocity U_1 upstream of the engine can be assumed zero, thus for an ideal expansion ($p_\infty = p_j$), *Equation 6.4* is simplified to

$$F_t = U_j(\dot{m}_{air} + \dot{m}_f)$$

Equation 6.5

where the subscript '*j*' is used to describe the fully-mixed jet characteristics. With a take-off thrust F_t = 31 kN and a total mass flow rate of 87.378 kg/s, U_j is estimated to be 356 m/s.

Using *Equation 6.2*, *Equation 6.3* and *Equation 6.5*, and solving for the mixed jet temperature T_j, the SFEE becomes

$$T_j = T_\infty - \frac{\dot{m}_f LCV}{\dot{m}_{air} c_p} - \frac{1}{2c_p}\left(\frac{F_t}{\dot{m}_{air} + \dot{m}_f}\right)^2$$

Equation 6.6

The exhaust jet density is then calculated from the Ideal Gas Law

$$\rho_j = \frac{p_\infty}{RT_j}$$

Equation 6.7

where R is the specific gas constant for dry air R, equal to 287 J/(kgK). The choice of R is an assumption dictated primary from the unknown exact composition of gases in the exhaust jet and the high bypass ratio of the ALF502R-5 engines.

With estimated ambient temperature T_∞ = 288 K and barometric pressure p_∞ = 1016 hPa, the full-scale jet temperature T_j and density ρ_j is calculated as 411 K and 0.861 kg/m^3 respectively. Thus, with the necessary values for the mixed jet speed, temperature and density at full scale, a sub-scale model of the jet, exiting from a stationary nozzle, can now be created.

6.1.2 Sub-scale jet parameters

As discussed in Chapter 2.6.1, the most important scaling parameters for a buoyant plume in ambient wind are the Froude number *Fr* (see *Equation 1.3*), the Richardson number *Ri* (see *Equation 2.9*) and the ratio of ambient wind to jet exit speed U_∞ / U_j. Since the Froude and Richardson numbers are related by $Ri = 1 / Fr^2$, an equality at full scale and sub scale of one of *Fr* or *Ri* would mean equality of the other as well. Therefore, the calculations in the sub-scale model are done on the basis of the

equality of U_∞ / U_j and the jet Froude number Fr_j, defined in *Equation 6.8*, where d is the nozzle diameter. This method of sub-scale modelling has been reported by Littlebury (1981) and Garry (1989) for gas turbine exhaust plumes. It also includes an equality of the exhaust jet density ratio at full scale and sub scale, which was already addressed in Chapter 3.3.

$$Fr_j = \frac{U_j}{\sqrt{gd}}$$

Equation 6.8

Another important parameter to be considered is the jet Reynolds number Re_j (see *Equation 1.1*, where the nozzle diameter is the characteristic length scale). As highlighted in Chapter 1.5, the issue with the Reynolds number equality at full scale and sub scale is that *Re* is proportional to both the velocity and the length scale. Thus, at a reduced scale, the velocity needs to be increased proportionally, since there are no significant differences between the ambient conditions at full scale and sub scale. Such increase is not possible in the 8'×4' ABLWT experiments, neither at 1:100 nor at 1:200 scale, therefore a full Reynolds number equality cannot be achieved. In view of this issue and considering the results of the force balance measurements (see Chapter 5.2), where the drag of the array of baffles was shown to be nearly independent of Reynolds number even at local speeds of less than 5 m/s, Re_j was not used as scaling parameter in the sub-scale jet model.

With the full-scale mixed jet speed U_{jF}, temperature T_{jF} and density ρ_{jF} calculated from *Equation 6.4*, *Equation 6.6* and *Equation 6.7* respectively, the sub-scale jet parameters (denoted with subscript '*M*') are obtained by matching the jet Froude number and the ratio of ambient wind speed and jet exit speed at full scale and model. With $\lambda = l_M / l_F$ defined as the scaling of the wind tunnel experiment, where l is a characteristic length, the following relationships for the sub-scale jet speed and wind tunnel speed are obtained:

$$U_{jM} = U_{jF}\lambda^{0.5}$$

Equation 6.9

$$U_{\infty M} = U_{\infty F}\lambda^{0.5}$$

Equation 6.10

It should be noted that, during the wind tunnel tests, only the volumetric flow rate was measured. Therefore, U_{jM} is the average speed of a jet exiting with a volumetric flow rate Q_{jM} from a nozzle of diameter d. It is calculated from

$$Q_{jM} = U_{jM} A_M$$

Equation 6.11

where A_M is the nozzle area, equal to $\pi(0.5d)^2$.

The necessary sub-scale volumetric flow rate Q_{jM}, representing the BAe 146-301 exhaust jet, is scaled from the total full-scale mass flow rate of all four engines $\dot{m}_F$, using the Continuity Equation as follows:

$$\dot{m}_F = \rho_{jF} U_{jF} A_M \lambda^{-2}$$

Equation 6.12

Substituting *Equation 6.9* and *Equation 6.11* in *Equation 6.12*, yields the following relationship for the subscale volumetric flow rate:

$$Q_{jM} = \frac{\dot{m}_F}{\rho_{jF}} \lambda^{2.5}$$

Equation 6.13

Finally, the required nozzle diameter is calculated from *Equation 6.11*:

$$d = \sqrt{\frac{4Q_{jM}}{\pi U_{jM}}}$$

Equation 6.14

The values, obtained from the above calculation sequence for a jet model in 1:100 and 1:200 scale, are presented in *Table 6.1* in the following section together with the results of the jet buoyancy modelling calculations.

6.1.3 Jet buoyancy modelling

The general method of modelling the high exhaust temperature of the full-scale jet was outlined in detail in Chapter 3.3. This section presents the additional calculations needed in order to account for the presence of methane (tracer gas) in the exhaust jet during the FID experiments. A mixture gas of 98% nitrogen and 2% methane was combined with a less dense gas (helium) to form a sub-scale jet of nominally ambient temperature and density lower than the ambient air density in order to match the ratio of

jet and ambient density at full scale and model (see *Equation 3.2*). Under the assumptions stated in Chapter 3.3, the sub-scale ratio of jet density ρ_{jM} to ambient air density $\rho_{\infty M}$ equals the ratio of the jet molar mass M_{jM} and ambient air molar mass M_{air} = 28.97 g/mol (see *Equation 3.8*). For a mole fraction of helium f in the sub-scale exhaust jet, M_{jM} is expressed as

$$M_{jM} = M_{He} f + M_{N-Me}(1-f)$$

Equation 6.15

where M_{He} = 4 g/mol and $M_{N\text{-}Me}$ = 27.77 g/mol are the molar masses of helium and the mixture gas of 98% nitrogen and 2% methane respectively. Analogous to *Equation 3.11*, the mole fraction of helium is then given by

$$f = \frac{1-(M_{air}/M_{N-Me})(\rho_j/\rho_\infty)_M}{1-(M_{He}/M_{N-Me})} = \frac{1-(M_{air}/M_{N-Me})(T_\infty/T_j)_F}{1-(M_{He}/M_{N-Me})}$$

Equation 6.16

The results of the above presented methods for estimating the parameters of the modelled exhaust jet are shown in *Table 6.1* for scaling of 1:100 and 1:200, considered for the 8'×4' ABLWT tests. The cases 'Sortie 9'to 'Sortie 12' refer to the four take-off runs perfomed during the field trials. The corresponding measured full-scale ambient wind speed values, given in *Table 8.3* in Chapter 8.5, are scaled with *Equation 6.10*.

Table 6.1: Summary of the calculated sub-scale jet parameters in 1:100 and 1:200 scale

Sub-scale jet parameter		λ = 1:100	λ = 1:200
U_{jM}		35.6 m/s	25.2 m/s
$U_{\infty M}$	Sortie 9	0.71 m/s	0.50 m/s
	Sortie 10	0.54 m/s	0.38 m/s
	Sortie 11	0.70 m/s	0.49 m/s
	Sortie 12	0.72 m/s	0.51 m/s
Q_{jM}		243.5 l/min	43.0 l/min
d		12.0 mm	6.0 mm
f		0.314	0.314
Q_{HeM}		76.4 l/min	13.5 l/min
ρ_{jM}		0.848 kg/m^3 *	0.848 kg/m^3 *
$\dot{m}_{jM}$		3.440 g/s *	0.608 g/s *

* Calculated for typical wind tunnel ambient conditions: $T_\infty \approx 290$ K, $p_\infty \approx 1000$ hPa

It is evident that 1:100 scale would require almost six times the amount of helium, nitrogen and methane compared to 1:200 scale. At the same time, at 1:200 scale the wind tunnel speed $U_{\infty M}$ would be at the very low range of the vane anemometer available. The advantages and disadvantages are further discussed in Chapter 6.3.

6.1.4 Moving jet source

For the subscale representation of the take-off run, a moving jet source was considered in the ABLWT experiments. The issues and aspects of such arrangement are briefly addressed here.

The main parameter to be scaled would be the linear acceleration of the nozzle from the starting position away from the baffle array. Using Froude number equality, analogous to the proposed scaling for the UAV turbine field trials in Chapter 8.8, the sub-scale acceleration would equal the full-scale acceleration of 3.1 m/s^2 of the BAe 146-301 (see calculations in Appendix I). In the opinion of the author, such acceleration at scaling λ of 1:100 and 1:200 would be too large to capture the effect of the moving source on the plume due to the significant difference in the relative movement between the source and the exhaust jet at full scale and sub scale (at sub scale the exit jet velocity is reduced by a factor of $\lambda^{0.5}$). Therefore, the tests could be executed at a considerably reduced acceleration. The main difficulties in preparing and executing the experiments with regard to the 8'×4' ABLWT working section arrangement and the measurement equipment used would be:

- the space needed for the acceleration run
- the additional equipment needed to move the nozzle
- the required instantaneous measurements to capture the starting plume.

First, the 2.4 m long working section of the wind tunnel does not allow for a sufficient distance on the floor to accelerate the nozzle. Upstream of the working section, the floor of the development section is covered with LEGO® boards and small blocks, as described in the ABL modelling arrangement in Chapter 6.2, which would not allow movement of the nozzle on the floor. For example, with an acceleration of 3.1 m/s^2, the distances travelled by an initially stationary nozzle would be 1.55 m, 6.20 m and 13.95 m after travel times of 1 s, 2 s and 3 s respectively. If the acceleration is reduced to 1 m/s^2, the distances would be 0.5 m, 2.0 m and 4.5 m for the same travel times respectively. Furthermore, as the field trials took place in cross-flow conditions, i.e. the ambient wind direction was at an angle relative to the exhaust jet direction, the baffle array and nozzle had to be rotated relative to the longitudinal direction of the working section (see *Figure 7.1* in Chapter **Error! Reference source not found.**), which is the

direction of the ambient (wind tunnel) flow. Therefore, the available distance for nozzle acceleration is significantly reduced and cannot be extended to the development section due to the angled Runway 21 centre line relative to the wind tunnel longitudinal direction and the presence of the wind tunnel side walls.

If a moving nozzle arrangement is to be implemented, another issue would be the equipment needed to achieve the necessary acceleration. In all static tests, the exhaust gas was fed to the nozzle via tubing through the working section floor, which would not be possible for a moving nozzle. Therefore, the tubing would need to be located inside the working section, for which care should be taken in order to minimise the tubing wake and its influence on the flow field downstream. The movement of the nozzle could be provided by a small support structure on wheels, mounted on rails and powered by an electrical motor. In all cases, attempts should be made to reduce the wake created by any additional equipment used. Alternatively, the starting plume could be simulated by stopping the nozzle flow with an additional valve, built in the tubing. Such arrangement would be simpler compared to the moving nozzle and would avoid the interference with the flow as a result of the additional equipment placed in the working section. However, it would be more complex in terms of execution and timing during the experiments as the operation of the valve has to be coordinated carefully with the measurements.

Finally, capturing the starting plume would require instantaneous, time-dependent measurements to be taken during the experiments. With regard to the available FID measurement equipment and the occurring lag in the concentration measurements, addressed in more detail in Chapter 7.1.2, this is the most important issue to be considered. The lag, i.e. delay in the response of the detector, is mainly due to the long tubing connecting the probe in the working section and the detector. The location of the detector outside of the control room is a key issue and needs to be reconsidered in order to shorten the tubing and the time response. Another important issue with regard to taking instantaneous measurements is the slow oscillation of the measured concentration values with time. This was thought to be mainly due to the high turbulence in the boundary layer close to the working section floor where the measurements were taken.

6.2 ABL model

The method of calculating the mean velocity and turbulence intensity profiles of the Atmospheric Boundary Layer (ABL), as given by ESDU (1982) and ESDU (1983), was outlined in Chapter 3.4. The results of the ESDU calculations are presented here

together with the experimental arrangement of the 8'×4' ABLWT development section and the measured profiles in the working section.

First, the type of boundary layer over the particular terrain of interest needs to be determined. In the method by ESDU, this is defined with the roughness length z_0. An overview of the types of terrain and the corresponding roughness lengths is given in *Figure F.1* in Appendix F, reproduced from ESDU (1982). For Cranfield Airport, a roughness length of $z_0 = 0.03$ m was chosen, characteristic for airport runways and level countryside with low vegetation. Approximate values for the zero-surface displacement z_d are also given in *Figure F.1*. However, z_d is strongly dependent on the density of the obstacles present and their orientation relative to the wind direction. It is usually considered in modelling of terrain where the presence of obstacles causes a significant portion of the flow close to the ground to be unresolved, such as areas of dense vegetation, forests and urban areas. In areas of low vegetation, the general obstruction height is very low and therefore z_d is close to zero. *Figure F.1* does not specify exact values of z_d for such cases, stating that it varies between 0 and 2. Based on the above considerations, the zero-surface displacement is neglected in the calculations, therefore

$$z' = z$$

Equation 6.17

Following this assumption, all heights considered in the ESDU method are taken from the ground and the index z' is replaced by z in further notation used.

The Coriolis parameter f_c, needed for the ESDU turbulence intensity calculations, is obtained from Cranfield Airport's latitude of $\varphi = 52.07^{o}$ and the Earth's angular velocity $\omega \approx 7.29\times10^{-5}$ rad/s:

$$f_c = 2\omega\sin(\varphi) = 1.15\times10^{-5} \text{ rad/s}$$

Equation 6.18

With z_0 and f_c, the mean velocity U_z and turbulence intensity I_u were calculated from *Equation 3.18*, *Equation 3.22* and *Equation 3.23*. The friction velocity u^* was determined graphically by plotting *Equation 3.16* (see *Figure F.2* in Appendix F). The results are included in *Table F.1* and *Table F.2* in Appendix F for 1:100 scale and 1:200 scale respectively. In order to obtain the profiles of U_z and I_u with height, the array of vertical points, used in the boundary layer measurements in the 8'×4' ABLWT working section, was taken. The experimental arrangement and the performed measurements are described below.

The 15 m long development section of the 8'×4' ABLWT is arranged using a standard ABL modelling method (*Figure 6.2*), similar to the one described by Cook (1978) and to the method used in the initial experiments. The main difference is the use of considerably smaller roughness elements to allow for finer adjustments of the boundary layer profile. At the start of the section, a hardware configuration consisting of a turbulence grid, a 190 mm high castellated barrier and four elliptic vortex generators, arranged symmetrically along the wind tunnel depth, is used (see *Figure 6.2a* and *Figure 6.2c*, right). After a short distance downstream of the elliptic vortex generators where the floor surface was smooth, the remainder of the development section floor was covered by LEGO® boards with rows of roughness elements (15 mm long, 30 mm wide and 10 mm high LEGO® blocks) to create the necessary long fetch of high surface roughness, over which the boundary layer is developed upstream of the working section. The roughness elements were arranged in a diamond formation, similar to the arrangement of Cook (1978), in rows of seventeen and eighteen LEGO® blocks with a lateral spacing of 127 mm and a longitudinal spacing of 400 mm between each row (*Figure 6.2b* and *Figure 6.2c*, left). It should be noted that the arrangement of the roughness elements was based mainly on previous experience and results of past experiments conducted in the 8'×4' ABLWT. Adjustments were made to the type of turbulence grid and castellated barrier position in order to obtain the best possible match of the mean velocity and turbulence intensity profiles with the ESDU calculations.

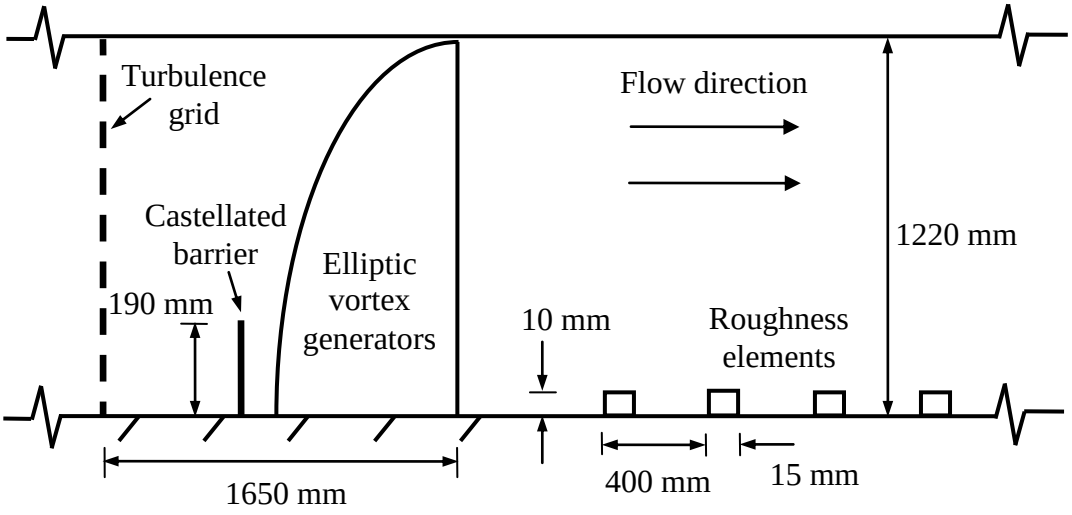

(a)

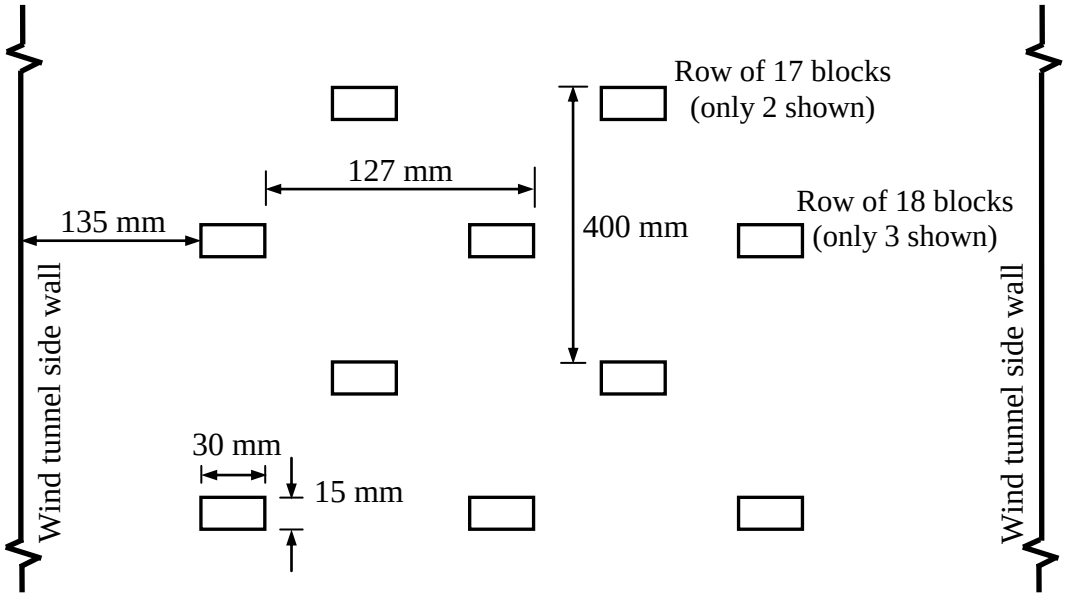

(b)

(c)

Figure 6.2: Arrangement of the 8'×4' ABLWT development section for tests with modelled Atmospheric Boundary Layer (not to scale): (a) schematic of the start of the development section (side view), (b) schematic of the roughness elements arrangement (top view), (c) images of the development section just upstream of the working section (left) and of the elliptic vortex generators and castellated barrier upstream of the LEGO® boards, in green, without roughness elements (right)

The boundary layer measurements were performed at the centre of the empty working section with a single-sensor hot-wire probe recording the mean velocity and the longitudinal component of turbulence. An array of forty vertical points above the working section floor was chosen in order to obtain sufficient data for the U_z and I_u profiles up to a height of 500 mm (see z_M column of *Table F.1* and *Table F.2* in

Appendix F). The height intervals between the points were increased gradually as the height increased. The measurements were performed with a freestream speed of approximately 2 m/s, which is greater compared to the freestream speed (i.e. < 1 m/s) during the planned experiments replicating the field trials. The speed of 2 m/s was chosen in order to reduce the scatter in the recorded data.

The measured vertical profiles of mean velocity, expressed as the ratio of local velocity U_z to the velocity U_{10} at a reference height of 10 m at full scale, and longitudinal turbulence intensity I_u in the working section are compared in *Figure 6.3a* and *Figure 6.3b* to profiles calculated with the ESDU methods at 1:100 and 1:200 scale respectively. In both cases the velocity profile is well matched up to 50 m above the ground, except very close to the ground (below 5 m). At 1:200 scale, the velocity profile gives a slightly better match with the experimental data.

The measured turbulence intensity values close to the ground in both cases are considerably lower than the calculated ones. While at 1:200 scale the difference is smaller and there is a good match at heights between 30 and 50 m at full scale, no match is evident between the measured profile and the calculated one at 1:100 scale.

Overall, there is a considerable scatter in the data due to the low wind tunnel speed, however, the U_z / U_{10} and I_u profiles are clearly identified and seem to follow the shape of the calculated ESDU profiles. The measured turbulence intensity profile gives a significantly better match at 1:200 scale. At this scale, above heights of 50 m at full scale, the experimental data shows reduced values of U_z / U_{10} compared to the calculated profile. The opposite is true for the turbulence intensity data – the experimental values of I_u are larger compared to the calculated ones. As this only occurs at heights far from the ground-based jet and the baffles, these discrepancies were not considered of high importance. The major issue with respect to the baffles would be the considerable differences between the measured and predicted turbulence intensity values close to the ground (below 5 m at full scale where the baffles would be located). Attempts were made to increase the turbulence intensity close to the ground using different types of turbulence grids and by changing the position of the castellated barrier. The results shown in *Figure 6.3* are the best possible match achieved from all attempted configuration changes with the used development section arrangement. It was considered to be sufficiently accurate for the simulation of the field trials at sub scale.

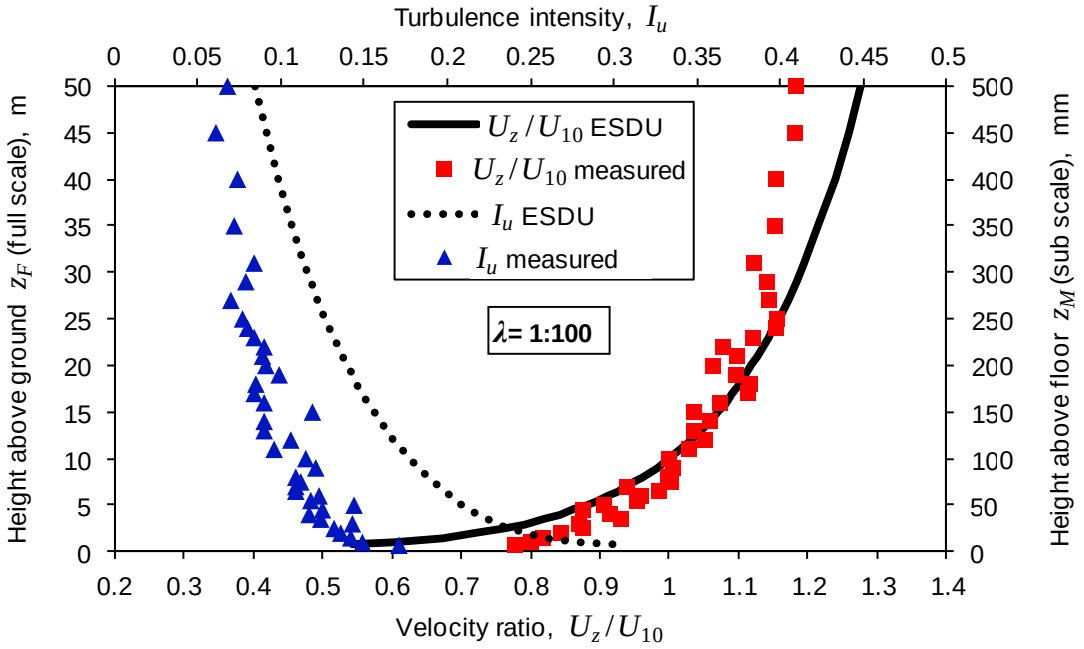

(a)

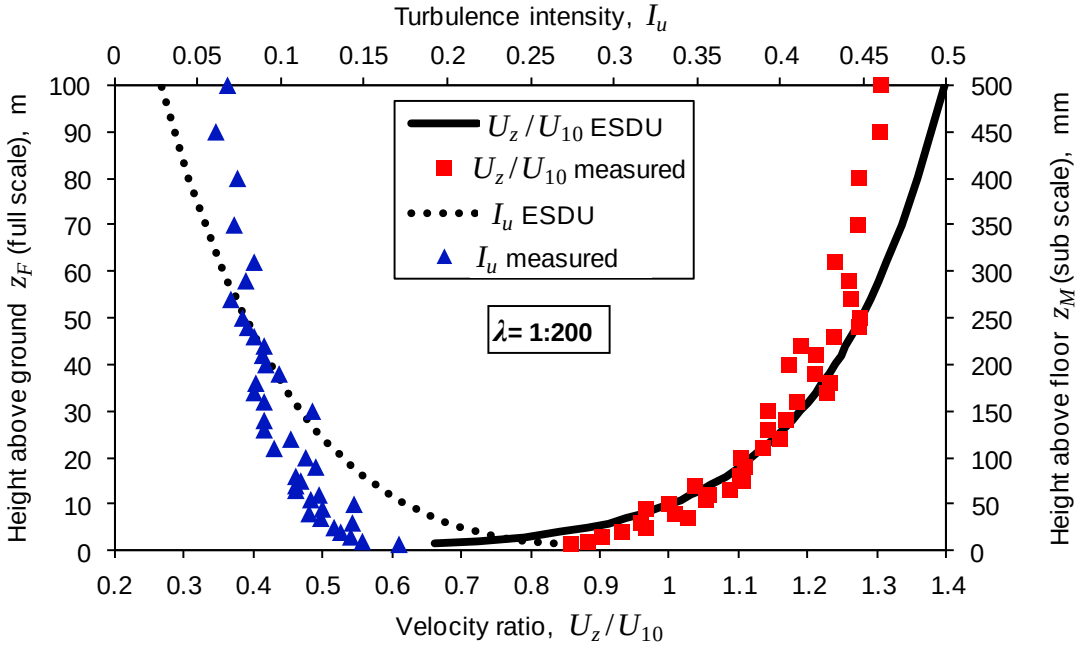

(b)

Figure 6.3: Comparison of measured mean velocity and turbulence intensity profiles in the 8'×4' ABLWT working section with the profiles calculated using the method by ESDU: (a) 1:100 scale, (b) 1:200 scale

6.3 Discussion

In this chapter were presented the modelling methods used to replicate the BAe 146-301 field trials at sub scale. The main issues were the lack of data on the full-scale exhaust jet characteristics, the choice of sub-scale jet source and the scale, i.e. 1:100 or 1:200, of the 8'×4' ABLWT experiments.

Since no data on the key full-scale exhaust jet parameters, such as speed and temperature, necessary to model the jet at sub scale, were collected during the field trials, these had to be derived from the available data on the engines' fuel flow rate and thrust. Therefore, a relatively simple analytical method was adopted, based on energy and momentum balance across an imaginary control volume around one engine. The main assumption made is the state of fully-mixed core and bypass flow several nozzle diameters downstream of the nozzle exit, the characteristics of which correspond to the one at the nozzle exit at sub scale. This assumption was justified with examples of modern engine nozzle designs and built-in devices promoting the mixing of the core and bypass flow (see Chapter 3.3). A further simplification was used to determine the jet velocity (*Equation 6.5*) from the total flow rate and the engine thrust. Both assumptions simplify the high-bypass-ratio turbofan engine to a turbojet engine analysis without accounting for the different characteristics of the bypass and core flows. Overall, the calculation method is suitable mostly due to its simplicity and quick analytical solution. The obtained jet velocity and temperature are approximate values needed to create a sub-scale model of the jet. Their accuracy is discussed briefly below with an example of another high-bypass-ratio engine.

Generally, engine manufacturers do not provide data on the exhaust jet. However, approximate values can be obtained from data sheets published by Airbus and Boeing on their aircraft characteristics, which are used for airport and maintenance planning. For example, for a PW4000 engine, used on the A330 family and A300-600 aircraft, Airbus (2014a) specifies an exhaust temperature of 300 ºF (≈ 422 K) and a jet velocity of 682 mph (≈ 305 m/s) at take-off power. The Pratt & Witney manufactured PW4000 family of engines has a bypass ratio of 5.5 and a maximum thrust of ~250 kN, delivered at a fuel flow rate of 4.25 kg/s and an air mass flow rate through the fan of 802 kg/s. With these parameters, the velocity and temperature of the mixed exhaust jet are calculated as 310 m/s and 467 K from *Equation 6.5* and *Equation 6.6* respectively. There is a considerable difference between the calculated temperature and the one given by Airbus (2014a), however the velocity values are in good agreement. It should be noted that the PW4000 is a family of engines with variable thrust depending on the exact engine model, thus the above specified parameters are approximate values.

Attempts were made to obtain data for other high-bypass-ratio engines used on the A320 family (data sheets published in Airbus, 2014b). Contours for the IAE V2500 (bypass ratio ~ 5) and CFM56 (bypass ratio ~ 6) engine series specify maximum velocity values extending from the nozzle exit to 60 m downstream. In the opinion of the author, this does not represent the actual velocity distribution and is perhaps a conservative overestimation as the data are published to serve purposes of safe aircraft ground operation. However, the specified exhaust temperatures of 400 K and 425 K for the IAE V2500 and CFM56 respectively are similar to the calculated exhaust temperature of 411 K for the ALF502-R5 engine. Data available from Boeing's online database (Boeing, 2014), for example for high-bypass-ratio turbofan engines on the 737 and 747 families, proved unsuitable for the calculations since all jet velocity and temperature values are given for the area behind the aircraft's tail where they are below approximately 110 m/s and 60 ºC respectively.

With regard to the sub-scale jet model, the main decisions taken are the use of a stationary jet source and a single nozzle to represent the four engines of the BAe 146-301. The choice of a stationary jet source is predicated on the static burn, performed by the BAe 146-301 during the field trials prior to each take-off, and on the time-averaged Lidar results on the plume concentration. A moving source would be representative for an actual take-off run, however, it would require additional equipment and changes in the working section arrangement to allow acceleration of the nozzle away from the baffle array. Furthermore, considering the high turbulence intensity of the modelled ABL in the working section and the apparent lag in the FID equipment used, only time-averaged concentration measurements could be performed successfully at sub scale.

The decision to use a single nozzle as the sub-scale jet source is based mainly on the practical issues of positioning four separate nozzles in the 8'×4' ABLWT working section. In terms of the general jet development downstream, this choice is justified due to the tendency of the multiple jets to merge into a single jet after a relatively short distance downstream. This was shown in Chapter 2.5 by means of experimental results found in the literature. Substituting a merged jet, originally from four separate sources, with a jet of the same total mass flow rate from a single nozzle, raises the question of the choice of the nozzle's longitudinal position relative to the first row of baffles and its ground clearance in order to produce the same flow field at the array of baffles. From the experimental results presented in Chapter 2.4, the start of the wall jet region for a single nozzle jet, downstream of which the flow would become independent of the nozzle ground clearance, could be estimated to be at a distance of approximately 20 nozzle diameters. This distance is significantly smaller than the scaled distance between the BAe 146-301 and the first row of baffles during Sortie 11, i.e. when the distance was the smallest (see *Table 8.3* in Chapter 8.5). Therefore, the ground clearance was not

considered a parameter of primary importance. The position of the nozzle relative to the baffles was not investigated further due to the practical difficulties of positioning four nozzles. Ideally, the flow field downstream of the single-nozzle and four-nozzle configurations should be studied in order to determine the distance of the single nozzle to the first baffle row on the basis of the flow development.

In view of the above, the ground clearance and longitudinal position of the nozzle were scaled geometrically from the full-scale values (see *Table 7.1* in Chapter 7.1.1 for the nozzle position). The full-scale ground clearance to the centre line of the engine nozzle was measured as 2.4 m on the actual aircraft at Cranfield Airport.

For the replication of the field trials in the 8'×4' ABLWT, scaling λ of 1:100 and 1:200 was considered. Based on equality of the jet Froude number and ratio of ambient velocity to jet velocity at full scale and sub scale, the sub-scale jet velocity, nozzle diameter and flow rate were determined. With the calculated full-scale exhaust temperature, the mole fraction of helium was calculated by matching the ratio of jet and ambient density at full scale and model. The results for λ = 1:100 and λ = 1:200 were compared in *Table 6.1*. The main difference in terms of costs and practicality is the significantly larger nozzle flow rate at 1:100 scale, i.e. nearly six times larger than the one at 1:200 scale. Besides the apparent increase in costs for gas supplies such as methane, nitrogen and helium, the larger nozzle flow rate would increase significantly the amount of methane released in the environment during testing. Considering that the 8'×4' ABLWT is located in a closed hangar, the released amounts of methane would be hazardous and therefore would require regular interruptions of the tests in order to keep the methane levels in the hangar within the allowed safe limit. Such procedures would increase considerably the amount of time needed to complete the tests and add more costs due to the additional wind tunnel running time, needed during the intermissions to reduce the methane levels. Another disadvantage of performing the tests at 1:100 scale is the less accurate representation of the Atmospheric Boundary Layer, in particular the considerably lower turbulence intensity values. At the same time, at 1:100 scale both the wind tunnel (ambient wind) velocity and the exit jet velocity are greater, which would create a greater drag force by the baffle array. Thus, at this scale it would be possible to perform further force balance measurements, replicating the exact baffle arrangement without a buoyant jet (f = 0). Furthermore, the greater wind tunnel velocity (~0.6-0.7 m/s) would be easier to measure with the vane anemometer available, while at 1:200 the wind tunnel velocity (~ 0.4-0.5 m/s) would be at its very low measurement range.

Following the above considerations, a decision was taken to manufacture two sets of baffle models, in 1:100 and in 1:200 scale, which would be used in the planned force balance and FID measurements respectively.

7 ABLWT experiments

The last sub-scale experiments in the 8'×4' Atmospheric Boundary Layer Wind Tunnel (ABLWT) consisted of mean concentration and velocity measurements at 1:200 scale using Flame Ionisation Detector (FID) and Hot-Wire Anemometry (HWA) methods respectively, and additional force balance measurements at 1:100 scale. The first set of experiments replicated the exact full-scale field trials arrangement and ambient wind conditions, described in detail in Chapter 8. These were complemented with additional FID and HWA measurements performed without cross flow, i.e. the wind tunnel (ambient wind) flow was in the direction of the nozzle jet.

7.1 ABLWT measurements with cross flow

The first part of the ABLWT tests targeted the replication of the full-scale BAe 146-301 aircraft field trials at 1:200 scale. The arrangements of Sortie 10, Sortie 11 and Sortie 12 of the field trials were chosed to be replicated, as they delivered the most reliable results of all sorties performed. These are described in the following section. Throughout the chapter, the three different arrangements are referred to as ‘Sortie 10’, ‘Sortie 11’and ‘Sortie 12’ in oder to allow comparison with the corresponding full-scale cases.

7.1.1 Test arrangement

The ABLWT experiments were conducted using more accurate models of the full-scale baffles compared to the prism-shaped models of the force balance tests (Chapter 5). The main concern with the previously used ‘wedges’ was the vertical rear side (‘base’), resulting in a different base pressure compared to an inclined flat plate. The new models (see *Figure G.1a* in Appendix G) were manufactured from 0.5 mm thin solid aluminium sheets, cut and bent to create a 15 mm long foot which was glued to the floor during tests using double-sided adhesive tape. The ground clearance of the full-scale baffles (~260 mm) was not represented in the models due to practical difficulties. The dimensions and characteristics of the models at 1:200 scale, scaled down from the full-scale baffle dimensions (see *Table 8.2* in Chapter 8.3), are shown in *Table G.1* in Appendix G. It should be noted that the width of the individual baffles was not scaled directly from the full-scale individual width, i.e. 2.1 m. In order to reduce the time needed to arrange the baffle rows in the working section, the individual baffle models

were manufactured with a width of 21 mm, which was sufficiently small to follow accurately the arcs drawn on the balance plate. As the total width of rows A and C was not divisible by 21, three of the baffles of row A and one of the baffles of row C were manufactured with a width of 10.5 mm and were arranged symmetrically in the centre of each row.

The working section arrangement, shown in *Figure 7.1a*, was scaled at 1:200 from the field trials arrangement (see *Table 8.2* for the baffles arrangement and *Table 8.3* for the engine position on Runway 21). The development section was arranged as described in Chapter 6.2, giving the measured mean velocity and turbulence intensity profiles in the working section shown in *Figure 6.2b*. The nozzle and baffles were mounted on a 360º rotating turntable of 2 m diameter and were arranged symmetrically with respect to a line drawn through the centre of the turntable representing the runway centre line direction. For each sortie tested the turntable was rotated at an angle ε between the runway direction and the working section centre line, i.e. the wind tunnel (ambient wind) direction. The nozzle had an inner diameter of 6 mm and was positioned at 12 mm height to its centre and at a distance b_0 along the runway direction from a point representing the runway threshold. The nozzle was approximately 10d long in order to ensure a smooth flow at the nozzle exit after passing the corner connecting the vertical delivery pipe to the nozzle pipe. The flow was provided through a drilled hole in the turntable by means of external tubing, passing through analogue flow meters in the wind tunnel control room. The accuracy of the flow meter readings was estimated to be within 2 l/min. The delivered flow at the nozzle exit had a flow rate of 43 l/min, giving an exit jet velocity of approximate 25 m/s in accordance with the sub-scale model results at 1:200 scale (see *Table 6.1*).

The baffle models were arranged in three arc-shaped rows with radii of 180 mm, 266.5 mm and 370 mm for row A, B and C respectively, centred at a point, which represented the runway threshold. This point was chosen to be the origin of the coordinate system used with the x-axis in the nozzle jet direction along the runway line, the y-axis at right angles to the x-axis towards the Lidar location (see *Figure 7.1a*), and the z-axis in vertical direction at right angles to the working section floor. The Lidar location and azimuth lines are shown in *Figure 7.1a* to illustrate the horizontal area scanned by the Lidar during the full-scale field trials. The distance b_0 along the runway line was 285 mm (47.5d), 120 mm (20d) and 190 mm (31.7d) for Sortie 10, Sortie 11 and Sortie 12 respectively. Images of the tests replicating Sortie 10 and Sortie 12 (no baffles) are shown in *Figure 7.1b* and *Figure 7.1c* respectively.

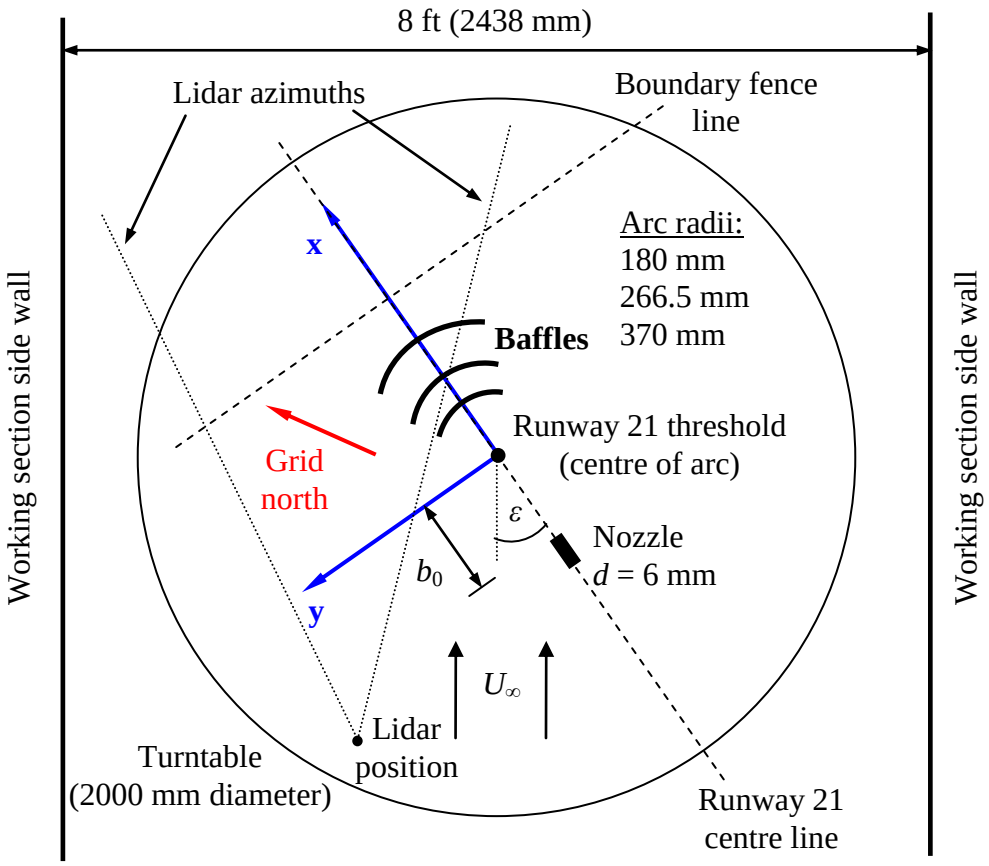

(a)

(b)

(c)

Figure 7.1: 8'×4' ABLWT working section arrangement at 1:200 scale: (a) schematic of the replication of the field trials (top view, distances and angles shown as in Sortie 10), (b) image of Sortie 10 (isometric view, flow direction is from top left); (c) image of Sortie 12 (isometric view, flow direction is from left to right)

Lidar position and azimuths are shown only to illustrate the domain scanned by the Lidar during the field trials

Three different working section arrangements were tested, representing Sortie 10, Sortie 11 and Sortie 12. The first two gave a comparison of the 'baffles up' case (baffles present) for different longitudinal positions of the jet source relative to the baffles. Sortie 12 was chosen to represent the 'baffles down' case (no baffles) over Sortie 9 because of the virtually identical mean wind speed and ambient conditions with those of Sortie 11. The arrangement for each sortie was done by keeping the nozzle at the same position in the working section and by moving the baffles and rotating the turntable. Thus, the location of the runway threshold, i.e. the coordinate system origin, also changed between the three cases. Subsequently, all x-coordinates in this chapter are given from the corresponding runway threshold position for each case. The full-scale parameters, taken from the field trials arrangement (Chapter 8.5) and the full-scale exhaust model (Chapter 6.1.1), and the corresponding wind tunnel test parameters at 1:200 scale are presented in *Table 7.1*. It should be noted that the full-scale exhaust jet temperature T_{jF} = 427 K, corresponding to the mole fraction of helium in the sub-scale jet f = 0.344, is greater than the estimated value from *Equation 6.6* of 411 K. This is because at the time of the tests the mole fraction of helium was estimated using the molar mass of air (28.97 kg/kmol), which is higher compared to the molar mass of the mixture of nitrogen and methane (27.77 kg/kmol). If the temperature 411 K is considered approximately correct, the simulated plume at 1:200 scale would have greater buoyancy compared to the full-scale one. From the Ideal Gas Law, the corresponding reduction in density of the full-scale exhaust jet is approximately 3.5 %.

Table 7.1: Full-scale and 1:200 scale test parameters for Sortie 10, Sortie 11 and Sortie 12

	Full scale			Wind tunnel		
	T_{jF} = 427 K U_{jF} = 356 m/s			f = 0.347, Q_{jM} = 43 l/min U_{jM} = 25 m/s		
	Sortie 10	Sortie 11	Sortie 12	Sortie 10	Sortie 11	Sortie 12
b_0	57 m	24 m	38 m	285 mm	120 mm	190 mm
U_∞	5.4 m/s	7.0 m/s	7.2 m/s	0.4 m/s	0.5 m/s	0.5 m/s
ε	35º	36º	31º	35º	36º	31º

7.1.2 Measurements and data post-processing

The concentration measurements were performed using the FID method and equipment described in Chapter 3.2.5. As the majority of the measurements were performed with two 3000HM hydrocarbon analysers, measuring the concentration at two spatial points at the same time, two separate probes were used. They were steel

tubes of 1 mm diameter and were mounted on a computer controlled over-head traverse system in the working section, providing precise movement in all three coordinate axes. The probes were fixed together on the traverse and were carefully aligned on the same vertical line with sufficient spacing between the orifices, i.e. 25 mm during the replication of the field trials. The orientation of the probe orifices was at right angles to the runway direction and initial jet direction. Each probe was connected to a hydrocarbon analyser through tubing passing through the ceiling of the working section. The hydrocarbon analysers were in turn connected to the computer in the control room, where all operations during testing were performed using a custom-designed *LabView* programme. The programme allowed manual input of the measured ambient temperature and barometric pressure, as well accurate time measurement of each test run from the moment of opening the valves of the containers which provided the helium and the mixture gas of nitrogen and methane.

The wind tunnel speed in the working section, U_{40}, was measured with a Schiltknecht MiniAir6 Mini vane anemometer at a reference height above the wind tunnel floor of 40 mm, representing the full-scale ambient wind measurements during the field trials, taken at a height of 8 m. Examples of data recorded during simulations of Sortie 10 and Sortie 11 are shown in *Figure G.2* in Appendix G. There is a significant scatter of the measured values as the targeted mean velocity was at the very low limit of the vane anemometer range (0.5 m/s), and even lower for Sortie 10 (0.4 m/s). However, in the latter case the mean value of 0.4 m/s could be measured at virtually the same wind tunnel power setting, provided that the ambient conditions did not vary significantly. Therefore the measurements of the vane anemometer were considered sufficiently accurate. The presence of fluctuations in the flow was further increased by the relatively high turbulent intensity of the simulated boundary layer, especially close to ground, as was shown in *Figure 6.3b*.

The concentration measurements were taken on parallel lines downstream of the nozzle, oriented at right angles to the runway direction. *Figure G.3* in Appendix G shows the generic grid of spatial points where the concentrations were measured. The longitudinal position of the lines (x coordinate) was different for each sortie, as the nozzle position relative to the coordinate system origin (b_0) was different. The lateral coordinates close to the centre line were initially selected to match the position of the micro-monitors on the boundary fence during the field trials and were later extended in order to capture the plume. In both longitudinal and lateral direction, the extent of the measurement points was limited by the movement range of the traverse. The exact coordinates for each sortie are included in *Table G.2* to *Table G.13* in Appendix G.

At full scale, the Lidar measurements were performed at elevations of 0.7º and 4.5º, for which the vertical heights were estimated from *Figure H.10* of Appendix H to

be between 6.5 m and 8 m and between 22 m and 40 m respectively. These are for the scanned area just downstream of the baffle array and the area at distances about 250 m north and 400 m east of the Lidar position respectively. At 1:200 scale, the corresponding heights are between 30 mm and 42.5 mm, and between 110 mm and 200 mm respectively. In order to create a homogenous grid of measurement points, the FID concentration measurements were performed at height levels of 25 mm, 50 mm, 75 mm and 100 mm (or 4.2*d*, 8.3*d*, 12.5*d* and 16.7*d*), differing from the elevated scanning planes of the Lidar. The heights of 25 mm and 50 mm were chosen to be just below and just above the limit heights of the 0.7º elevation scan. The heights of 50 mm and 100 mm were considered sufficient to capture a possible lift-off of the plume.

Each test consisted of starting the wind tunnel and adjusting the speed in the working section, which was followed by starting the data sampling. After a time period of 15 seconds, the gas container valves were opened and the measurements were taken. Each test was performed for approximately 80 seconds at a sampling frequency of 50 Hz to allow for sufficient data to be recorded. The calculation method is shown in *Figure 7.2* by means of an example data set for one measurement point, where the recorded data are plotted against the elapsed time from the start of the data sampling. First, a mean value of the ambient concentration was calculated from the data recorded during the first 15 seconds, which was then subtracted from all subsequently measured values. The mean concentration was obtained by taking the geometric average of the newly-calculated values for a 30 second period between the 43rd and the 73rd second. These values were selected in order to allow sufficient time for the jet to reach the probe and for the probe samples to be detected by the hydrocarbon analyser. For several data sets, the start and end time of averaging period were varied in order to study their influence on the average value obtained. The calculated maximum deviations between ±5 ppm and ±10 ppm (parts per million) were considered small with regard to the apparent fluctuations of the recorded data with time.

An alternative calculation method of obtaining the mean concentrations by numerically integrating the recorded data over the period of 30 seconds was also considered. Some results of this method indicated differences of up to only 0.5 ppm, regardless of the measured concentration values, therefore the simpler method of taking a geometric average was used.

A considerable lag in the measurements of approximately 10 seconds was observed, as shown in *Figure 7.2*, mainly due to the time needed for the probe sample to reach the hydrocarbon analyser. Further delay was created due to the movement of the flow from the containers to the nozzle and from there to the location of the probe. The fluctuations in the measurements and the lag in the tubing, connecting the probe and the hydrocarbon analyser, did not allow for instantaneous measurements of the starting

plume to be performed. At this stage, only mean concentrations could be obtained with the measurement method used.

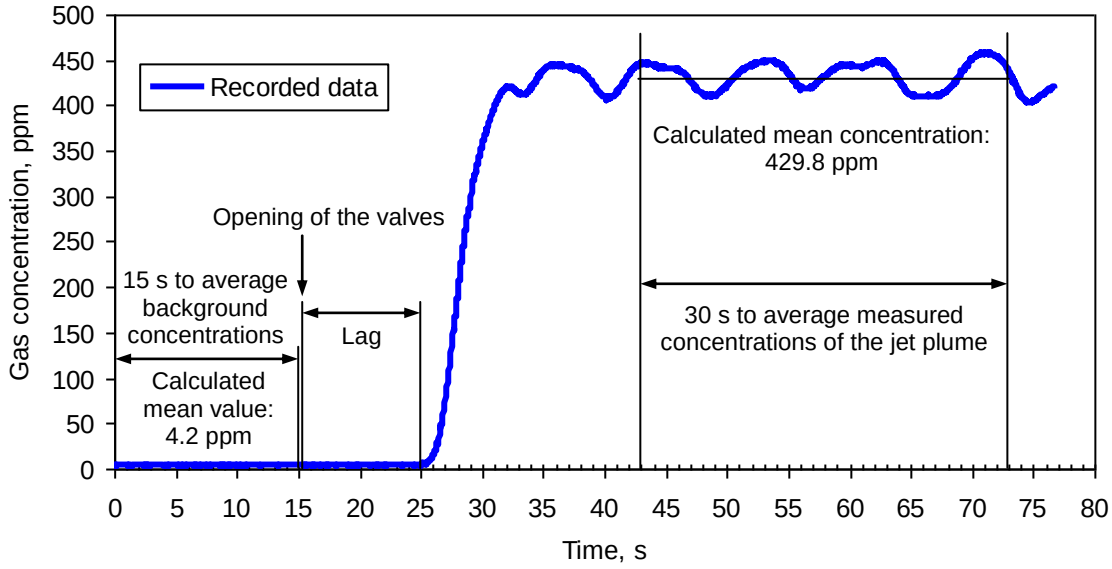

Figure 7.2: Example of data post-processing of measured concentrations for Sortie 10 (ε = 35°, b_0 = 285 mm) at a random spatial point with coordinates (605, -240, 25), in mm x-axis shows the time passed from the start of the FID measurements, y-axis shows the measured concentration in parts-per-million (recorded data)

Additional tests were performed in order to study the repeatability of the obtained results. For measured concentrations within the rage of 300 to 1100 ppm, the repeatability was within nominally 50 ppm to 70 ppm, while below 100 ppm, it was within nominally 10 ppm. Generally, the repeatability of the results can be estimated to be within 10% of the measured value.

7.1.3 Results

The obtained mean concentrations in parts per million (ppm), denoted with *c*, for the simulated static burn of Sortie 10, Sortie 11 and Sortie 12 are included in *Table G.2* to *Table G.13* in Appendix G together with the corresponding spatial coordinates. The concentrations are presented in percent of the mole fraction of methane at the nozzle, c_j, equal to 20000 ppm. The analysis of the results was done by comparing the measured concentrations at the boundary fence line (x/d = 84.2) and at lines perpendicular to the runway direction, located at equal distances from the nozzle position, $(b_0 + x)/d$, for all three sorties. Only qualitative comparisons to the full-scale Lidar measurements (see *Figure H.7* to *Figure H.9* in Appendix H) could be made, as the Lidar data was not

directly available. Furthermore, the Lidar data was measured relative to the ambient concentration, while the wind tunnel experiments were performed with a known concentration at the nozzle exit, i.e. 20000 ppm.

Comparing the measurements at the boundary fence (*Figure 7.3*), only small differences in the peak concentrations are evident at the lowest height (z/d = 4.2). The peak value for Sortie 11 ($c/cj \approx 3\%$), is greater than those of Sortie 10 and Sortie 12 (no baffles), however, the nozzle was located considerably closer to the baffle array, i.e. 27.5d and 11.7d closer compared to the nozzle position of Sortie 10 and Sortie 12 respectively. The reductions in peak concentration for Sortie 10 and Sortie 11 are significantly smaller between z/d = 4.2 and z/d = 8.3, corresponding to full-scale heights z_F of 5 m and 10 m, compared to the one of the jet without baffles (see *Figure 7.3a* and *Figure 7.3b*). Thus, a significant part of the plume is deflected upwards by the baffles and its vertical spread is increased. This is consistent with the observations during the initial flow visualisation tests with a single baffle row, presented in Chapter 4.2. In the case of Sortie 12, the plume appears to be close to the ground, as the concentrations reduce rapidly with height. Further away from the ground (*Figure 7.3c* and *Figure 7.3d*), particularly at z/d = 16.7, the concentrations are reduced considerably in the cases of Sortie 10 and Sortie 11, while in the case without baffles these are very close to zero.

Close to the runway line (y = 0), at $-10 < y/d < 10$, the concentrations are greater for Sortie 12, in particular at the lowest measurement height z/d = 4.2 (*Figure 7.3a*). The measured profile appears to be shifted towards the runway line compared to the ones of Sortie 10 and Sortie 11. This is mainly due to the stronger cross flow in the cases of Sortie 10 and Sortie 11, i.e. larger angle ε between the wind tunnel flow and the runway line, which causes the plumes to drift in negative y direction in *Figure 7.3a* and *Figure 7.3b*. The cross flow effect is stronger on the measured plume of Sortie 10, due to its lower horizontal momentum, which has decayed over a longer distance.

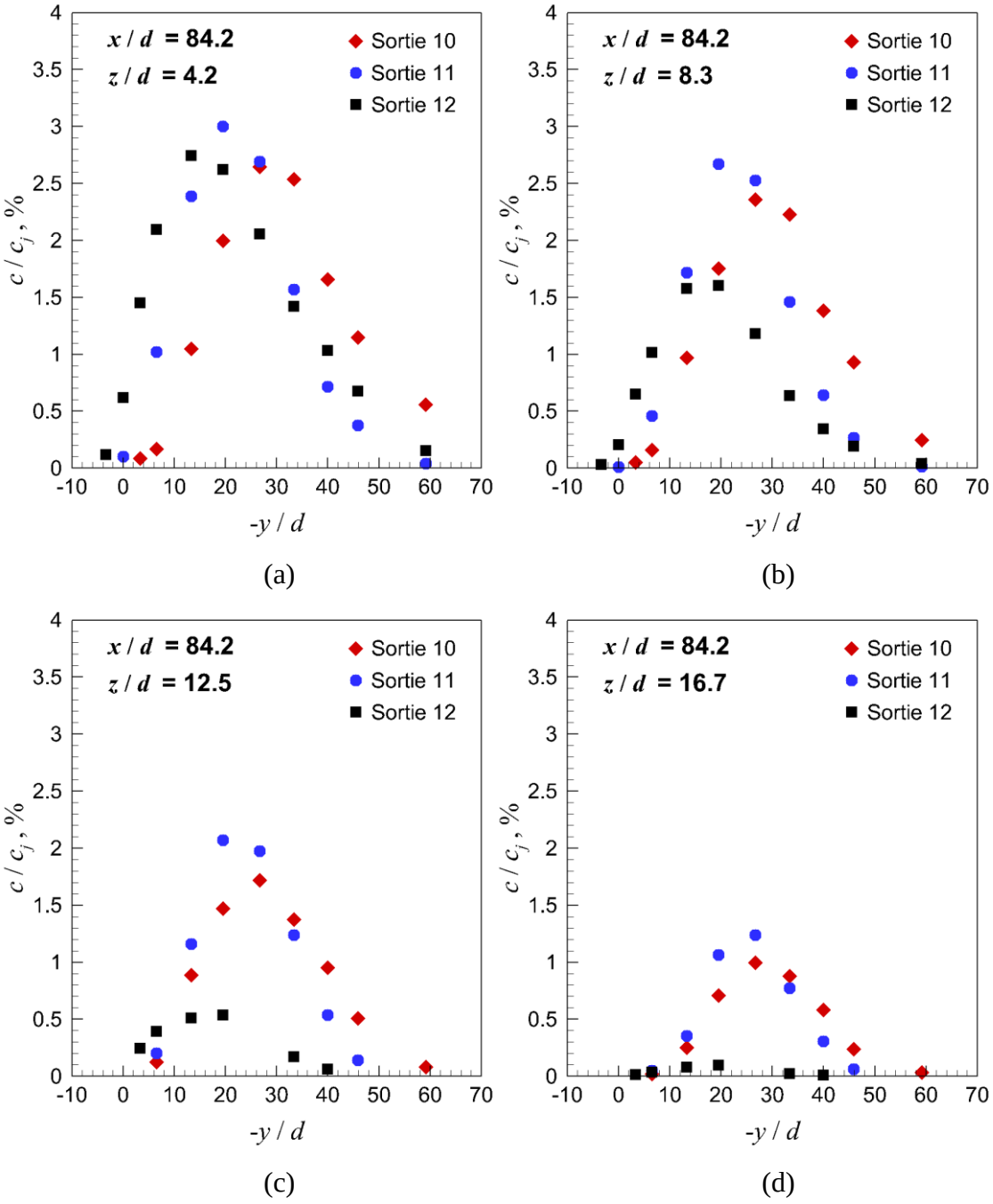

Figure 7.3: Mean plume concentrations, measured at 1:200 scale at x / d = 84.2 for Sortie 10, Sortie 11 and Sortie 12 at: (a) z / d = 4.2, (b) z / d = 8.3, (c) z / d = 12.5, (d) z / d = 16.7 x-axis shows the lateral coordinates in nozzle diameters (negative values are plotted positive), y-axis shows the measured concentrations in percentage of the mole fraction of methane at the nozzle c_j = 20000 ppm

Additional measurements at the boundary fence line were taken close to the ground at z/d = 0.4 (z_F = 0.5 m). The lateral locations chosen were those of the air

quality sensors during the field trials, shown in *Figure 8.5* in Chapter 8.4 and denoted with S1 to S6. Sensors S4, S5 and S6 were located on the windward side (relative to the ambient wind direction) of the extended Runway 21, i.e. in positive *y*-direction at sub scale, thus all concentrations were nominally zero. The measured mean concentrations at 1:200 scale at the locations of S1 to S4 are shown in *Figure 7.4*. It is evident that close to the ground the concentrations downstream of the baffles are reduced compared to the case of no baffles, thus the baffles provide a local sheltering effect within a certain distance downstream of the last row. Sortie 10 gives lower concentrations compared to Sortie 11, for which a possible explanation is the significantly closer distance of the nozzle to the baffles for Sortie 11. While at S3 the reduced concentrations can be partially caused by the drift of the plume in negative *y* direction for Sortie 10 and Sortie 11, the reduction at S2 concerns the concentration peak values and can be attributed primarily to the sheltering effect of the baffles.

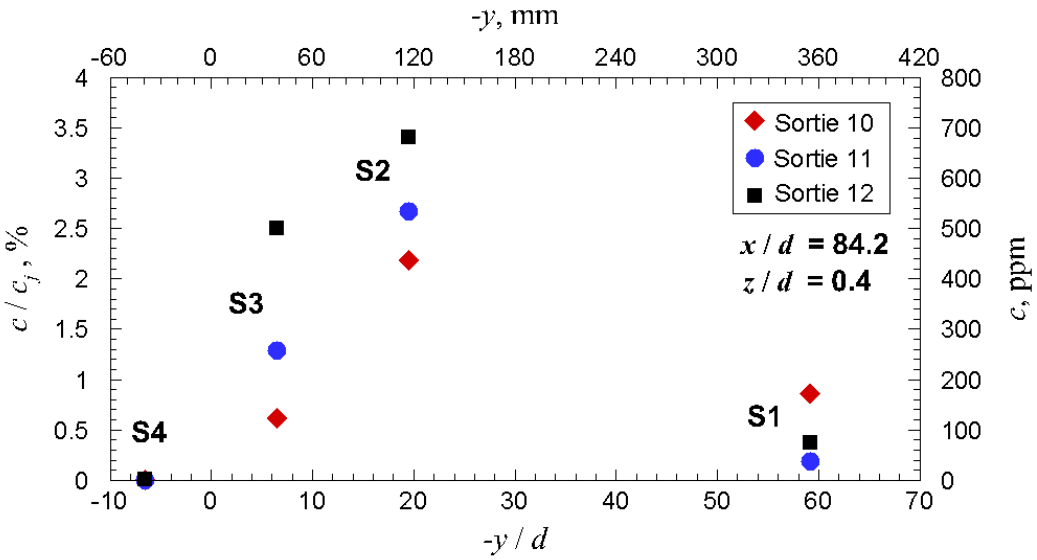

Figure 7.4: Mean plume concentrations, measured at 1:200 scale at the micro-monitor locations on the boundary fence line at 2.5 mm height (z / d = 0.4)
x-axis and y-axis as in Figure 7.3; additional axes are included, giving the measured mean concentrations in ppm and the lateral coordinates in mm; S1, S2, S3 and S4 denote the locations of the air quality sensors on the fence, shown in Figure 8.5 for the full-scale field trials

The measurements at $z/d = 0.41$ at the locations S2 and S3 are compared to the full-scale measurements of nitrogen oxide (NO) by the air quality sensors in *Table 7.2*. The full-scale NO values, taken from Bennett et al. (2013), have been obtained by integration of the summed measured values from all sensors over the time passage of the plume. A qualitative comparison shows that, at full scale, the concentrations during Sortie 10 were lower than those of Sortie 12, but higher than those of Sortie 11. The latter comparison does not agree with the measured concentrations in the wind tunnel,

where Sortie 10 gave the lowest concentrations of all three. In order to obtain a quantitative comparison of the reduction in concentration by the sheltering effect of the baffles, the measured values of Sortie 10 and Sortie 11 are given in percent reduction relative to the ones of Sortie 12. At S2, the sub-scale Sortie 11 gives a reduction of 48.5% compared to Sortie 12, which is in excellent agreement with the full-scale value of 47.8%. At S3, there is a considerable difference between the calculated percentages at full scale and sub scale (21.6%). As will be discussed later when comparing the Lidar results to the wind tunnel measurements (see Chapter 8.7), this difference is caused by the drift of the plume in negative *y*-direction away from the runway line at sub scale, which is not present in the Lidar results (*Figure H.8a* in Appendix H).

Table 7.2: Comparison of wind tunnel and full-scale concentration measurements at $z/d = 0.4$ at the boundary fence ($x/d = 84.2$)

Sortie No.	Wind tunnel, 1:200 scale			Field trials	
	Location on fence line $x/d = 84.2$ $z/d = 0.4$	Mean concentrations c [ppm]	% reduction of Sortie 12	Measured NO concentrations* [ppm]	% reduction of Sortie 12
10	S2, $-y/d = 6.5$	123.3	75.3 %	62.8	24.1 %
	S3, $-y/d = 19.5$	435.6	36.1 %		
11	S2, $-y/d = 6.5$	257.4	48.5 %	43.2	47.8 %
	S3, $-y/d = 19.5$	534.2	21.6 %		
12	S2, $-y/d = 6.5$	499.4	-	82.7	-
	S3, $-y/d = 19.5$	681.8	-		

*Values are summed over all point-sample sensors and integrated over the time passage of the plume

The variation of mean concentration with height at the boundary fence line is shown in *Figure 7.5a* and *Figure 7.5b* for the lateral positions $y/d = -6.5$ (S3) and $y/d = -19.5$ (S2) respectively. For Sortie 10 and Sortie 12 the maximum concentration is on the ground, decreasing gradually with height, while for Sortie 11 at $y/d = -19.5$ the maximum is at a height of nominally 4*d* above the ground, or an approximate height of 5 m at full scale. The location of the plume close to the ground in Sortie 12 is indicated by the considerably 'flatter' slope of the data in *Figure 7.5b*. As already discussed above, it is evident that the plume of Sortie 11 is deflected upwards and the concentrations are reduced in the region near the ground due to the sheltering effect of the baffle array. At the same time the plume of Sortie 10 appears to be deflected upwards as well due to the high concentrations away from the ground, however, the area close to the ground is not protected by the baffles as in Sortie 11. Thus, the effect of the baffles of deflecting the plume is stronger for a plume of greater momentum. This general conclusion is in agreement with the observations during the field trials, stated in

Bennett et al. (2013), of the increased efficiency of the baffles when the aircraft is located closer to the runway threshold, and is consistent with the findings of the initial exhaust jet experiments (Chapter 4).

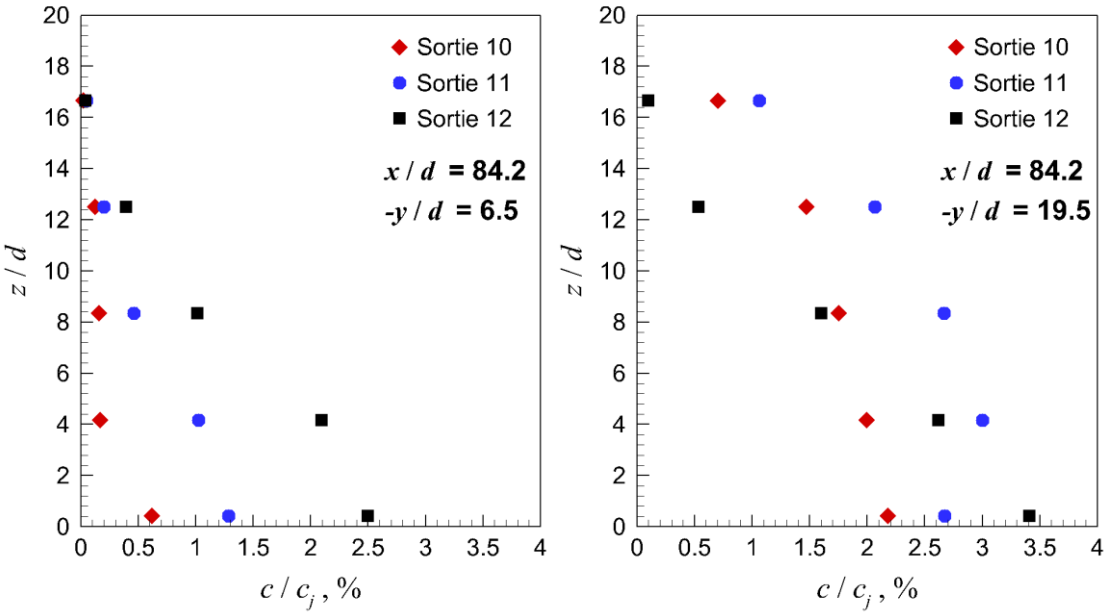

(a) (b)

Figure 7.5: Variation of mean plume concentration with height, measured at the boundary fence line (x / d = 84.2) for Sortie 10, Sortie 11 and Sortie 12: (a) -y / d = 6.5, (b) -y / d = 19.5 x-axis shows the measured concentrations in percentage of the mole fraction of methane at the nozzle c_j = 20000 ppm, y-axis shows the height from the ground in nozzle diameters

The effect of the baffles is further investigated at locations of equal distance from the nozzle, (b_0 + x). At 131.7d (*Figure 7.6a*) and 148.3d (*Figure 7.7a*), corresponding to distances from the runway threshold of 134 m and 154 m at full scale respectively, the measured concentrations of Sortie 11 at z / d = 4.2 are lower compared to the ones of Sortie 10 and Sortie 12. However, as evident from the remaining plots of *Figure 7.6* and *Figure 7.7*, the concentrations of both Sortie 10 and Sortie 11 reduce with height, thus the plume does not lift off. These results of Sortie 11 disagree with the Lidar measurements during the field trials (*Figure H.8a* in Appendix H), where downstream of the boundary fence line only small concentrations were observed between heights of approximately 6 m and 7 m (between 5d and 6d at 1:200 scale). From the differences in sub-scale mean concentrations of Sortie 11 and Sortie 12, it can be concluded that the plume dispersion during Sortie 11 is enhanced in vertical direction compared to the plain jet without baffles. Thus, there is a small positive effect of the baffles also further downstream, not just in the wake of the baffle array. In order to confirm this, further

measurements close to the ground are needed. These were done without cross flow (ε = 0°) and are described in Chapter 7.2.1.

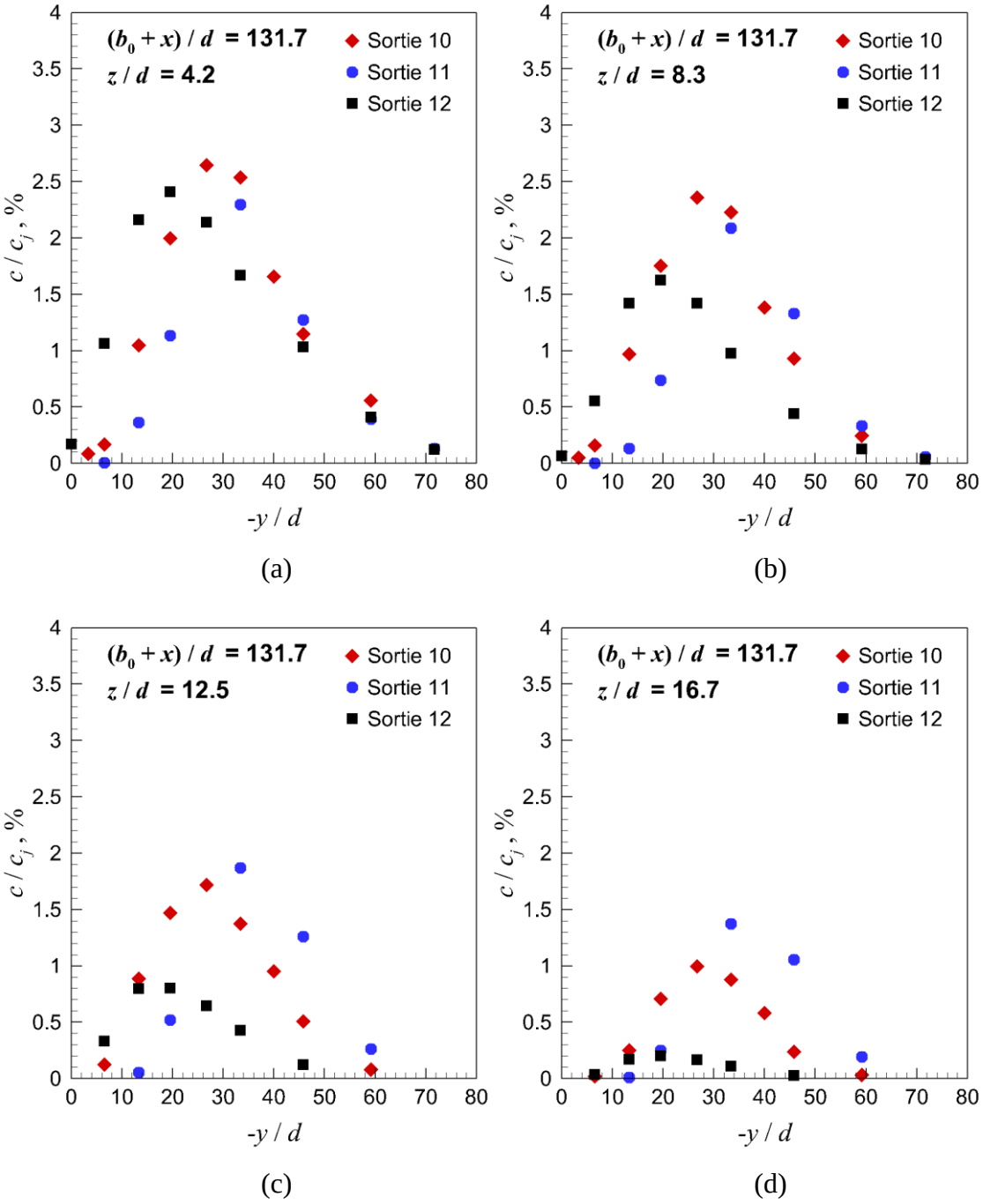

Figure 7.6: Mean plume concentrations, measured at 1:200 scale at $(b_0 + x) / d$ = 131.7 for Sortie 10, Sortie 11 and Sortie 12 at: (a) z / d = 4.2, (b) z / d = 8.3, (c) z / d = 12.5, (d) z / d = 16.7 x-axis shows the lateral coordinates in nozzle diameters (negative values are plotted positive), y-axis shows the measured concentrations in percentage of the mole fraction of methane at the nozzle c_j = 20000 ppm

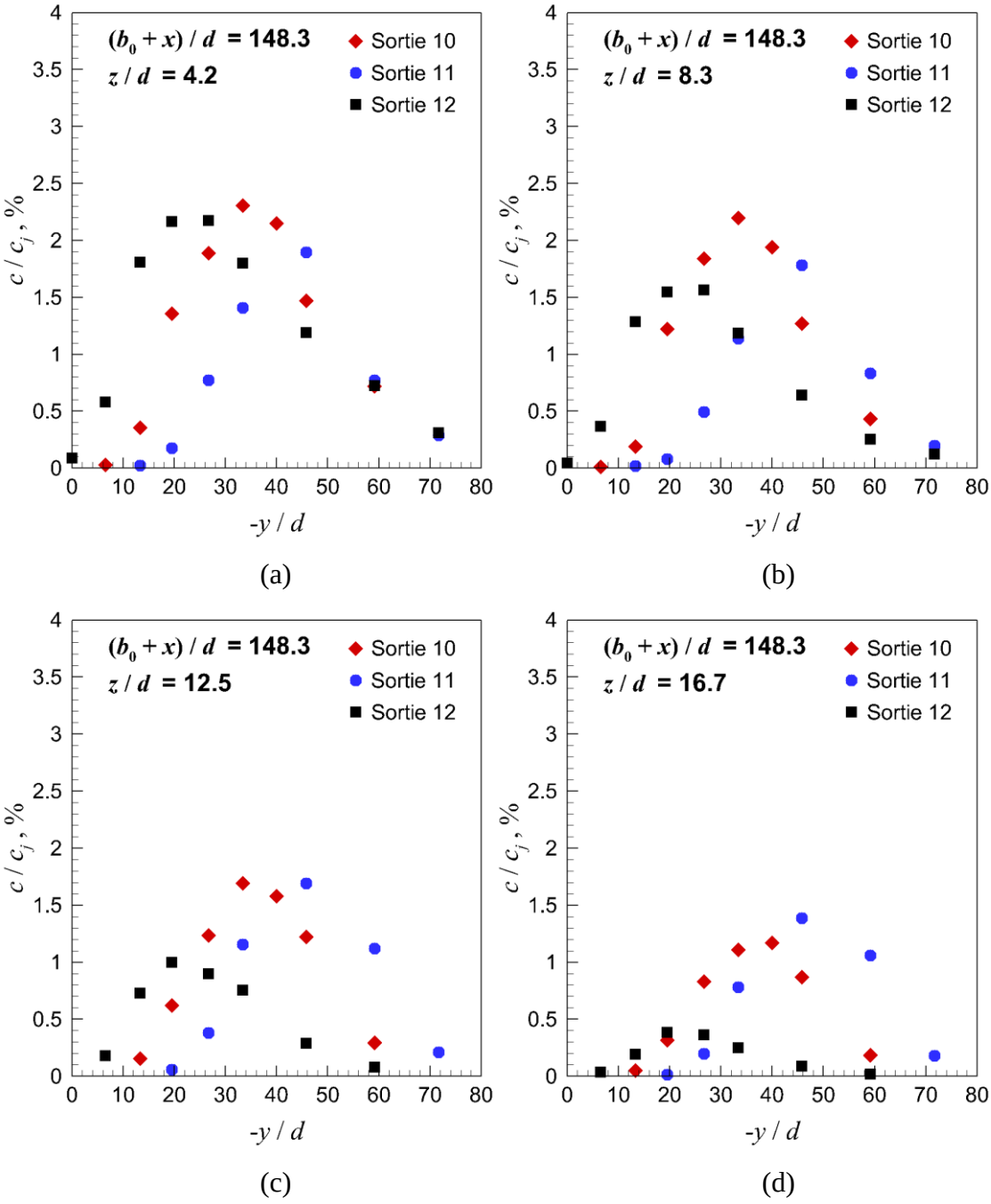

Figure 7.7: Mean plume concentrations, measured at 1:200 scale at $(b_0 + x)/d = 148.3$ for Sortie 10, Sortie 11 and Sortie 12 at: (a) $z/d = 4.2$, (b) $z/d = 8.3$, (c) $z/d = 12.5$, (d) $z/d = 16.7$; x-axis shows the lateral coordinates in nozzle diameters (negative values are plotted positive), y-axis shows the measured concentrations in percentage of the mole fraction of methane at the nozzle $c_j = 20000$ ppm

To conclude the analysis of the experiments replicating the field trials, contour plots of the measured mean concentrations were obtained, showing the plume

development behind the baffle array. In order to allow a direct comparison to the full-scale Lidar data (see *Figure H.7* to *Figure H.9* in Appendix H), the measured values of c / c_j in the ABLWT were plotted using their corresponding full-scale coordinates at heights z_F equal to 5 m, 10 m, 15 m and 20 m (see *Figure 7.8* and *Figure 7.9*). The coordinate system origin was placed at the Lidar location, shown schematically in *Figure 7.1a*, and the orientation of the Cartesian axes was so that the *x* and *y* axes were in east and grid north direction respectively. The contours of c / c_j were created in *Tecplot* using a triangulation method to interpolate between the measured data points. Due to the limited set of data points, the contours show occasional discontinuities, in particular, close to the baffles where the measured concentration values change significantly within short distances, and between the last two measurement lines located at a considerable distance from each other (see *Figure G.3* and *Table G.2* to *Table G.13* in Appendix G for the sub-scale coordinates).

The obtained contours show the effect of the baffles within the complete measurement domain. The observed reductions in mean concentrations of Sortie 11 compared to the ones of Sortie 12 at z_F = 5 m (see *Figure 7.6a* and *Figure 7.7a*) are difficult to be identified with the contour scaling used in *Figure 7.8*, as their magnitude is relatively small. Furthermore, they were shown only when using longitudinal coordinates relative to the nozzle exit position. At the same time, the effect of deflecting the plume upwards and the influence of the nozzle position relative to the baffles on this effect are clearly visible in *Figure 7.9* for z_F = 15 m and z_F = 20 m. *Figure 7.8* and *Figure 7.9* are further compared to the Lidar data in Chapter 8.7 discussing possible correlations and differences in the plume development in sub scale and full scale.

In conclusion, the sub-scale measurements of the plume have shown that the baffles have the effect of deflecting the plume upwards and increasing the concentrations away from the ground. In close proximity downstream of the baffle array, at the boundary fence, the concentrations are reduced due to the sheltering effect and the deflected plume upwards. The maximum concentration at the fence was not on the ground in the case of Sortie 11. Comparing the results for all three sorties at equal distances from the nozzle, Sortie 11 gives a small reduction in the mean peak concentrations, measured at the lowest height from the ground, i.e. z / d = 4.2. With regard to the results of Sortie 10 and Sortie 11, the dispersing effect of the baffles appears to be enhanced if the jet source is located closer to the baffle array. However, the plume was not observed to lift off within the distances tested, as the mean concentrations reduced with increasing height. The obtained results show no trend that a lift-off of the plume may occur further downstream of the distances tested.

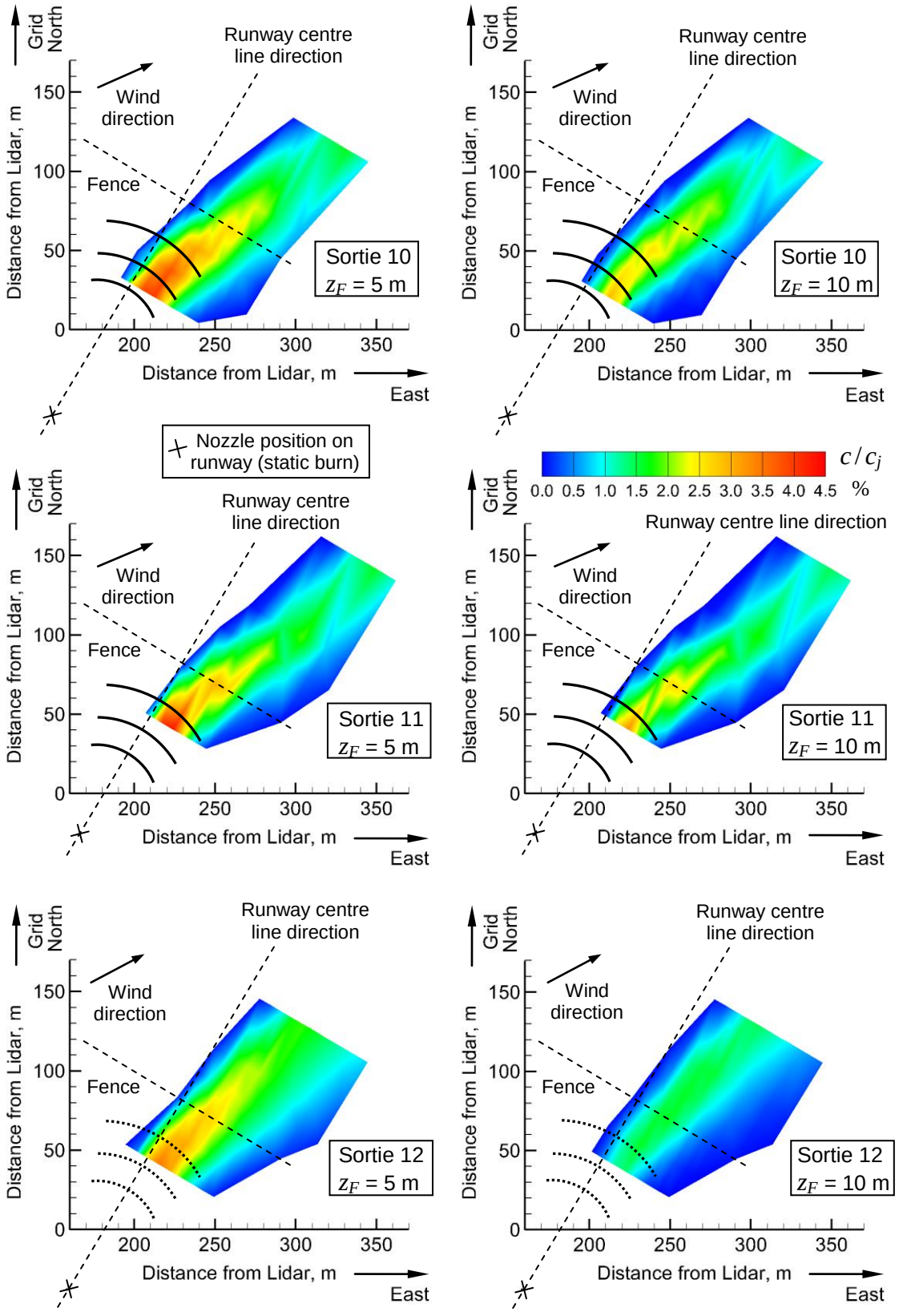

Figure 7.8: Contours of mean concentrations, measured at 1:200 scale at z/d = 4.2 and z/d = 8.3 and plotted in full-scale coordinates (z_F = 5 m and z_F = 10 m)

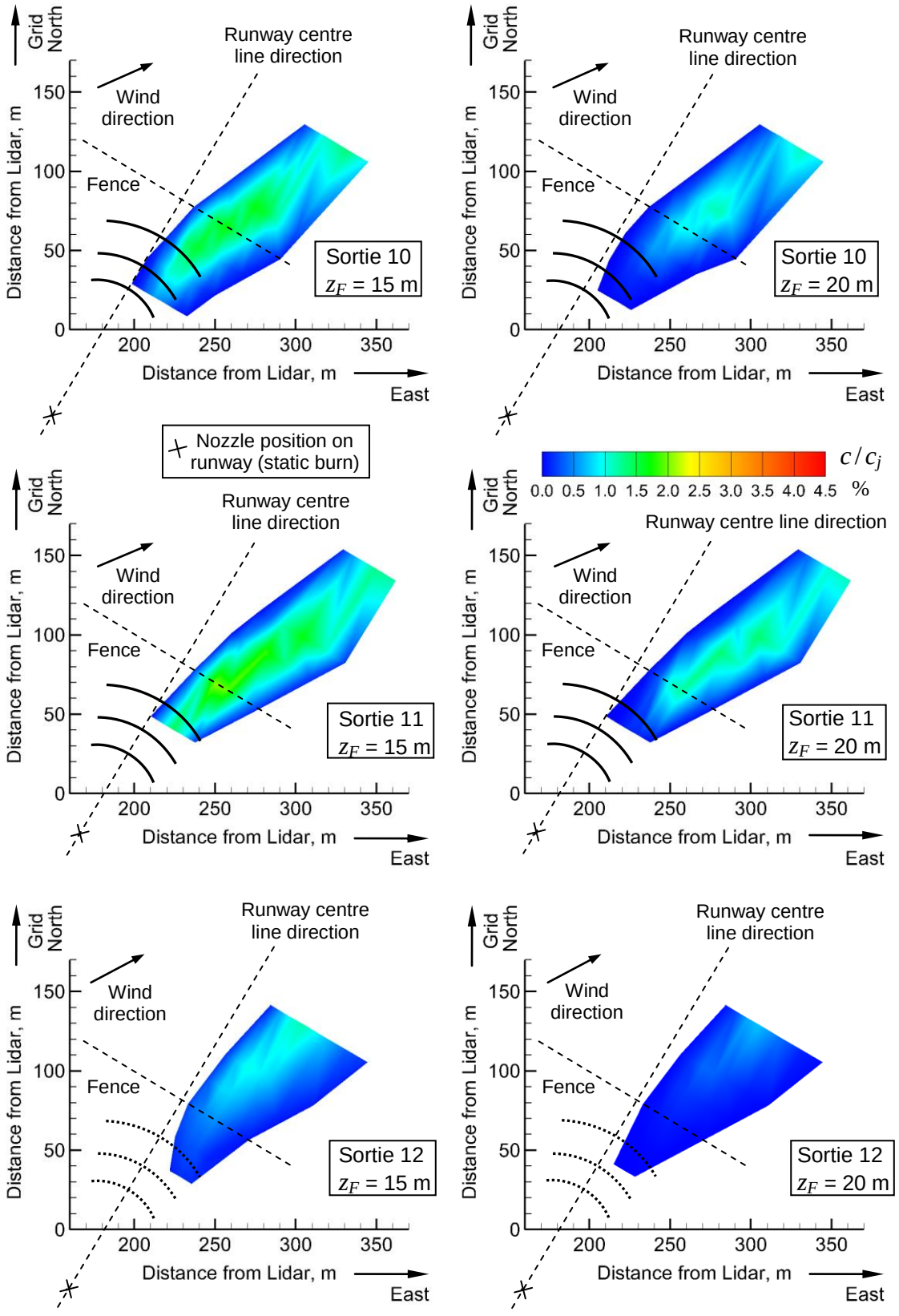

Figure 7.9: Contours of mean concentrations, measured at 1:200 scale at z/d = 12.5 and z/d = 16.7 and plotted in full-scale coordinates (z_F = 15 m and z_F = 20 m)

7.2 ABLWT measurements without cross flow

The experiments replicating the field trials were conducted at different nozzle positions and wind tunnel flow conditions, which made exact comparisons between the sorties difficult. Also, the tests focused primarily on measurements at heights close to the ones measured by the Lidar, scaled at 1:200, which did not include measurements very close to the ground. Therefore, additional measurements were conducted for cases with and without baffles at the same wind tunnel flow direction and speed, in order to allow a direct comparison of the cases and to demonstrate solely the effect of the baffles. The tests were conducted with the wind tunnel flow aligned with the runway direction and included FID mean concentration measurements and mean velocity measurements, using Hot-Wire Anemometry (HWA).

7.2.1 FID measurements

The FID measurements without cross flow were executed in a similar manner to the one described in Chapter 7.1.1 and 7.1.2 at the same nozzle flow rate Q_{jM} and f. The arrangement was modified by aligning the runway centre line (x-axis of the coordinate system used) with the wind tunnel flow direction (see *Figure G.4* in Appendix G). The origin of the coordinate system was defined on the ground at the nozzle exit position. Considering the positive results of Sortie 11, observed in the previous FID measurements, the nozzle was placed at the position of Sortie 11 at $b_0 = 20d$ (120 mm) relative to the runway threshold. In order to minimise the effect of the wind tunnel flow, the tests were performed at the smallest stable wind tunnel velocity U_{40} at 40 mm above the ground, of 0.4 m/s. Initially, the same array of three baffle rows was used, centred at the runway threshold with radii of 180 mm, 266.5 mm and 370 mm respectively.

Additional tests were performed with a baffle array of three rows of double height, centred at the runway threshold with radii of 180 mm, 480 mm and 690 mm respectively (see *Table G.14* in Appendix G). The radii were determined from Large Eddy Simulation results on the velocity flow field by Spanelis (2013), in order to reduce the sheltering effect of the first and second row. Further tests were performed with a straight row C of *Table G.14*, placed at right angles to the jet direction at the runway threshold. Images of the working section arrangement are shown in *Figure 7.10*.

The measurements were taken predominantly at the runway centre line at heights between $z/d = 0.5$ and $z/d = 35$ and longitudinal distances x from the nozzle exit of up to $200d$. Lateral distances of up to $y/d = 40$ were also tested to study the lateral spread of the plume. The results were obtained using the post-processing method of *Figure 7.2*.

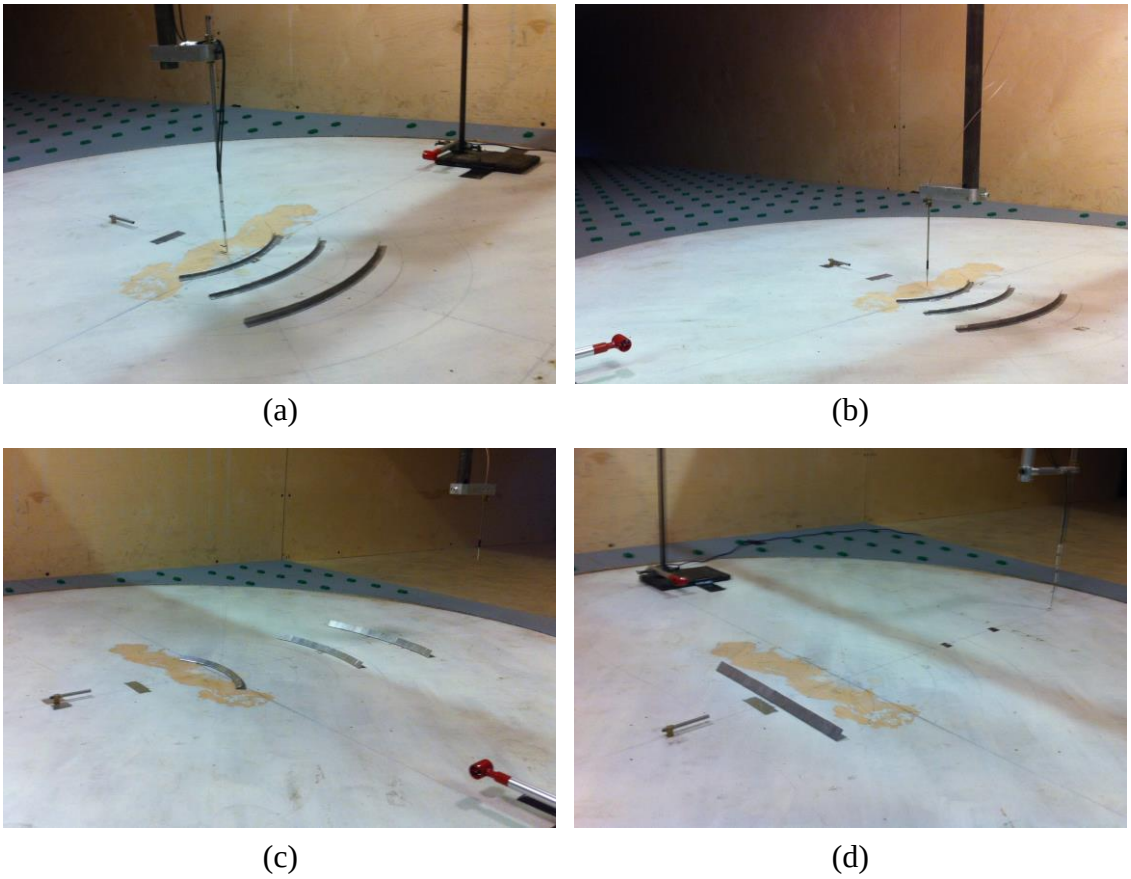

Figure 7.10: Images of the 8'×4' ABLWT working section during FID and HWA experiments at 1:200 scale without cross flow: (a) FID measurements with original baffles (flow direction is from top left), (b) HWA measurements with original baffles (flow direction is from top left); (c) HWA measurements with double baffles (flow direction is from bottom left), (d) FID measurements with row C at the runway threshold (flow direction is from bottom left)

Results along the runway line at $z/d = 1$ above the ground (*Figure 7.11*) show that the mean concentrations downstream of the baffle array of Sortie 11, referred to as 'original baffles', are lower compared to the plain jet (no baffles) at distances between 90d and 110d from the nozzle. At $x/d > 110$, corresponding to full-scale distances greater than 132 m, the concentrations downstream of the original baffles are higher and the difference becomes increasingly greater with x. Thus, the baffles provide only a short-distance sheltering effect downstream of the last row. These results do not agree with the results of the replication of the field trials, where the positive effect was observed as far as 148d at $z/d \approx 4$. The single baffle row at the runway threshold (x/d = 20d) gives significantly lower concentrations compared to the plain jet, however, the effect gradually diminishes with x. At the furthest distance tested, $x/d = 200$, the single row and the array of double-height baffles, referred to as 'double baffles', give approximately the same concentrations as the plain jet.

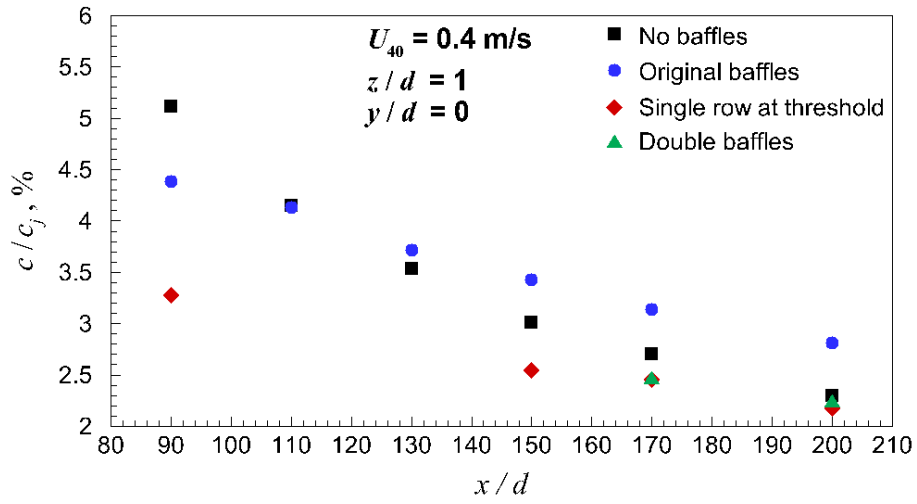

Figure 7.11: Variation of mean concentrations with distance from the nozzle exit (x/d) on the runway line ($y/d = 0$)

Plots of the measured concentrations at the runway line versus height above the ground (*Figure 7.12*) show that, at all distances tested, the original baffles give higher concentrations above $z/d = 3$ compared to the plain jet. Thus, there is an increased spread of the concentrations in vertical direction downstream the baffle array, which was shown by the results of the replication of the field trials as an increase in vertical spread of the plume in comparison to the case without baffles. The vertical height of the plume is considerably greater between distances of $x/d = 90$ and $x/d = 150$ compared to the plain jet, however, its maximum height (i.e. ~ 22d) does not vary significantly between $x/d = 90$ and $x/d = 200$.

The double baffles and the single baffle row at the runway threshold show qualitatively similar results in terms of increased concentrations in vertical direction. Overall, neither of the baffle configurations causes the plume to a lift-off. In terms of reduced concentrations close to the ground, the single baffle row at the runway threshold gives the best reduction for $x/d < 200$.

The apparent spread of the concentrations in vertical direction close to the *xz* plane is evident from the lateral shape of the plume. *Figure 7.13* shows the half-width plume contours of c/c_j in planes perpendicular to the flow direction at $x/d = 170$. These were obtained with the same method, used for *Figure 7.8* and *Figure 7.9*. The plume of the plain wall jet (*Figure 7.13a*) is 'flat', i.e. has a low aspect ratio, and exhibits similar concentrations at the edges and close to the *xz* plane. At the same time, the plumes downstream of the original and double baffles (*Figure 7.13b* and *Figure 7.13c* respectively) have a large concentration gradient in lateral direction, i.e. high concentrations close to the *xz* plane and lower concentrations at the plume edges.

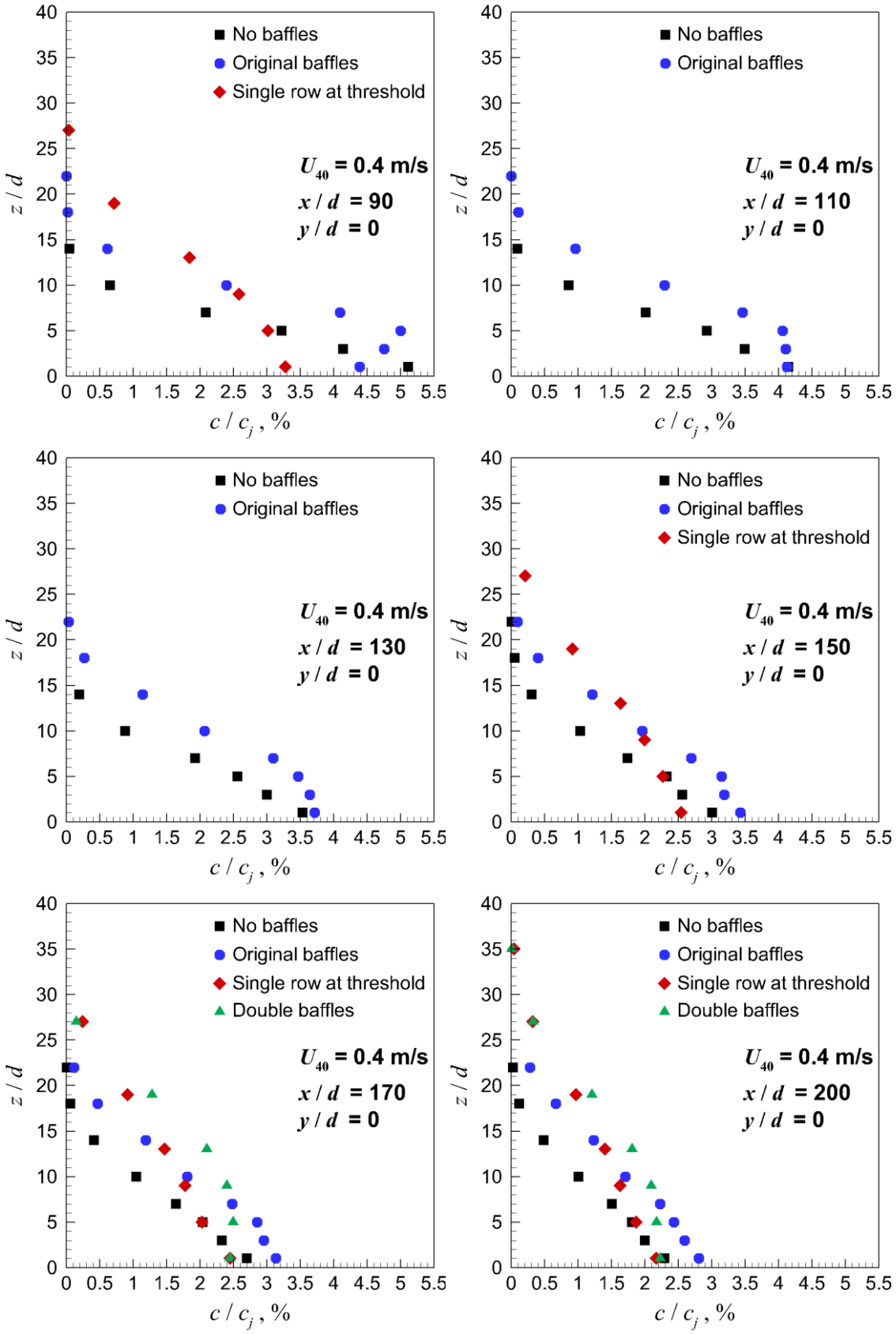

Figure 7.12: Variation of mean concentrations with height (z/d) on the runway line (y/d = 0)

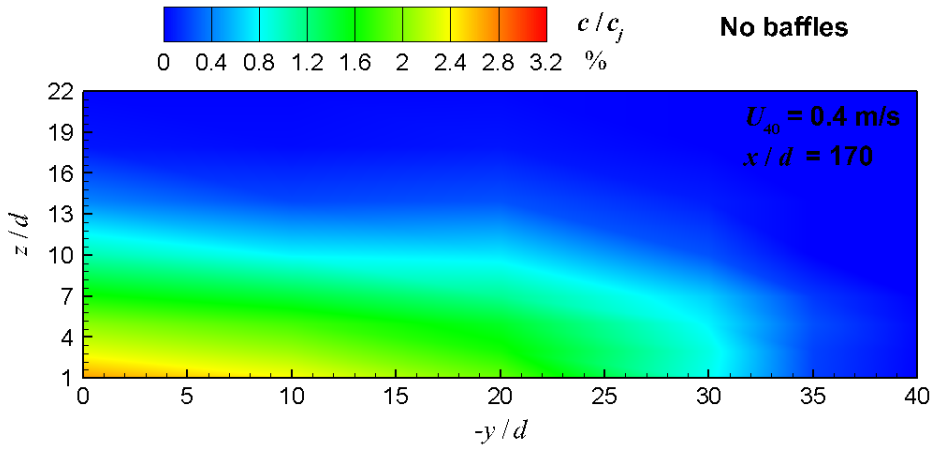

(a)

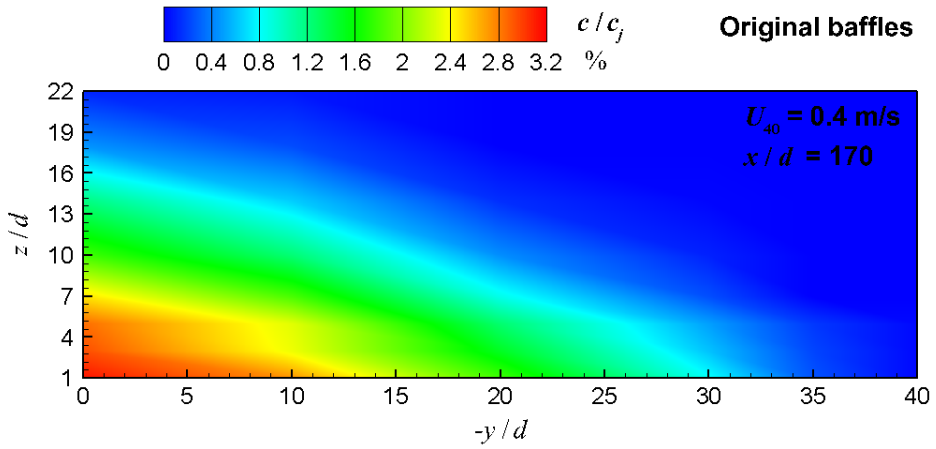

(b)

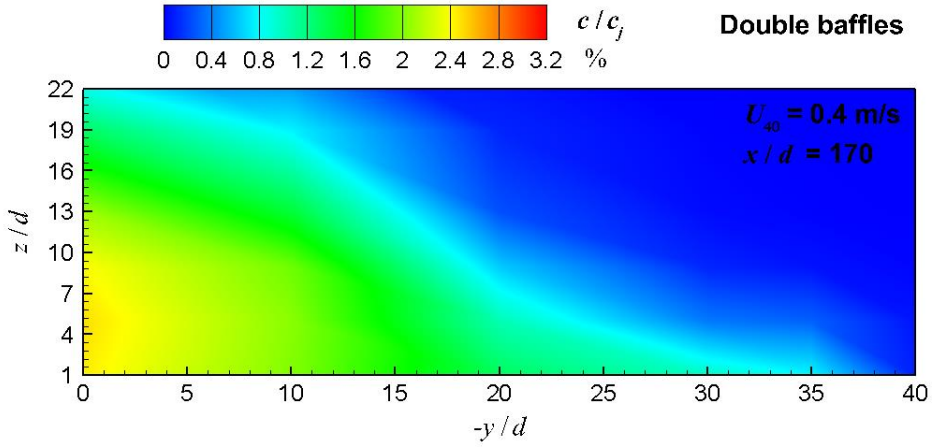

(c)

Figure 7.13: Contours of FID measured mean concentrations at x/d = 170 without cross flow: (a) no baffles, (b) original baffles, (c) double baffles

Figure 7.13c and *Figure 7.13b* can be considered to represent the development of the generic plume shape at right angles to the flow. Although the concentrations were measured at the same distance from the nozzle, the relative distances to the last row of baffles were different, i.e. at 35*d* downstream of the double baffle array and at 88.3*d* downstream of the original baffle array. The upwards deflected plume by the baffle array has an increased maximum height compared to a wall jet and shows significantly higher concentrations close to its symmetry plane (i.e. $0 \leq y \leq 10d$ in *Figure 7.13c*), resembling a bell curve. Further downstream, the plume becomes flatter with increased concentrations towards its edges (*Figure 7.13b*). It should be noted that in the case of *Figure 7.13c*, a larger deflection is expected due to the double height of the baffle array, increasing the maximum height further.

Overall, the FID measurements without cross flow showed similar development of the plume to the one observed in the experiments replicating the field trials. However, the small positive reduction of plume concentration, reported previously for Sortie 11, was not identified at distances $x/d > 110$, corresponding to 132 m in full scale.

7.2.2 HWA measurements

The FID concentration measurements without cross flow were supported by measurements of mean velocity using Hot-Wire Anemometry. The exact same arrangement of the working section was used (see *Figure G.4* in Appendix G), substituting the FID probe on the traverse with a Dantec 55P13 hot-wire probe. The method of operation of the hot-wire anemometer was described previously in Chapter 3.2.6. The measurements were performed at similar spatial points to ones of the FID measurements at a frequency of 1 kHz and a sampling time of 5 seconds. The sampling time was minimised in order to reduce the time for execution of the tests without significantly affecting the results. The repeatability of the results was checked regularly during tests and was determined to be within 0.15 m/s. Since all measured mean velocities U are given in terms of the jet velocity at the nozzle U_j, equal to 25 m/s, the quoted repeatability of U/U_j is within 0.006.

The calibration of the hot-wire anemometer was done in the wind tunnel freestream using the Schiltknecht MiniAir6 Mini vane anemometer. As all measurements were performed in the presence of helium in the plume, an attempt was made to quantify the influence of the helium on the hot-wire output. This was done at the nozzle exit by measuring the mean velocity of a jet of helium (U_{jHe}), i.e. $f = 1$, and of a jet of air (U_{jAir}) within a range of U_{jAir} between approximately 2 m/s and 13 m/s. These measurements are plotted in *Figure 7.14*, showing a good linear fit. From the linear fit,

the maximum increase in the HWA measured velocity values due to the presence of helium in the plume is quantified as approximately 13 %. It should be noted that the used flow meters did not allow accurate measurement of the volumetric flow rate below an exit velocity of 2 m/s, therefore the line was extrapolated to the origin of the coordinate system of *Figure 7.14*. In reality, the fraction of helium in the plume downstream of the nozzle, where the measurements were performed, was significantly smaller than 1. Therefore, its influence on the measured velocities was neglected.

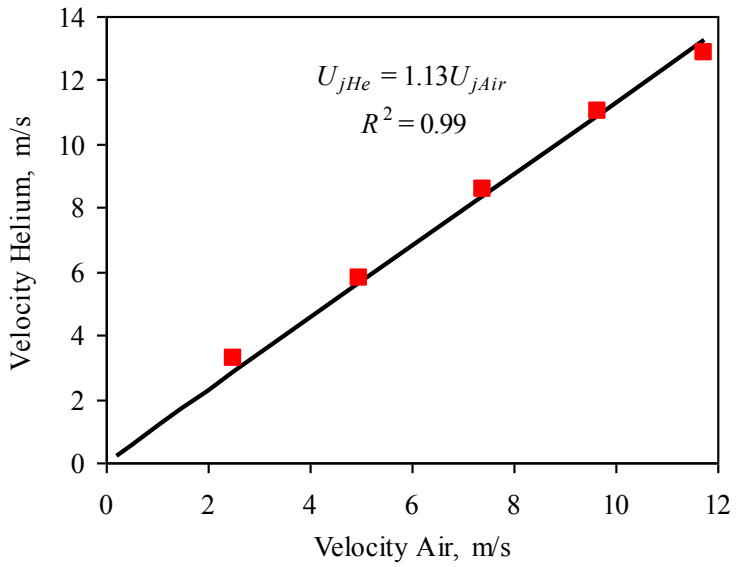

Figure 7.14: Correlation of Hot-Wire Anemometry data for air and helium

Figure 7.15 shows the variation of measured mean velocity with x along the runway centre line. Close to the ground at $z/d = 1$, the reduction of velocity at $x/d = 90$ due to presence of the original baffle array is significant, i.e. ~ 89 % compared to the natural velocity decay of the plain jet (no baffles). The array of baffles is located between $50d \leq x/d \leq 81.7d$, therefore $x/d = 90$ is within the recirculation zone of row C. A smaller reduction of ~ 29 % is evident at the furthest measurement point, $x/d = 170$. The corresponding reductions at a height of $z/d = 3$, equal to nominally two times the height of row C, are ~ 46 % and ~ 23 % at $x/d = 90$ and $x/d = 170$ respectively. The velocity decay of the plain jet, calculated at $z/d = 1$ to be approximately $U \sim x^{-0.98}$, agrees reasonably well with the results found in the literature (see *Table 2.2*).

The case of a single baffle row at the runway threshold shows a smaller reduction of mean velocity close to the ground at $x/d = 90$ compared to the original baffles, while at $x/d = 170$ the reduction is greater.

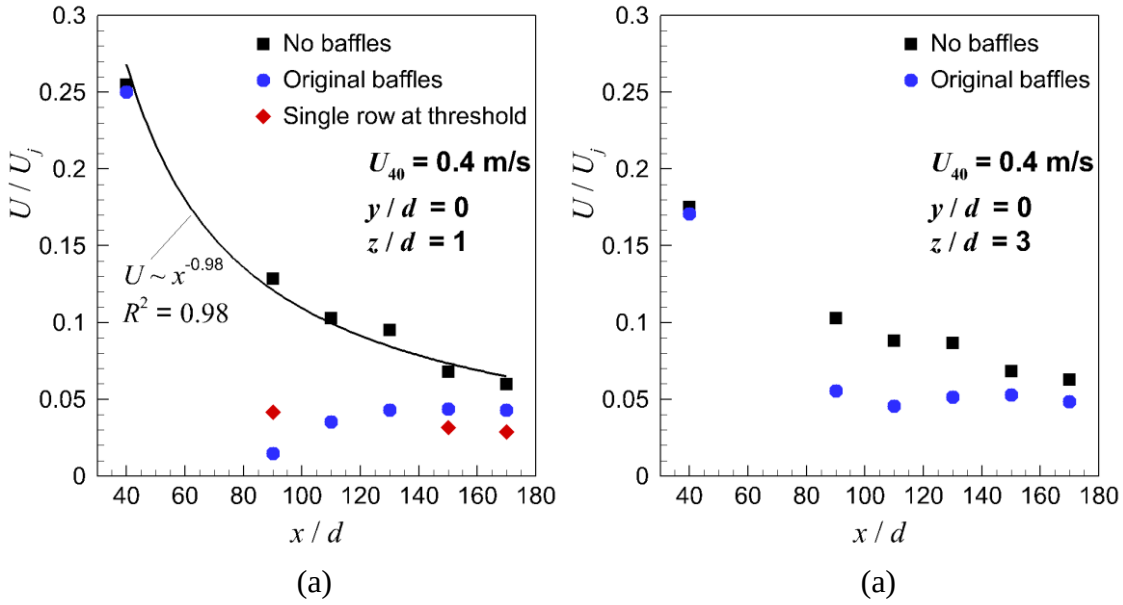

Figure 7.15: Variation of mean velocity with longitudinal distance from the nozzle (x/d) on the runway line (y/d = 0) at: (a) y/d = 3, (b) z/d = 3

The measured concentrations at the runway line are plotted versus height above the ground in *Figure 7.16*. The observed reduction in mean velocity is evident for heights below 5*d* at all distances *x* tested. The local maximum velocity downstream of the original baffle array at all distances *x* occurs at an approximately constant height above the ground, i.e. between 5*d* and 7*d*, while the local maximum velocity of the plain jet is generally very close to the ground. This is an indication of the deflection of the plume and increased vertical spread, observed during the FID measurements. It is also supported by the increased velocities above $z/d = 7$ downstream of the baffle array. The cases of the double baffles and the single baffle row at the runway threshold show a significant reduction in mean velocity at $z/d < 5$, however, the plume is not observed to lift-off.

Additional velocity measurements at $x/d = 170$ and lateral stations between $y/d = 0$ and $y/d = -40$ are included in *Figure G.5* in Appendix G. For the plain jet, they show only small reduction in the measured mean velocity below $z/d = 5$ between $y/d = -20$ and $y/d = -30$, compared to the original and double baffle arrays. This is consistent with the presence of higher concentrations towards the edges of the plain jet plume and with the 'flat' shape of the plume (see *Figure 7.13a*).

Overall, the FID and HWA measurements show good agreement with regard to the effect of the baffles of increasing the vertical spread of the plume. Although the baffles cause a significant reduction of jet momentum close to the ground, neither of the three baffle configurations causes a lift-off of the plume.

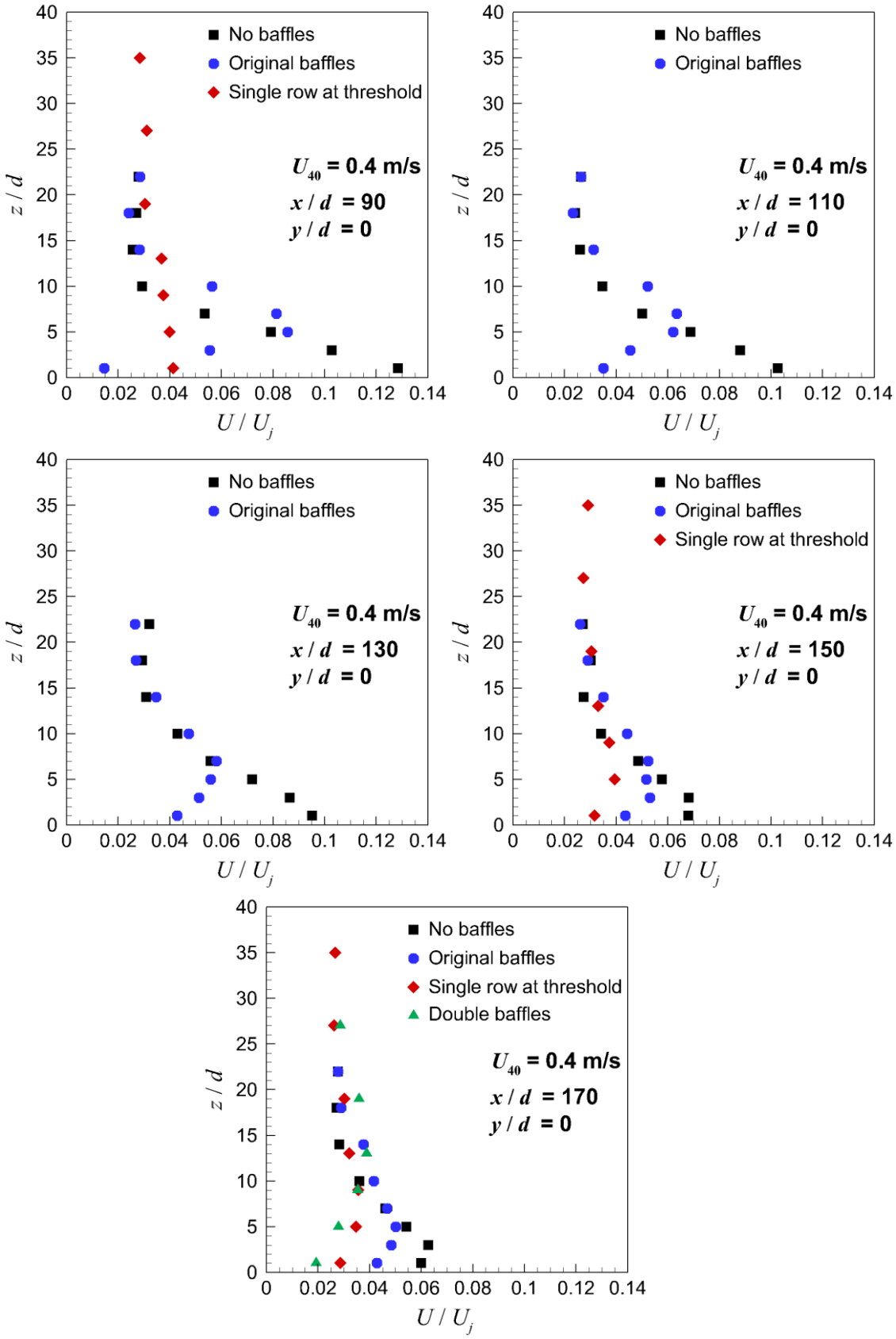

Figure 7.16: Variation of mean velocity with height (z/d) on the runway line (y/d = 0)

7.3 Further force balance measurements

Since no lift-off of the plume was observed from the mean concentration and velocity measurements at 1:200 scale, additional force balance measurements were performed to investigate whether the arrangement of the baffle array delivers the targeted total drag, estimated as 25 % of the total take-off thrust force. These experiments completed the sub-scale investigation within the thesis work. In order to obtain repeatable measurements, i.e. sufficiently large drag values registered by the skin-friction balance, the size of the baffles was changed to a 1:100 geometric scale. The arrangement and results of the experiments are described below.

The models used were geometrically identical to the models of the 8'×4' ABLWT experiments. Their dimensions were doubled to give a 1:100 geometric scale (see *Table G.15* in Appendix G for dimensions and characteristics). The individual baffle models were manufactured with a width of 42 mm, which was small enough to follow accurately the arcs drawn on the balance plate. As the total width of rows A and C was not divisible by 42, three of the baffles of row A and one of the baffles of row C were manufactured with a width of 21 mm and were arranged symmetrically in the centre of each row. Images of the baffle rows on the skin-frction balance are shown in *Figure 7.17b*, *Figure 7.17c* and *Figure G.1b* of Appendix G.

The working section arrangement of the force balance tests, shown in *Figure 7.17a*, was similar to the arrangement of the 8'×4' ABLWT experiments. The development section was arranged as described in Chapter 6.2. The baffle arcs were drawn on the balance plate with radii of 360 mm, 535 mm and 740 mm for row A, B and C respectively, centred at a point on the floor centre line representing the runway threshold. The distance b_0 along the centre line from the nozzle exit to this point was 570 mm (47.5d) and 240 mm (20d) for Sortie 10 and Sortie 11 respectively. In accordance with the sub-scale model results (see *Table 6.1*), a nozzle of diameter d = 12 mm was used, delivering a neutrally-buoyant jet (f = 0) at a flow rate of 244 l/min and giving an exit velocity of approximately 36 m/s. The nozzle was positioned at 24 mm vertical distance from the ground to the nozzle centre line and was approximately 10d long in order to ensure a smooth flow at the nozzle exit after passing the corner connecting the vertical delivery pipe to the nozzle pipe. Due to practical difficulties of turning the balance, all force measurements were performed without cross flow. With regard to Sortie 10 and Sortie 11, there is virtually no difference between the measured mean wind directions (see *Table 8.3*), thus aligning the wind tunnel flow with the runway direction is expected to have a similar effect on the drag results of both cases.

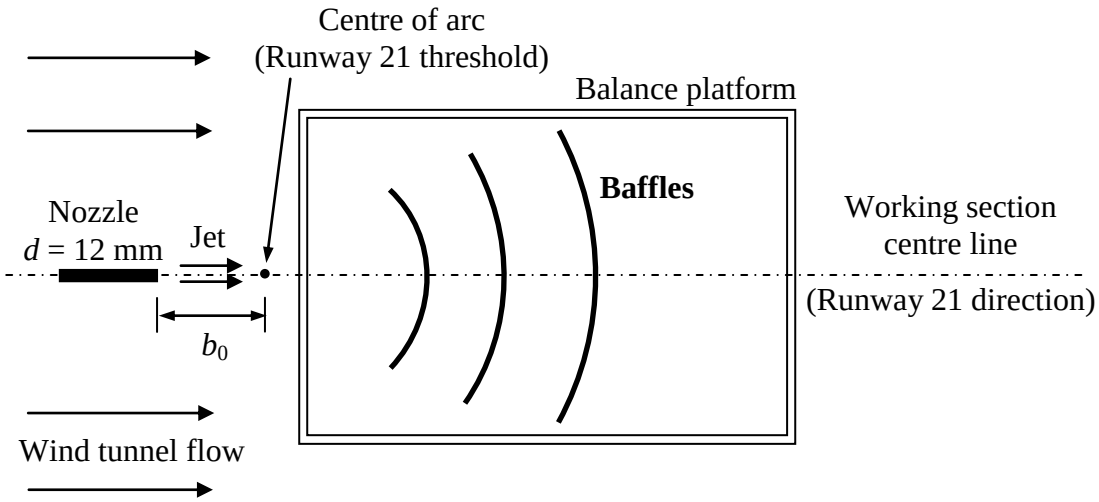

(a)

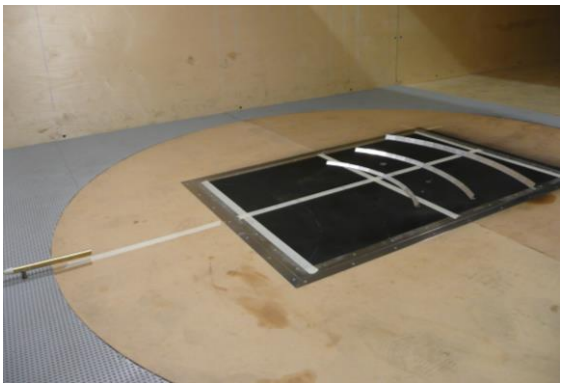

(b)

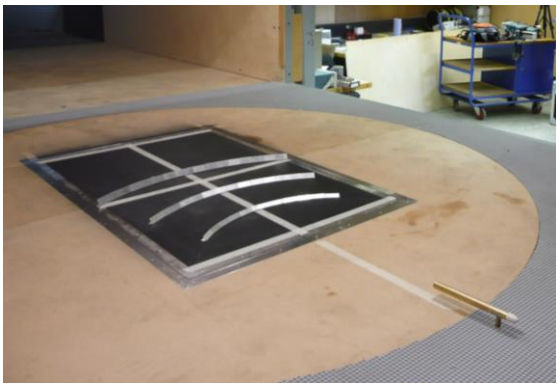

(c)

Figure 7.17: 8'×4' ABLWT working section arrangement for force balance measurements at 1:100 scale: a) schematic of Sortie 11 (top view, turntable not shown); b) image of Sortie 10 (isometric view, flow direction is from bottom left); c) image of Sortie 11 (isometric view, flow direction is from bottom right)

The tests were performed at a wind tunnel velocity in the working section, measured at 80 mm above the ground, of 0 m/s, 0.5 m/s and 0.7 m/s. The height was scaled at 1:100 from the height of the van mast, i.e. 8 m, at which the ambient wind speed and direction were measured during the field trials. Repeatability tests were performed in order to study the precision of the balance. Additional measurements were taken at higher velocities up to 5 m/s to study the effect of the ambient flow. During tests, the nozzle position was fixed and the baffles were moved on the balance plate (see *Figure 7.17b* and *Figure 7.17c*), thus there was no need to take measurements of the balance plate alone at different nozzle positions, as was done in the previous force balance tests. As discussed in Chapter 5.3, only minor variations in the drag of the array, subjected to a freestream (wind tunnel) flow, were observed if the whole array is moved

on the balance plate, therefore this was not studied further here. Readings of the ambient temperature and barometric pressure were taken for each test and were used to calculate the jet density ρ_j from the Ideal Gas Law. The jet thrust was then calculated with:

$$F_{t\,M} = \dot{m}_j U_j = \rho_j U_j{}^2 \frac{\pi d^2}{4}$$

Equation 7.1

With U_j = 36 m/s and an average jet density of 1.158 kg/m^3 determined from the recorded temperature and pressure readings during the tests, the jet thrust was calculated as approximately 0.170 N.

The total drag F_T (baffles and plate) and the balance plate drag F_b, measured during three separate tests, are presented in *Table 7.3* for the baffles and nozzle arrangement of Sortie 10 and Sortie 11. The results are significantly lower than the ones measured during the first force balance tests, however, they show excellent repeatability within 0.004 N. Although during the calibration tests the balance precision was determined to be within ±0.01 N, the current results show consistency for even lower measured forces. The results of the additional tests performed without wind tunnel flow and at different velocities for the nozzle configurations of Sortie 10 and Sortie 11 (see *Table G.16* and *Table G.17* in Appendix G) show similar repeatability and are consistent with the trend of an increase drag with increased in wind tunnel velocity.

As evident from the results of *Table 7.3*, the closer position of the nozzle and greater wind tunnel velocity of Sortie 11 give a significantly higher drag, estimated to be about ~37% of the jet thrust, compared to the ~26% for Sortie 10. In both cases, the percentage is larger than the targeted 25 %, thought to be sufficient to demonstrate the effects of the baffles on the plume dispersion. Evidently, the measured percentage values would be lower if the direction of the ambient wind did not coincide with the jet direction. If the wind tunnel velocities for the two nozzle positions are exchanged, i.e. 0.7 m/s for Sortie 10 and 0.5 m/s for Sortie 11 (see *Table G.17*), the drag of the baffles for Sortie 10 rises considerably to 30.4 %, while in the case of Sortie 11 it reduces only to 35.6 %. Thus, in terms of increased drag, the ambient wind has a stronger effect when the nozzle is positioned farther from the baffles. If we consider the measured drag results of the configurations of Sortie 10 and Sortie 11 both at 0.7 m/s and compare them to the drag results without wind tunnel flow (*Table G.16*), the percentage values reduce from 30.4% to 23.8% for Sortie 10 and from 36.8% to 32.3% for Sortie 11. If in both configurations the wind tunnel velocity is reduced from 0.5 m/s to 0 m/s, the corresponding reductions are from 25.9% to 23.8% for Sortie 10 and from 35.6 % to 32.3% for Sortie 11.

As the wind tunnel velocity is increased up to 5 m/s (see *Figure G.6* in Appendix G), the measured drag becomes independent of the nozzle position. This indicates that the dynamic pressure, to which the array of baffles is subjected, comes predominantly from the wind tunnel flow.

Table 7.3: Measured drag for Sortie 10 and Sortie 11 at 1:100 scale without cross flow

Measurements		b_0 = 570 mm (Sortie 10)	b_0 = 240 mm (Sortie 11)
Wind tunnel (ambient wind) velocity at z = 80mm		0.5 m/s	0.7 m/s
Total measured drag, F_T	Test 1	0.073 N	0.093 N
	Test 2	0.074 N	0.091 N
	Test 3	0.075 N	0.095 N
Measured balance plate drag F_b	Test 1	0.031 N	0.032 N
	Test 2	0.030 N	0.030 N
	Test 3	0.030 N	0.032 N
Average baffles drag in % of jet thrust*		**25.9%**	**36.8%**

* Percentage values are calculated by converting the measured forces into dimensionless coefficients in order to account for the changes in ambient pressure and density during the tests. If calculated directly from the measured forces, differences up to 0.2 % were observed.

Attempts were made to quantify the drag of the baffles subjected to a wind tunnel velocity only, i.e. 0.5 m/s and 0.7 m/s measured at z = 80 mm. Due to the very low dynamic pressure, the exerted force on the baffles were also very small, approximately 0.002 N or 1.2 % of the jet thrust, which is lower than the quoted repeatability. While this value could not be measured accurately, it would be safe to conclude that the increase in drag is not due to the added dynamic pressure of the ambient wind, but is caused predominantly by the secondary effect, observed during the flow visualisation tests and during the previous drag measurements (Chapter 4 and Chapter 5 respectively). It is to reduce the entrainment of ambient air and thus reduce the jet's rate of spread, predominantly in lateral direction in case of a wall jet. As a consequence, the rate of velocity decay with distance downstream of the nozzle is reduced. Thus the ambient wind contributes positively to the drag of the baffles, subjected to an exhaust jet, and allows more momentum to be taken away from the jet. At the same time, higher ambient wind would keep the wall jet attached to the ground due to its greater horizontal momentum above the ground-based plume.

8 BAe 146-301 field trials

This chapter of describes the full-scale field trials performed to complement the sub-scale wind tunnel test programme. The full-scale trials were conducted with a BAe 146-301 aircraft, performing 12 take-off runs at Cranfield Airport (52º 4' 20" N, 0º 37' 0" W). Lidar, acoustic and point-sample air quality measurements were performed in collaboration with researchers from Manchester Metropolitan University, University of Southampton and University of Cambridge. The outcome and conclusions were published as Bennett et al. (2013). This chapter includes a summary of the preparation, execution and results of the field trials.

8.1 Baffle prototypes

The wind tunnel results of Chapter 4 and 5 provided sufficient information for the aerodynamic design of the baffles in terms of baffle porosity, number of rows and row spacing and orientation with respect to the runway. In full-scale, the rows were to be composed of individual baffle prototypes of certain width. Regarding the mechanical design of the prototypes, the following key features were targeted, in order of priority:

1) Compliance with the failure mode and frangibility criteria, specified by the International Civil Aviation Organization (ICAO, 2006a) for structures located in the Runway End Safety Area (RESA). The RESA is defined as the "area symmetrical about the extended runway centre line and adjacent to the end of the strip primarily intended to reduce the risk of damage to an aeroplane undershooting or overrunning the runway" (ICAO, 2006a, p. 1-2). At the same time, the prototypes should be able to withstand the jet blast from the four BAe 146-301 engines.

2) The design should provide a relatively quick and easy way to erect and deflate the baffle prototypes, since planned tests included measurements with and without baffles. In the latter case, the prototypes are to be laid flat on the grass with their base still fixed to the ground. Such design would reduce the time between take-off runs and at the same time reduce the manpower required to erect and deflate the prototypes.

3) The prototypes should be relatively quick to assemble, as they would be transported in parts to the testing site and assembled prior to the first test.

4) The design should take into account the limited storage space available for the prototypes before and after the trials. Recyclable materials for the baffle rigid components should be considered in order to reduce overall cost.

Dividing the rows into individual baffles satisfied one of the possible failure mode criteria, described in ICAO (2006b, p. 4-2) as 'windowing'. It refers to the collapse of a part of the structure on impact with the aircraft, which 'opens a window' for the aircraft to pass through. In terms of frangibility, ICAO (2006b, p. 4-9) gives the following:

"4.9.2 ***Yield device****. Each elevated light fixture should have a yield point near the point or position where the light attaches to the base plate or mounting stake. The yield point should be no more than 38 mm above the ground surface and should give way before any other part of the fixture is damaged. The yield point should withstand a bending moment of 204 J without failure but should separate cleanly from the mounting system before the bending moment reaches 678 J."*

In order to be conservative, the maximum permissible width $w_{n\,max}$ of the individual baffles of each row was calculated with a bending moment of $M_{B\,max}$ = 600 Nm about the base of the baffle (see *Figure D.1* in Appendix D.1 for a schematic illustration of the wind loading on the baffle). The calculation sequences for the baffle wind loading and the resulting $w_{n\,max}$ are shown in Appendix D.1 and D.2 respectively. The estimated values for $w_{n\,max}$ for the field trials are discussed further in Chapter 8.3.

The baffle prototypes were designed in collaboration with Manchester Metropolitan University and were manufactured at Cranfield University. Example images of a single baffle from row C (see *Figure 8.4* and *Table 8.2* for row designation) are shown in *Figure 8.1*. The main features include:

- An A-frame made from four aluminium tubes of 38 mm diameter (nominal wall thickness 3 mm). At the joints the frame rigidity was achieved by means of aluminium Kee-Lite connectors.

- A porous mesh (γ = 0.20), made of plastic windbreak material, mounted on the frame by means of sewn pockets in all four sides. The ground clearance to the bottom of the screen (i.e. ~ 260 mm) was kept approximately constant for all three baffle sizes.

- Two aluminium feet made from U-section channels (50 mm wide, 38 mm high and 500 mm long); two pivot pins linking the frame (uprights) to the feet allowed the frame to rotate freely and fold near flat; each foot was held in

position with two 200 mm long steel pegs driven into the ground through pre-drilled holes in the channel base.

- Two aluminium angle stays holding the frame at the required angle α to the jet efflux and preventing it from folding flat; each stay was linked to a wooden foot through a pivot pin which allowed it to rotate freely and lie flat on the ground when frangible pins were removed and the baffle was stowed. The wooden feet were held in place with steel pegs, similarly to the baffle feet.

- Two frangible shear pins (size M6) linking the stays and uprights; the shear pins were designed to fail at a bending moment about the baffle base (pivot pin connection) of 600 Nm, resulting in the baffle folding near flat on the ground; prior to the field trials, failure tests were performed with known weights, attached to the top of the frame.

The yield points (i.e. the shear pins), as defined by ICAO (2006b, p. 4-9), were located close to the top of the baffle, much higher than the defined maximum height of 38 mm. This was necessary, since only failure of the pivot pin at the feet would not necessarily give the desired flat folding of the baffle if the shear pin connecting the upright and stay didn't fail.

With the above prototype design, all targeted design features were addressed. The height of the U-channel feet above the ground was kept sufficiently small, so that they would not be a hazard for ambulances and fire engines driving over the baffles in case of an airport emergency operation. This was necessary since the prototypes would be left lying flat on the ground at the test site for the duration of the field trials (~10 days period). The choice of aluminium frame provided the necessary rigidity and at the same time fulfilled the requirement for a relatively lightweight structure, facilitating the transportation and installation of the baffle prototypes. The frames can also be recycled to keep the overall material costs low. It should be noted that, the presence of metallic objects, such as the baffles, in proximity of the runway could interfere with the airport's Instrument Landing System (ILS) and generally restrictions apply, see for example Transport Canada (2010). At Cranfield Airport, ILS is available for Runway 21 only, therefore the localiser antenna array is located at the opposite runway end and is sufficiently far from the baffles. The glide slope antennas are also sufficiently far at approximately 300 m from the piano keys of Runway 21, thus the transmitted beam would pass above the height of the baffles (minimum vertical angle of 1.25º, equal to a height of approximately 6 m at the piano keys).

Figure 8.1: Design features of the baffle prototypes used in the field trials

8.2 BAe 146-301 aircraft

The field trials were conducted with a BAe 146-301 aircraft (*Figure 8.2*), based at Cranfield Airport. It is an atmospheric research aircraft, part of the Facility for Airborne Atmospheric Measurements (FAAM), which is the result of a collaboration between the Natural Environment Research Council (NERC) and the Met Office (FAAM, 2014). The FAAM BAe 146-301 is an aircraft measurement platform with a wide scope of research applications including tropospheric chemistry measurements, boundary layer and turbulence studies, studies of weather systems and cloud dynamics etc., for which specific measurement instruments are used on board (FAAM, 2014). Of interest for the field trials were the primary data recording systems, such as the Flight Data Recorder (FDR), providing information on the aircraft's speed as well as the engine exhaust temperature and fuel flow rate.

Figure 8.2: FAAM BAe 146-301 atmospheric research aircraft (taken from FAAM, 2014)

The FAAM aircraft is a modified BAe 146, originally manufactured as a model 100 and later extended to a 300 model (registration: G-LUXE), see *Figure H.1* and *Table H.1* in Appendix H for the aircraft's dimensions and weight, as well as some performance characteristics. The FAAM BAe 146-301 has four Honeywell ALF502R-5 high-bypass turbofan engines. Some useful ALF502R-5 characteristics are included in *Table 8.1*. Of particular interest for the exhaust jet sub-scale modelling are the maximum thrust and the air and fuel mass flow rates. The ground clearance of the

engines, taken to the fan axis of rotation, was measured when the aircraft was parked at Cranfield Airport with empty fuel tanks. The average ground clearance for the inboard and outboard engines was estimated to be approximately 2.5 m.

Table 8.1: Honeywell ALF502-R5 engine specifications (IHS, 2011)

Length	1615 mm
Dry weight	606 kg
Fan diameter	1022 mm
Maximum thrust	31 kN
Specific fuel consumption	41.4 kg/(kNhr)
Bypass ratio	5.7:1
Mass flow rate (through fan)	87 kg/s
Fuel flow rate (during static burn)	0.378 kg/s *

* Mean value from the recorded data by the BAe 146-301 Flight Data Recorder during the field trials

8.3 Field trials arrangement

The field trials took place at Cranfield Airport between September 14th and 21st 2011 and consisted of twelve take-off and landing cycles (sorties) of the BAe 146-301: six with deflated baffles ('baffles down') and six with erected baffles ('baffles up') in the RESA of Runway 21 (see example images in *Figure 8.3*). During each sortie the aircraft would taxi to the starting take-off position, where it would perform a static burn for a nominal 10 s at full thrust with the brakes on before starting the take-off run. After take-off, the aircraft would fly a circuit and land. Sufficient time was allowed between sorties for the aircraft brakes to cool down and for the baffles to be erected (or deflated).

Figure 8.3: FAAM BAe 146-301 during field trials, September 2011: (a) starting take-off run, baffles deflated (image by Bennett, 2012), (b) during landing approach, baffles erected (image taken from Bennett et al., 2013)

Based on the wind tunnel results of Chapter 5, the baffles were arranged in three arc-shaped rows of spacing equal to 12 times the slope height of the previous row. The parameters for each row are given in *Table 8.2*. The centre of arc was placed at the intersection of the runway threshold (line of runway end lights) and the extension of the runway centre line (see *Figure 8.4a*). Using a rope of the corresponding arc radius, the arcs were marked on the grass with a temporary spray paint and the baffles were fixed to the ground in a flat (deflated) position in the days leading up to the tests. The width of the individual baffles was determined as 2.1 m, using the method outlined in Appendix D.2 (see *Equation D.8*) with $M_{B\,max}$ = 600 Nm. It should be noted that at the time this estimation was made, the position and arrangement of the baffles in the RESA were not yet determined from the wind tunnel tests. Therefore, the value of 2.1 m was based on calculations for the originally-proposed arrangement of five straight rows of slope angle α = 60º to the horizontal and spacing of 12 times the slope height of the previous row, where the first row was located 60 m from the edge of the runway piano keys. For the three-row configuration, an individual baffle width of 2.1 m would be sufficient if the jet source was located on the runway at a distance of 24 m from the edge of the piano keys (or 60 m from the runway threshold).

The rows consisted of eighty-four individual baffles in total: twenty-three, twenty-eight and thirty-three for rows A, B and C respectively. For each row this gives a total edge-to-edge distance perpendicular to the runway direction of nominally 2.5 times the predicted jet width at the corresponding position, assuming the jet source is at the edge of the piano keys. Originally, all rows were designed with α = 60º, however, during the course of the field trials the angle was changed to 40º, 50º and 60º starting from the smallest row respectively. The change was necessary due to structural failure of the shear pins of the first two rows as a result of the strong jet blast. Possible reasons for the structural failure could be an underestimation of the jet speed by the method presented in Appendix D or the adopted new location of the three-row baffle configuration compared to the original five-row configuration, which is closer to the runway threshold.

With regard to the longitudinal arrangement of the baffle rows, for the duration of the tests the runway threshold was displaced by 150 m to ensure sufficient clearance (i.e. > ~8 m) between the baffles and the typical 3º approach surface (see *Figure 8.4b*).

Table 8.2: Parameters of the baffle rows for the BAe 146-301 field trials

Baffle row label	Arc radius [m]	Slope height h' [m]	Vertical height h [m]	No. of individual baffles	Slope angle α [º]	Individual baffle width [m]
A	36.0	1.4	0.90	23	40	2.1
B	53.3	1.7	1.30	28	50	2.1
C	74.0	2.0	1.73	33	60	2.1

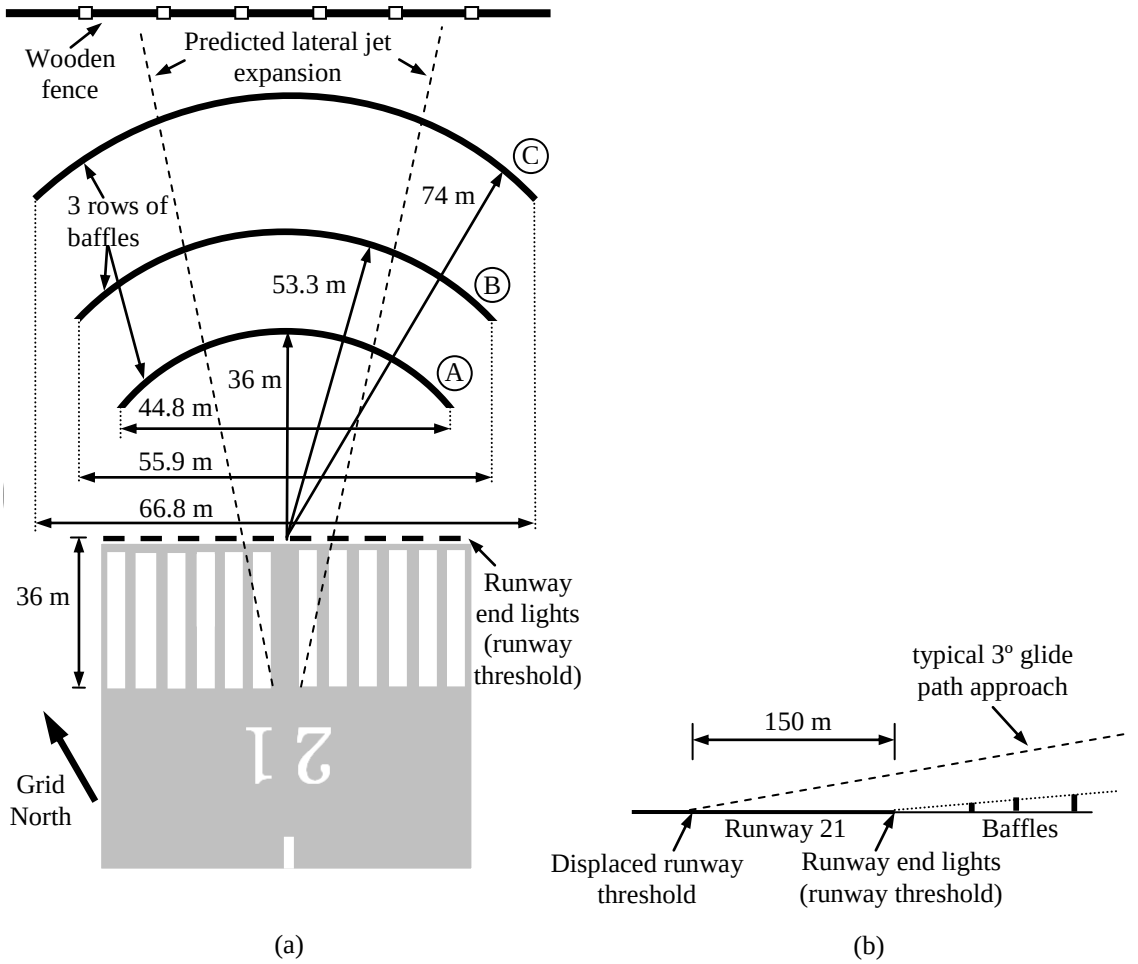

Figure 8.4: Schematic illustration of the field trials arrangement in the Runway End Safety Area (RESA) of Runway 21 at Cranfield Airport (not to scale): (a) top view, (b) side view

8.4 Measurement equipment

Measurements during the field trials were performed to investigate: 1) the dispersion of the exhaust plume, 2) the exhaust jet speed behind the baffles and 3) any occurring acoustic effects. Cranfield University was not directly involved in performing the measurements therefore the measurement equipment and procedures are only briefly discussed here. The majority of the information included is based on the published article, i.e. Bennett et al. (2013), where more details can be found.

The exhaust plume dispersion was measured using Lidar scans, point-sample air quality sensor nodes and optical particle counters. The Lidar uses a Nd:YAG frequency-tripled laser with a 9 ns pulsed output of 355 nm wavelength (eye-safe), and has a spatial resolution of 5 m. During the field trials, the Lidar vehicle (see *Figure H.3* in

Appendix H) was located at nominally 5 m north (grid north) and 178 m west of the intersection of the runway threshold and the runway centre line (see *Figure 8.5*; additional satellite image of the area around the runway is shown in *Figure H.4* in Appendix H). The laser source of the Lidar vehicle is located at 3 m above the ground. Scans were performed for elevations of 0.7º and 4.5º typically at azimuths between 79.5º and 40º relative to grid north in successive shots of 0.5º steps, i.e. 80 shots per scan (see *Figure 8.5*, where the two azimuth angles are shown with arrows starting from the Lidar positions). The 4.5º elevation angle was chosen in order to capture any occurring lift-off of the exhaust plume from the ground. The total scanning time for each test, including scans at both elevation angles, was about 10-11 seconds.

The point-sample sensor nodes, developed at the University of Cambridge, consisted each of three electrochemical cells for detection of CO, NO and NO_2, and supplementary electronics, GPS and GPRS, the latter allowing for transmission of recorded data in near real time over the mobile telephone network (Bennett et al., 2013, p. 2349). Six nodes, denoted with 'S' in *Figure 8.5*, were deployed along the boundary fence, located at 101 m from the runway threshold along the extension of the runway centre line. Air quality measurements were also taken with two Osiris particle counters, which use an optical scattering measurement technique to size and counter aerosol particulate matter (PM), giving results for PM_{10}, $PM_{2.5}$ and PM_1 (Bennett et al., 2013, p. 2350). These measurements were taken at a height of 1.35 m above the ground. Each Osiris particle counter was mounted on a tetrapod support structure, also including a vane anemometer for wind speed measurements at a height of 2.1 m. The structures were positioned at two locations 1 m from the fence at its runway side – one on the extension of the runway centre line and one at 32.5 m from the centre line in order to capture the laterally-displaced plume due to the prevailing west-south-westerly ambient wind during the field trials (see *Figure 8.5*).

The acoustic measurement equipment included Bruel & Kjaer 2250 sound level meters, monitoring the noise level at six locations (numbered 1 to 6 in *Figure 8.5*) behind the boundary fence, a Norsonics environmental noise recorder, located near the runway threshold to monitor the acoustic strength of the aircraft noise, and a high-power omnidirectional acoustic source providing a reference for monitoring changes in noise propagation (Bennett et al., 2013, p. 2351).

Other equipment used included a camcorder to record each take-off and landing and, most importantly, the aircraft starting position, and four run-of-wind anemometers located on the boundary fence (see *Figure H.4* in Appendix H).

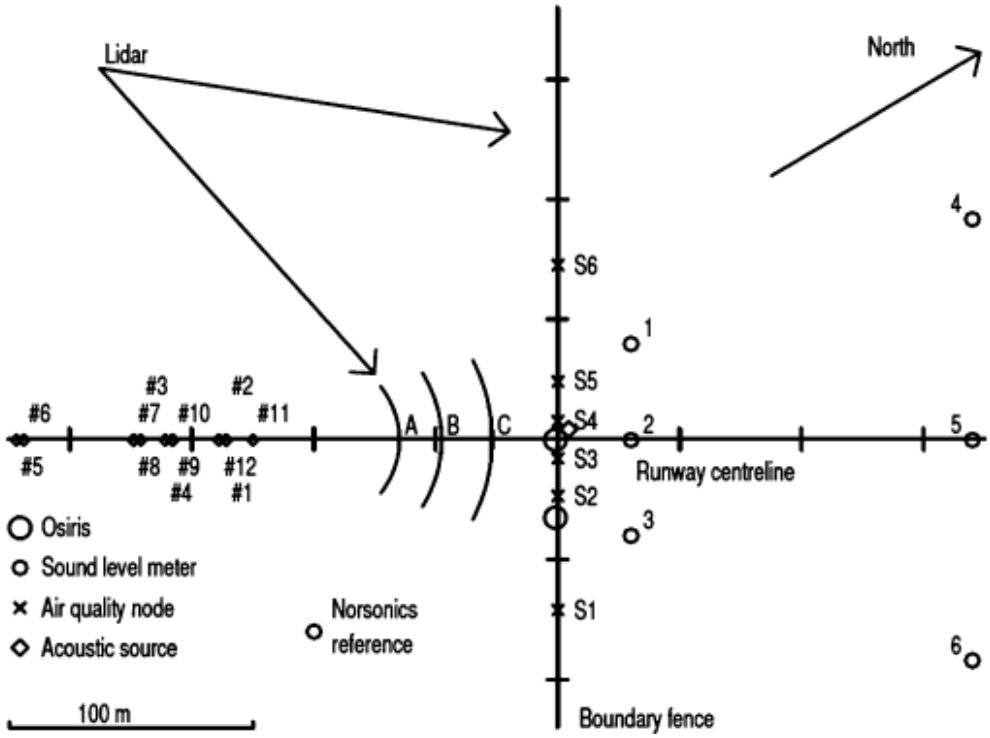

Figure 8.5: Schematic illustration of the deposition of the instruments during the field trials (taken from Bennett et al., 2013)

The aircraft starting position for each sortie is denoted with #; the six air quality sensor nodes are denoted with S; the sound level meters are numbered 1 to 6, the acoustic source is located beside S4

8.5 Test conditions

As discussed in Chapter 8.3, during the first take-offs with extended baffles (i.e. Sortie 2 and 3), the strong jet blast led to structural failure of the central baffles of rows A and B, i.e. located close to the extension of the runway centre line. In subsequent sorties, the baffle arrangement was changed to the one of *Table 8.2* and the aircraft take-off starting position was moved further away from the runway threshold. Taking this into account, the recorded data of the last test day (i.e. Sortie 9 to 12) were considered most reliable in terms of test arrangement, favourable ambient conditions and quality of the measurements performed. These were used in the modelling and replication of the field trials at sub scale, described previously in Chapter 6 and 7 respectively.

The test conditions of Sortie 9 to 12 are shown in *Table 8.3*. Ambient temperature and barometric pressure readings were obtained from the meteorological database of Cranfield Airport. The ambient wind speed and direction were measured every 10 s by

the Lidar vehicle mast anemometer and wind vane respectively at 8 m above the ground. The values given in *Table 8.3* are the averaged values over the duration of the take-off run for each sortie. The ambient wind direction was measured relative to magnetic north, which for Cranfield Airport is nominally 3º west of grid north. Runway 21 is oriented at 211º to grid north, thus the ambient wind angle relative to the Runway 21 centre line is obtained by subtracting 214º from the value given in *Table 8.3* (see *Figure H.5* in Appendix H for a schematic illustration explaining the angular relationships). It should be noted that the wind direction value for Sortie 11, i.e. 250º, differs by 2º from the value quoted for the same sortie in Bennett et al. (2013). The estimated engine position, given in *Table 8.3*, is relative to the runway threshold along the runway centre line.

Table 8.3: Test conditions for Sortie 9 to 12 during the BAe 146-301 field trials

Sortie No.	Baffles	Ambient temperature [ºC]	Ambient pressure [Pa]	Wind speed* [m/s]	Wind direction** [º]	Engine position*** [m]
9	down	12.5	101600	7.1	239	57
10	up	14.5	101600	5.4	249	57
11	up	14.5	101550	7.0	250	24
12	down	15.5	101500	7.2	245	38

* Measured at 8 m above the ground at Lidar vehicle location

** Measured relative to magnetic north at 8 m above the ground at Lidar vehicle location

*** Longitudinal (along centre line) position on Runway 21 relative to the runway threshold

From *Table 8.3*, it is evident that Sortie 10 and Sortie 11 were performed at practically the same averaged wind direction, however, the ambient wind speed was considerably higher in the case of Sortie 11. Given the expected influence of the ambient wind on the plume behaviour, a comparison between both sorties would not necessarily show the influence on the plume dispersion of the distance between the jet source and the baffles, which is significantly closer in the case of Sortie 11. At the same time, Sortie 11 and Sortie 12 were performed at approximately the same ambient wind speed, thus a direct comparison showing the effect of the baffles should be possible. The difference in ambient wind direction (≈ 5º) in the two cases is considered of less importance given the width of the baffles relative to the estimated plume lateral spread.

8.6 Results

With regard to this sub-scale study, only the performed Lidar scans and air quality measurements are of high importance. A brief summary of the results, as presented in

Bennett et al. (2013), is included in this section, while a comparison to the wind tunnel experiments is provided in Chapter 8.7. The final averaged Lidar data of each sortie from 9 to 12 for both elevation angles of 0.7º and 4.5º, provided by Bennett (2012), are plotted in *Figure H.6* to *Figure H.9* in Appendix H, including the basic schematic arrangement in the RESA of Runway 21.

Comparing the averaged Lidar scans of Sortie 11 and 12 for the low elevation of 0.7º (see *Figure 8.6*), it is evident that the concentrations behind the array of baffles are reduced considerably when the baffles are erected. For example, at 0.7º elevation and initial height of the laser source of 3 m the height of the scans above the intersection of the boundary fence and the extension of the runway centre line is approximately 6 m (see *Figure H.* in Appendix F for the calculated contours of Lidar scanning height at elevation of 0.7º and 4.5º). At 4.5º elevation, the observed plume concentrations for Sortie 11 appear to be higher compared to Sortie 12 (see *Figure H.8b* and *Figure H.9b* in Appendix H). Furthermore, the plume of Sortie 12 appears to be located close to the ground with only small individual parts detected at 4.5º elevation, while in case of Sortie 11 a coherent plume of small concentrations can be detected downstream of the boundary fence between heights of 26 m and 36 m, estimated from *Figure H.10b*.

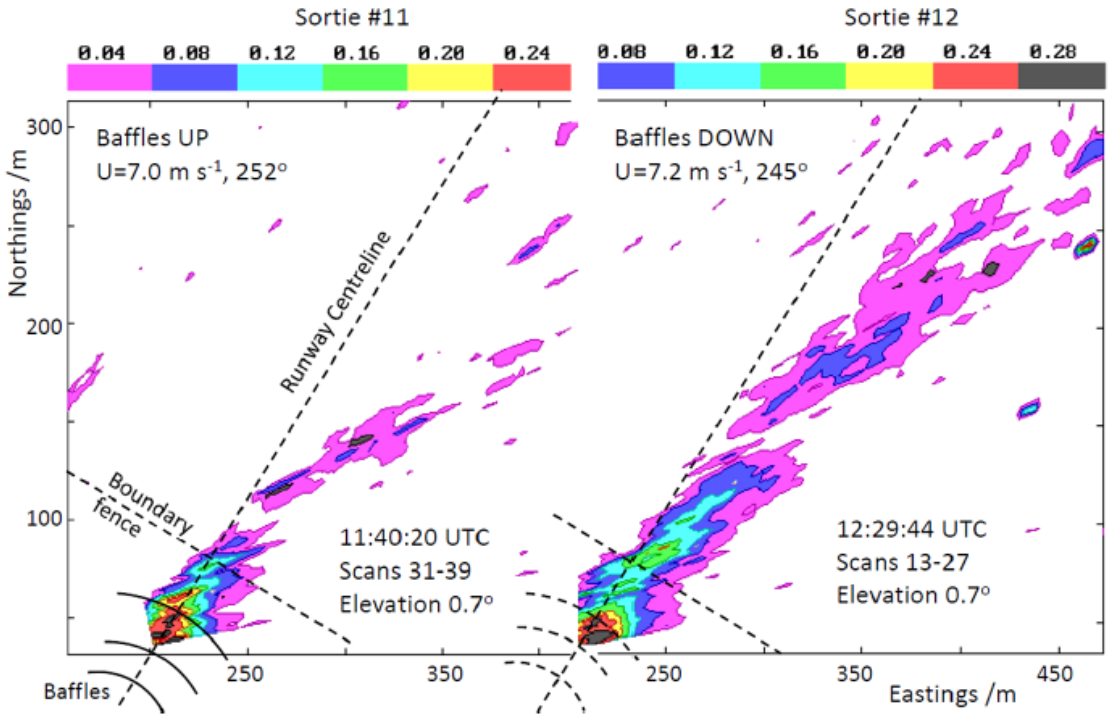

Figure 8.6: Comparison of averaged Lidar results for Sortie 11 (baffles up) and Sortie 12 (baffles down) for an elevation of 0.7º (taken from Bennett et al., 2013)

Coordinates are given in east (x) and grid north (y) direction relative to the Lidar position; plot contours are given as excess concentration relative to the measured ambient concentration

Comparing Sortie 9 and 10 (*Figure H.6* and *Figure H.7* in Appendix H), the plume concentrations near the baffles at 0.7º elevation appear to be reduced in the case of Sortie 10 as the plume is deflected upwards. However, further away from the baffles the concentrations appear to be the same at 0.7º and slightly higher at 4.5º in the case of Sortie 10. Bennett et al. (2013) concluded that the effect of the baffles in reducing near-surface concentrations is extremely sensitive to the distance between the jet source and the array of baffles. The analysis showed that in the case of Sortie 10 the jet had already lifted far enough from the ground for the baffles to be no longer fully effective (Bennett et al., 2013, p. 2350), while in the case of Sortie 11 the jet had been still close to the ground. At the same time, the plume of Sortie 10 was also observed to remain coherent at 4.5º elevation (see *Figure H.7b*), similarly to Sortie 11, while no coherent plume was observed at this elevation in the cases without baffles (Sortie 9 and Sortie 12).

The measurements of the point-sample air quality sensors (see NO data column of *Table 8.4*) are consistent with the Lidar results with regard to the baffle effectiveness between Sortie 10 and Sortie 11. The detected NO concentrations are significantly lower in the case of Sortie 11, i.e. nearly half the concentrations recorded during Sortie 12, and are similar for Sortie 9 and 10. At the same time, the peak values of particulate matter, measured by the Osiris particle counters, do not show the same trend (see *Table 8.4*). The data for PM_{10} show clearly a significant reduction when the baffles are present (both Sortie 10 and Sortie 11), however, the results for $PM_{2.5}$ and PM_1 are inconclusive as they also show low values in the case of Sortie 12. From all three cases, Sortie 10 appears to give the lowest peak values of particulate matter.

The vane anemometer measurements at the boundary fence and 2.1 m height above the ground also show significant reduction in wind speed for Sortie 10 and Sortie 11. The higher value for Sortie 11 is due to the closer starting position of the aircraft and the higher ambient wind speed.

Table 8.4: Lidar and air quality measurements for Sortie 9 to 12 (data from Bennett et al., 2013)

Sortie No.	Baffles	Lidar, peak values*	Osiris, peak values**				NO data*** [ppm]
			Wind speed [m/s]	PM_{10} [$\mu g/m^3$]	$PM_{2.5}$ [$\mu g/m^3$]	PM_1 [$\mu g/m^3$]	
9	down	0.47	46.4	47.92	16.61	6.70	69.5±0.6
10	up	0.47	22.4	10.11	5.24	2.08	62.8±0.5
11	up	0.27	26.0	12.35	7.27	2.70	43.2±0.4
12	down	0.66	44.8	63.15	6.18	2.74	82.7±0.6

* Peak values above the Osiris unit close to the intersection of the boundary fence and the extended runway centre line

** Data measured by the Osiris unit located close to the intersection of the boundary fence and the extended runway centre line; PM data are measured aerosol peak values above the background values

*** Values are summed over all point-sample sensors and integrated over the time passage of the plume

The acoustic measurements showed that the presence of the baffles yielded a modest acoustic benefit of ~2 dB along the extended runway centre line, attributed to their shielding effect, i.e. creating an acoustic barrier (Bennett et al., 2013, p. 2351). This is a positive result since noise reduction is not considered of primary importance within the baffles concept. In fact, the acoustic measurements were performed mostly to identify whether any negative effects in terms of ambient noise occur due to the presence of the baffles.

8.7 Discussion

As stated in Bennett et al. (2013), the performed measurements during the field trials appear to be conclusive on the positive effect of the baffles on the plume dispersion, provided that the baffles are located sufficiently close to the starting position of the jet source. This is in agreement with the conclusions of the sub-scale wind tunnel tests. In practice, it would require the aircraft starting position for the take-off run to be as close as possible to the runway threshold for the array of baffles to be effective. This is usually the case for large, heavy aircraft which wish to use all of the available runway distance and which in turn also have a greater impact on local air quality. If the baffles concept is to be implemented in practice, the individual baffles must be sufficiently robust to withstand the strong jet blast and at the same time they need to comply with the statutory frangibility criteria in case they are stuck by an aircraft. During the field trials, after the occurred structural failure during Sortie 2 and Sortie 3, the necessary robustness was achieved by using stronger shear pins, increasing the prescribed maximum bending moment of 600 Nm. For a permanent installation, the array needs to consist of narrower baffles in order to distribute the wind loading on a larger number of individual baffles and thus reduce their individual wind loading whilst maintaining the same baffle height.

Considering the practical relevance of the performed measurements, it should be noted that during the field trials the aircraft was allowed a 10 s static burn prior to starting the take-off run in order to produce a jet exiting from a stationary source and thus to allow more time for the measurements to be performed and to be able to identify the effect of the baffles more clearly. Such measurements during a static burn are not entirely representative for a typical aircraft take-off run, where the jet source accelerates away from the baffles, making them less effective. In practice, the effect of the baffles would be mostly on the initial jet blast. At the same time, the performed static burn and averaged Lidar scans allow for a simplified take-off run representation at sub scale, using a stationary nozzle and taking averaged concentration measurements.

In terms of data correlation, the available Lidar results are relative to the background (ambient) concentrations, measured prior to each sortie, while the conducted Flame Ionisation Detector (FID) measurements at sub scale provided point-sample concentration data in parts per million (ppm) of a tracer gas in the exhaust plume. Therefore a complete correlation is not possible, however, the Lidar results provide important information on the plume lateral spread and near-surface concentrations, showing the effect of the baffles. Comparing *Figure H.7a* (Sortie 10) and *Figure H.8a* (Sortie 11) to *Figure 7.8*, close to the ground, there is a noticeable difference between the lateral location of the plume at full scale and sub scale relative to the extended runway centre line. The Lidar measurements during Sortie 11 show that the plume was approximately symmetrical to the extended runway centre line at the boundary fence. This is due to the close position of the aircraft relative to the baffle array and the resulting exhaust jet of greater velocity at the fence, not affected significantly by the ambient wind. At the same time, the sub-scale measurements show a displaced plume towards the leeward side of the runway line (relative to the ambient wind direction). Thus, at this location and height, the ambient wind at sub scale (wind tunnel flow) has a more significant influence on the plume compared to the ambient wind at full scale. As the ratio of ambient wind velocity to jet velocity was matched at full scale and sub scale at the jet source, a possible explanation for this difference would be a greater velocity decay with distance downstream of the sub-scale nozzle jet compared to the engine jet. This would increase the ratio of ambient wind velocity to local jet velocity at sub scale, resulting in a possible drift of the plume from the centre line in the direction of the cross flow.

Further comparisons between full scale and model can be made in terms of the lateral spread of the observed plume, i.e. at right angles to the runway direction. At sub scale, the edges of the plume were difficult to estimate from *Figure 7.8* and *Figure 7.9*, therefore the y coordinates of zero concentration were extrapolated numerically from the measured concentrations. At the boundary fence line, i.e. 101 m from the runway threshold, the lateral spread of the plume is estimated to be 73 m and 81 m for Sortie 11 and Sortie 12 respectively. The corresponding values at full scale are 39 m and 42 m, estimated from the plots of *Figure H.8a* and *Figure H.9a* respectively. For Sortie 12 in full-scale, a lateral spread of 54 m was also calculated at 86 m from the runway threshold. There is a significant difference between the estimated values at full scale and model, i.e. the sub-scale plume appears to be approximately double in size. Therefore, they were further compared to the typical values for the lateral spread of a three-dimensional wall jet, found in the literature and listed in *Table 2.2* in Chapter 2.3. For a distance x from the source, the half-width of a wall jet in lateral direction is estimated to be between $0.25x$ and $0.3x$. Thus, at a distance of 139 m, i.e. the distance of the aircraft's engines from the fence during Sortie 12, the estimated lateral spread would be

between approximately 70 m and 83 m. This is in good agreement with the calculated sub-scale lateral spread. However, it appears that the Lidar data shows a much narrower plume. Furthermore, from *Figure H.9a* it is evident that the lateral spread of the plume decreases between 86 m and 101 m from the runway threshold. In general, the plumes detected by the Lidar do not exhibit the expected lateral growth rate. In the opinion of the author, the Lidar plots do not show the low concentrations near the edges of the plume, therefore the estimated lateral spread is not representative for the complete plume.

While the measurements during Sortie 9 to 12 were successful in terms of the quality of the data and the robustness of the baffle arrangement, two possible issues should be mentioned: 1) There are no additional measurements to confirm the repeatability of the favourable results of Sortie 11 in terms of reduction of near-surface concentrations; 2) The ambient wind influence on the results is not taken into account when comparing Sortie 10 and Sortie 11 to determine the effect of the source distance to the array of baffles. The importance of the latter is highlighted by the lower ambient wind speed during Sortie 10, which would have a smaller suppressing effect on the lift-off of the jet compared to the higher ambient wind speed of Sortie 11. The strong influence of the secondary (ambient) flow on the jet development and possible lift-off was also observed during the initial experiments (see Chapter 4). With regard to 1), additional Lidar measurements were planned at Cranfield Airport using a sub-scale baffle array and an Unmanned Aerial Vehicle (UAV) model gas turbine, mounted on a trailer. These are described in the following section.

8.8 UAV turbine field trials

The positive outcome of the BAe 146-301 field trials and the observed differences between Sortie 10 and Sortie 11 aroused further interest to investigate the influence of the distance between the baffles and the jet source on the baffles' effectiveness. Further full-scale measurements were not possible due to the high cost and limited availability for hiring the BAe 146-301, therefore additional field trials were planned with sub-scale baffle models and a small gas turbine, used primarily on radio-controlled UAVs. To date, two unsuccessful attempts to conduct Lidar measurements with this arrangement were made at Cranfield Airport due to adverse weather conditions and problems with the UAV gas turbine and the measurement equipment. This section includes a brief description of the planned test arrangement and a summary of the key scaling issues to be addressed.

The available engine is an Olympus HP gas turbine (see *Figure I.1* in Appendix I), manufactured by AMT Netherlands, with a maximum thrust of 230 N. More specifications are included in *Table I.1* in Appendix I. The engine is started using flows of compressed air and propane, delivered from external cylinders via two separate tubing systems, to spin the compressor and to ignite the burning process respectively. Once started, the engine is fuelled with a mixture of 95% kerosene and 5% AeroShell 500 synthetic turbine oil, delivered by a small electric pump. At maximum thrust, the engine has a total mass flow rate of 0.45 kg/s for a fuel consumption of 0.64 kg/min. The turbine operation is controlled remotely with an automatic Electronic Control Unit (ECU). More information on the Olympus HP can be found in AMT Netherlands (2014).

During tests, the Olympus HP and the auxiliary equipment, needed for its operation, are mounted on a trailer at nominally 0.75 m ground clearance to the exhaust nozzle centre line. This distance is the smallest ground clearance that could be achieved with the planned test equipment, since the turbine has to be mounted safely on a wooden support fixed to the trailer body. Another issue with the trailer to be used is the presence of a large wake downstream which would interfere with the exhaust jet. The wake can be reduced by using a smaller trailer or alternatively its influence can be minimised by performing the tests at low ambient wind or with the baffles arrangement angled, creating a cross flow. However, the latter two cases are of little practical significance since low-wind conditions would not represent a realistic environment to demonstrate the effects of the baffles and a cross flow would deflect the exhaust plume away from the baffles. If dynamic tests are to be considered, where the take-off run would be simulated by an accelerating ground vehicle pulling the trailer away from the baffle array, the wake behind the turbine would be enhanced by the presence of the vehicle and its movement relative to the ambient air.

Further issues with the experimental arrangement would be the measurement equipment to be used and the appropriate scaling of the experiment with regard to the full-scale BAe 146-301 trials. The plume dispersion measurements are to be performed with the same Lidar, which during the BAe-146 trials had a range resolution of 5 m. At the reduced scale of the experiment, such resolution would not be able to capture sufficient details of the exhaust plume (see predicted jet width in *Table I.2* in Appendix I, as given by Bennett, 2012). Therefore, efforts were made to reduce the Lidar resolution to 1.2 m using an onboard digitiser card (Bennett, 2012). To create a visible exhaust jet, which is advantageous for the Lidar detection, a modest quantity of low-volatility oil would be injected at the UAV turbine exit through a simple Venturi system. Since the Lidar requires a measurement distance of 250-300 m between its position and the plume, a suitable location was proposed at the eastern end of Cranfield Airport's taxiway (see *Figure I.2* in Appendix I). With the exhaust jet path and baffle array

aligned at the taxiway in direction of Runway 03, as shown in *Figure I.2*, the Lidar van would be located close to the intersection of the runway and the taxiway. Such arrangement is adopted due to the predominant south-westerly winds at Cranfield Airport. In case of cross winds, the arrangement can be turned into the cross wind and the Lidar can be moved towards the south-eastern end of the airport. The only foreseeable issue in such case would be any vegetation (< 0.5 m) surrounding the taxiway, which would obstruct the Lidar measurements close to the ground.

Aside from the Lidar measurements, plans are made for velocity profile measurements downstream of the baffle array using a Pitot-rake of 15 probes, located at nominally 10 cm intervals and connected to Omega PX139 pressure transducers. The data acquisition and data processing systems are to be powered using an external battery.

The main issue of the UAV trial arrangement is to determine the scaling of the baffle models, resulting from the smaller thrust of the engine used (230 N) compared to the total thrust of the BAe-146 engines (124 kN) during the full-scale field trials. A possible scaling parameter would be the jet Froude number, identified in Chapter 2.6 as one of the governing similarity parameters in buoyant flows. Using Froude number equality, a geometric scaling $\lambda \approx (\dot{m}_M / \dot{m}_F)^{0.4}$ can be obtained with the calculation sequence included in Appendix G, where $\dot{m}_M / \dot{m}_F$ is the ratio of the total engine mass flow rates at sub scale and at full scale. With $\dot{m}_F$ = 349.5 kg/s (all four ALF502-R5 engines) and $\dot{m}_M$ = 0.45 kg/s, the calculated scaling is approximately 1:14.3. It should be noted that in the calculation sequence a geometric similarity is assumed between the UAV turbine and a fictive single engine, which would combine the mass flow of all four full-scale engines.

Another method of determining the size of the baffles is to scale them relative to the estimated plume size, as proposed by Bennett (2012). During the BAe 146-301 field trials, the baffle vertical heights were typically $0.015\Delta z$, where Δz is the estimated plume height at each baffle row. With full-scale slope heights of 1.0 m, 1.7 m and 2.0 m, this scaling method yields model slope heights of 9.9 cm, 12.3 cm and 15.2 cm respectively. The corresponding values using Froude number scaling (λ = 1:14.3) are 9.8 cm, 11.9 cm and 14.0 cm, thus both methods yield similar scaled values. The second method was adopted for the provisional baffle models.

Further scaling issues would arise if dynamic tests are to be performed, where the jet source is accelerated away from its initial position. Using Froude number equality the sub-scale acceleration would equal the one at full scale (see derivation in Appendix I), which during the BAe 146-301 trials was approximately 3.1 m/s^2. Another method of calculating the sub-scale acceleration is on the basis of the mass of the jet (Bennett, 2012), which estimated a sub-scale acceleration of $0.9g$, i.e. nearly three times the full-scale acceleration and too large to be considered. An acceleration of 3.1 m/s is more

realistic, however, still practically not achievable by a ground vehicle pulling a trailer. It is evident that if dynamic tests are to be conducted, the jet source acceleration would be limited by the ground vehicle's performance characteristics.

The aim of the UAV trials is to confirm the results of the full-scale field trials and to demonstrate further the positive effect of the baffles on the exhaust plume dispersion, investigating the influence of the distance between source and baffles in a controlled experiment. For this purpose, the original full-scale arrangement is modified as follows. First, the baffle array consists of straight rows of simple wooden plates, all inclined at 60º to the horizontal and arranged laterally at right angles to the jet (see *Figure I.2* and *Figure I.3* in Appendix I). The baffles can be arranged relatively easy using a rope with knots to mark the distances between each row. Second, a fourth, smaller row is added closer to the jet source (see *Figure I.3*) – due to the simple baffle models used, adding another row is not as expensive as it would have been in the full-scale trials. The distances between the rows are not scaled down from the full-scale arrangement, but are determined from the predicted point of the jet reaching the ground and the start of the expected buoyant rise without the baffles present, which are 4 m and 8 m respectively (Bennett, 2012). The spacing is nominally 8.3 times the slope height of the previous row. The arrangement parameters are shown in *Table I.2* of Appendix I.

To date, two attempts were made to conduct the UAV trials with the above arrangement – in November 2012 and July 2013. No measurements could be performed due to adverse weather conditions and issues with the Lidar and the UAV turbine. Plans have been made for a third attempt in 2014, however, their fulfilment depends on the available funding by the team of researchers from Manchester Metropolitan University, performing the Lidar measurements, and the availability of the UAV engine, which is owed by the Department of Aerospace Sciences of Cranfield University.

9 Conclusion

The principle aim of the research project was to explore the possibility of using aerodynamic baffles to enhance the dispersion of the aircraft exhaust plume at take-off and thus improve local air quality at airports. The thesis work focused primarily on the design and sub-scale modelling of the baffles, using a variety of wind tunnel testing methods. This final chapter includes a general discussion on the key findings and issues, followed by the reached conclusions and suggestions for future work.

9.1 Summary

The general concept of this work consists of placing an array of windbreaks (‘baffles’) in the runway end safety area, which should remove sufficient horizontal momentum from the high-temperature exhaust jet at take-off, allowing its vertical momentum due to buoyancy to become dominant and lift the exhaust plume away from the ground (‘lift-off’). Such buoyant rise would reduce the concentration of exhaust emissions at ground level.

In view of the above, the planned wind tunnel experiments were conducted in two stages. First, during the initial stage, the effects of the baffles on the flow development were studied using flow visualisation. Additional wind tunnel tests were performed to study the flow field around porous screens in order to obtain preliminary design parameters of the baffles, such as slope angle and porosity, i.e. the ratio of the open area to the total area of the screen. Second, the aerodynamic drag of various baffle configurations was measured with a one-component force balance, in order to identify a suitable configuration to be tested at full scale using baffle prototypes.

The initial flow visualisation experiments with a plain wall jet (no baffles) showed that increasing the jet buoyancy, i.e. by adding helium to the nozzle flow, and reducing the ratio of freestream velocity to exit jet velocity β both increased the vertical spread of the plume. Reducing β also significantly increased the lateral spread of the plume. At increased buoyancy, parts of the top of the plume were observed to separate, however the main plume body remained attached to the ground.

Additional tests were performed with a single baffle row in the path of the jet and a lift-off of the coherent plume, i.e. complete detachment from the working section floor surface, was observed only under the following conditions:

- no freestream ($\beta = 0$) and
- a baffle row present in the path of the jet.

Without the baffle row and at $\beta = 0$, no lift-off was observed within the rage of tested longitudinal distances (up to 177 nozzle diameters). The baffle concept of promoting the lift-off of the plume was demonstrated by comparing the plume at the same distance downstream of the nozzle without a baffle row in the path of the jet (no lift-off observed) and with a baffle row in the path of the jet (the plume was observed to separate from the surface). Overall, the velocity ratio β and the position of the baffle row relative to the nozzle exit were observed to have a significant role in the development of the plume with distance downstream.

The experimental results on the flow in the near field of porous screens showed that the pressure drop coefficient of the screens, representative for their aerodynamic drag, approached a constant value as the flow Reynolds number increased, suggesting Reynolds number independency. This was a positive result in view of the small scale (1:200) of the planned wind tunnel experiments, where complete Reynolds number equality could not be achieved. The flow visualisation experiments showed that significant vortex shedding occurred downstream of screens of porosity smaller than 0.20, similarly to the flow around a solid flat plate. In view of this, a material of 0.20 porosity was chosen for the baffle prototypes, in order to reduce the aerodynamic load from the jet blast and t avoid vortex shedding.

In order to obtain an optimum baffle configuration to be tested at the full-scale field trials, the drag of various configurations of baffle rows, subjected to a freestream and a nozzle jet, was measured with a one-component force balance. The measurements were performed with straight and arc-shaped baffle rows, orientated perpendicular to the flow direction. Configurations of three, four and five rows of progressively increasing height were considered for the field trials. The method was found to be sufficiently accurate to investigate the trends of drag behaviour with number of baffle rows, their spacing and slope angle.

The drag results showed only small variations with freestream Reynolds number for $Re > 18000$, based on the baffe row height h_5. This is of significant importance as it suggests that precise sub-scale wind tunnel modelling of the effects of the baffles can be performed at a significantly lower Reynolds number compared to full scale, while at the same time a complete Froude number equality at sub scale and full scale can be achieved. A complete Reynolds number equality at sub scale and full scale was not possible due to the low scale of the wind tunnel experiments. In a freestream, a three-row configuration of spacing between the rows equal to 12 times the slope height of the previous row was found to exhibit ~ 90% of the drag of the corresponding five-row configuration. In a combination of a freestream and nozzle jet, the same results were observed if the first row of each of the configurations was located at the same distance from the nozzle. In order to minimise the costs for manufacturing of the baffle

prototypes and to reduce the time and costs needed for transportation and preparation of the field trials arrangement, the three-row configuration was favoured over the initially proposed five-row configuration. Since no significant differences in the drag results were observed between the arc-shaped and straight rows, the arc-shaped configuration was favoured as it is advantageous in case of cross winds.

With an identified baffle configuration to be tested, the effects of the baffles were first investigated in full-scale field trials, which were later replicated in sub scale in Cranfield University's 8'×4' Atmospheric Boundary Layer Wind Tunnel. Additional wind tunnel tests were conducted with a modified arrangement in order to expand the scope of the experiment.

Following the results of the force balance tests, baffle prototypes were designed in accordance with the failure mode and frangibility criteria, specified by the International Civil Aviation Organization (ICAO, 2006a) for structures located in the runway end safety area. Apart from complying with the regulations, the design was also concerned with the need for a relatively quick and easy way to erect and deflate the prototypes.

The baffle prototypes were tested during field trials at Cranfield Airport in cooperation with researchers from other academic institutions in the UK. The tests consisted mainly of dispersion measurements, using Lidar scans, particle counters and air quality sensors, of the exhaust plume of a BAe 146-301 aircraft performing take-off and landing cycles (sorties). The measurements were taken during 10 seconds of static burn (brakes engaged) before each take-off. Reliable results were collected from four sorties – two with the baffles erected (Sortie 10 and Sortie 11) and two with the baffles deflated (Sortie 9 and Sortie 12). The Lidar measurements show reduced concentrations close to the ground and downstream of the baffles only during Sortie 11 when the aircraft was located closer to the baffle array. The positive results of Sortie 11 were confirmed by the air quality measurements of nitrogen oxide downstream of the baffles. The peak values measured by the particle counters were lower for Sortie 10 compared to Sortie 11. However, both values were considerably lower compared to the ones of Sortie 9 and Sortie 12

While the results of Sortie 11 and Sortie 12 appear to be conclusive about the enhanced dispersion of the plume near the ground, caused by the baffles, there are no additional measurements to confirm this. The unfavourable results of Sortie 10 also indicate that the aircraft would need to be located very close to the runway threshold in order for the baffles to be effective. Such starting position is normally requested by large aircraft which require a longer take-off distance. With regard to the applicability of the baffles, they would need to be sufficiently robust to withstand the strong jet blast. During the first sorties of the field trials, the shear pins failed as a result of the strong

blast, which led to the baffle rows collapsing. For this reason, during Sortie 11 the baffles were already reinforced with stronger shear pins.

It should also be noted, that the results of the field trials to a large extent show the effect of the baffles following a static burn of 10 seconds, which cannot be considered entirely representative for the standard take-off run.

In view of the above considerations, based solely on the results of Sortie 11, the applicability of the baffles at present time is not possible without an infringement of the ICAO regulations. Furthermore, in the opinion of the author, the results of Sortie 11, as accurate as they may be, cannot be considered conclusive without verifying their repeatability by means of additional results. Therefore, further tests are needed in order to assess accurately the effect of the baffles with regard to their applicability at airports.

Two attempts were made to conduct additional, sub-scale field trials with a UAV model gas turbine. Due to adverse weather conditions and issues with the equipment used, no measurements could be performed. The planning and progress made to date are described in Chapter 8.8.

In order to replicate the field trials in sub scale, the temperature and exit velocity of the BAe 146-301 exhaust jet were calculated with an analytical method, applying the Thrust Equation and the Steady Flow Energy Equation across a control volume around the engine. It assumed fully-mixed jet conditions shortly downstream of the exit nozzle. The method was applied to a PW4000 engine, for which contours of temperature and velocity downstream of the engine were available at Airbus (2014a). The calculated exit velocity showed excellent agreement, i.e. less than 2% difference, while the exit temperature was overestimated by approximately 10%. By all means, the calculated temperature and velocity with such method would be representative for a turbojet engine of the same mass flow rate, fuel consumption and maximum thrust.

The aircraft was modelled in sub scale with a single, stationary nozzle providing the jet. While the use of a stationary nozzle is justified by the performed static burn during the field trials, the choice of single nozzle to model a merged jet of initially four single jets was necessary for practical reasons. Ideally, the single-jet and merged-jet development with distance from the nozzle should be studied and compared in terms of velocity decay and plume growth rates in lateral and vertical direction in order to determine a suitable position of the single-jet nozzle relative to the baffle array.

The full-scale exhaust jet was modelled in the wind tunnel according to the method by Littlebury (1981) and Garry (1989). The sub-scale calculations were done by means of three similarity parameters: the jet Froude number, the ratio of jet density to ambient density and the ratio of ambient wind velocity to jet exit velocity. Due to the low scale of the experiments, the Reynolds number could not be equalled in full scale

and sub scale. A positive result with regard to this issue was observed during the drag measurements of the baffle configurations, where only minor variations of the results with Reynolds number were evident. The nozzle flow rate and diameter were calculated from the total mass flow rate of the BAe 146-301 engines.

The Atmospheric Boundary Layer profiles of mean velocity and turbulence intensity were calculated in sub scale using the methods of ESDU (1982) and ESDU (1983). A good match of the calculated and measured mean velocity profile in the working section was obtained, except very close to the ground. The measured turbulence intensity profile showed considerable differences compared to the ESDU calculations up to heights corresponding to 40 m at full scale. In the initial plume flow visualisation experiments, the size of the plume was shown to increase considerably if the turbulence intensity of the boundary layer was increased significantly by modelling the Atmospheric Boundary Layer. The lower measured turbulence intensity values close to the ground compared to the ESDU profile are considered to have an effect on the development of the plume.

Sortie 10, 11 and 12 were replicated at 1:200 scale in terms of the aircraft engine position relative to the baffle array and the recorded ambient speed and direction. Mean concentration measurements were performed at locations downstream of the baffles as far as 200 nozzle diameters d, using a Flame Ionisation Detector (FID) method.

The results at 1:200 scale show higher mean concentrations of Sortie 11 compared to Sortie 10 and 12 at all heights from the ground between 4.2d and 16.7d at the boundary fence line. Very close to the ground, at 0.4d, Sortie 11 has significantly lower concentrations compared to Sortie 12. At equal distances from the respective nozzle position, Sortie 11 gives a small reduction in the peak concentrations at 4.2d, compared to Sortie 10 and Sortie 12. This was observed at 132 and 148 diameters downstream of the nozzle, corresponding to full-scale distances of 134 m and 154 m from the runway threshold respectively. At greater heights, the concentrations are higher compared to Sortie 10 and Sortie 12.

Thus, it can be concluded that the effect of the baffles is predominately to increase the vertical spread of the plume, giving higher concentrations away from the ground. By comparing Sortie 10 and Sortie 11, it was found that this effect was stronger if the source was located closer to the baffles, which is in agreement with the general conclusions of the field trials. It appears that there is a small positive effect of the baffles also further downstream, observed up to 148 nozzle diameters. The plume of Sortie 11 was not observed to lift off within the distances tested, thus the positive Lidar results could not be reproduced in sub scale.

A qualitative comparison of the contours of mean concentrations with the Lidar data shows a noticeable difference in the lateral position of the plume of Sortie 11 between full scale and sub scale. The full-scale plume is oriented approximately

symmetrical to the extended centre line, while the sub-scale plume is shifted in the direction of the ambient wind. Thus, the ambient wind seems to have a more significant influence on the sub-scale plume. A possible explanation for this could be a greater velocity decay of the sub-scale nozzle with distance downstream, compared to the engine jet. In such case, the ratio of ambient wind velocity to local jet velocity would increase with distance from the nozzle at sub scale, affecting considerably the development of the flow and the accuracy of the model.

Finally, in the experiments without cross flow the mean concentrations and velocities were measured at the runway centreline. The FID measurements showed the sheltering effect of the baffles, reducing the concentrations on the runway line and extending to a downstream distance of 110 diameters (132 m in full scale). The plume downstream of the baffle array was found to have a bell shape, as a result of the increased vertical spread and higher concentrations away from the ground in close proximity to the plane of symmetry of the plume. A single baffle row, located at the runway threshold, was also tested and was found to reduce considerably the mean concentrations up to 200 nozzle diameters. It was not observed to cause lift off of the plume.

Measurements of mean velocity showed that although the baffle array increased the concentrations on the runway line downstream of 110 diameters, the reduction in velocity downstream of the array continued until 170 diameters (furthest measurement point) and possibly beyond.

9.2 Conclusions of work

Coming back to the aims of the thesis, the experimental investigation aimed to answer the following research question:

Can an array of windbreaks (baffles) cause the plume of an aircraft at take-off to overcome sooner the Coanda effect and lift-off from the ground, thus enhancing the dispersion of the plume and reducing the exhaust emissions close to the ground?

The following conclusions were reached from the conducted research:

- The baffle concept of promoting the rise of a ground-based buoyant jet was demonstrated successfully in the wind tunnel. The presence of a baffle row causes the plume to separate from the surface after a shorter travel distance. However,

lift-off was shown to occur only in tests without the presence of wind tunnel flow. Thus, the baffles concept was found to be significantly dependent on the ambient wind speed.

- The full-scale Lidar measurements during Sortie 11 showed low concentrations close to the ground downstream of the baffle array, which was attributed to a lift-off of the plume and thus highlighted the positive effect of the baffles on the emissions dispersion away from the ground. An attempt was made to reproduce this in 1:200 scale, however, no lift-off was observed. The observed shift of the jet position with respect to runway line, compared to the symmetrical orientation of the jet in the Lidar images, suggests a stronger wind effect in sub scale, which would constrain the buoyant plume.

- In sub scale, the effect of the baffles on the plume concentrations was observed to be mainly local with regard to the reduction of mean concentrations. The concentrations close to the ground are reduced downstream of the last row due to the sheltering effect of the baffle array and the vertical extent of the plume is increased. This leads to increased concentrations away from the ground, which were observed to persist far downstream. After a certain distance downstream, the reduced concentrations on the ground become higher than those of the plain jet.

- A small positive effect of the baffle array was observed for Sortie 11 compared to Sortie 12 in terms of mean peak concentration as far as 148 diameters downstream (154 m from the runway threshold in full scale).

- Overall, the results of the full-scale and sub-scale investigations seem to be inconclusive with regard to the applicability of the baffles at full scale. The sub-scale model indicates only local effects in proximity of the baffles, while the full-scale measurements, based on one particular measurement, suggest a positive effect if the aircraft is located sufficiently close. Additional field trials are recommended to attempt to replicate the positive full-scale result.

9.3 Future work

Based on the results of the full-scale Lidar measurements and the wind tunnel experiments at 1:200 scale, further field trials were planned at Cranfield Airport with an Unmanned Aerial Vehicle (UAV) model gas turbine providing the exhaust jet. The tests would attempt to repeat the successful results of Sortie 11 in terms of reduced exhaust emissions close to the ground, replicating the full-scale field trials with a similar baffle

arrangement in a smaller scale. To date, two attempts were made to perform the tests, both of which were unsuccessful due to adverse weather conditions and issues with the test equipment. The planned test arrangement was discussed in Chapter 8.8 together with the proposed scaling of the baffle models and some practical issues with regard to the Lidar measurements. During the first two attempts, only static tests were planned, as they required a simpler test arrangement and less demanding execution procedure. While the results of such tests would contribute significantly to the research work, of decisive importance in future attempts would be to conduct tests with an accelerating or moving source away from the baffle array, in order to model an aircraft take-off run.

With regard to future wind tunnel experiments, the accuracy of the jet model should be considered of high importance in order to reproduce the correct jet development at sub scale. If a multiple-engine configuration is modelled with a single nozzle, the flow development of both the single-nozzle and the multiple-nozzle jets should be studied and compared in terms of jet development and velocity decay with distance downstream. Based on this comparison, the distance between the single nozzle and the baffle array should be determined such as to give the correct multiple-nozzle jet dimensions and velocity at the location of the baffle array. Furthermore, care should be taken when modelling the ambient wind at sub scale in order to represent accurately its effect on the jet development. As was shown in this investigation, the ambient wind plays a key role in preventing the plume from lifting off.

Additionally, more accurate jet source models could be considered, such as a moving nozzle in order to simulate an aircraft take-off run. The effect of the moving nozzle on the jet development should be studied in order to determine a suitable rate of acceleration. Such arrangement would also require performing instantaneous measurements in order to capture the starting plume. The issues observed in this investigation, preventing the execution of such measurements, were the lag in the measurement equipment and the high turbulence intensity within the modelled Atmospheric Boundary Layer. Attempts to minimise the lag in the measurement equipment should be made, however, more importantly, it should be accurately quantified and accounted for in the post-processing of the measurements. With regard to the high turbulence intensity, the fluctuations in the measured data could be used to draw conclusions on the peak concentrations and their probability of occurrence. For such analysis, the Atmospheric Boundary Layer should have a good match at full scale and sub scale in terms of the mean velocity and turbulence intensity profiles in the working section.

Finally, extending the domain of the measurements could prove important in observing a plume lift-off, for example, Aloysius & Wrobel (2009b) reported a lift-off distance of 363 diameters downstream of the engines in a numerical investigation of an exhaust jet at take-off. Due to constraints in the movement of the traverse, in this

investigation the maximum distance tested was 200 nozzle diameters from the nozzle exit, or 240 m at full scale. When considering the possibility of installing arrays of baffles at airports, their impact on the local air quality should be demonstrated over significantly larger distances.

References

ABRAHAMSSON, H., JOHANSSON, B., LÖFDAHL, L. (1994). A turbulent plane two-dimensional wall-jet in a quiescent surrounding. *European Journal of Mechanics: B/Fluids*, 13(5), p. 533-556.

ABRAHAMSSON, H., JOHANSSON, B., LÖFDAHL, L. (1996). An investigation of the turbulence field in a three-dimensional wall jet. In: *Turbulence VI. Proceedings of the 6th European Turbulence Conference*, Lausanne, Switzerland, 2nd-5th July 1996, edited by S. Gavrilakis, L. Machiels, P.A. Monkewitz. Kluwer Academic Publishers, Dordrecht, The Netherlands, p. 417-420.

AGELIN-CHAAB, M., TACHIE, M.F. (2011a). Characteristics of turbulent three-dimensional wall jets. *Journal of Fluids Engineering*, 133(2) 021201, p. 1-12, DOI: 10.1115/1.4003277.

AGELIN-CHAAB, M., TACHIE, M.F. (2011b). Characteristics of turbulent three-dimensional offset jets. *Journal of Fluids Engineering*, 133(5) 051203, p. 1-12, DOI: 10.1115/1.4004071.

AIRBUS (2007). *Flying by nature: Global market forecast 2007-2026*. Report. Airbus, France. Available at: http://xesc.cat/pashmina/attachments/Flying%20by%20nature%20Global%20Market%20Forecast%202007_2026%20Airbus%20Report.pdf (accessed 18th September 2013)

AIRBUS (2014a). *A330 aircraft characteristics. Airport and maintenance planning*. Available at: http://www.airbus.com/fileadmin/media_gallery/files/tech_data/AC/Airbus-AC-A330-20140101.pdf (accessed 21st September 2014)

AIRBUS (2014b). *A320 aircraft characteristics. Airport and maintenance planning*. Available at: http://www.airbus.com/fileadmin/media_gallery/files/tech_data/AC/Airbus-AC_A320_May2014.pdf (accessed 21st September 2014)

ALOYSIUS, S.S., WROBEL, L.C. (2009a). Comparison of flow and dispersion properties of free and wall turbulent jets for source dynamics characterisation. *Environmental Modelling & Software*, 24(8), p. 926-937.

ALOYSIUS, S.S., WROBEL, L.C. (2009b). Large eddy simulation of plume dispersion behind an aircraft in the take-off phase. *Environmental Fluid Mechanics*, 9(4), p. 457-470.

AMT NETHERLANDS (2014). *Olympus HP turbine specifications*. Available at: http://www.amtjets.com/pdf/Olympus_HP_specification.pdf (accessed 21st September 2014)

ANDERSON, J.D. (2001). *Fundamentals of aerodynamics*, 3rd ed. McGraw-Hill, New York City, NY, USA.

ANNAND, J.D. (1953). The resistance to air flow of wire gauzes. *Journal of the Royal Aeronautical Society*, 57, p. 141-146.

ARMITT, J., COUNIHAN, J. (1968). The simulation of the atmospheric boundary layer in a wind tunnel. *Atmospheric Environment*, 2(1), p. 49-71.

AZIM, M.A. (2013). On the structure of a plane turbulent wall jet. *Journal of Fluids Engineering*, 135(8) 084502, p. 1-4, DOI: 10.1115/1.4024114.

BÄCHLIN, W., THEURER, W., PLATE, E.J. (1992). Dispersion of gases released near the ground in built up areas: Experimental results compared to simple numerical modelling. *Journal of Wind Engineering and Industrial Aerodynamics*, 44, p. 2721-2732.

BAKKE, P. (1957). An experimental investigation of a wall jet. *Journal of Fluid Mechanics*, 2, p. 467-472.

BARATIAN-GHORGHI, Z., KAYE, N.B., KHAN, A.A., SMITH, J.R. (2012). The merging of two unequal axisymmetric parallel turbulent jets. *Journal of Hydrodynamics*, Series B, 24(2), p. 257-262.

BARBOSA, P.H.A., CATALDI, M., FREIRE, A.P.S. (2002). Wind tunnel simulation of atmospheric boundary layer flows. *Journal of the Brazilian Society of Mechanical Sciences*, 24(3), p. 177-185.

BARENBLATT, G.I., CHORIN, A.J., PROSTOKISHIN, V.M. (2005). The turbulent wall jet. A triple-layered structure and incomplete similarity. *Proceedings of the National Academy of Sciences*, 102(25), p. 8850–8853.

BARLOW, J.B., RAE, W.H., POPE, A. (1999). *Low-speed wind tunnel testing*, 3rd ed. John Wiley & Sons, Inc., New York, NY, USA.

BENNETT, M. (2012). Private communication. Centre for Air Transport and the Environment, Manchester Metropolitan University, Manchester, UK.

BENNETT, M., CHRISTIE, S., GRAHAM, A., RAPER, D.W. (2010). Lidar observations of aircraft exhaust plumes. *Journal of Atmospheric and Oceanic Technology*, 27(10), p. 1638-1651, DOI: 10.1175/2010JTECHA1412.1.

BENNETT, M., CHRISTIE, S.M., GRAHAM, A., GARRY, K.P., VELIKOV, S., POLL, D.I.A., SMITH, M.G., IQBAL MEAD, M., POPOOLA, O.A.M., STEWART, G., JONES, R.L. (2013). Abatement of an aircraft exhaust plume using aerodynamic baffles. *Environmental Science & Technology*, 47(5), p. 2346-2352.

BENNETT, M., SUTTON, S., GARDINER, D.R.C. (1992a). Measurements of wind speed and plume rise with a rapid-scanning Lidar. *Atmospheric Environment*, 26A(9), p. 1675-1688.

BENNETT, M., SUTTON, S., GARDINER, D.R.C. (1992b). An analysis of Lidar measurements of buoyant plume rise and dispersion at five power stations. *Atmospheric Environment*, 26A(18), p. 3249-3263.

BLOCKEN, B., STATHOPOULOS, T., CARMELIET, J. (2007). CFD simulation of the atmospheric boundary layer: Wall function problems. *Atmospheric Environment*, 41(2), p. 238-252.

BOEING (2008). *Current market outlook 2009-2028*. Report. Boeing, USA. Available at: http://xesc.cat/pashmina/attachments/Boeing_Current_Market_Outlook_2009_to_2028.pdf (accessed 18th September 2013)

BOEING (2014). *Airport compatibility. Airplane characteristics for airport planning*. Available at: http://www.boeing.com/boeing/commercial/airports/plan_manuals.page (accessed 21st September 2014)

BRADSHAW, P., GEE, M. T. (1962). *Turbulent wall jets with and without external stream*. Aeronautical Research Council Reports & Memoranda No. 3252. Her Majesty's Stationary Office, Ministry of Aviation, London, UK.

BRIGGS, G.A. (1973). *Lift-off of buoyant gas initially on the ground*. Technical Report, ATDL Contribution No. 87. Atmospheric Turbulence and Diffusion Division, National Oceanic and Atmospheric Administration, Oak Ridge, TN, USA.

BRIGGS, G.A. (1975). Plume rise predictions. In: *Lectures on Air Pollution and Environmental Impact Analyses*, American Meteorological Society, Boston, MA, USA, p. 59-111.

BRUNDRETT, E. (1993). Prediction of pressure drop for incompressible flow through screens. *Journal of Fluids Engineering*, 115, p. 239-242.

BRUUN, H.H. (1995). *Hot-wire anemometry. Principles and signal analysis*. Oxford University Press, Oxford, UK.

BSI (1997). *Loading for buildings. Part 2: Code of practice for wind loads*. BS 6399, British Standards Institution, London, UK.

BUSSMAN, W., KARAN, J., FENNELL, T. (2003). A new method of reducing NOx emissions from heat treatment furnaces. In: Dahotre, N.B., Gaster, R.J., Hill, R.A., Popoola, O.O. (editors), *Proceedings of the 22nd Heat Treating Society Conference and the 2nd International Surface Engineering Congress*. Indianapolis, IN, USA, 15-17th September 2003.

CARLSON, J.D., FOSTER, M.R. (1986). Numerical study of some unstably stratified boundary-layer flows over a valley at moderate Richardson number. *Journal of Climate and Applied Meteorology*, 25(2), p. 203-213.

CARROTHERS, P.J.G., BAINES, W.D. (1965). Forces on screens inclined to a fluid flow. *Journal of Fluids Engineering*, 97, p. 116-117.

CERMAK, J.E. (1975). Applications of fluid mechanics to wind engineering – a Freeman Scholar lecture. *Journal of Fluids Engineering*, 97(1), p. 9-38, DOI: 10.1115/1.3447225.

CHEN, H.-B. (1991). *Turbulent buoyant jets and plumes in flowing ambient environments*. PhD Thesis. Department of Civil Engineering, Aalborg University, Aalborg, Denmark (Series Paper No. 3).

CHÈZE, B., CHEVALLIER, J., GASTINEAU, P. (2011). Forecasting world and regional air traffic in the mid-term (2025): An econometric analysis of air traffic determinants

using dynamic panel-data models. In: *18th Annual EAERE Conference*, Rome, Italy, 29th June - 2nd July 2011.

CHRISTIE, S. (2011). *Aerodynamic baffles trials at Cranfield Airport: Operational management and instructions during September 2011 trials*. Document Reference No. MMU/OM1.2. Manchester Metropolitan University, Manchester, UK (unpublished report).

CHU, C.-R., CHANG, C.-Y., HUANG, C.-J., WU, T.-R., WANG, C.-Y., LIU, M.-Y. (2013). Windbreak protection for road vehicles against crosswind. *Journal of Wind Engineering and Industrial Aerodynamics*, 116, p. 61-69.

CINI, C. (2008). *Modelling the interaction between aircraft wing trailing vortices and an engine exhaust plume in an atmospheric boundary layer*. MSc Thesis. Cranfield University, Cranfield, UK.

COOK, N.J. (1978). Wind-tunnel simulations of the adiabatic atmospheric boundary layer by roughness, barrier and mixing-device methods. *Journal of Industrial Aerodynamics*, 3, p. 157-176.

COOK, N.J. (1990). *The designer's guide to wind loading of building structures. Part 2: Static structures*. Building Research Establishment: Butterworths, London, UK.

COUNIHAN, J. (1969). An improved method of simulating an atmospheric boundary layer in a wind tunnel. *Atmospheric Environment*, 3(2), p. 197-214.

CRAFT, T.J., LAUNDER, B.E. (2001). On the spreading mechanism of the three-dimensional turbulent wall jet. *Journal of Fluid Mechanics*, 435, p. 305-326.

CULLOM, R.R., JOHNSEN, R.L. (1977). *Full-scale altitude engine test of a turbofan exhaust-gas-forced mixer to reduce thrust specific fuel consumption*. NASA TM X-3568. National Aeronautics and Space Administration, Washington, DC, USA.

DAI, Z., TSENG, L.-K., FAETH, G.M. (1994). Structure of round, fully developed, buoyant turbulent plumes. *Journal of Heat Transfer*, 116(2), p. 409-417, DOI:10.1115/1.2911413.

DANTEC DYNAMICS (2002). *How to measure turbulence with hot-wire anemometers – a practical guide*. Publication no. 9040U6151. Dantec Dynamics, Skovlunde, Denmark. Available at:

http://www.dantecdynamics.com/docs/support-and-download/research-and-education/practicalguide.pdf (accessed 21st September 2014)

DAVIDSON, M.J., MYLNE, K.R., JONES, C.D., PHILLIPS, J.C., PERKINS, R.J., FUNG, J.C.H., HUNT, J.C.R. (1995). Plume dispersion through large groups of obstacles – a field investigation. *Atmospheric Environment*, 29(22), p. 3245-3256.

DAVIDSON, M.J., SNYDER, W.H., LAWSON, W.E., HUNT, J.C.R. (1996). Wind tunnel simulations of plume dispersion through groups of obstacles. *Atmospheric Environment*, 30(22), p. 3715-3731.

DAVIS, M.R., WINARTO, H. (1980). Jet diffusion from a circular nozzle above a solid plane. *Journal of Fluid Mechanics*, 101(1), p. 201-221.

DEBONIS, J.R. (2008). RANS analyses of turbofan nozzles with wedge deflectors for noise reduction. In: *46th AIAA Aerospace Sciences Meeting*, Reno, NV, USA, 7-10th January 2008.

DECC (2014). *Annual Mean Speed Map*. Available at: https://restats.decc.gov.uk/cms/annual-mean-wind-speed-map (accessed 08th April 2014)

DONG, Z., LUO, W., QIAN, G., WANG, H. (2007). A wind tunnel simulation of the mean velocity fields behind upright porous fences. *Agricultural and Forest Meteorology*, 146, p. 82-93.

DONG, Z., LUO, W., QIAN, G., WANG, H. (2010). A wind tunnel simulation of the turbulence fields behind upright porous wind fences. *Journal of Arid Environments*, 74(2), p. 193-207.

DURVE, A., PATWARDHAN, A.W., BANARJEE, I., PADMAKUMAR, G., VAIDYANATHAN, G. (2012). Numerical investigation of mixing in parallel jets. *Nuclear Engineering and Design*, 242, p. 78-90.

EPA (1999). *Nitrogen oxides (NOx), why and how they are controlled*. Report EPA-456/F-99-006R. Office of Air Quality Planning and Standards, United States Environmental Protection Agency, Research Triangle Park, NC, USA.

EPA (2013a). *Carbon dioxide emissions*. Available at: http://www.epa.gov/climatechange/ghgemissions/gases/co2.html (accessed 21st September 2014)

EPA (2013b). *Sulfur dioxide*. Available at: http://www.epa.gov/airquality/sulfurdioxide/index.html (accessed 21st September 2014)

EPSRC (2009). *Sandpit: A study of practical abatement techniques for exhaust jets from commercial aircraft*. Available at: http://gow.epsrc.ac.uk/NGBOViewGrant.aspx?GrantRef=EP/H002987/1 (accessed 21st September 2014)

ERIKSSON, J.G., KARLSSON, R.I., PERSSON, J. (1994). An experimental study of a two-dimensional plane turbulent wall jet. *Experiments in Fluids*, 25, p. 50-60.

ESDU (1970). *Fluid forces and moments on flat plates*. Data item 70015, issued September 1970, with amendments A and B October 1972. Engineering Sciences Data Unit, IHS Inc., UK.

ESDU (1982). *Strong winds in the atmospheric boundary layer*. *Part 1: Hourly-mean wind speeds*. Data item 82026, issued September 1982, with amendments A to E March 2002. Engineering Sciences Data Unit, IHS Inc., UK.

ESDU (1983). *Strong winds in the atmospheric boundary layer*. *Part 2: Discrete gust speeds*. Data item 83045, issued November 1983, with amendments A to C March 2002. Engineering Sciences Data Unit, IHS Inc., UK.

ESDU (1989). *Boundary walls, fences and hoardings: Mean and peak wind loads and overturning moments*. Data item 89050, issued September 1989, with amendments A and B October 1990. Engineering Sciences Data Unit, IHS Inc., London, UK.

EUROPEAN COMMISSION (1999). *Council directive 1999/30/EC. Annex II: Limit values for nitrogen dioxide (NO_2) and oxides of nitrogen (NO_x) and the alert threshold for nitrogen dioxide*. Office for Official Publications of the European Communities, Luxembourg.

EWING, D., POLLARD, A. (1997). Evolution of the large scale motions in a three-dimensional wall jets. In: *28th AIAA Fluid Dynamics Conference / 4th AIAA Shear Flow Control Conference*, Snowmass Village, CO, USA, 29th June - 2nd July 1997, AIAA Paper No. 97-1964.

FAA (2005). *Aviation & emissions – a primer*. Report. Office of Environment and Energy, Federal Aviation Administration, Washington, DC, USA. Available at:

http://www.faa.gov/regulations_policies/policy_guidance/envir_policy/media/aeprimer.pdf (accessed 21st September 2014).

FAAM (2014). *Facility for Airborne Atmospheric Measurements*. Available at: http://www.faam.ac.uk (accessed 21st September 2014).

FABER, J., GREENWOOD, D., LEE, D., MANN, M., MENDES DE LEON, P., NELISSEN, D., OWEN, B., RALPH, M., TILSTON, J., VAN VELZEN, A., VAN DE VREEDE, G. (2008). *Lower NO_x at higher altitudes. Policies to reduce the climate impact of aviation NO_x emission*. Report 7.536.1, commissioned by the Directorate-General for Transport and Energy of the European Commission. CE Delft, Delft, The Netherlands. Available at: http://ec.europa.eu/transport/modes/air/studies/doc/environment/oct_2008_nox_final_report.pdf (accessed 21st September 2014)

FÖRTHMANN, E. (1936). *Turbulent jet expansion*. NACA TM-789. National Advisory Committee for Aeronautics, Washington, DC, USA.

FRANKE, J., HIRSCH, C., JENSEN, A.G., KRÜS, H.W., SCHATZMANN, M., WESTBURY, P.S., MILES, S.D., WISSE, J.A., WRIGHT, N.G. (2004). Recommendations on the use of CFD in wind engineering. In: van Beeck, J.P.A.J. (editor), *Proceedings of the International Conference on Urban Wind Engineering and Building Aerodynamics: COST Action C14 – Impact of wind and storm on city life built environment*, Sint-Genesius-Rode, Belgium, 5-7th May 2004.

FRAPORT AG (2013). *Lufthygienischer Jahresbericht 2013. Bericht über die Ergebnisse der lufthygienischen Überwachung am Flughafen Frankfurt* (Report on the results of air quality monitoring at Frankfurt Airport for the year 2013). Report. Fraport AG Frankfurt Airport Services Worldwide, Frankfurt am Main, Germany (in German). Available at: http://www.fraport.de/content/fraport/de/misc/binaer/nachhaltigkeit/lufthygienischer-jahresbericht-2013/jcr:content.file/lufthygienischer-jahresbericht-2013.pdf (accessed 21st September 2014)

FUJISAWA, N., NAKAMURA, K., SRINIVAS, K. (2004). Interaction of two parallel plane jets of different velocities. *Journal of Visualization*, 7(2), p. 135-142.

GAO, N., EWING, D. (2007). Experimental investigation of planar offset attaching jets with small offset distances. *Experiments in Fluids*, 42, p. 941-954, DOI: 10.1007/s00348-007-0305-3.

GARRY, K.P. (1989). A simulation technique for the study of buoyant plume dispersion from offshore platforms. In: *Proceedings of an International Seminar on Problems of Simulations in Wind Tunnels*, Novosibirsk, USSR, 25-29th July 1988, Volume 1.

GARRY, K.P. (2008). *An introduction to viscous flow*. Cranfield University, UK (lecture notes for 'Viscous flow' module).

GARRY, K.P. (2009a). *Aerodynamic experimental methods. Introduction to the scaling parameters relevant to wind tunnel studies*. Cranfield University, UK (lecture notes for 'Experimental methods' module).

GARRY, K.P. (2009b). *Experimental methods. Wind tunnel layout*. Cranfield University, Cranfield, UK (lecture notes for 'Experimental methods' module).

GARRY, K.P. (2009c). *Introduction to aircraft contrails*. Cranfield University, Cranfield, UK (lecture notes for 'Technology for sustainable aviation' module).

GATWICK AIRPORT LTD. (2006). *Gatwick 2010 baseline emission inventory*. Report (public access version). Gatwick Airport Limited, UK. Available at: http://83.98.24.64/Documents/business_and_community/Publications/2006/2010_basline_emissions_inventory.pdf (accessed 18th September 2013)

GEORGE, W.K., ABRAHAMSSON, H., ERIKSSON, J., KARLSSON, R.I., LÖFDAHL, L., WOSNIK, M. (2000). A similarity theory for the turbulent plane wall jet. *Journal of Fluid Mechanics*, 425, p. 368-411.

GEROVA, K., VELIKOV, S., GARRY, K. (2013). The effects of porosity and inclination on the pressure drop across porous screens and honeycombs used for heat exchanger simulations in wind tunnel studies. *SAE International Journal of Passenger Cars – Mechanical Systems*, 6(2), p. 483-494.

GERZ, T., EHRET, T. (1997). Wingtip vortices and exhaust jets during the jet regime of aircraft wakes. *Aerospace Science and Technology*, 1(7), p. 463-474.

GILES, B.D. (1977). Fluidics, the Coanda effect and some orographic winds. *Archiv für Meteorologie, Geophysik und Bioklimatologie*, Serie A, 25, p. 273-279.

GLAUERT, M.B. (1956). The wall jet. *Journal of Fluid Mechanics*, 1(6), p. 625-643.

GOOD, M.C., JOUBERT, P.N. (1968). The form drag of two-dimensional bluff-plates immersed in turbulent boundary layers. *Journal of Fluid Mechanics*, 31(3), p. 547-582.

GOOGLE MAPS (2014). Available at: https://maps.google.com/ (accessed 21st September 2014)

GRAHAM, A. (2009). *Aviation emissions and their impact on air quality*. Report. Manchester Metropolitan University, Manchester, UK. Available at: http://www.cate.mmu.ac.uk/wp-content/uploads/2012/06/2.-Final-Report-Aviation-Emissions-and-their-Impact-on-Air-Quality.pdf (accessed 21st September 2014)

GRAHAM, A., BENNETT, M., CHRISTIE, S. (2008). Representing the dispersion of emissions from aircraft on runways. In: *12th International Conference on Harmonization within Atmospheric Dispersion Modeling for Regulatory Purposes*, Cavtat, Croatia, 6-9th October 2008.

GUAN, D., ZHANG, Y., ZHU, T. (2003). A wind-tunnel study of windbreak drag. *Agricultural and Forest Meteorology*, 118, p. 75-84.

GUYOT, G. (1995). *Aerodynamics and microclimate effects of windbreaks and regional networks*. Silsoe Research Institute Translation New Series No. 53 (translated by I.A. Ashworth), p. 1-39.

HALASZ, I., SCHNEIDER, W. (1961). Quantitative gas chromatographic analysis of hydrocarbons with capillary column and flame ionization detector. *Analytical Chemistry*, 33(8), p. 978-982.

HALL, D.J., WATERS, R.A. (1986). *Further experiments on a buoyant emission from a building*. Report No. LR 567 PA. Warren Spring Laboratory, Stevenage, UK, cited in HANNA, S.R., BRIGGS, G.A, CHANG, J.C. (1998). Lift-off of ground-based buoyant plumes. *Journal of Hazardous Materials*, 59, p. 123-130.

HALL, J.W., EWING, D. (2007a). Three-dimensional turbulent wall jets issuing from moderate-aspect-ratio rectangular channels. *AIAA Journal*, 45(6), p. 1177-1186, DOI: 10.2514/1.20386.

HALL, J.W., EWING, D. (2007b). The asymmetry of the large-scale structures in turbulent three-dimensional wall jets exiting long rectangular channels. *Journal of Fluids Engineering*, 129(7), p. 929-941. DOI: 10.1115/1.2742721.

HALL, J.W., EWING, D. (2010). Spectral linear stochastic estimation of the turbulent velocity in a square three-dimensional wall jet. *Journal of Fluids Engineering*, 132(5) 051203, p. 1-9, DOI: 10.1115/1.4001490.

HANNA, S.R., BRIGGS, G.A, CHANG, J.C. (1998). Lift-off of ground-based buoyant plumes. *Journal of Hazardous Materials*, 59, p. 123-130.

HANNA, S.R., BRIGGS, G.A., HOSKER JR, R.P. (1982). *Handbook on atmospheric diffusion*. No. DOE/TIC-11223. Atmospheric Turbulence and Diffusion Laboratory, National Oceanic and Atmospheric Administration, Oak Ridge, TN, USA.

HARRIS, G.L. (1965). *The turbulent wall jet on plane and curved surfaces beneath an external stream*. VKI TN 27. Von Karman Institute for Fluid Dynamics, Sint-Genesius-Rode, Belgium.

HARRIS, R.I., DEAVES, D.M. (1981). The structure of strong winds. In: *Wind Engineering in the Eighties. Proceedings of CIRIA Conference*, London, UK, 12-13th November 1980, Paper No. 4.

HEATHROW AIRPORT LTD. (2011). *Heathrow air quality strategy 2011-2020*. Available at: http://www.heathrowairport.com/static/Heathrow/Downloads/PDF/air-quality-strategy_LHR.pdf (accessed 18th September 2013)

HEATHROW AIRPORT LTD. (2013). *Heathrow – Press releases – Heathrow unveils a new approach to third runway*. 17th July 2013. Available at: https://mediacentre.heathrowairport.com/Press-releases/Heathrow-unveils-a-new-approach-to-third-runway-5e2.aspx (accessed 18th September 2013)

HEISLER, G.M., DEWALLE, D.R. (1988). Effects of windbreak structure on wind flow. *Agriculture, Ecosystems and Environment*, 22/23, p. 41-69.

HIGSON, H.L., GRIFFITHS, R.F., JONES, C.D., HALL, D.J. (1994). Concentration measurements around an isolated building: A comparison between wind tunnel and field data. *Atmospheric Environment*, 28(11), p. 1827-1836.

HOCH, J., JIJI, L.M. (1981). Two-dimensional turbulent offset jet-boundary interaction. *Journal of Fluids Engineering*, 103(1), p. 154-161.

HOERNER, S.F. (1965). *Fluid-dynamic drag*, 2nd ed. Hoerner Fluid Dynamics, Brick Town, NJ, USA.

HOLMES, J.D. (1986). Pressure and drag on surface-mounted rectangular plates and walls. In: *9th Australasian Fluid Mechanics Conference*, Auckland, New Zealand, 8-12th December 1986.

HOU, Q.F., GUO, B.Y., LI, L.F., YU, A.B. (2009). Numerical simulation of gas flow in an electrostatic precipitator. In: *7th International Conference on CFD in the Minerals and Process Industries*, CSIRO, Melbourne, Australia, 9-11th December 2009.

HOULT, D.P., FAY, J.A., FORNEY, L.J. (1969). A theory of plume rise compared with field observations. *Journal of the Air Pollution Control Association*, 19(8), p. 585-590.

HSIAO, F.B., SHEU, S.S. (1994). Double row vortical structures in the near field region of a plane wall jet. *Experiments in Fluids*, 17, p. 291-301.

HUBER, A.H. (1991). Wind tunnel and Gaussian plume modeling of building wake dispersion. *Atmospheric Environment*, 25A(7), p. 1237-1249.

IATA (2009). *A global approach to reducing aviation emissions*. Available at: http://www.iata.org/SiteCollectionDocuments/Documents/Global_Approach_Reducing_Emissions_251109web.pdf (accessed 18th September 2013).

IATA (2011). *Vision 2050*. Report. International Air Transport Association, Singapore. Available at: http://www.iata.org/pressroom/facts_figures/Documents/vision-2050.pdf (accessed 21st September 2014)

IATA (2013). *2012 – Best in history of continuous safety improvements*. Available at: http://www.iata.org/pressroom/pr/pages/2013-02-28-01.aspx (accessed 21st September 2014)

ICAO (2006a). *Aerodrome design manual. Part 1: Runways*. Doc 9157 AN/901. International Civil Aviation Organization.

ICAO (2006b). *Aerodrome design manual. Part 6: Frangibility*. Doc 9157 AN/901. International Civil Aviation Organization.

ICAO (2012). *Forecasts of scheduled passenger traffic*. Available at: http://www.icao.int/sustainability/pages/eap_fp_forecastmed.aspx (accessed 21st September 2014)

IDELCHIK, I.E. (2004). *Handbook of hydraulic resistance*, 3rd ed. CRC Press Inc., New York City, NY, USA.

IHS (2011). *Jane's Aero Engines*. Available at: http://www.ihs.com/products/janes/defence/det-products/aero-engines.aspx (accessed 21st December 2011)

IIDA, S., MATSUDA, H. (1988). An experimental study of circular turbulent wall-jet along a convex wall. *Transactions of the Japan Society of Mechanical Engineers*, Series B, 54(498), p. 354-360 (in Japanese).

INPERC (2013). *Image analysis – Intelligent perception*. Available at: http://inperc.com/wiki/index.php?title=Image_analysis (accessed 21st September 2014)

IPCC (1999). *Aviation and the global atmosphere*. Report. Intergovernmental Panel of Climate Change, Geneva, Switzerland. Available at: http://www.grida.no/publications/other/ipcc_sr/?src=/climate/ipcc/aviation/index.htm (accessed 21st September 2014).

IPCC (2007). *Climate Change 2007*. 4th Assessment Report of the Intergovernmental Panel of Climate Change, Geneva, Switzerland. Available at: http://www.ipcc.ch/publications_and_data/ar4/syr/en/spm.html (accessed 21st September 2014)

ITO, A., GARRY, K.P. (1998). Pressure measurements around a two-dimensional gauze at incidence. *Journal of Fluids and Structures*, 12(2), p. 171-181.

JANE'S ALL THE WORLD'S AIRCRAFT (1993). *1993-1994. Eighty-fourth year of issue*, Lambert, M. (editor). Jane's Information Group, London, UK, ISBN 0 7106 10661.

JANICKE, U., JANICKE, L. (2001). A three-dimensional plume rise model for dry and wet plumes. *Atmospheric Environment*, 35(5), p. 877-890.

KACKER, S.C., WHITELAW, J.H. (1968). Some properties of the two-dimensional, turbulent wall jet in a moving stream. *Journal of Applied Mechanics*, 35(4), p. 641-651, DOI: 10.1115/1.3601286.

KAISER, G.D. (1977). Radioactive plumes. In: *Proceedings of the 4th International Congress of the International Radiation Protection Association*. Paris, France, 24-30th April 1977, Paper No. 060.

KAMINSKI, E., TAIT, S., CARAZZO, G. (2005). Turbulent entrainment in jets with arbitrary buoyancy. *Journal of Fluid Mechanics*, 526, p. 361-376.

KANDA, I., UEHARA, K., YAMAO, Y., YOSHIKAWA, Y., MORIKAWA, T. (2006). A wind-tunnel study on exhaust gas dispersion from road vehicles. Part I: Velocity and concentration fields behind single vehicles. *Journal of Wind Engineering and Industrial Aerodynamics*, 94(9), p. 639–658.

KOSO, T., OHASHI, H. (1982). Turbulent diffusion of a three-dimensional wall jet. 1st report: Mean and turbulent characteristics of velocity and temperature field. *Bulletin of the Japan Society of Mechanical Engineers*, 25(200), p. 173-181.

KRUKA, V., ESKINAZI, S. (1964). The wall-jet in a moving stream. *Journal of Fluid Mechanics*, 20(4), p. 555-579.

KÜCHEMANN, D. (1949). *Jet diffusion in proximity of a wall*. NACA TM-1214. National Advisory Committee for Aeronautics, Washington, DC, USA.

LAUNDER, B.E., RODI, W. (1981). The turbulent wall jet. *Progress in Aerospace Sciences*, 19, p. 81-128.

LAUNDER, B.E., RODI, W. (1983). The turbulent wall jet – measurements and modelling. *Annual Review of Fluid Mechanics*, 15, p. 429-459.

LAW, A.W.-K., HERLINA (2002). An experimental study on turbulent circular wall jets. *Journal of Hydraulic Engineering*, 128(2), p. 161-174.

LAWS, E.M., LIVESEY, J.L. (1978). Flow through screens. *Annual Review of Fluid Mechanics*, 10, p. 247-266.

LEE, S.-J., KIM, H.-B. (1999). Laboratory measurements of velocity and turbulence field behind porous fences. *Journal of Wind Engineering Industrial Aerodynamics*, 80(3), p. 311–326.

LETCHFORD, C.W. (1994). *Further studies of wind loads on walls*. Report OUEL 1620/86. University of Oxford, Department of Engineering Science, Oxford, UK.

LETCHFORD, C.W., HOLMES, J.D. (1994). Wind loads on free-standing walls in turbulent boundary layers. *Journal of Wind Engineering Industrial Aerodynamics*, 51(1), p. 1-27.

LIEPMANN, D., GHARIB, M. (1992). The role of streamwise vorticity in the near-field entrainment of round jets. *Journal of Fluid Mechanics*, 245, p. 643-668.

LIN, X.-J., BARRINGTON, S., NICELL, J., CHOINIERE, D., VEZINA, A. (2006). Influence of windbreaks on livestock odour dispersion plume in the field. *Agriculture, Ecosystems and Environment*, 116, p. 263–272.

LIN, Y.F., SHEU, M.J. (1991). Interaction of parallel turbulent plane jets. *AIAA Journal*, 29(9), p. 1372-1373, DOI: 10.2514/3.10749.

LITTLEBURY, K.H. (1981). Wind tunnel model testing techniques for offshore gas/oil production platforms. In: *Proceedings of the 13th Annual Offshore Technology Conference*, Houston, TX, USA, 4-7th May 1981, p. 99-103, Paper OTC 4125.

LUBITZ, W.D., WHITE, B.R. (2004). Atmospheric boundary layer wind tunnel applications in wind turbine siting. In: *Proceedings of World Wind Energy Conference*, Beijing, China, 31st October – 4th November 2004.

LYNCH, P.J. (1996). Cirrus clouds: Their role in climate and global change. *Acta Astronautica*, 38(11), p. 859-863.

MACDONALD, R.W., GRIFFITHS, R.F., CHEAH, S.C. (1997). Field experiments of dispersion through regular arrays of cubic structures. *Atmospheric Environment*, 31(6), p. 783-795.

MACMANUS, D. (2009). *Engine aerodynamics. Part 1: Architecture, cycles and performance*. Cranfield University, UK (lecture notes for 'Engine aerodynamics' module).

MATSUDA, H., IIDA, S., HAYAKAWA, M. (1990). Coherent structures in a three-dimensional wall jet. *Journal of Fluids Engineering*, 112(4), p. 462-467.

MAVROIDIS, I., GRIFFITHS, R.F. (2001). Local characteristics of atmospheric dispersion within building arrays. *Atmospheric Environment*, 35(16), p. 2941-2954.

MAVROIDIS, I., GRIFFITHS, R.F., HALL, D.J. (2003). Field and wind tunnel investigations of plume dispersion around single surface obstacles. *Atmospheric Environment*, 37(21), p. 2903–2918.

MCLEAN, J.D., HERRING, H.J. (1974). *Discrete wall jets in quiescent air*. Report NASA CR-2388. National Aeronautics and Space Administration, Washington, DC, USA.

MERLOT, D. (2010). *Effect of distributed roughness on surface drag*. MSc Thesis. Cranfield University, Cranfield, UK.

MERONEY, R.N. (1979). Lift off of buoyant gas initially on the ground. *Journal of Industrial Aerodynamics*, 5, p. 1-11.

MIGUEL, A.F. (1998). Airflow through porous screens: from theory to practical considerations. *Energy and Buildings*, 28, p. 63-69.

MILES, J.W. (1961). On the stability of heterogeneous shear flows. *Journal of Fluid Mechanics*, 10(4), p. 496-508.

MILLER, D.R., COMINGS, E.W. (1960). Force-momentum fields in a dual-jet flow. *Journal of Fluid Mechanics*, 7(2), p. 237-256.

MNP (2006). *De luchtkwaliteit rond Schiphol. MNP-bevindingen over het onderzoek naar de uitstoot van het vliegverkeer en de luchtkwaliteit rond Schiphol door ADECS Airinfra BV in het kader van de Evaluatie Schipholbeleid* (The air quality around Schiphol. MNP's conclusions of the investigation by ADECS Airinfra BV on air-traffic emissions and air quality around Schiphol within the framework of Schiphol's Evaluation Policy). Report No. 500133001/2006. Milieu- en Natuurplanbureau, Bilthoven, The Netherlands (in Dutch). Available at: http://www.rivm.nl/bibliotheek/rapporten/500133001.pdf (accessed 21st September 2014)

MORTON, B.R. (1959). Forced plumes. *Journal of Fluid Mechanics*, 5, p. 151-163.

MORTON, B.R., TAYLOR, G., TURNER, J.S. (1956). Turbulent gravitational convection from maintained and instantaneous sources. *Proceedings of the Royal Society of London*, Series A, 234, p. 1-23.

MYERS, G.E., SCHAUER, J.J., EUSTIS, R.H. (1961). *The plane turbulent wall jet. Part I: Jet development and friction factor*. Technical Report No. 1. Department of Mechanical Engineering, Stanford University, Stanford, CA, USA.

NAEGELI, W. (1965). Über die Windverhältnisse im Bereich gestaffelter Windschutzstreifen (On the wind behaviour in areas of staggered windbreaks). *Mitteilungen der Schweizerischen Anstalt für das forstliche Versuchswesen*, 41(5), p. 221-300 (in German).

NAMGYAL, L., HALL, J.W. (2013). Coherent streamwise vortex structures in the near-field of the three-dimensional wall jet. *Journal of Fluids Engineering*, 135(6) 061204, p. 1-7, DOI: 10.1115/1.4023855.

NARAIN, J.P. (1975). Three dimensional turbulent wall jets. *The Canadian Journal of Chemical Engineering*, 53(3), p. 245-251.

NARASIMHA, R., NARAYAN, K.Y., PARTHASARATHY, S.P. (1973). Parametric analysis of turbulent wall jets in still air. *Aeronautical Journal*, 77, p. 335-345.

NASR, A., LAI, J.C.S. (1997). Comparison of flow characteristics in the near field of two parallel plane jets and an offset plane jet. *Physics of Fluids*, 9(10), p. 2919-2931, DOI: 10.1063/1.869404.

NASR, A., LAI, J.C.S. (1998). A turbulent plane offset jet with small offset ratio. *Experiments in Fluids*, 24, p. 47-57.

NETTERVILLE, D.D.J. (1990). Plume rise, entrainment and dispersion in turbulent winds. *Atmospheric Environment*, 24A(5), p. 1061-1081.

NEWMAN, B.G. (1969). The prediction of turbulent jets and wall jets. *Canadian Aeronautics and Space Journal*, 15, p. 282-305.

NEWMAN, B.G., PATEL, R.P., SAVAGE, S.B., TJIO, H.K. (1972). Three-dimensional wall jet originating from a circular orifice. *Aeronautical Quarterly*, 23, p. 188-200.

NOZAKI, T. (1983). Reattachment flow issuing from a finite width nozzle. *Bulletin of the Japan Society of Mechanical Engineers*, 26(221), p. 1884-1890.

PADMANABHAM, G., LAKSHMANA GOWDA, B.H. (1991a). Mean and turbulence characteristics of a class of three-dimensional wall jets. Part 1: Mean flow characteristics. *Journal of Fluids Engineering*, 113(4), p. 620-628.

PADMANABHAM, G., LAKSHMANA GOWDA, B.H. (1991b). Mean and turbulence characteristics of a class of three-dimensional wall jets. Part 2: Turbulence characteristics. *Journal of Fluids Engineering*, 113(4), p. 629-634.

PELFREY, J.R.R., LIBURDY, J.A. (1986). Mean flow characteristics of a turbulent offset jet. *Journal of Fluids Engineering*, 108(1), p. 82-88.

PERERA, M.D.A.E.S. (1981). Shelter behind two-dimensional solid and porous fences. *Journal of Wind Engineering and Industrial Aerodynamics*, 8, p. 93-104.

PINKER, R.A., HERBERT, M.V. (1967). Pressure loss associated with compressible flow through square-mesh wire gauzes. *Journal of Mechanical Engineering Science*, 9(1), p. 11-23.

PLATE, E.J. (1964). The drag on a smooth flat plate with a fence immersed in its turbulent boundary layer. In: *ASME Fluids Engineering Conference*, Philadelphia, PA, USA, 18th - 21st May, Paper No. 64-FE-17.

PLATE, E.J. (1971). *Aerodynamic characteristics of atmospheric boundary layers*. Report TID-15465. Division of Technical Information, US Atomic Energy Commission, Oak Ridge, TN, USA.

POLL, D.I.A. (2009). *Aviation and the environment*. Cranfield University, Cranfield, UK (lecture notes for 'Technology for sustainable aviation' module).

POREH, M., CERMAK, J.E. (1988). 'Lift-off' of buoyant horizontal plumes. In: *8th Symposium on Turbulence and Diffusion*, San Diego, CA, USA, 25-29th April 1988.

POREH, M., HASSID, S. (1982). Simulation of buoyancy and wind induced ventilation. In: *Wind Tunnel Modeling for Civil Engineering Applications*. *Proceedings of the International Workshop on Wind Tunnel Modeling Criteria and Techniques in*

Civil Engineering Applications, Gaithersburg, Maryland, USA, April 1982, edited by T.A. Reinhold. Cambridge University Press, Cambridge, UK.

POURNAZERI, S., PRINCEVAC, M., VENKATRAM, A. (2012). Scaling of building affected plume rise and dispersion in water channels and wind tunnels – Revisit of an old problem. *Journal of Wind Engineering and Industrial Aerodynamics*, 103, p. 16-30.

RAINE, J.K., STEVENSON, D.C. (1977). Wind protection by model fences in a simulated atmospheric boundary layer. *Journal of Industrial Aerodynamics*, 2(2), p. 159–180.

RAJARATNAM, N. (1965). *Plane turbulent wall jets on rough boundaries*. Technical Report. Department of Civil Engineering, University of Alberta, Edmonton, Canada.

RAJARATNAM, N., PANI, B.S. (1974). Three-dimensional turbulent wall jets. *Journal of the Hydraulics Division*, 100, p. 69-83.

RAJARATNAM, N., SUBRAMANYA (1967). Plane turbulent free jet and wall jet. *Journal of the Royal Aeronautical Society*, 71, p. 585-587.

RAJARATNAM, N., SUBRAMANYA, K., (1968). Plane turbulent reattached wall jets. *Journal of the Hydraulics Division*, 94(1), p. 95-112.

RAMSDALE, S.A., TICKLE, G.A. (2001). *Review of lift-off models for ground based buoyant clouds*. AEA Technology Report AEAT-4262(2) for EC URAHFREP Project.

RANGA RAJU, K.G. (1983). Drag characteristics of sharp-edged bodies in turbulent boundary layer flow. In: *8th Australasian Fluid Mechanics Conference*, University of Newcastle, Newcastle, NSW, Australia, 28th November - 2nd December 1983.

RANGA RAJU, K.G., LOESER, J., PLATE, E.J. (1976). Velocity profiles and fence drag for a turbulent boundary layer along smooth and rough flat plates. *Journal of Fluid Mechanics*, 76(2), p. 383-399.

RANGA RAJU, K.G., SHARMA, L.R. (1997). Form drag of fences placed in disturbed turbulent boundary layers. *Journal of Engineering Mechanics*, 125(4), p. 419-425.

RAVISHANKARA, A.R., DANIEL, J.S., PORTMANN, R.W. (2009). Nitrous oxide (N_2O): The dominant ozone-depleting substance emitted in the 21st century. *Science*, 326, p. 123-125, DOI: 10.1126/science.1176985.

REIBLE, D.D. (1998). *Fundamentals of environmental engineering*. CRC Press, Boca Raton, FL, USA.

REYNOLDS, A.J. (1969). Flow deflection by gauze screens. *Journal of Mechanical Engineering Science*, 11(3), p. 290-294.

ROBERTSON, A.P., HOXEY, R.P., SHORT, J.L., FERGUSON, W.A., OSMOND, S. (1996). Full-scale testing to determine the wind loads on free-standing walls. *Journal of Wind Engineering and Industrial Aerodynamics*, 60(1), p. 123-137.

ROBINS, A.G., CASTRO, I.P. (1977). A wind tunnel investigation of plume dispersion in the vicinity of a surface mounted cube – I. The flow field. *Atmospheric Environment*, 11(4), p.291-297.

ROGERS, H.L., LEE, D.S., RAPER, D.W., FOSTER, P.M.F., WILSON, C.W., NEWTON, P.J. (2002). The impact of aviation on the atmosphere. *Aeronautical Journal*, 106, p. 521-546.

ROSTAMY, H., BERGSTROM, D.J., SUMNER, D., BUGG, J.D. (2011). An experimental study of a turbulent wall jet on smooth and transitionally rough surfaces. *Journal of Fluids Engineering*, 133(11) 111207, p. 1-8, DOI: 10.1115/1.4005218.

SAKAMOTO, H., ARIE, M. (1983). Flow around a normal plate of finite width immersed in a turbulent boundary layer. *Journal of Fluids Engineering*, 105(1), p. 98-104.

SANGAI, V., LAKSHMANAN, B. (2001). Optimum mixing of core- and bypass-streams in a high bypass civil turbofan. In: *37th AIAA / ASME / SAE/ ASEE Joint Propulsion Conference and Exhibit*, Salt Lake City, UT, USA, 8-11th July 2001, AIAA Paper No. 2001-3618.

SANGRAS, R., FAETH, G.M. (1999). *Buoyant turbulent jets and plumes: III. Round turbulent nonbuoyant starting jets and puffs and buoyant starting plumes and thermals*. Report No. GDL/GMF-99-03. Department of Aerospace Engineering, University of Michigan, Ann Arbor, MI, USA.

SANTIAGO, J.L., MARTÍN, F., CUERVA, A., BEZDENEJNYKH, N., SANZ-ANDRÉS, A. (2007). Experimental and numerical study of wind flow behind windbreaks. *Atmospheric Environment*, 41(30), p. 6406-6420.

SCARANO, F., ASTARITA, T., CARLOMAGNO, G.M. (1999). Analysis of a turbulent wall jet with D-PIV. In: *8th International Conference on Laser Anemometry, Advances and Applications*, Rome, Italy, 6-8th September 1999.

SCHATZMANN, M. (1979). An integral model of plume rise. *Atmospheric Environment*, 13(5), p. 721-731.

SCHLICHTING, H. (1979). *Boundary-layer theory*, 7th ed (translated by J. Kestin). McGraw-Hill, USA.

SCHNEIDER, M. E., GOLDSTEIN, R. J. (1994). Laser Doppler measurement of turbulent parameters in a two-dimensional plane wall jet. *Physics of Fluids*, 6(9), p. 3116-3129, DOI: 10.1063/1.868136.

SCHUBAUER, G.B., SPANGENBERG, W.G., KLEBANOFF, P.S. (1950). *Aerodynamic characteristics of damping screens*. NACA TN-2001. National Advisory Committee for Aeronautics, Washington, DC, USA.

SCHWARZ, W. H., COSART, W. P. (1960). The two-dimensional turbulent wall jet. *Journal of Fluid Mechanics*, 10, p. 481-495.

SFORZA, P.M., HERBST, G. (1967). *A study of three-dimensional, incompressible, turbulent wall jets*. PIBAL Report No. 1022. Department of Aerospace Engineering and Applied Mechanics, Polytechnic Institute of Brooklyn, New York, NY, USA.

SHABAYEK, S.A. (2011). Plane turbulent wall jets in limited tailwater depth. *International Journal of Engineering & Technology*, 11(6), p. 192-197.

SHABBIR, A., GEORGE, W.K. (1994). Experiments on a round turbulent buoyant plume. *Journal of Fluid Mechanics*, 275(1), p. 1-32.

SHARP, J.J., VYAS, B.D. (1977). The buoyant wall jet. *Proceedings of the Institution of Civil Engineers*, Part 2, 63, p. 593-611.

SIGALLA, A. (1958a). Experimental data on turbulent wall jets. *Aircraft Engineering*., 30, p. 131-134.

SIGALLA, A. (1958b). Measurements of skin friction in a plane turbulent wall jet. *Journal of the Royal Aeronautical Society*, 62 (576), p. 873-877.

SIGNAL INSTRUMENTS (2014). *3000HM Heated THC Analyser*. Available at: http://www.signal-group.com/index.php/technology-used-for-gas-anaylsis-and-emissions-monitoring/mfid/m3000hm (accessed 11th March 2014)

SIMIU, E., SCANLAN, R.H. (1978). *Wind effects on structures: An introduction to wind engineering*. John Wiley & Sons, New York, NY, USA.

SINCLAIR, J.R., SLAWSON, P.R., DAVIDSON, G.A. (1990). Three-dimensional buoyant wall jets released into a coflowing turbulent boundary layer. *Journal of Heat Transfer*, 112(2), p. 356-362, DOI: 10.1115/1.2910385.

SMITH, B.S. (2008). *Wall jet boundary layer flows over smooth and rough surfaces*. Ph.D. thesis. Virginia Polytechnic Institute and State University, Blacksburg, VA, USA.

SPANELIS, A. (2013). *Engine exhaust plume mixing simulations for minimizing environmental emissions impact*. PhD Thesis. Cranfield University, Cranfield, UK.

SPIEGEL, E.A., VERONIS, G. (1960). On the Boussinesq approximation for a compressible fluid. *Astrophysical Journal*, 131, p.442-447.

STEIN, S. (2009). *Modelling aircraft trailing vortex systems within the atmospheric boundary layer*. MSc Thesis. Cranfield University, Cranfield, UK.

SU, C.-C., HUANG, C-.C. (1978). Experimental studies of flow through single gauzes. *International Journal of Heat and Fluid Flow*, 12(3), p. 273-278.

SUBBARAO, E. (1989). The effects of Reynolds number and Richardson number on the structure of a vertical co-flowing buoyant jet. In: *20th AIAA Fluid Dynamics, Plasma Dynamics and Lasers Conference*, Buffalo, NY, USA, 12th-14th June 1989, AIAA Paper No. 89-1800.

SUN, H., EWING, D. (2002). The development of three-dimensional wall jet. In: *Proceedings of the 48th Annual Conference of the Canadian Aeronautics and Space Institute*, Toronto, ON, Canada, 30th April - 2nd May 2001, p. 509-516.

TACHIE, M.F., BALACHANDAR, R., BERGSTROM, D.J. (2004). Roughness effects on turbulent plane wall jets in an open channel. *Experiments in Fluids*, 37, p. 281-292, DOI 10.1007/s00348-004-0816-0.

TANAKA, E. (1970). The interference of two-dimensional parallel jets. 1st report: Experiments on dual jet. *Bulletin of the Japan Society of Mechanical Engineers*, 13(56), p. 272-280.

TANAKA, E. (1974). The interference of two-dimensional parallel jets. 2nd report: Experiments on the combined flow of dual jet. *Bulletin of the Japan Society of Mechanical Engineers*, 17(109), p. 920-927.

TAYLOR, G.I. (1944). *Air resistance of a flat plate of very porous material*. Reports and Memoranda No. 2236. Aeronautical Research Council, HM Stationery Office, UK.

TAYLOR, G.I., DAVIES, R.M. (1944). *The aerodynamics of porous sheets*. Reports and Memoranda No. 2237. Aeronautical Research Council, HM Stationery Office, UK.

TEITEL, M., DVORKIN, D., HAIM, Y., TANNY, J., SEGINER, I. (2009). Comparison of measured and simulated flow through screens: Effects of screen inclination and porosity. *Biosystems Engineering*, 104(3), p. 404-416.

TETEVIN, N. (1948). *Laminar flow of a slightly viscous incompressible fluid that issues from a slit and passes over a flat plate*. NACA TN-1644. National Advisory Committee for Aeronautics, Washington, DC, USA.

TIAN, W., CHIPPERFIELD, M.P., LU, D. (2009). Impact of increasing stratospheric water vapor on ozone depletion and temperature change. *Advances in Atmospheric Sciences*, 26(3), p. 423-437.

TOLLMIEN, W. (1945). *Calculation of turbulent expansion processes*. NACA TM-1085. National Advisory Committee for Aeronautics, Washington, DC, USA.

TRANSPORT CANADA (2010). *2.5 Instrument Landing System (ILS)*. Available at: http://www.tc.gc.ca/eng/civilaviation/publications/tp1247-part2-part2-5-1446.htm (accessed 11th May 2014)

TRENTACOSTE, N. AND SFORZA, P. M. (1966). *An experimental investigation of three-dimensional free mixing in incompressible, turbulent free jets*. PIBAL Report No. 871. Department of Aerospace Engineering and Applied Mechanics, Polytechnic Institute of Brooklyn, Farmingdale, NY, USA.

TURNER, J.S. (1973). *Buoyancy effects in fluids*. Cambridge University Press, London, UK.

UK DEPARTMENT FOR TRANSPORT (2006). *Project for sustainable development of Heathrow*. Report of the air quality technical panels. Department for Transport, London, UK.

VALERA, D.L., MOLINA, F.D., ÁLVAREZ, A.J., LÓPEZ, J.A., TERRÉS-NICOLI, J.M., MADUEÑO, A. (2005). Contribution to the characterization of insect-proof screens: experimental measurements in wind tunnel and CFD simulations. *Acta Horticulturae*, 691, p. 441-448.

VAN EIMERN, J., KARSCHON, R., RAZUMOVA, L.A., ROBERTSON, G.W. (1964), *Windbreaks and shelterbelts*. Technical Note No. 59. World Meteorological Organization, Geneva, Switzerland.

VERHOFF, A. (1963). *The two-dimensional, turbulent wall jet with and without an external free-stream*. Report No. 626. Department of Aeronautical Engineering, Princeton University, Princeton, NJ, USA.

WANG, H., LAW, A.W.-K. (2002). Second-order integral model for a round turbulent buoyant jet. *Journal of Fluid Mechanics*, 459, p. 397-428.

WAYSON, R.L., FLEMING, G.G., NOEL, G., MACDONALD, J., EBERHARD, W.L., MCCARTY, B., MARCHBANKS, R., SANDBERG, S., GEORGE, J. (2008). *Lidar measurements of exhaust plume characteristics from commercial jet turbine aircraft at the Denver International Airport*. Final Report FAA-AEE-08-02. Federal Aviation Administration. United States Department of Transportation, Washington, DC, USA.

WHO (2003). *Health aspects of air pollution with particulate matter, ozone and nitrogen dioxide*. Report EUR/03/5042688. Regional Office for Europe, World Health Organization, Copenhagen, Denmark.

WIEGHARDT, K. (1953). Erhöhung des turbulenten Reibungswiderstandes durch Oberflächenstörungen (Increase of turbulent skin-friction drag using surface disturbances). *Forschungshefte für Schiffstechnik*, 1, p. 65-81 (in German).

WILD, O., PRATHER, M.J., AKIMOTO, H. (2001). Indirect long-term global radiative cooling from NO_x emissions. *Geophysical Research Letters*, 28(9), p.1719-1722.

WINTER, K.G., GAUDET, L. (1973). *Turbulent boundary-layer studies at high Reynolds numbers at Mach numbers between 0.2 and 2.8*. Technical Report 70251. Royal Aeronautical Establishment, Bedford, UK.

WIUFF, R. (1977). *Experiments on the surface buoyant jet*. Series Paper No. 16. Institute of Hydrodynamics and Hydraulic Engineering, Technical University of Denmark, Kongens Lyngby, Denmark.

WMO (2002). *Scientific assessment of ozone depletion: 2002*. Report No. 47 of the Global Ozone Research and Monitoring Project. World Meteorological Organization, Geneva, Switzerland.

WYGNANSKI, I., KATZ, Y., HOREV, E. (1992). On the applicability of various scaling laws to the turbulent wall jet. *Journal of Fluid Mechanics*, 234, p. 669-690.

YANG, S., GAO, S.-T., WANG, D.-H. (2007). A study of Richardson number and instability in moist saturated flow. *Chinese Journal of Geophysics*, 50(2), p. 365-375.

ZHU, G., PAL ARYA, S., SNYDER, W.H. (1998). An experimental study of the flow structure within a dense gas plume. *Journal of Hazardous Materials*, 62(2), p. 161–186.

Appendix

Appendix A: Additional equations

Sutherland's Law (Anderson, 2001, p. 723)

$$\mu = \mu_0 \left(\frac{T}{T_0} \right)^{3/2} \left(\frac{T_0 + 110}{T + 110} \right)$$

Equation A.1

- μ dynamic viscosity (kg/(ms))
- μ_0 reference dynamic viscosity, equal to 1.7894×10^{-5} kg/(ms)
- T absolute temperature (K)
- T_0 reference absolute temperature, equal to 288.16 K

'2 / 3 law', plume trajectory near source (travel distance of ~ 50 m) (Hanna et al. 1982, p. 13)

$$z = \left(\frac{3}{\beta^2} \frac{M}{u^2} x + \frac{3}{2\beta^2} \frac{F_0}{u^3} x^2 \right)^{1/3}$$

Equation A.2

- F_0 initial buoyancy flux (m^4/s^3), equal to $gQ_p(T_p - T_\infty) / T_p$, where Q_p is the initial volume flux from the source, T_p is the initial plume absolute temperature, T_∞ is the ambient absolute temperature at the initial height of the source
- M momentum flux (m^4/s^2), equal to the product of the plume volume flux and plume velocity
- x distance downstream of the source (m)
- z vertical distance to plume centre line measured from the initial source height (m)
- u ambient wind velocity (m/s)
- β proportionality factor; $\beta = R / z$, where R is the plume radius. $\beta = 0.6$ for buoyant plumes

Gaussian plume equation, used commonly for calculations of concentrations caused by stationary sources, i.e. power plants, chimneys (Bächlin et al., 1992, p. 2726)

$$c = \frac{Q_j}{2\pi\sigma_z\sigma_y U} e^{-0.5y^2/\sigma_y{}^2} \left[e^{-0.5(z-h)^2/\sigma_z{}^2} + e^{-0.5(z+h)^2/\sigma_z{}^2} \right]$$

Equation A.3

c	pollutant concentration (ppm)
h	effective emission height above the ground (m)
Q_j	source volumetric flow rate (m^3/s)
U	mean wind speed affecting the plume (m/s)
y	lateral coordinate (m)
z	vertical coordinate (distance above ground) (m)
σ_y	lateral dispersion coefficient (m)
σ_z	vertical dispersion coefficient (m)

Appendix B: NO_x emissions

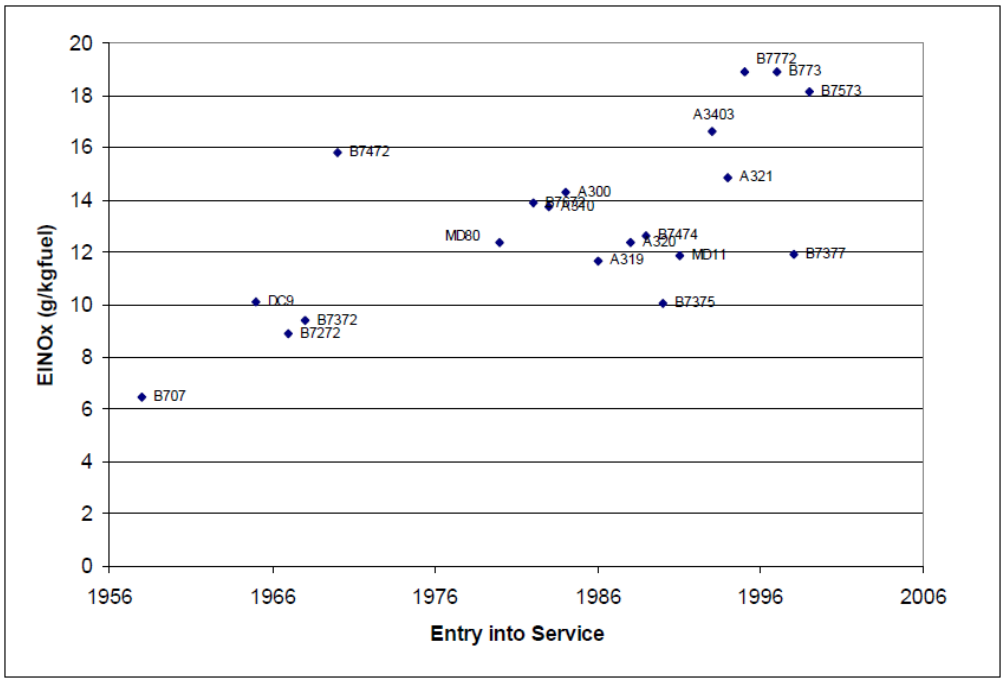

Figure B.1: Aircraft NO_x emissions vs. year of entry into service (taken from Faber et al., 2008), y-axis: Emissions Index (EI) – grams NO_x produced per kilogramme of fuel burned

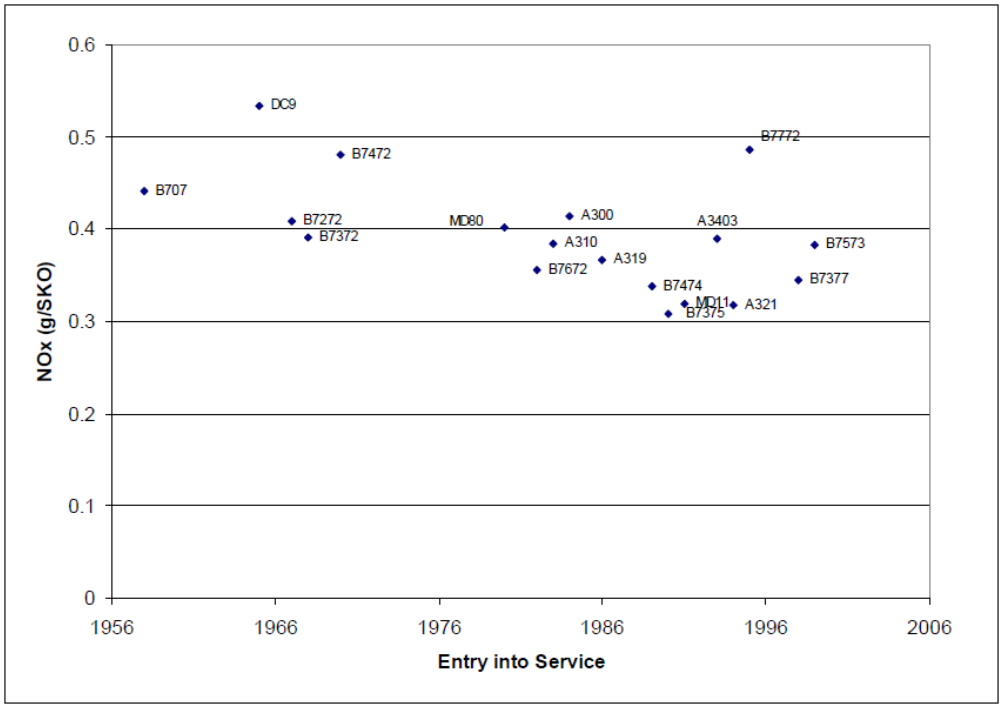

Figure B.2: Aircraft NO_x emissions in grams per seat kilometre offered (SKO) vs. year of entry into service (taken from Faber et al., 2008)

Appendix C: Initial experiments

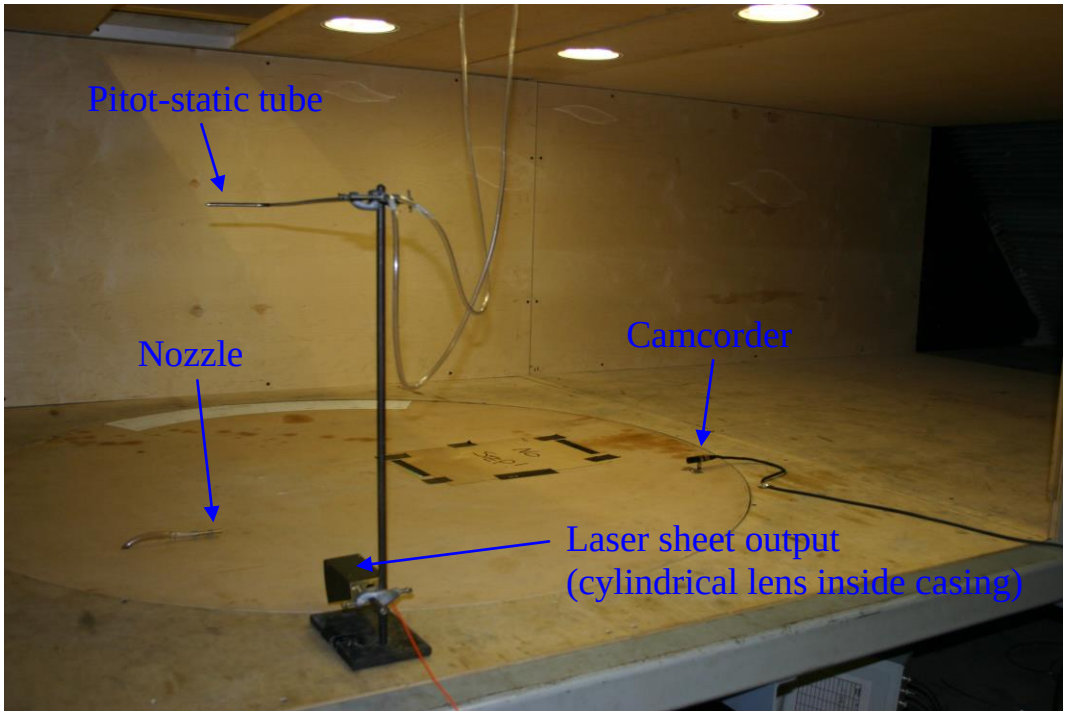

Figure C.1: Experimental arrangement of the 8'×4' ABLWT working section for laser flow visualisation

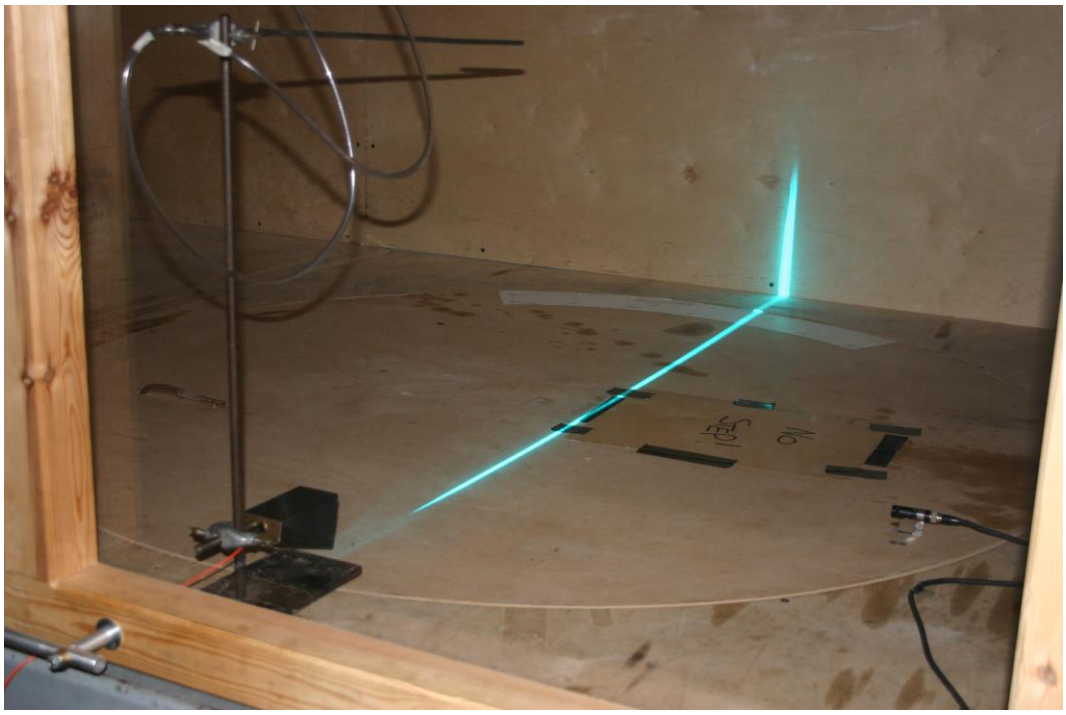

Figure C.2: 8'×4' ABLWT working section prior to starting a flow visualisation test (laser beam switched on)

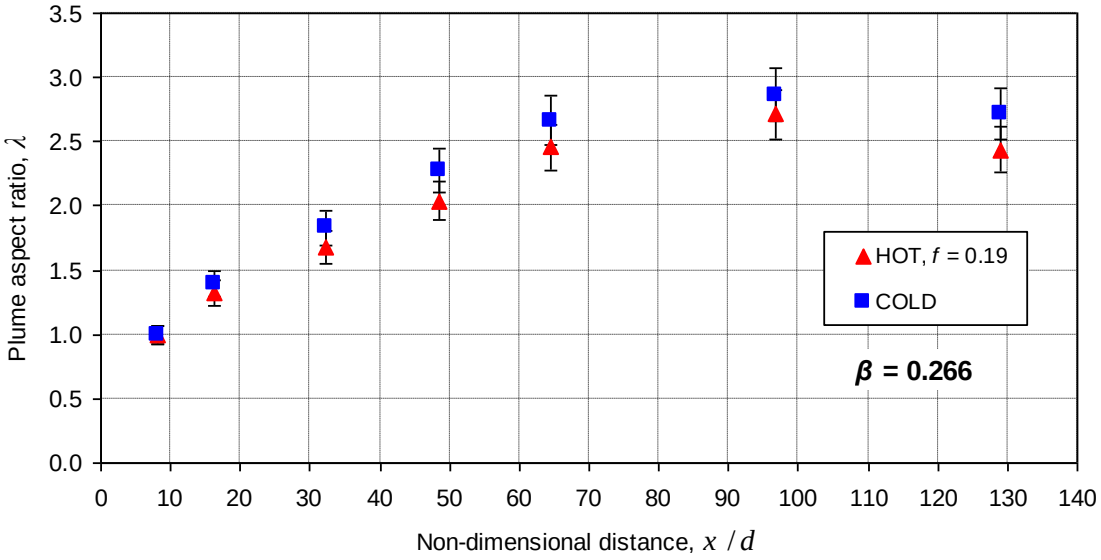

Figure C.3: Variation of plume aspect ratio with non-dimensional longitudinal distance downstream of nozzle exit for β = 0.266

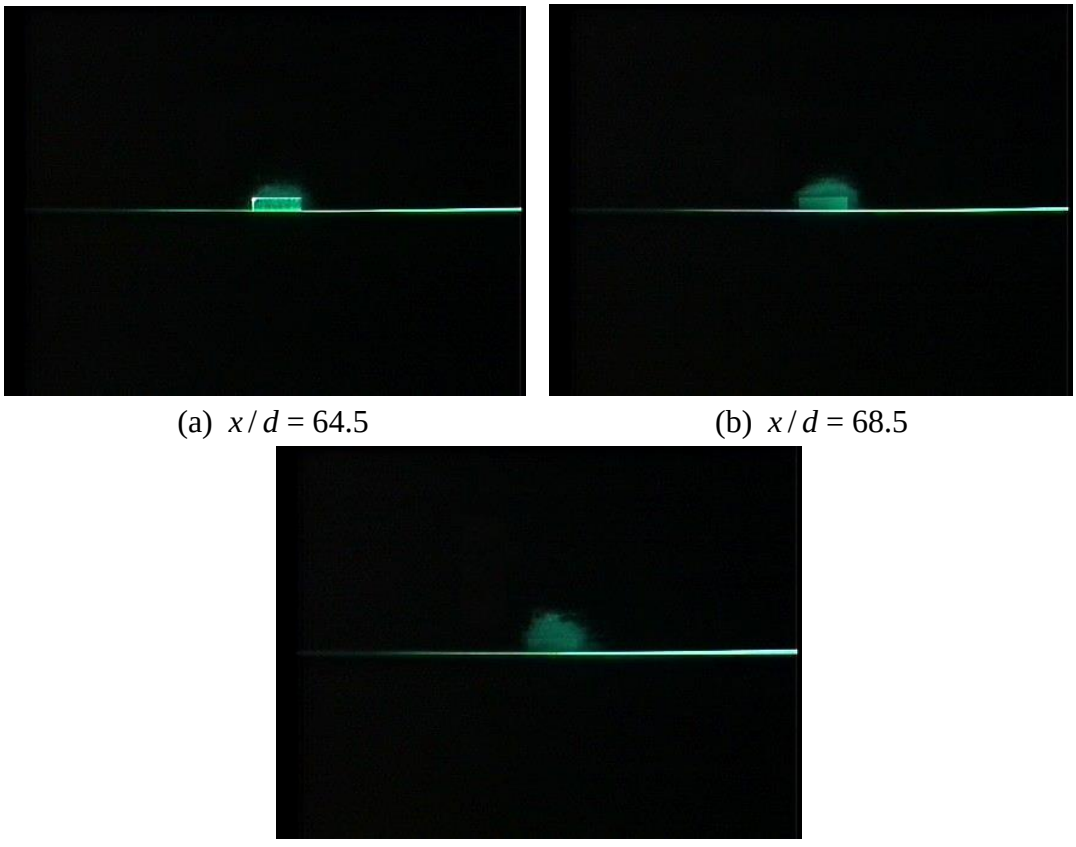

(a) $x/d = 64.5$ (b) $x/d = 68.5$

(c) $x/d = 76.4$

Figure C.4: Effect of placing a deflector ($w/d = 11.3$) at $D = 64$ in the path of the jet

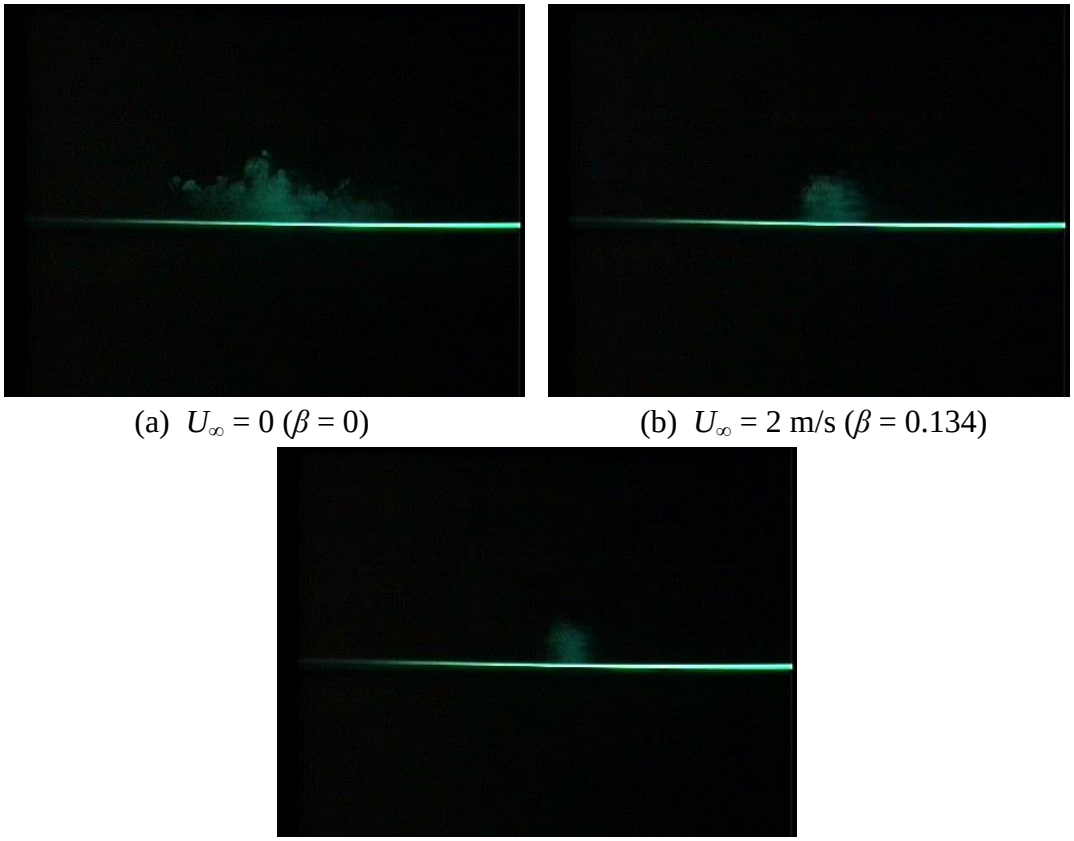

(a) $U_\infty = 0$ ($\beta = 0$)

(b) $U_\infty = 2$ m/s ($\beta = 0.134$)

(c) $U_\infty = 5$ m/s ($\beta = 0.335$)

Figure C.5: Effect of wind tunnel speed on the spread of the plume in the yz plane; x / d = 64

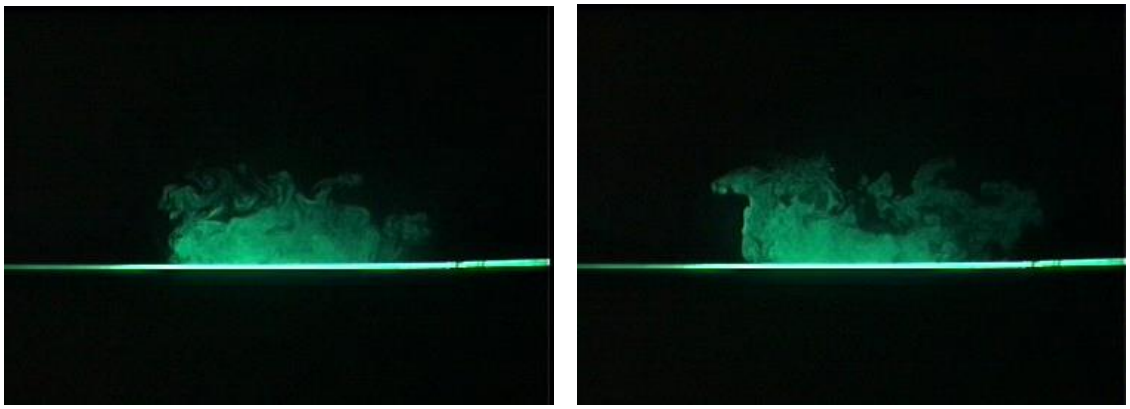

(a) no deflector

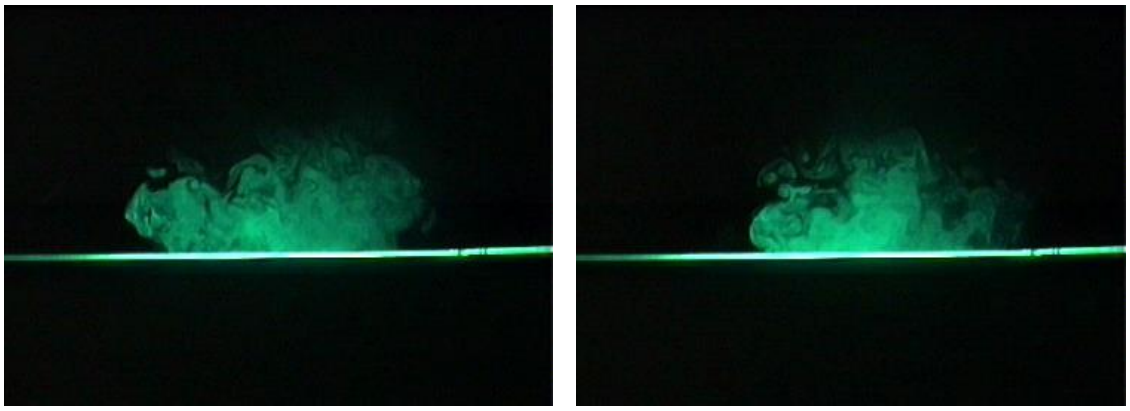

(b) deflector, $w / d = 11.3$

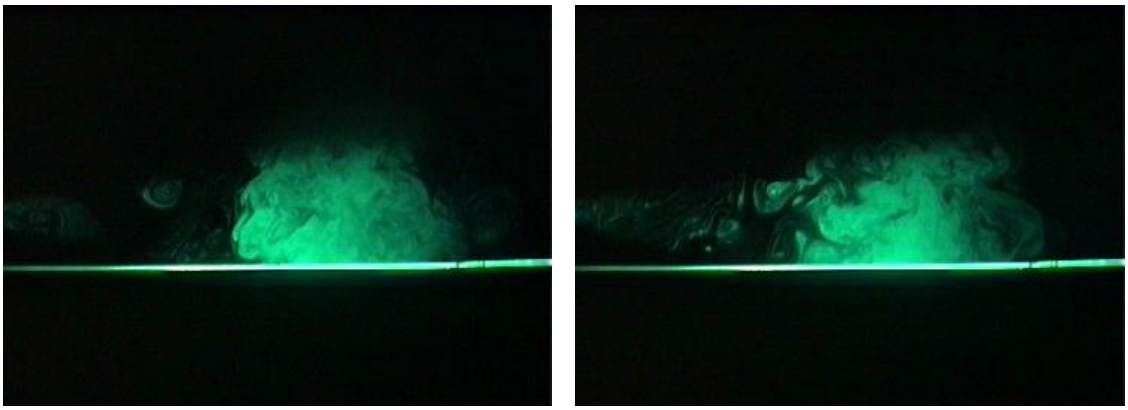

(c) deflector $w / d = 80.6$

Figure C.6: Effects of placing a deflector in the path of the jet at D = 64 without freestream (U_∞ = 0 m/s); x / d = 129

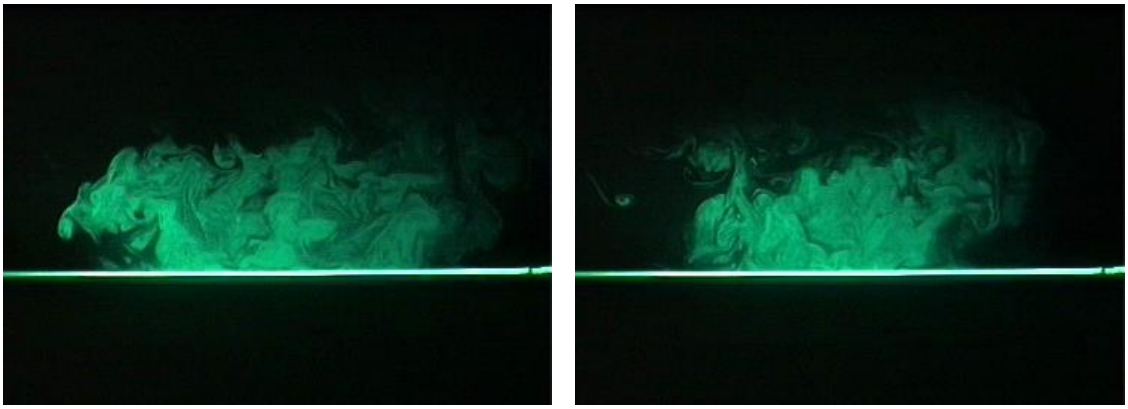

(a) no deflector

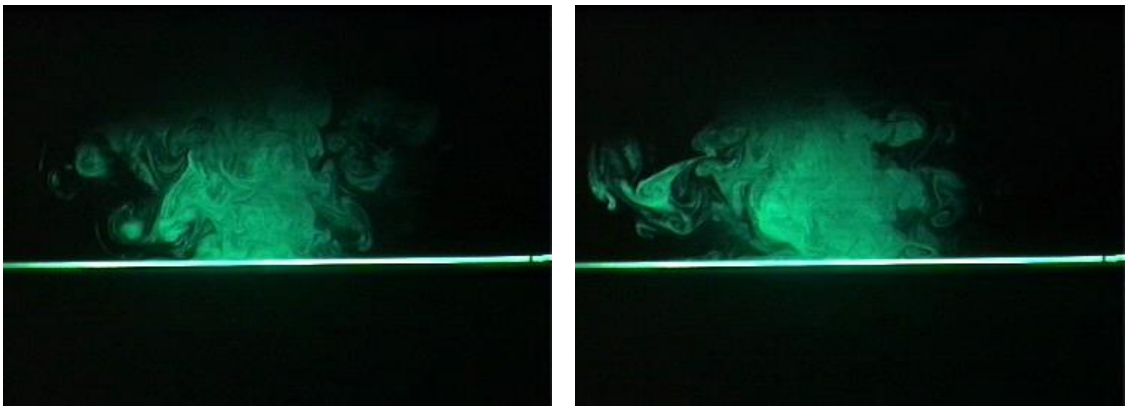

(b) deflector $w / d = 11.3$

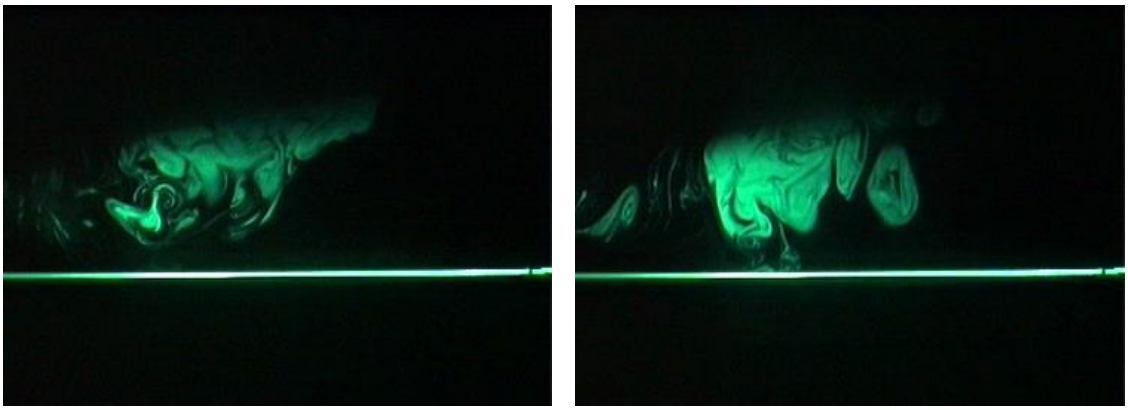

(c) deflector $w / d = 80.6$

Figure C.7: Effects of placing a deflector in the path of the jet at D = 64 without freestream (U_∞ = 0 m/s); x / d = 177

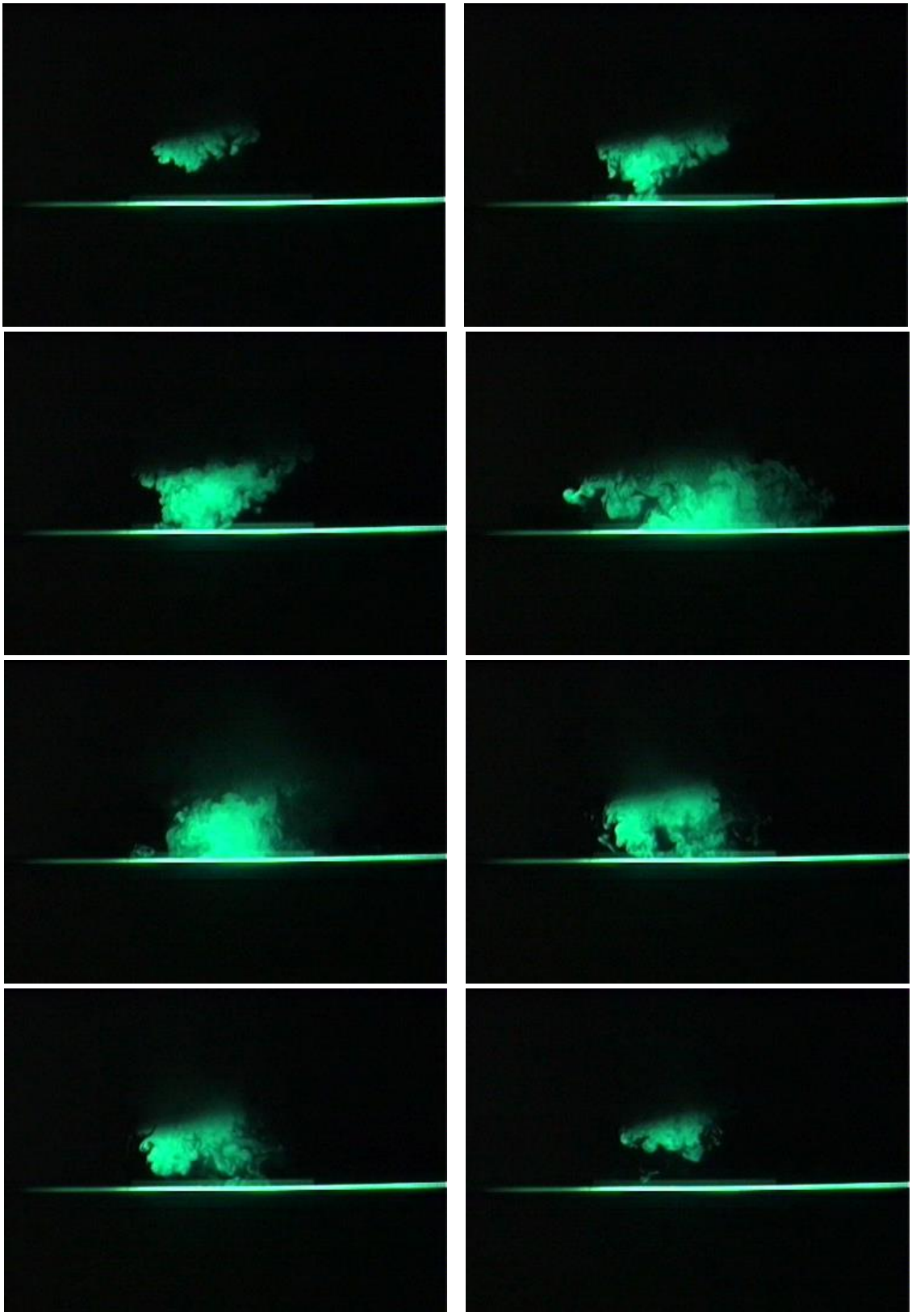

Figure C.8: Plume separation and re-attachment at x / d = 65 downstream of a deflector of width w / d = 80.6 at D = 32; U_∞ = 0 m/s (progression in time is from left to right for a time span of 17 sec)

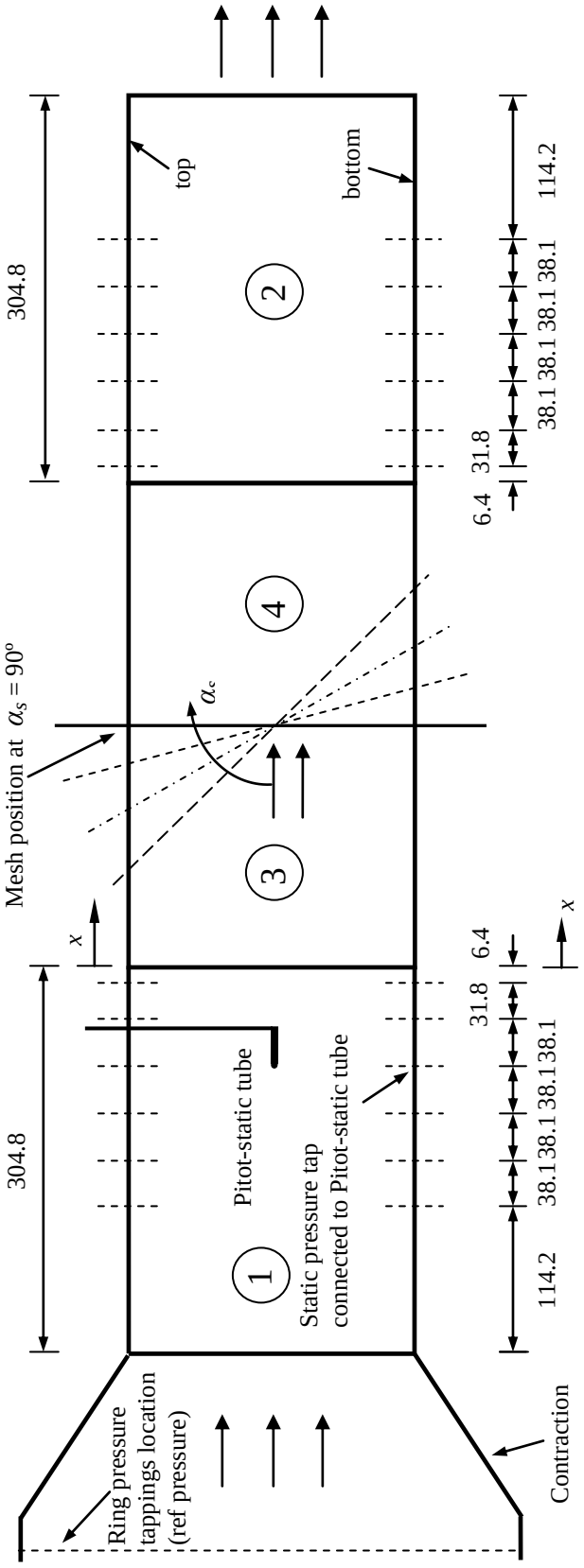

Figure C.9: Schematic illustration of the blower tunnel arrangement for pressure drop measurements (all dimensions in mm; side view; not to scale)

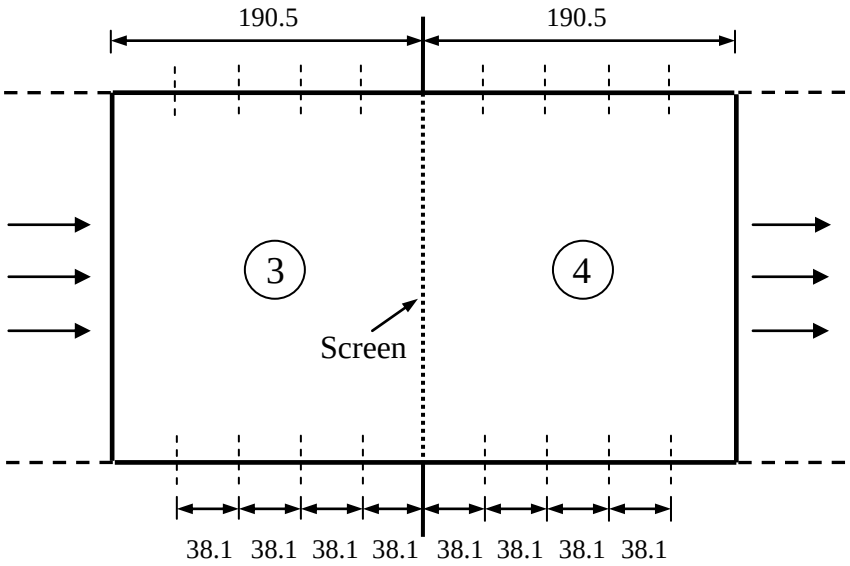

(a) $\alpha_s = 90^o$

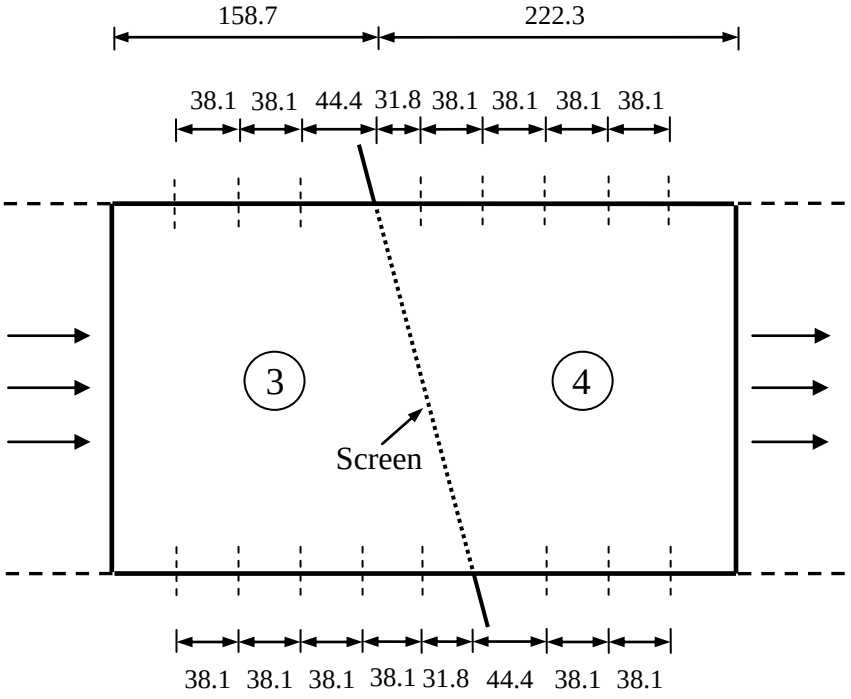

(b) $\alpha_s = 75^o$

Figure C.10: Schematic drawing of the variable blower tunnel working sections for (a) 90º and (b) 75º, to illustrate the pressure tappings locations used to establish the screen pressure drop (all dimensions in mm; side view; not to scale)

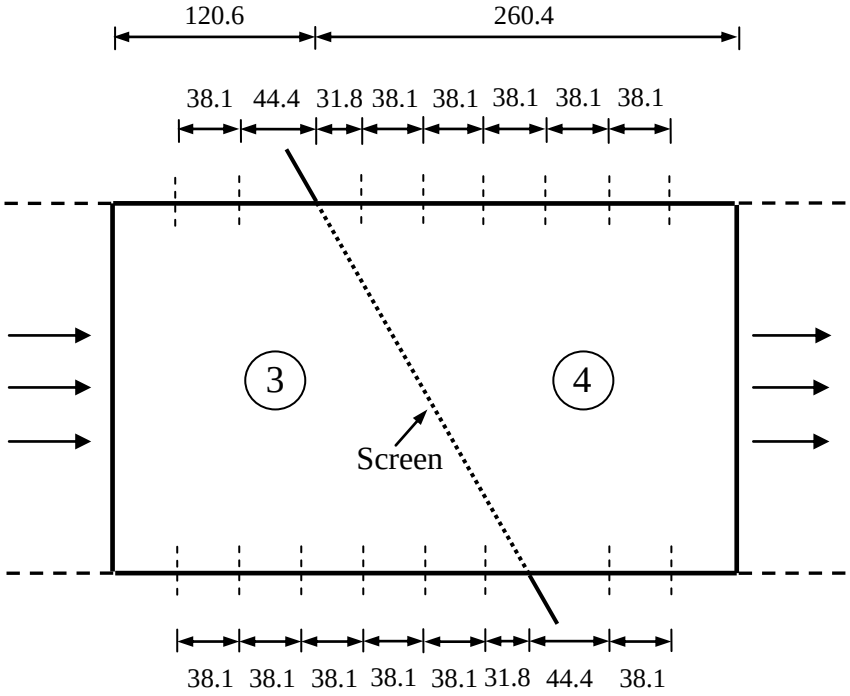

(a) $\alpha_s = 60^o$

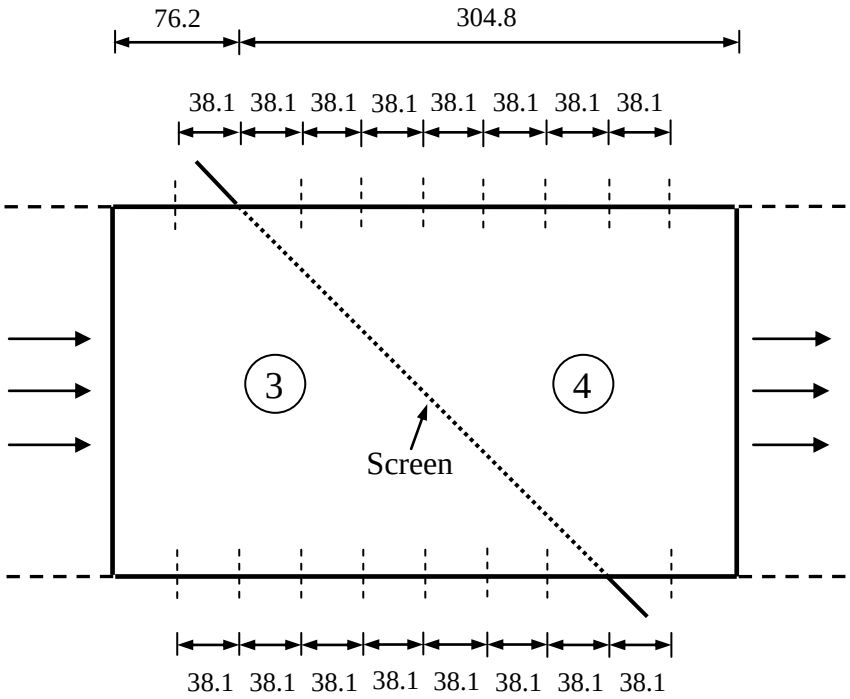

(b) $\alpha_s = 45^o$

Figure C.11: Schematic drawing of the variable blower tunnel working sections for (a) 60º and (b) 45º, to illustrate the pressure tappings locations used to establish the screen pressure drop (all dimensions in mm; side view; not to scale)

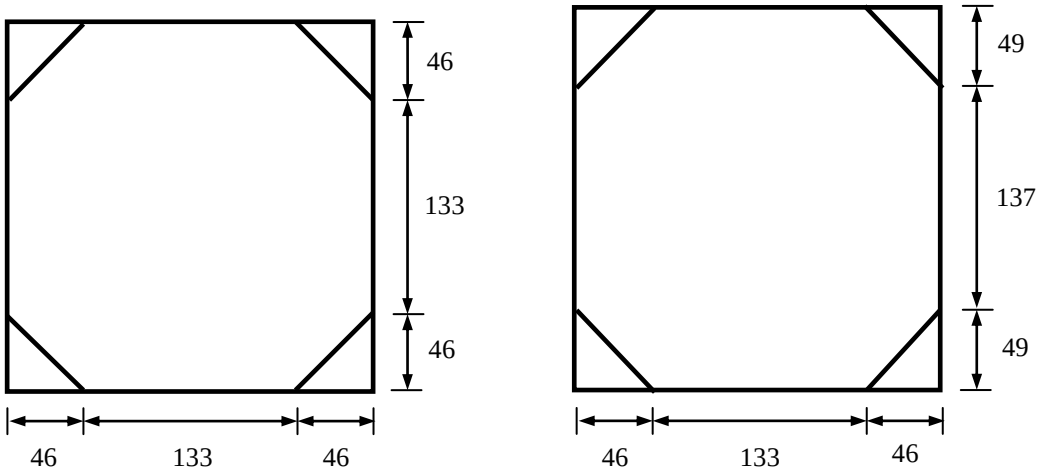

(a) α_s = 90º (b) α_s = 75º

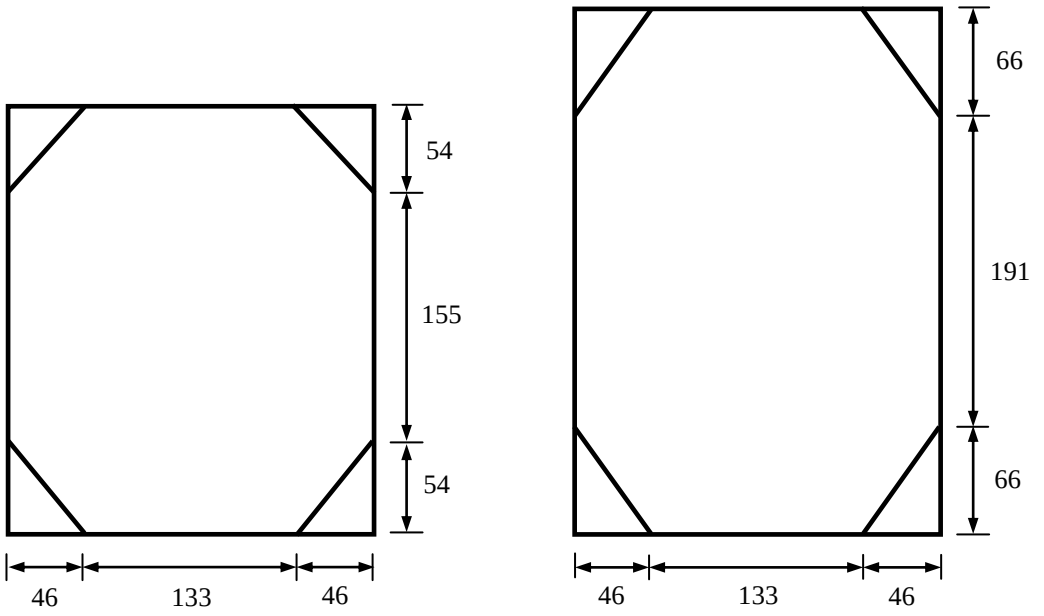

(a) α_s = 60º (b) α_s = 45º

Figure C.12: Schematic drawing of the cross sections along screen plane of the variable blower tunnel working sections for all screen angles tested (all dimensions in mm; side view; not to scale)

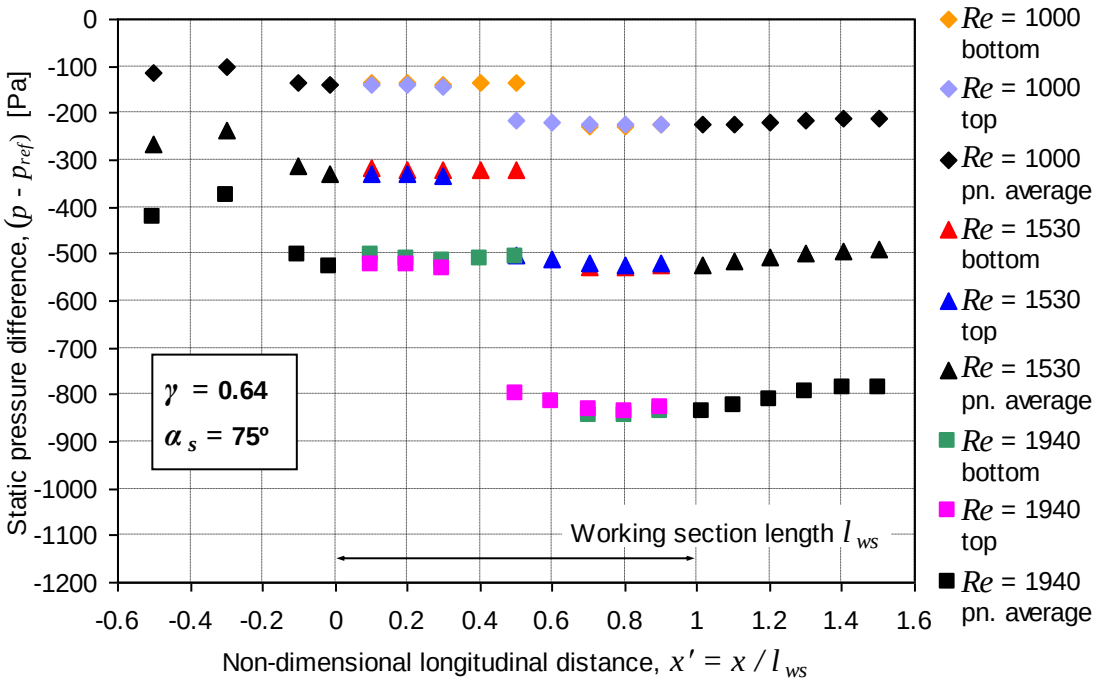

(a)

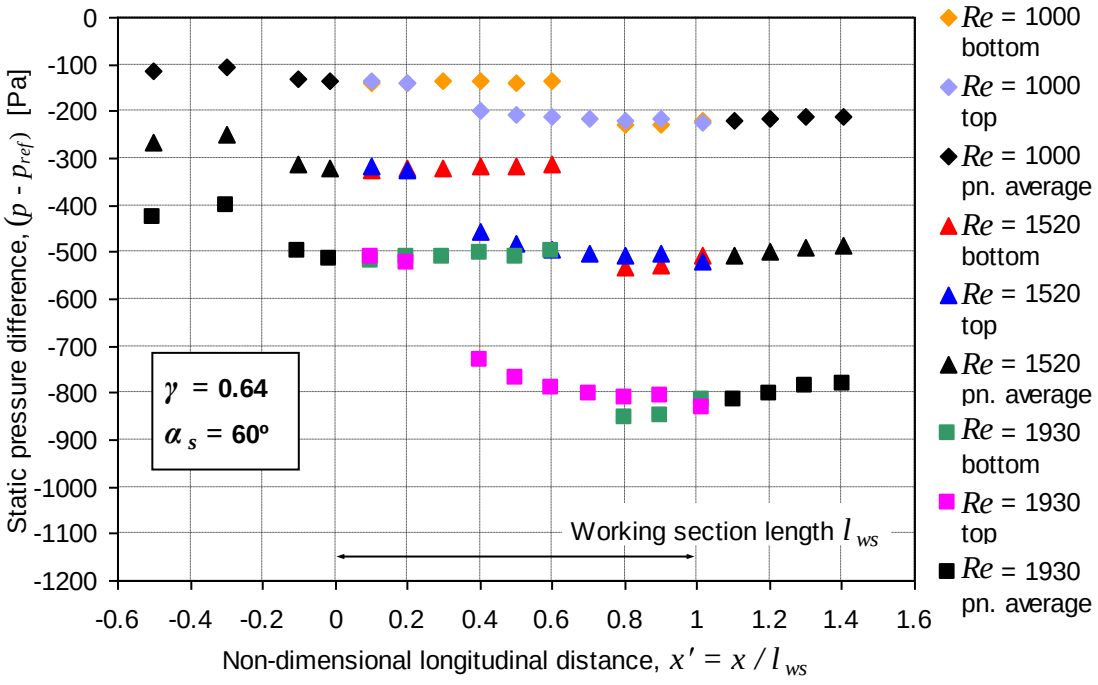

(b)

Figure C.13: Longitudinal static pressure distribution in the working section across a screen of 0.64 porosity at an angle of inclination of: (a) 75° and (b) 60°

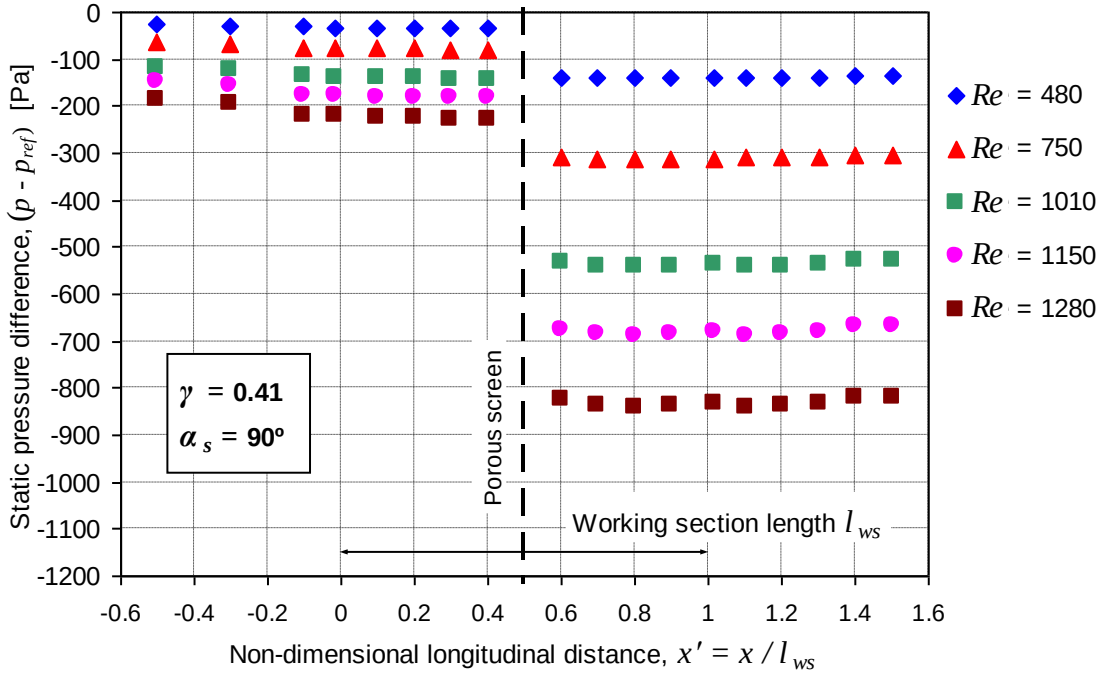

(a)

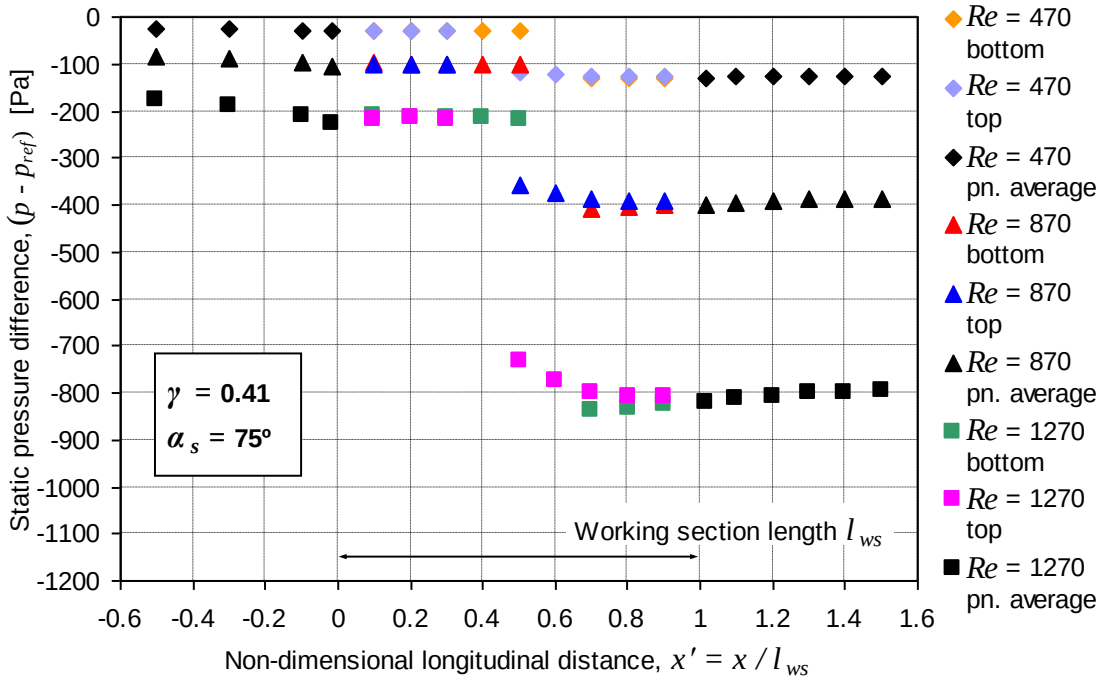

(b)

Figure C.14: Longitudinal static pressure distribution in the working section across a screen of 0.41 porosity at an angle of inclination of: (a) 90° and (b) 75°

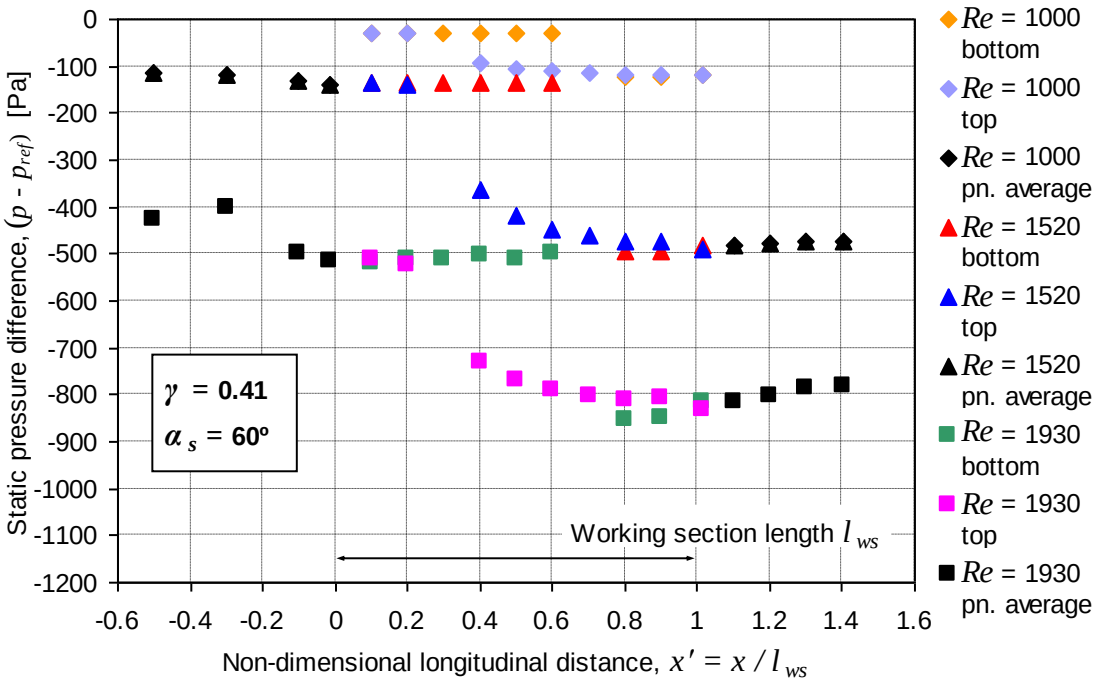

(a)

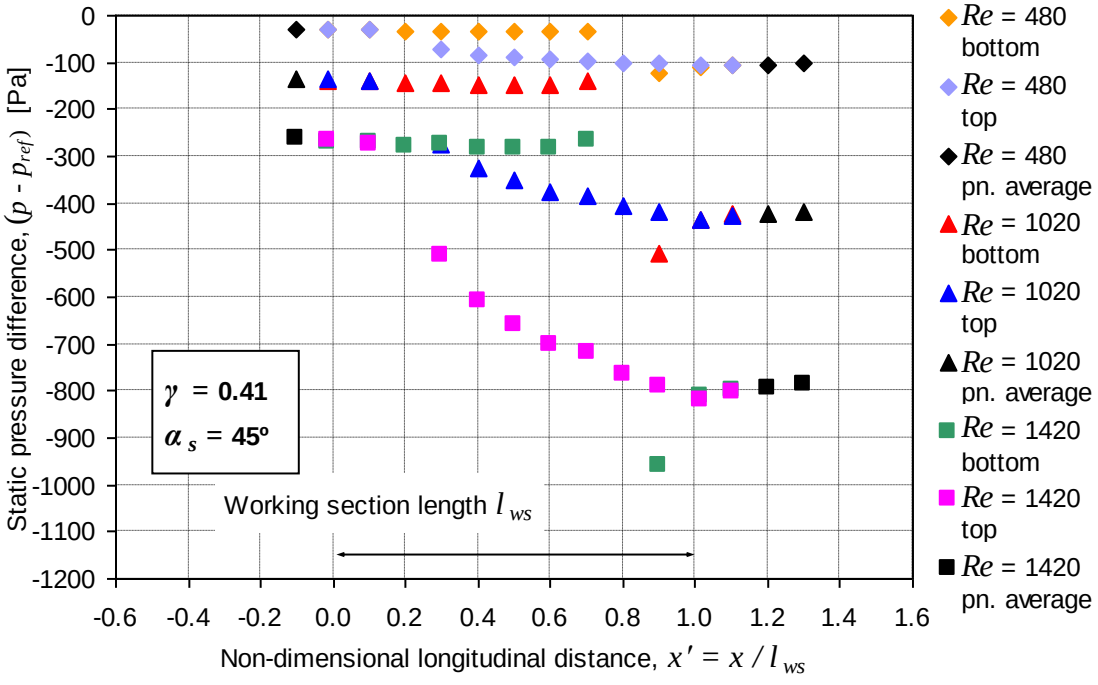

(b)

Figure C.15: Longitudinal static pressure distribution in the working section across a screen of 0.41 porosity at an angle of inclination of: (a) 60º and (b) 45º

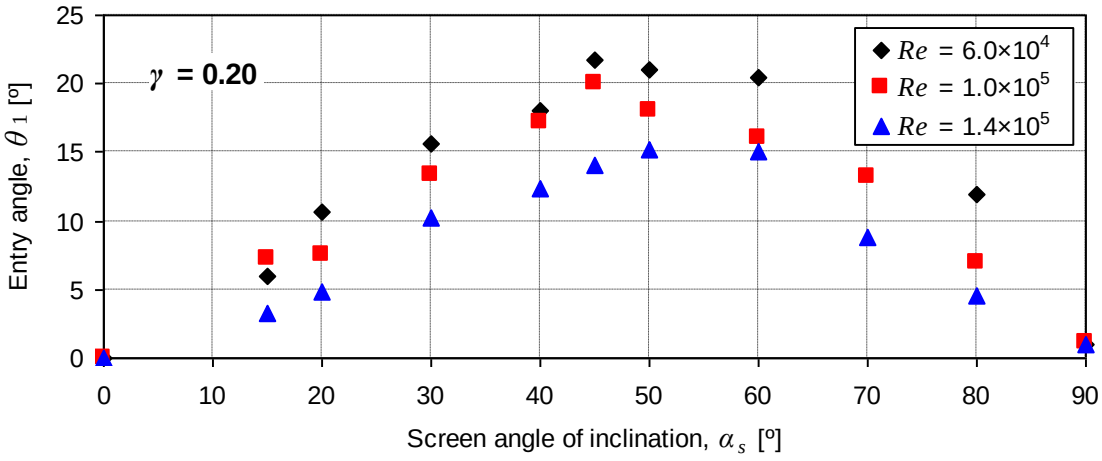

(a)

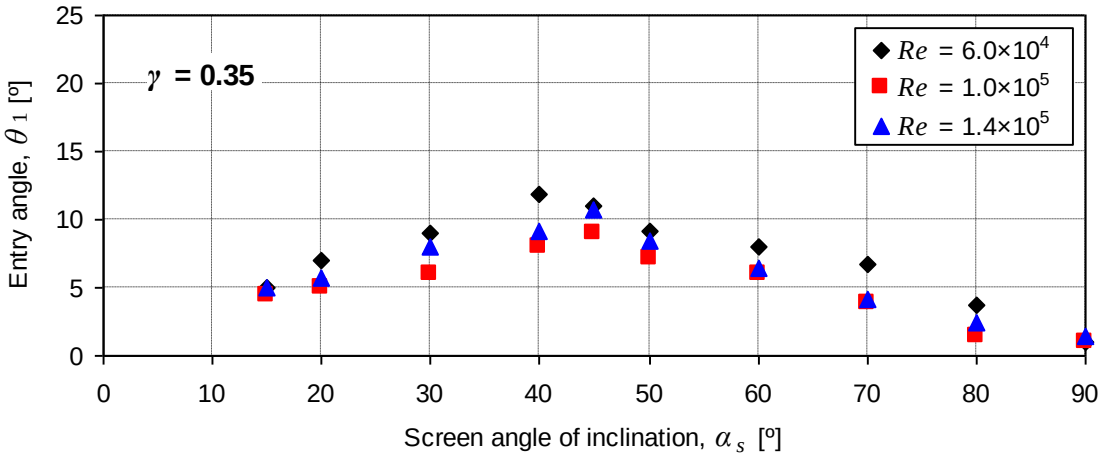

(b)

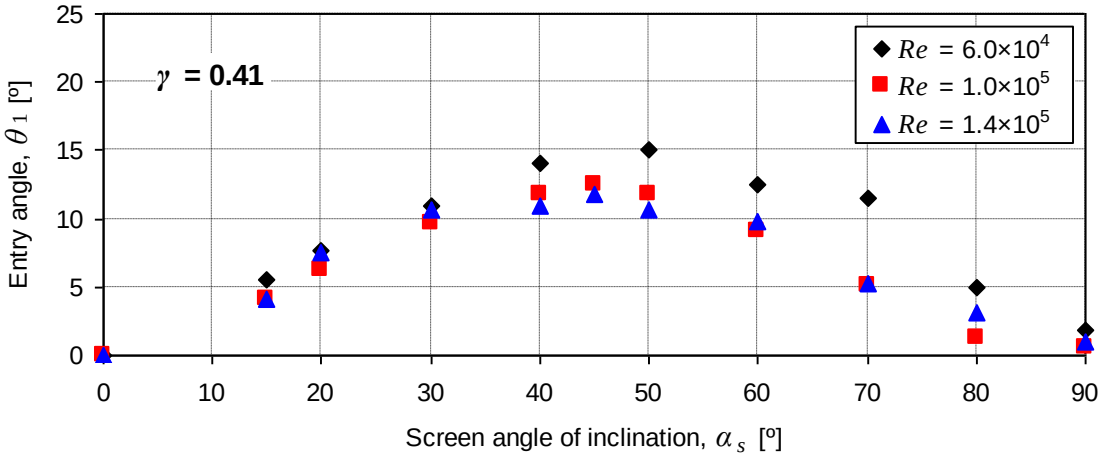

(c)

Figure C.16: Variation of entry angle (in degrees) with screen angle of inclination (in degrees) for screen porosity of (a) 0.20, (b) 0.35 and (c) 0.41

Appendix D: Baffle calculations

D.1 Estimation of baffle drag

In order to estimate the drag of each row of baffles, the following simplified calculation, proposed by Bennett (2011), was used. The following simplifications are assumed in the analysis:

1) The baffles are solid two-dimensional flat plates – a reasonable assumption given the low porosity (γ = 0.2) of the baffle prototypes and the high width-to-height ratios of the baffle rows, used in the field trials

2) Each row of baffles is subjected a constant local jet velocity U and jet density ρ, neglecting the non-uniform velocity distribution within the plume and the presence of a boundary layer close to the ground

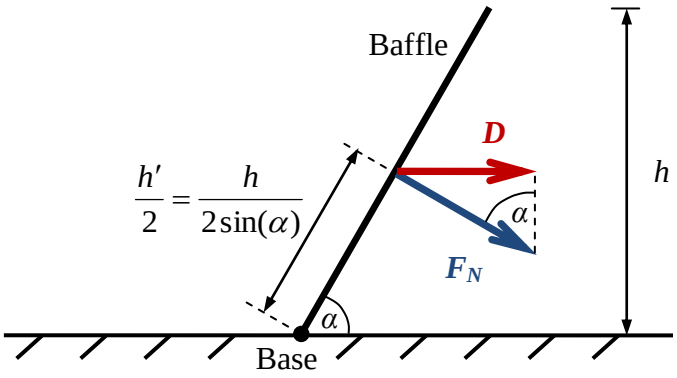

Figure D.1: Schematic illustration of the wind loading on a baffle

The wind loading on a baffle of height h can be represented by a normal force F_N acting normal to the baffle surface (*Figure D.1*). For a jet width W and a baffle slope height $h' = h / \sin(\alpha)$, the normal force F_N and drag D are calculated as follows:

$$F_N = \frac{1}{2}\rho U^2 C_N h' W$$

Equation D.1

$$D = F_N \sin(\alpha) = \frac{1}{2}\rho U^2 C_N h W$$

Equation D.2

The normal force coefficient C_N is a function of the baffle slope angle α. For a flat plate of infinite slenderness (i.e. height-to-thickness ratio) in a freestream at zero yaw, Cook (1990, Figure 16.20) gives $C_{N\infty}$ = 2.10, 1.96 and 1.69, based on freestream velocity, for α = 90º, 60º and 45º respectively. For surface-mounted fences, ESDU (1989, Figure 7) gives C_N = 1.15, based on the velocity at the height h of the fence, for α = 90º and $w/h \geq 10$. Similar value (C_N = 1.2) is reported by Cook (1990, Figure 16.1) for α = 90º and $2h/w \leq 1$. The normal force coefficient for an inclined surface-mounted baffle $C_N(\alpha)$ can then be estimated with

$$C_N(\alpha) = \frac{C_{N\infty}(\alpha)}{C_{N\infty}(\alpha = 90^\circ)} C_N(\alpha = 90^\circ)$$

Equation D.3

With $C_N(\alpha$ = 90º) = 1.15, for baffles inclined at 45 and 60 to the flow, the coefficients are $C_N(\alpha$ = 45º) = 0.93 and $C_N(\alpha$ = 60º) = 1.07.

The jet momentum flux per unit area, ρU^2, is in the order of $F_t/(WH)$, where F_t is the total thrust of the BAe 146-301, i.e. 124 N, and W and H are the lateral and vertical plume spread, which increase with longitudinal distance x from the BAe 146-301 engines. W and H were estimated from previous Lidar observations of the BAe 146-301 during take-off at Cranfield Airport as $W \approx 0.243x$ and $H \approx 0.111x$ (Bennett, 2011). Thus, the following relationship is used to estimate ρU^2 with x:

$$\rho U^2 \approx \frac{F_t}{0.027x^2}$$

Equation D.4

With $W \approx 0.243x$, the drag of each row, located at distance x downstream of the BAe 146-301 engines, is estimated from

$$D \approx \frac{F_t}{0.222x} C_N h$$

Equation D.5

Alternatively, the single-row drag coefficients C_F, obtained from the force balance tests (Chapter 5.3.1), can be used to estimate the drag of each row of baffles. Since C_F is based on the flow velocity at the baffle height h and the projected frontal area, the drag is given by:

$$D = \frac{1}{2}\rho U^2 C_F hW \approx \frac{F_t}{0.222x} C_F h$$

Equation D.6

For models of 90º, 60º and 45º (*Figure 5.5*) the obtained average values C_F are 0.87, 0.78 and 0.71 respectively. As discussed in Chapter 5.3.1, $C_F(\alpha = 90º) = 0.87$ is lower than the corresponding values given by ESDU (1989) and Cook (1990) of 1.15 and 1.2, which is mostly attributed to the boundary layer flow over the smooth surface in the working section. The reduction in C_F with decreasing surface roughness (i.e. z_0) is shown in *Figure E.5* in terms of Jensen number, defined as $Je = h / z_0$. For the purpose of this simplified drag estimation, the values of C_F for 60º and 45º can be extrapolated similarly to *Equation D.3*, with the ratio $(1.15 / 0.87) = 1.32$, using the normal force coefficient at 90º given by ESDU (1989). This yields values of 1.03 and 0.94 for 60º and 45º respectively, which compare well with $C_N(\alpha = 60º) = 1.07$ and $C_N(\alpha = 45º) = 0.93$. Thus, *Equation D.5* and *Equation D.6* would estimate practically the same drag values.

D.2 Estimation of baffle maximum permissible width

The width of the individual baffles w_n of each row is calculated from the maximum permissible bending moment, i.e. $M_{B\,max} = 678$ Nm, according to the design criteria for frangibility of elevated runway and taxing edge lights (ICAO, 2006b, p. 4-6). From *Figure D.1*, the bending moment about the base is

$$M_B = F_N \frac{h'}{2} \approx \frac{F_t}{0.108}\left(\frac{h'}{x}\right)^2 C_N w_n$$

Equation D.7

For a maximum bending moment $M_{B\,max}$, the maximum individual baffle width is

$$w_{n\,max} \approx \frac{0.108 M_{B\,max}}{C_N F_t}\left(\frac{x}{h'}\right)^2$$

Equation D.8

Appendix E: Force balance measurements

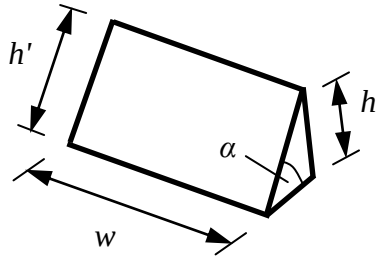

α = 45º Row No.	1:50 scale [mm]			Full scale [m]	
	h'_M	h_M	w_M	h_{FS}	w_F
1	16.6	11.8	292.1	0.59	14.61
2	20.1	14.2	351.4	0.71	17.57
3	28.4	20.2	421.7	1.01	21.09
4	34.3	24.4	506.0	1.22	25.30
5	41.4	29.3	606.3	1.47	30.32

(a)

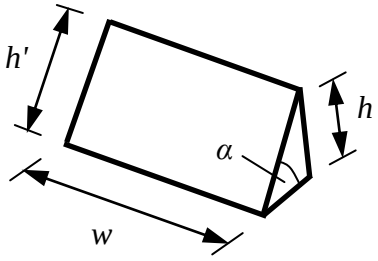

α = 60º Row No.	1:50 scale [mm]			Full scale [m]	
	h'_M	h_M	w_M	h_F	w_F
1	15.6	13.3	291.2	0.67	14.56
2	19.7	17.1	351.8	0.86	17.59
3	24.0	20.5	420.5	1.03	21.03
4	27.5	24.1	505.8	1.21	25.29
5	33.1	28.8	606.5	1.44	30.33

(b)

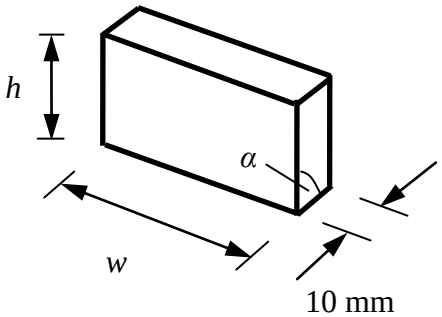

α = 90º Row No.	1:50 scale [mm]		Full scale [m]	
	$h'_M = h_M$	w_M	h_F	w_F
1	14.1	293.0	0.71	14.65
2	17.2	351.2	0.86	17.56
3	20.5	421.0	1.03	21.05
4	24.6	505.8	1.23	25.29
5	29.6	607.0	1.48	30.35

(c)

Figure E.1: Rows of baffle models at 1:50 scale

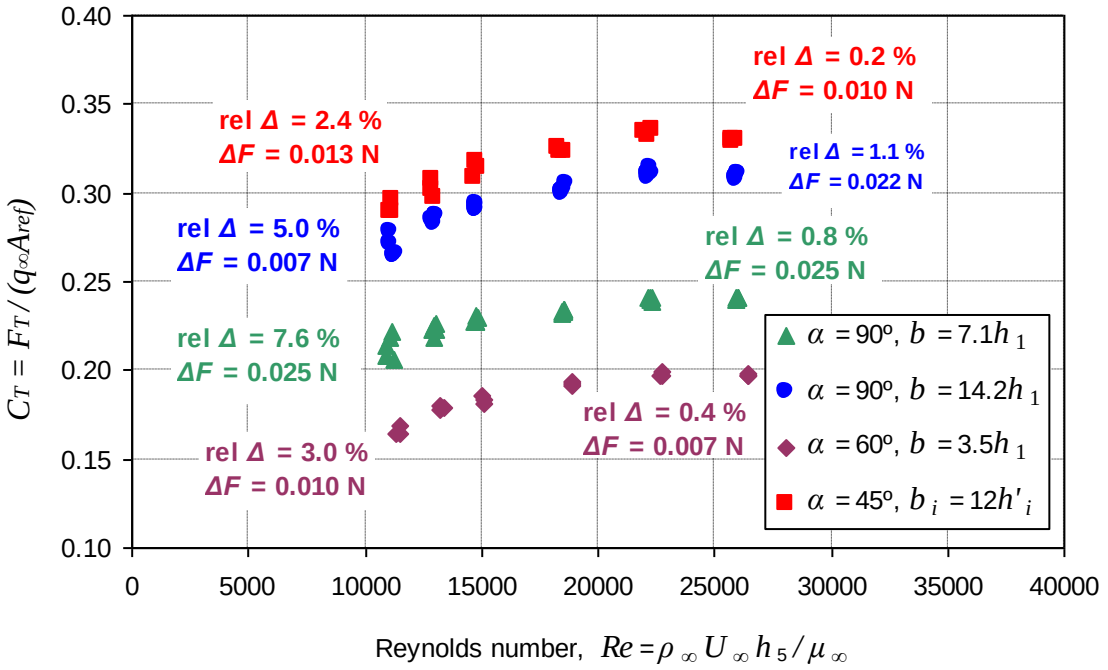

Figure E.2: Calculated relative errors of C_T and absolute errors of F_T (in N) from the minimum and maximum measured forces during repeatability runs at U_∞ = 6 m/s and U_∞ = 14 m/s

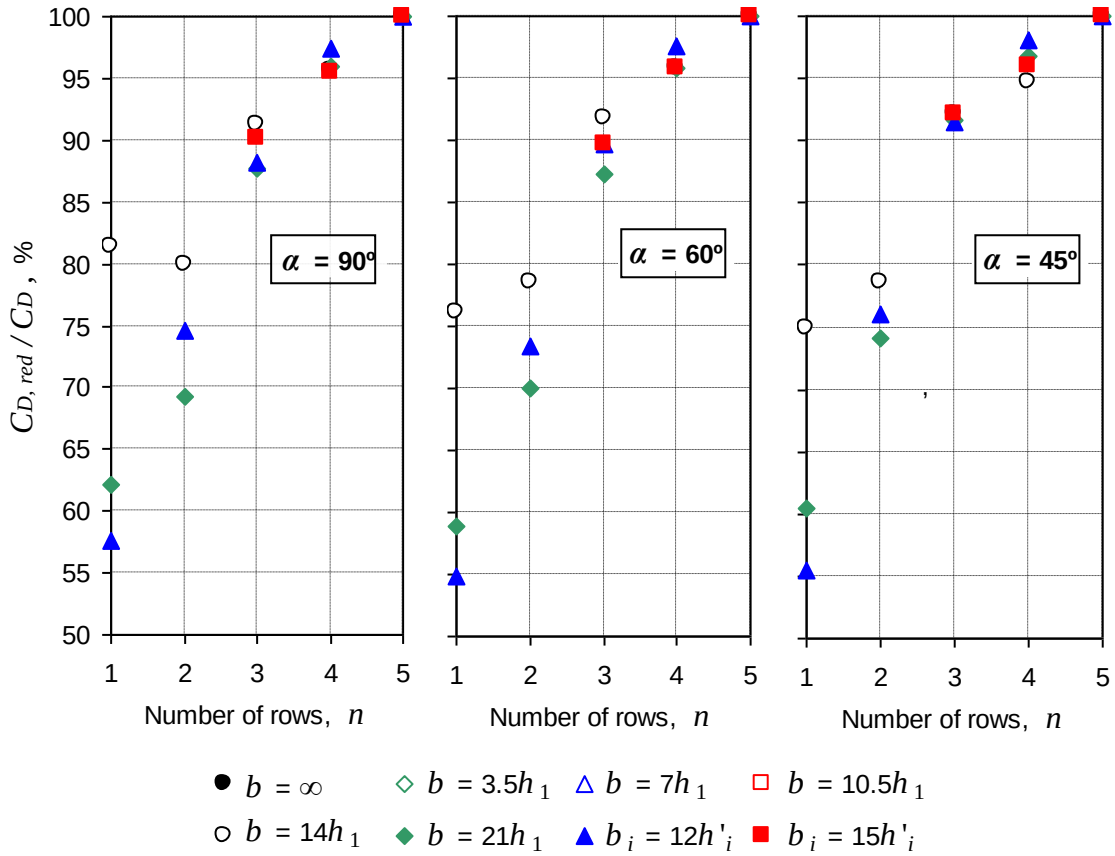

Figure E.3: Percentage variation of drag coefficient for configurations of reduced number of baffle rows compared to all 5 rows

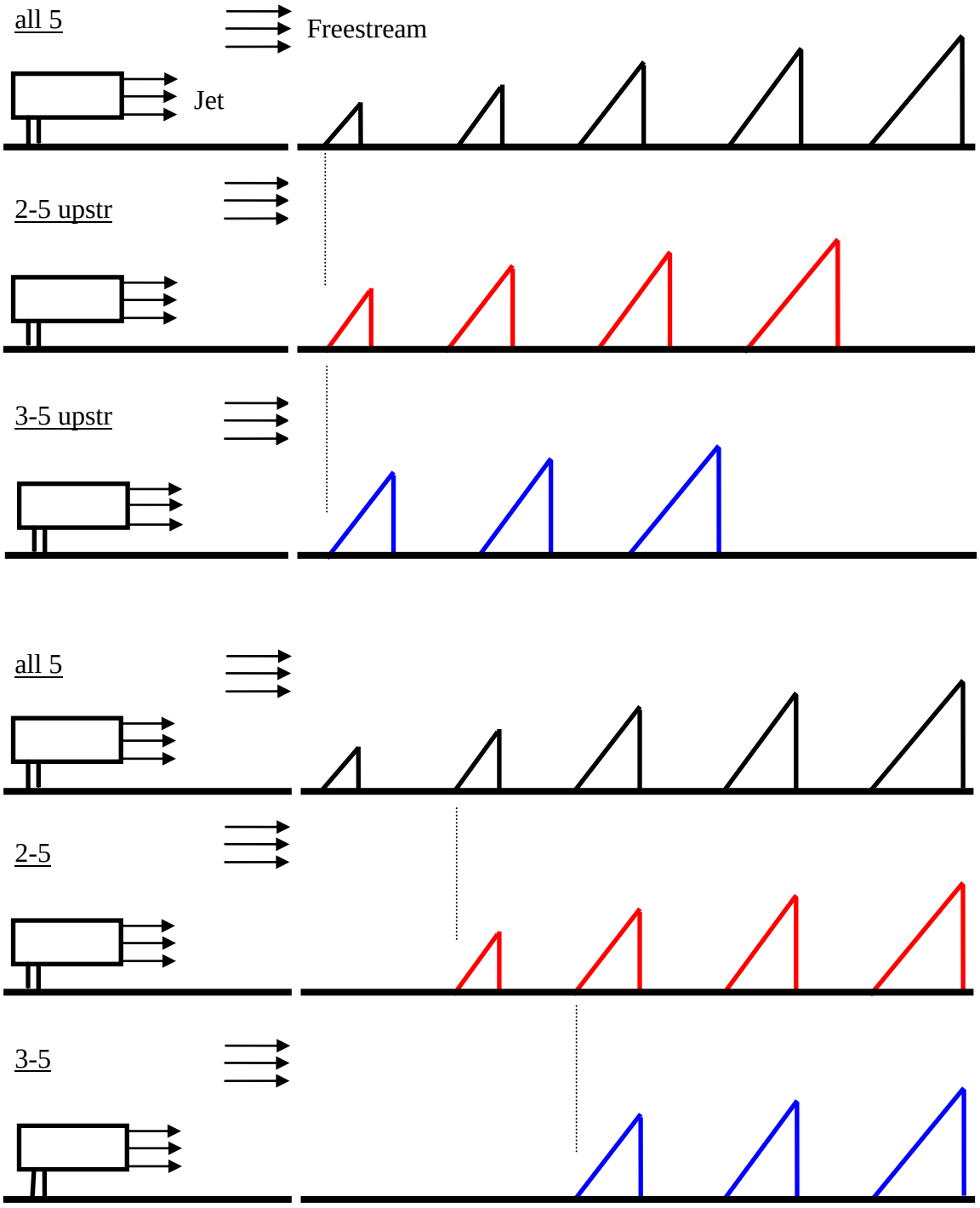

Figure E.4: Overview of baffle configurations tested in a nozzle jet

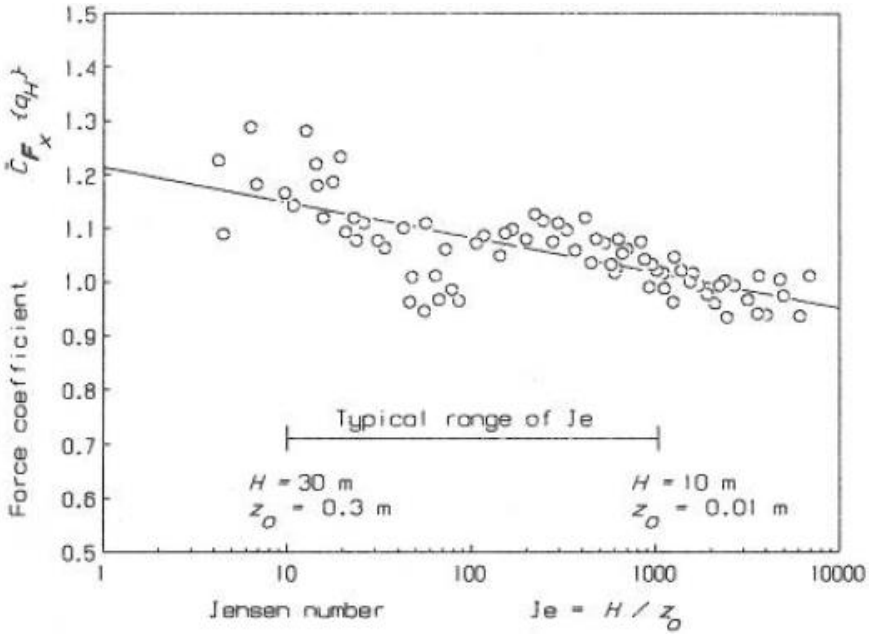

Figure E.5: Effect of ground roughness on the normal force acting on an infinitely long solid fence of height H (taken from Cook, 1990)

Appendix F: ABL calculations

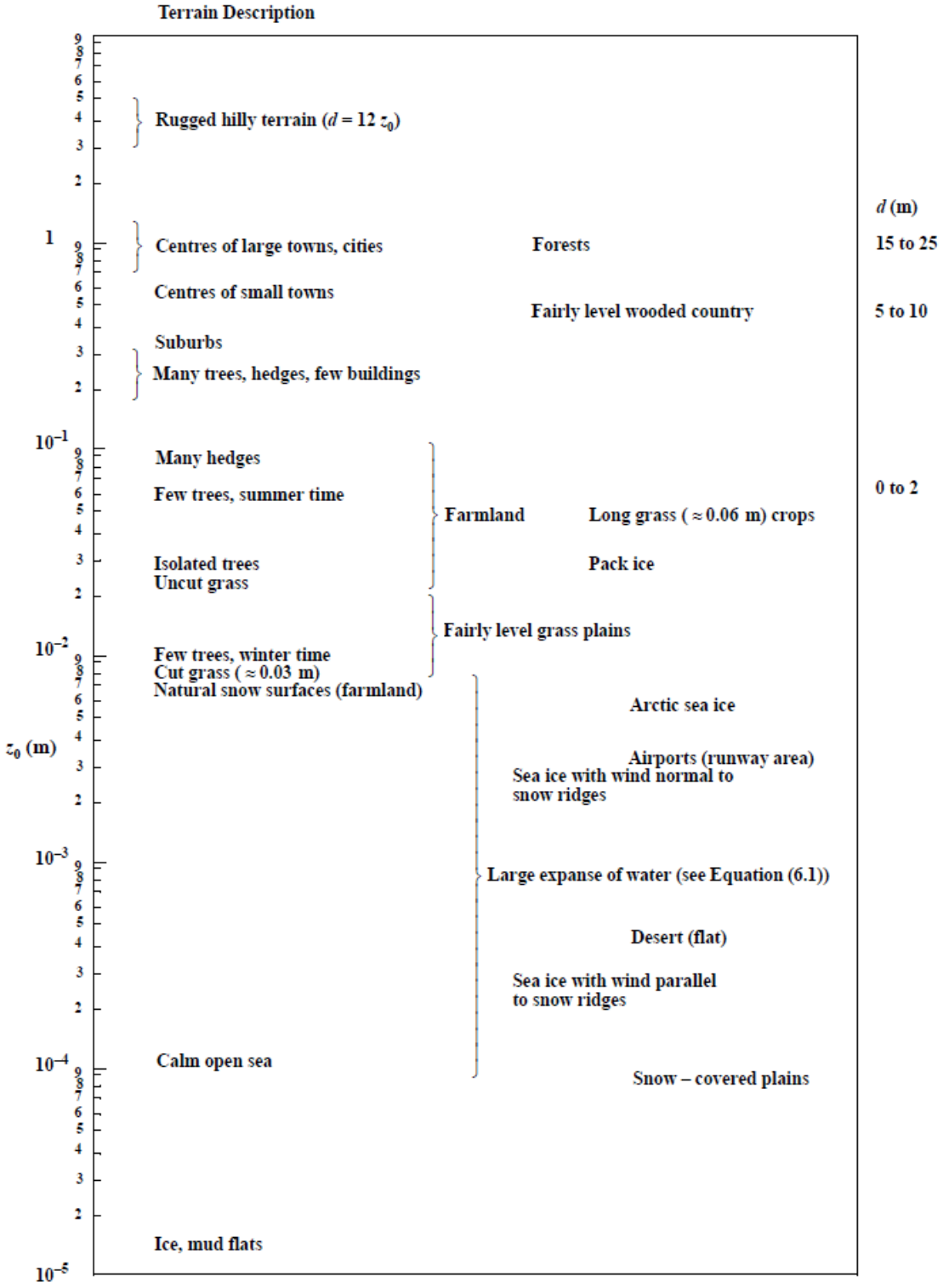

Figure F.1: Values of the roughness length z_0 for different types of terrain (taken from ESDU, 1982)

Table F.1: Calculated velocity and turbulence intensity profiles for the Atmospheric Boundary Layer (z_0 = 0.03 m) at 1:100 scale

Height		U_z	I_u	U_z / U_{10}		U_z / U_{10}	U_z	σ_u / u^*	U_z / u^*	I_u
z_M	z_F	measured	measured	measured	$\ln(z/z_0)$	ESDU	ESDU	ESDU	ESDU	ESDU
mm	m	m/s	-	-	-	-	m/s	-	-	-
7	0.7	1.213	0.171	0.778	3.150	0.542	0.846	2.379	7.939	0.300
10	1	1.249	0.149	0.801	3.507	0.604	0.942	2.471	8.859	0.279
15	1.5	1.276	0.142	0.818	3.912	0.673	1.051	2.572	9.919	0.259
20	2	1.317	0.136	0.844	4.200	0.723	1.128	2.637	10.684	0.247
25	2.5	1.367	0.132	0.876	4.423	0.761	1.188	2.683	11.288	0.238
30	3	1.357	0.143	0.870	4.605	0.793	1.237	2.715	11.790	0.230
35	3.5	1.452	0.124	0.931	4.759	0.819	1.278	2.739	12.222	0.224
40	4	1.426	0.117	0.914	4.893	0.842	1.314	2.755	12.602	0.219
45	4.5	1.367	0.125	0.876	5.011	0.863	1.346	2.767	12.942	0.214
50	5	1.414	0.144	0.906	5.116	0.881	1.374	2.774	13.252	0.209
55	5.5	1.488	0.118	0.954	5.211	0.897	1.399	2.779	13.536	0.205
60	6	1.496	0.123	0.959	5.298	0.912	1.423	2.780	13.800	0.201
65	6.5	1.537	0.109	0.985	5.378	0.926	1.444	2.780	14.046	0.198
70	7	1.466	0.109	0.940	5.452	0.939	1.464	2.778	14.278	0.195
75	7.5	1.564	0.112	1.003	5.521	0.950	1.483	2.774	14.496	0.191
80	8	1.558	0.109	0.999	5.586	0.962	1.500	2.769	14.704	0.188
90	9	1.568	0.121	1.005	5.704	0.982	1.532	2.756	15.091	0.183
100	10	1.560	0.115	1	5.809	1	1.560	2.740	15.446	0.177
110	11	1.605	0.096	1.029	5.904	1.016	1.586	2.722	15.777	0.173
120	12	1.640	0.106	1.051	5.991	1.031	1.609	2.703	16.087	0.168
130	13	1.616	0.090	1.036	6.072	1.045	1.630	2.683	16.379	0.164
140	14	1.652	0.090	1.059	6.146	1.058	1.650	2.662	16.657	0.160
150	15	1.616	0.119	1.036	6.215	1.070	1.669	2.641	16.922	0.156
160	16	1.675	0.090	1.074	6.279	1.081	1.686	2.619	17.176	0.152
170	17	1.736	0.084	1.113	6.340	1.091	1.702	2.598	17.419	0.149
180	18	1.741	0.085	1.116	6.397	1.101	1.718	2.576	17.655	0.146
190	19	1.711	0.099	1.097	6.451	1.110	1.732	2.554	17.882	0.143
200	20	1.659	0.091	1.063	6.502	1.119	1.746	2.533	18.103	0.140
210	21	1.713	0.089	1.098	6.551	1.128	1.759	2.512	18.317	0.137
220	22	1.682	0.09	1.078	6.598	1.136	1.772	2.490	18.526	0.134
230	23	1.749	0.084	1.121	6.642	1.143	1.784	2.469	18.729	0.132
240	24	1.800	0.080	1.154	6.685	1.151	1.795	2.449	18.928	0.129
250	25	1.803	0.077	1.156	6.725	1.158	1.806	2.428	19.122	0.127
270	27	1.784	0.070	1.144	6.802	1.171	1.827	2.387	19.500	0.122
290	29	1.780	0.079	1.141	6.874	1.183	1.846	2.347	19.863	0.118
310	31	1.751	0.084	1.122	6.941	1.195	1.864	2.308	20.214	0.114
350	35	1.798	0.072	1.153	7.062	1.216	1.896	2.230	20.887	0.107
400	40	1.800	0.074	1.154	7.195	1.239	1.932	2.135	21.683	0.098
450	45	1.843	0.061	1.181	7.313	1.259	1.964	2.041	22.439	0.091
500	50	1.845	0.068	1.183	7.419	1.277	1.992	1.948	23.164	0.084

Table F.2: Calculated velocity and turbulence intensity profiles for the Atmospheric Boundary Layer (z_0 = 0.03 m) at 1:200 scale

Height		U_z	I_u	U_z / U_{10}		U_z / U_{10}	U_z	σ_u / u^*	U_z / u^*	I_u
z_M	z_F	measured	measured	measured	$\ln(z/z_0)$	ESDU	ESDU	ESDU	ESDU	ESDU
mm	m	m/s	-	-	-	-	m/s	-	-	-
7	1.4	1.213	0.171	0.858	3.843	0.662	0.935	2.572	9.750	0.264
10	2	1.249	0.149	0.883	4.200	0.723	1.022	2.653	10.703	0.248
15	3	1.276	0.142	0.902	4.605	0.793	1.121	2.729	11.819	0.231
20	4	1.317	0.136	0.931	4.893	0.842	1.191	2.766	12.640	0.219
25	5	1.367	0.132	0.967	5.116	0.881	1.245	2.781	13.299	0.209
30	6	1.357	0.143	0.960	5.298	0.912	1.290	2.784	13.857	0.201
35	7	1.452	0.124	1.027	5.452	0.939	1.327	2.778	14.344	0.194
40	8	1.426	0.117	1.008	5.586	0.962	1.360	2.766	14.780	0.187
45	9	1.367	0.125	0.967	5.704	0.982	1.388	2.750	15.176	0.181
50	10	1.414	0.144	1.000	5.809	1.000	1.414	2.731	15.542	0.176
55	11	1.488	0.118	1.052	5.904	1.016	1.437	2.710	15.882	0.171
60	12	1.496	0.123	1.058	5.991	1.031	1.458	2.688	16.201	0.166
65	13	1.537	0.109	1.087	6.072	1.045	1.478	2.666	16.503	0.162
70	14	1.466	0.109	1.037	6.146	1.058	1.496	2.643	16.790	0.157
75	15	1.564	0.112	1.106	6.215	1.070	1.513	2.619	17.065	0.153
80	16	1.558	0.109	1.102	6.279	1.081	1.528	2.596	17.328	0.150
90	18	1.568	0.121	1.109	6.397	1.101	1.557	2.549	17.826	0.143
100	20	1.560	0.115	1.103	6.502	1.119	1.583	2.502	18.293	0.137
110	22	1.605	0.096	1.135	6.598	1.136	1.606	2.456	18.735	0.131
120	24	1.640	0.106	1.160	6.685	1.151	1.627	2.411	19.157	0.126
130	26	1.616	0.090	1.143	6.765	1.164	1.647	2.367	19.560	0.121
140	28	1.652	0.090	1.168	6.839	1.177	1.665	2.323	19.949	0.116
150	30	1.616	0.119	1.143	6.908	1.189	1.681	2.280	20.326	0.112
160	32	1.675	0.090	1.185	6.972	1.200	1.697	2.237	20.691	0.108
170	34	1.736	0.084	1.228	7.033	1.211	1.712	2.195	21.046	0.104
180	36	1.741	0.085	1.231	7.090	1.221	1.726	2.153	21.393	0.101
190	38	1.711	0.099	1.210	7.144	1.230	1.739	2.111	21.732	0.097
200	40	1.659	0.091	1.173	7.195	1.239	1.751	2.070	22.064	0.094
210	42	1.713	0.089	1.211	7.244	1.247	1.763	2.028	22.389	0.091
220	44	1.682	0.090	1.190	7.291	1.255	1.775	1.987	22.710	0.087
230	46	1.749	0.084	1.237	7.335	1.263	1.785	1.946	23.024	0.085
240	48	1.800	0.080	1.273	7.378	1.270	1.796	1.905	23.335	0.082
250	50	1.803	0.077	1.275	7.419	1.277	1.806	1.864	23.640	0.079
270	54	1.784	0.070	1.262	7.496	1.290	1.824	1.782	24.240	0.074
290	58	1.780	0.079	1.259	7.567	1.303	1.842	1.700	24.826	0.068
310	62	1.751	0.084	1.238	7.634	1.314	1.858	1.618	25.401	0.064
350	70	1.798	0.072	1.272	7.755	1.335	1.888	1.454	26.519	0.055
400	80	1.800	0.074	1.273	7.889	1.358	1.920	1.250	27.872	0.045
450	90	1.843	0.061	1.303	8.006	1.378	1.949	1.045	29.185	0.036
500	100	1.845	0.068	1.305	8.112	1.396	1.974	0.841	30.467	0.028

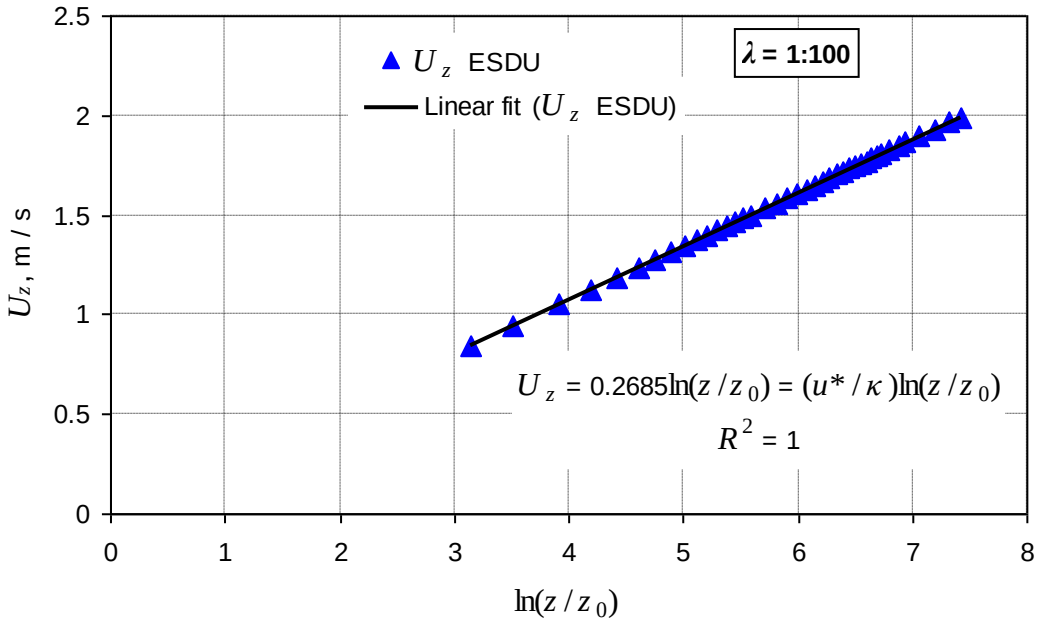

(a)

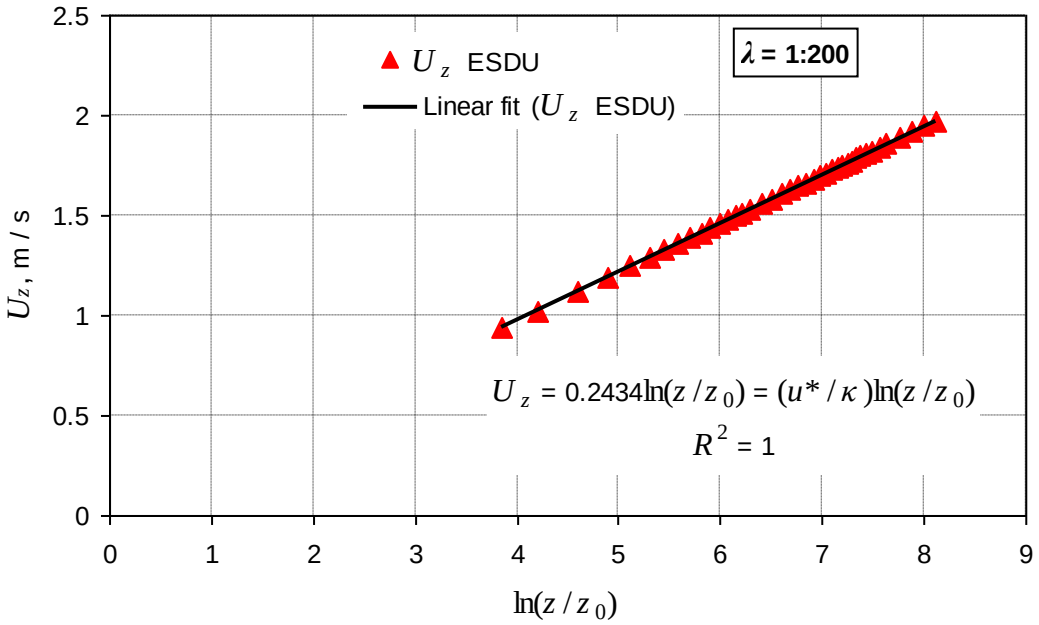

(b)

Figure F.2: Graphical calculation of the friction velocity u: (a) 1:100 scale, (b) 1:200 scale*

Appendix G: ABLWT experiments

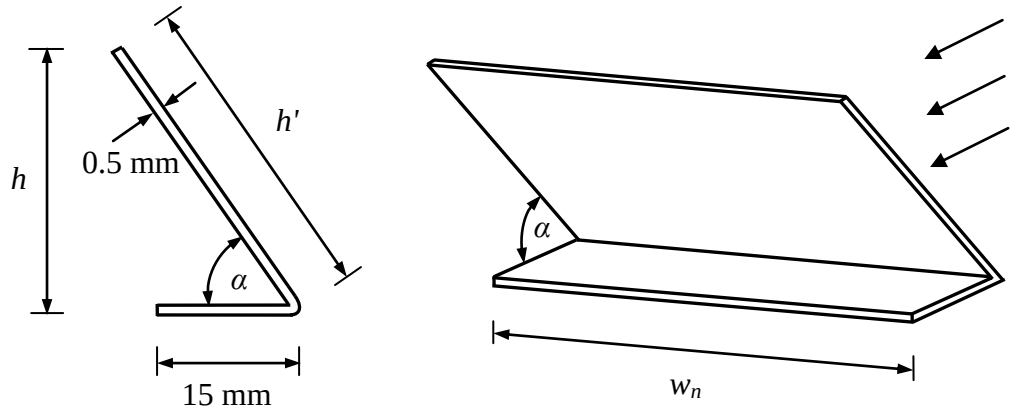

(a)

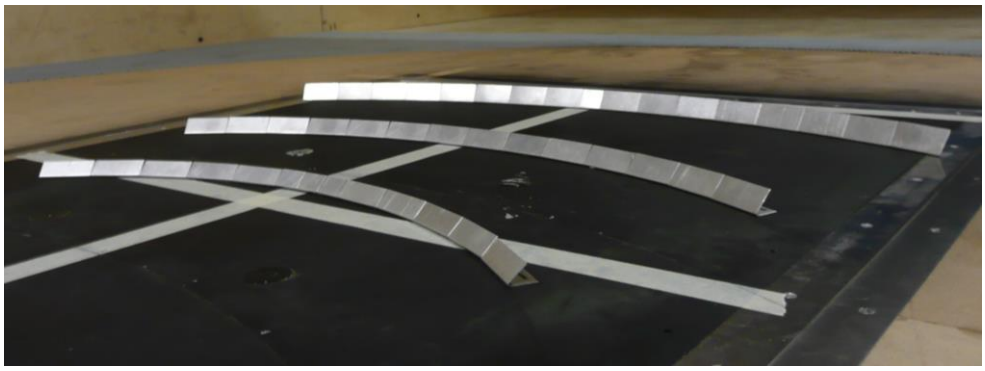

(b)

Figure G.1: Baffle models, used in the ABLWT experiments: (a) schematic (side view and isometric view), (b) image of the models on the force balance plate (isometric view, flow direction is from bottom left)

Table G.1: Parameters of the baffle models in 1:200 scale, used in the FID and HWA measurements

Baffle row label	Arc radius [mm]	Slope height *h'* [mm]	Vertical height *h* [mm]	Slope angle α [°]	Total row width *w* [mm]	Individual baffle width* w_n [mm]
A	180.0	7.0	4.5	40	241.5	21
B	266.5	8.5	6.5	50	294.0	21
C	370.0	10.0	8.7	60	346.5	21

* Row A has ten baffles of 21 mm width and three baffles of 10.5 mm width; Row B has fourteen baffles of 21 mm width; Row C has sixteen baffles of 21 mm width and one baffle of 10.5 mm width

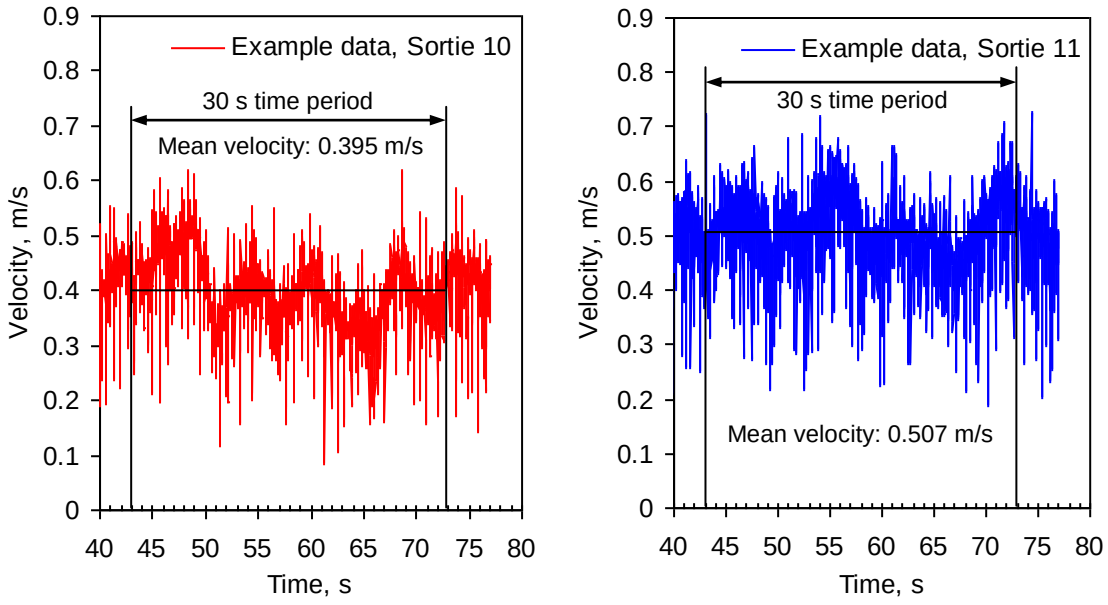

Figure G.2: Examples of velocity data measured at 40 mm height during Sortie 10 and Sortie 11

x-axis shows the time from the start of the run (data from 40 s onwards shown only), y-axis shows velocities measured at 40 mm height with the Schiltknecht MiniAir6 vane anemometer

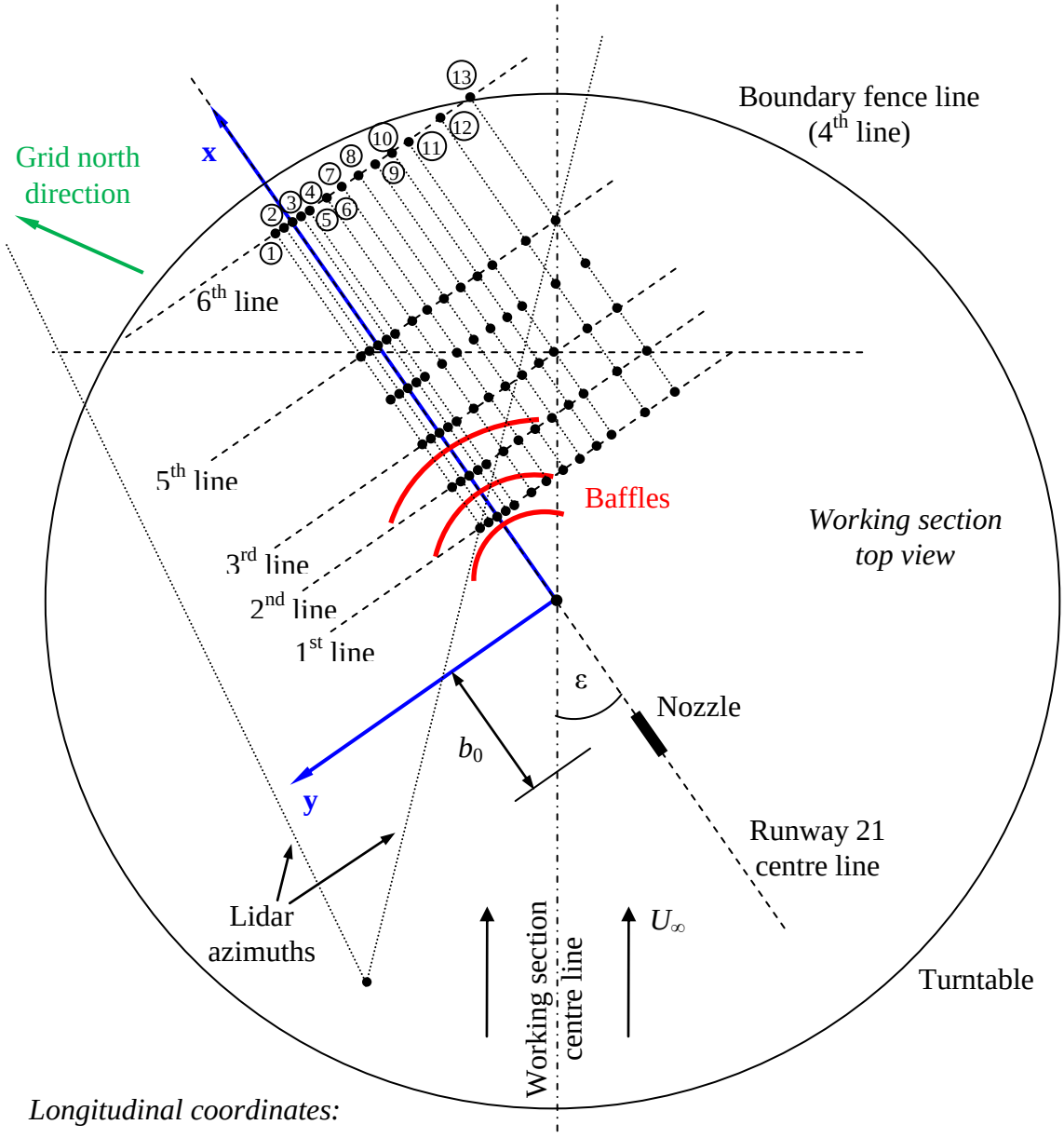

Longitudinal coordinates:

Different for each sortie, all measurement points included in *Table I.5* to *Table I.16*

Lateral coordinates:

① y = 39 mm ② y = 20 mm ③ y = 0 mm ④ y = -20 mm

⑤ y = -39 mm ⑥ y = -80 mm ⑦ y = -117 mm ⑧ y = -160 mm

⑨ y = -200 mm ⑩ y = -240 mm ⑪ y = -275 mm ⑫ y = -355 mm

⑬ y = -430 mm

Vertical coordinates:

z = 25 mm, z = 50 mm, z = 75 mm and z = 100 mm

Figure G.3: Schematic illustration of the FID measurement points used in the 1:200 scale replication of the field trials; arrangement for Sortie 10 shown (ε = 35°, b_0 = 285 mm)

Table G.2: FID concentration measurements for Sortie 10 at 1:200 scale at z / d = 4.2

Sortie 10 z = 25 mm		1st line	2nd line	3rd line	Fence line	5th line	6th line
		x = 200 mm	x = 300 mm	x = 400 mm	x = 505 mm	x = 605 mm	x = 908 mm
No.	y [mm]	[ppm]	[ppm]	[ppm]	[ppm]	[ppm]	[ppm]
1	39	25.4	8.7	-	-	-	-
2	20	138.8	82.6	-	-	-	-
3	0	479.9	175.4	67.4	-	-	-
4	-20	633.0	462.5	205.7	16.4	-	-
5	-39	778.5	613.4	288.8	33.2	5.5	-
6	-80	806.2	759.1	557.3	209.0	70.5	-
7	-117	515.1	654.4	616.5	398.8	271.3	-
8	-160	237.3	407.6	562.0	528.8	377.5	7.3
9	-200	91.1	236.7	402.1	506.8	460.8	79.3
10	-240	22.2	123.9	237.9	330.9	429.8	156.7
11	-275	-	62.6	143.5	229.2	293.3	266.0
12	-355	-	0.6	20.5	112.1	143.8	327.9
13	-430	-	-	-	-	-	183.2

Table G.3: FID concentration measurements for Sortie 10 at 1:200 scale at z / d = 8.3

Sortie 10 z = 50 mm		1st line	2nd line	3rd line	Fence line	5th line	6th line
		x = 200 mm	x = 300 mm	x = 400 mm	x = 505 mm	x = 605 mm	x = 908 mm
No.	y [mm]	[ppm]	[ppm]	[ppm]	[ppm]	[ppm]	[ppm]
1	39	-	-	-	-	-	-
2	20	25.7	7.5	-	-	-	-
3	0	87.7	45.3	16.3	-	-	-
4	-20	214.2	146.3	82.6	9.7	-	-
5	-39	304.9	313.0	153.4	31.6	2.2	-
6	-80	584.5	509.8	414.1	193.8	38.0	-
7	-117	479.2	473.1	519.9	350.5	243.7	-
8	-160	125.4	290.1	459.3	471.6	367.5	4.7
9	-200	32.0	138.2	298.1	444.8	438.8	58.4
10	-240	6.3	57.1	141.0	276.5	388.0	131.2
11	-275	-	18.5	77.0	186.1	253.4	227.3
12	-355	-	1.2	10.3	48.9	86.4	294.9
13	-430	-	-	-	-	-	172.4

Table G.4: FID concentration measurements for Sortie 10 at 1:200 scale at z / d = 12.5

Sortie 10 z = 75 mm		1st line	2nd line	3rd line	Fence line	5th line	6th line
		x = 200 mm	x = 300 mm	x = 400 mm	x = 505 mm	x = 605 mm	x = 908 mm
No.	y [mm]	[ppm]	[ppm]	[ppm]	[ppm]	[ppm]	[ppm]
1	39	-	-	-	-	-	-
2	20	-	-	-	-	-	-
3	0	3.3	9.6	-	-	-	-
4	-20	17.5	33.4	33.2	-	-	-
5	-39	48.0	93.8	67.1	24.5	-	-
6	-80	120.2	218.2	277.2	177.3	30.9	-
7	-117	90.3	219.5	319.1	293.7	124.2	-
8	-160	27.6	121.5	250.3	343.3	247.0	-
9	-200	6.5	41.2	141.5	274.6	338.0	30.6
10	-240	-	11.4	57.9	190.3	315.4	126.3
11	-275	-	-	25.7	101.3	244.2	216.4
12	-355	-	-	-	16.0	58.5	272.7
13	-430	-	-	-	-	-	174.7

Table G.5: FID concentration measurements for Sortie 10 at 1:200 scale at z / d = 16.7

Sortie 10 z = 100 mm		1st line	2nd line	3rd line	Fence line	5th line	6th line
		x = 200 mm	x = 300 mm	x = 400 mm	x = 505 mm	x = 605 mm	x = 908 mm
No.	y [mm]	[ppm]	[ppm]	[ppm]	[ppm]	[ppm]	[ppm]
1	39	-	-	-	-	-	-
2	20	-	-	-	-	-	-
3	0	3.3	9.6	-	-	-	-
4	-20	17.5	33.4	33.2	-	-	-
5	-39	48.0	93.8	67.1	24.5	-	-
6	-80	120.2	218.2	277.2	177.3	30.9	-
7	-117	90.3	219.5	319.1	293.7	124.2	-
8	-160	27.6	121.5	250.3	343.3	247.0	-
9	-200	6.5	41.2	141.5	274.6	338.0	30.6
10	-240	-	11.4	57.9	190.3	315.4	126.3
11	-275	-	-	25.7	101.3	244.2	216.4
12	-355	-	-	-	16.0	58.5	272.7
13	-430	-	-	-	-	-	174.7

Table G.6: FID concentration measurements for Sortie 11 at 1:200 scale at z / d = 4.2

Sortie 11 z = 25 mm		1st line	2nd line	Fence line	4th line	5th line
		x = 315 mm	x = 505 mm	x = 670 mm	x = 770 mm	x = 1073 mm
No.	y [mm]	[ppm]	[ppm]	[ppm]	[ppm]	[ppm]
1	39	-	-	-	-	-
2	20	54.1	-	-	-	-
3	0	227.3	20.5	-	-	-
4	-20	552.2	85.4	-	-	-
5	-39	809.2	204.4	1.1	-	-
6	-80	871.0	477.5	72.2	4.8	-
7	-117	495.6	600.4	226.5	34.7	-
8	-160	154.9	538.4	401.0	153.9	0.7
9	-200	26.0	313.8	459.4	281.1	14.9
10	-240	-	142.7	387.3	368.4	95.9
11	-275	-	75.5	254.1	379.4	226.6
12	-355	-	7.8	78.5	154.0	326.2
13	-430	-	-	26.3	57.7	198.9

Table G.7: FID concentration measurements for Sortie 11 at 1:200 scale at z / d = 8.3

Sortie 11 z = 50 mm		1st line	2nd line	Fence line	4th line	5th line
		x = 315 mm	x = 505 mm	x = 670 mm	x = 770 mm	x = 1073 mm
No.	y [mm]	[ppm]	[ppm]	[ppm]	[ppm]	[ppm]
1	39	-	-	-	-	-
2	20	1.8	-	-	-	-
3	0	34.8	1.9	-	-	-
4	-20	244.8	30.1	-	-	-
5	-39	474.3	92.0	0.2	-	-
6	-80	660.8	342.9	26.6	3.3	
7	-117	391.7	533.9	147.4	16.1	
8	-160	111.7	505.0	325.5	98.8	1.0
9	-200	13.6	291.8	417.6	227.9	9.2
10	-240	-	128.2	381.4	333.6	59.0
11	-275	-	53.1	266.0	356.5	179.0
12	-355	-	2.7	66.3	166.9	298.0
13	-430	-	-	11.2	39.6	219.7

Table G.8: FID concentration measurements for Sortie 11 at 1:200 scale at z / d = 12.5

Sortie 11 z = 75 mm		1st line	2nd line	Fence line	4th line	5th line
		x = 315 mm	x = 505 mm	x = 670 mm	x = 770 mm	x = 1073 mm
No.	y [mm]	[ppm]	[ppm]	[ppm]	[ppm]	[ppm]
1	39	-	-	-	-	-
2	20	-	-	-	-	-
3	0	5.2	-	-	-	-
4	-20	44.3	-	-	-	-
5	-39	147.4	40.0	-	-	-
6	-80	295.8	231.7	10.4	-	-
7	-117	191.9	413.5	103.5	11.6	-
8	-160	35.5	394.7	307.8	76.3	-
9	-200	-	247.4	373.5	230.9	-
10	-240	-	107.7	251.9	311.1	30.0
11	-275	-	28.1	52.2	337.8	115.8
12	-355	-	-	-	223.9	260.0
13	-430	-	-	-	41.6	239.4

Table G.9: FID concentration measurements for Sortie 11 at 1:200 scale at z / d = 16.7

Sortie 11 z = 100 mm		1st line	2nd line	Fence line	4th line	5th line
		x = 315 mm	x = 505 mm	x = 670 mm	x = 770 mm	x = 1073 mm
No.	y [mm]	[ppm]	[ppm]	[ppm]	[ppm]	[ppm]
1	39	-	-	-	-	-
2	20	-	-	-	-	-
3	0	-	-	-	-	-
4	-20	-	-	-	-	-
5	-39	4.9	9.7	-	-	-
6	-80	31.3	70.5	2.3	-	-
7	-117	27.0	212.8	50.0	2.9	-
8	-160	5.8	247.9	183.4	39.7	-
9	-200	-	154.3	274.3	156.0	-
10	-240	-	61.1	278.0	238.0	17.1
11	-275	-	12.5	211.1	276.9	71.8
12	-355	-	-	38.1	211.4	217.0
13	-430	-	-	-	36.0	227.3

Table G.10: FID concentration measurements for Sortie 12 at 1:200 scale at z / d = 4.2

Sortie 12 z = 25 mm		1st line	2nd line	3rd line	4th line	5th line	6th line
		x = 295 mm	x = 395 mm	x = 505 mm	x = 603 mm	x = 700 mm	x = 904 mm
No.	y [mm]	[ppm]	[ppm]	[ppm]	[ppm]	[ppm]	[ppm]
1	39	90.0	40.2	-	-	-	-
2	20	320.9	197.3	23.8	-	-	-
3	0	517.2	397.0	123.9	34.4	17.7	-
4	-20	631.9	509.8	289.7	108.0	51.8	-
5	-39	696.5	580.8	419.1	213.1	116.2	1.5
6	-80	624.8	612.2	549.0	432.4	361.8	58.8
7	-117	393.5	493.6	524.3	481.8	432.6	172.5
8	-160	186.6	329.1	411.4	427.9	434.9	346.9
9	-200	72.2	194.7	283.6	333.6	359.7	366.4
10	-240	16.3	101.8	207.0	263.7	293.9	332.8
11	-275	-	41.6	135.4	206.8	238.1	293.2
12	-355	-	-	30.8	81.7	145.1	213.3
13	-430	-	-	-	24.8	61.9	157.0

Table G.11: FID concentration measurements for Sortie 12 at 1:200 scale at z / d = 8.3

Sortie 12 z = 50 mm		1st line	2nd line	3rd line	4th line	5th line	6th line
		x = 295 mm	x = 395 mm	x = 505 mm	x = 603 mm	x = 700 mm	x = 904 mm
No.	y [mm]	[ppm]	[ppm]	[ppm]	[ppm]	[ppm]	[ppm]
1	39	4.8	5.5	-	-	-	-
2	20	38.9	42.8	6.5	-	-	-
3	0	92.6	120.6	41.5	13.3	8.6	-
4	-20	169.9	200.6	129.9	43.0	28.1	-
5	-39	238.9	258.4	202.8	110.9	72.9	
6	-80	281.3	323.8	315.7	284.5	257.4	42.7
7	-117	152.5	253.4	320.3	324.7	309.3	146.5
8	-160	42.6	135.7	235.8	284.5	313.1	274.1
9	-200	10.1	55.2	127.2	195.0	236.9	288.4
10	-240	2.2	18.9	69.4	133.4	179.1	264.2
11	-275	-	6.0	38.2	88.4	128.2	212.7
12	-355	-	-	8.1	25.9	50.4	133.6
13	-430	-	-	-	6.9	24.8	73.9

Table G.12: FID concentration measurements for Sortie 12 at 1:200 scale at z / d = 12.5

Sortie 12 z = 75 mm		1st line	2nd line	3rd line	4th line	5th line	6th line
		x = 295 mm	x = 395 mm	x = 505 mm	x = 603 mm	x = 700 mm	x = 904 mm
No.	y [mm]	[ppm]	[ppm]	[ppm]	[ppm]	[ppm]	[ppm]
1	39	-	-	-	-	-	-
2	20	-	-	-	-	-	-
3	0	-	-	-	-	-	-
4	-20	-	-	49.3	-	-	-
5	-39	-	37.6	78.4	66.7	36.1	-
6	-80	17.0	59.0	102.2	159.6	145.5	23.1
7	-117	33.9	57.8	106.9	160.2	199.7	121.0
8	-160	28.7	24.6	73.9	128.8	179.4	216.9
9	-200	-	-	33.9	85.1	151.0	233.0
10	-240	-	-	12.2	52.5	96.7	200.8
11	-275	-	-	-	24.8	57.4	155.6
12	-355	-	-	-	-	15.9	67.1
13	-430	-	-	-	-	-	29.8

Table G.13: FID concentration measurements for Sortie 12 at 1:200 scale at z / d = 16.7

Sortie 12 z = 100 mm		1st line	2nd line	3rd line	4th line	5th line	6th line
		x = 295 mm	x = 395 mm	x = 505 mm	x = 603 mm	x = 700 mm	x = 904 mm
No.	y [mm]	[ppm]	[ppm]	[ppm]	[ppm]	[ppm]	[ppm]
1	39	-	-	-	-	-	-
2	20	-	-	-	-	-	-
3	0	-	-	-	-	-	-
4	-20	-	-	3.0	-	-	-
5	-39	0.2	1.7	7.6	6.8	6.9	-
6	-80	0.7	2.7	15.9	33.9	38.4	10.3
7	-117	1.3	4.1	19.2	40.0	76.6	47.4
8	-160	-	1.5	14.3	33.5	72.6	126.3
9	-200	-	-	5.0	21.9	49.6	143.1
10	-240	-	-	1.6	9.7	29.9	117.3
11	-275	-	-	-	5.2	18.0	82.6
12	-355	-	-	-	-	4.1	25.3
13	-430	-	-	-	-	-	7.9

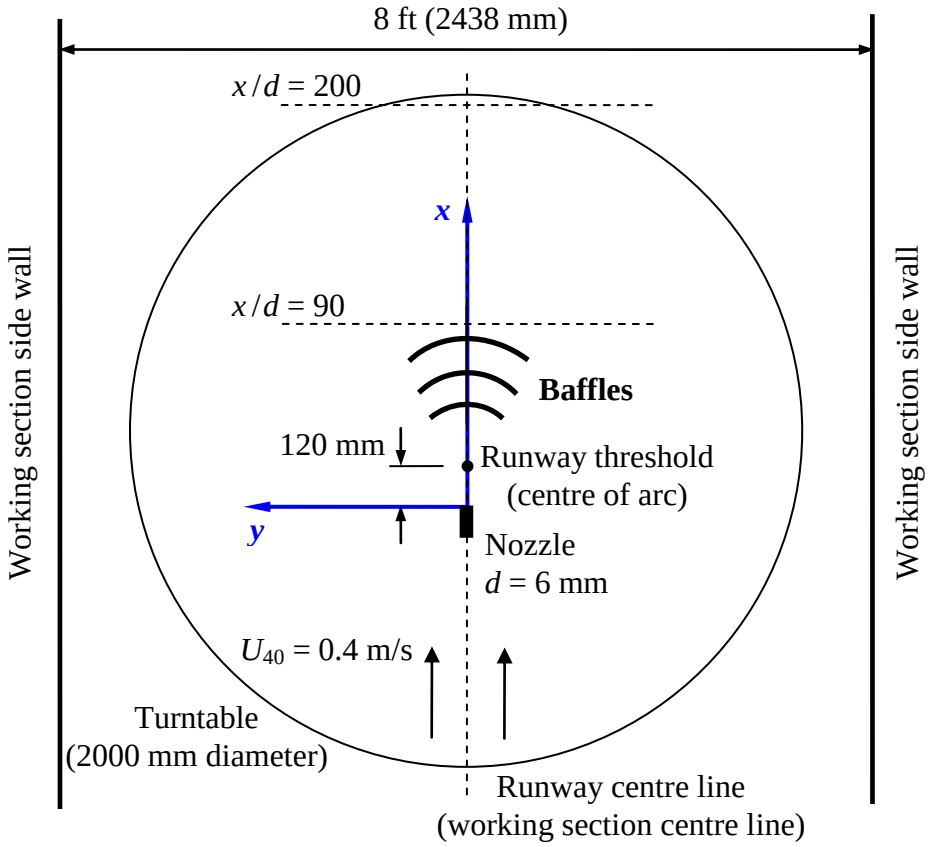

Figure G.4: Schematic illustration of the 8'×4' ABLWT working section arrangement in the 1:200 scale FID and HWA measurements without cross flow (top view)

Table G.14: Parameters of the 'double' baffle array arrangement, tested with modelled jet and Atmospheric Boundary Layer at 1:200 scale

Baffle row label	Arc radius [mm]	Slope height h' [mm]	Vertical height h [mm]	Slope angle α [º]	Total row width w [mm]	Individual baffle width* w_n [mm]
A	360	14	9.0	40	241.5	21
B	480	17	13.0	50	294.0	21
C	690	20	17.3	60	346.5	21

* Row A has 10 baffles of 21 mm width and 3 baffles of 10.5 mm width; Row B has 14 baffles of 21 mm width; Row C has 16 baffles of 21 mm width and 1 baffle of 10.5 mm width

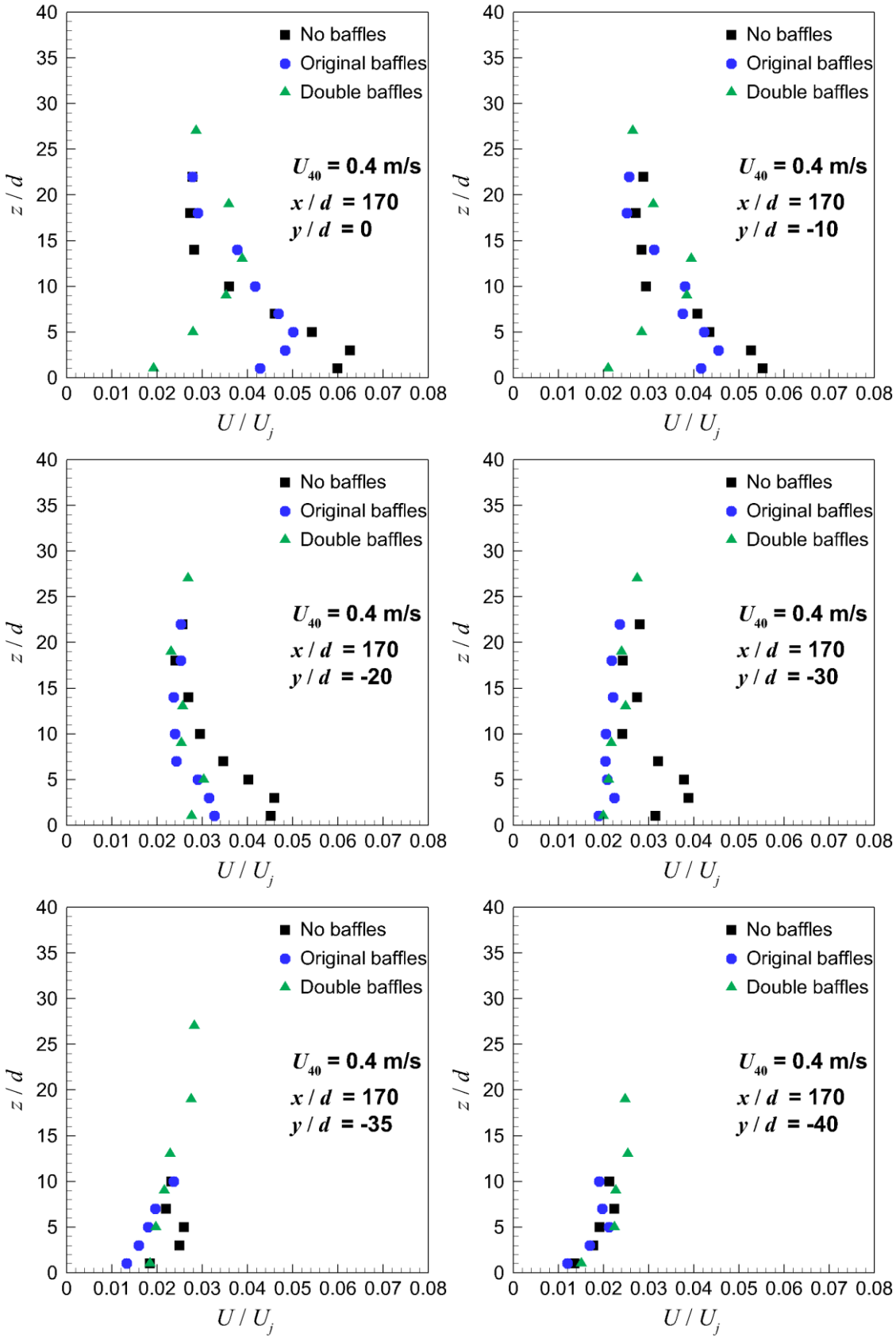

Figure G.5: Variation of measured mean velocities with height (z/d) for various lateral locations at x/d = 170

Table G.15: Parameters of the baffle models at 1:100 scale, used in the force balance measurements

Baffle row label	Arc radius [mm]	Slope height *h'* [mm]	Vertical height *h* [mm]	Slope angle α [º]	Total row width *w* [mm]	Individual baffle width* w_n [mm]
A	360	14	9.0	40	483	42
B	533	17	13.0	50	588	42
C	740	20	17.3	60	693	42

* Row A has ten baffles of 42 mm width and three baffles of 21 mm width; Row B has fourteen baffles of 42 mm width; Row C has sixteen baffles of 42 mm width and one baffle of 21 mm width

Table G.16: Drag results at 1:100 scale without wind tunnel flow for nozzle positions as in Sortie 10 and Sortie 11

Measurements		b_0 = 570 mm	b_0 = 240 mm
Wind tunnel (ambient wind) velocity		0 m/s	0 m/s
Total measured drag, F_T	Test 1	0.066	0.083
	Test 2	0.070	0.082
	Test 3	0.069	0.082
Measured balance plate drag F_b	Test 1	0.029 N	
	Test 2	0.028 N	
	Test 3	0.027 N	
Average baffles drag in % of jet thrust		**23.8%**	**32.3%**

Table G.17: Drag results at 1:100 scale for nozzle positions as in Sortie 10 and Sortie 11 with wind tunnel flow velocity of 0.7 m/s and 0.5 m/s respectively

Measurements		b_0 = 570 mm	b_0 = 240 mm
Wind tunnel (ambient wind) velocity at z = 80mm		0.7 m/s	0.5 m/s
Total measured drag, F_T	Test 1	0.083	0.089
	Test 2	0.083	0.089
	Test 3	0.082	0.092
Measured balance plate drag F_b	Test 1	0.032	0.031
	Test 2	0.030	0.030
	Test 3	0.032	0.030
Average baffles drag in % of jet thrust		**30.4%**	**35.6%**

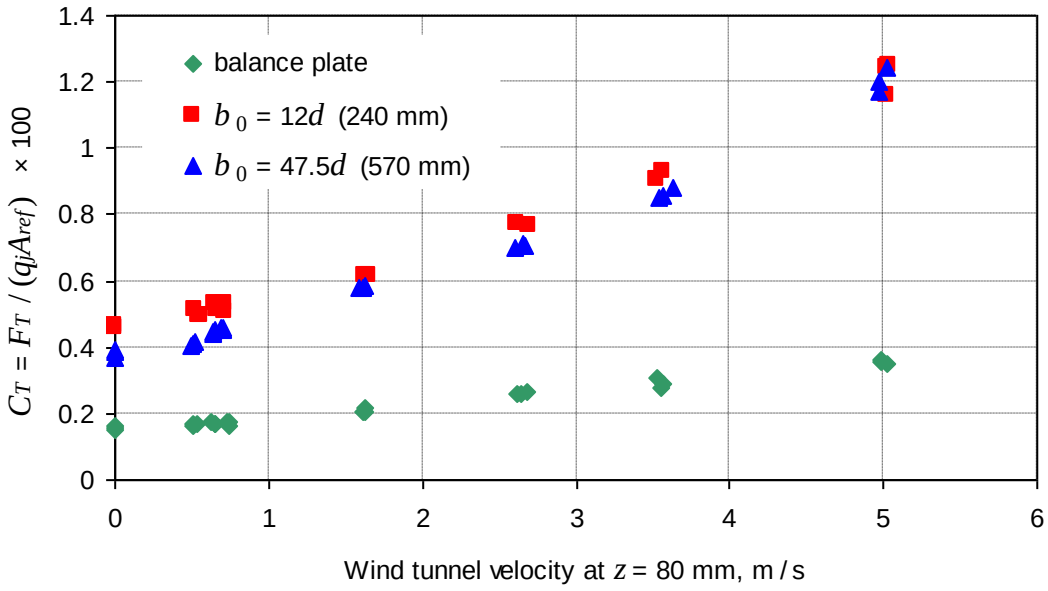

Figure G.6: Variation of drag coefficient with wind tunnel velocity at z = 80 mm for nozzle positions as in Sortie 10 and Sortie 11 and without the baffles (balance plate only)

The y-axis shows the drag coefficient C_T, calculated with the measured total drag of the balance, the exit jet dynamic pressure (U_j = 36 m/s) and the summed frontal area of all three baffle rows, equal to 0.02398, and multiplied by a factor of 100

Appendix H: BAe 146-301 field trials

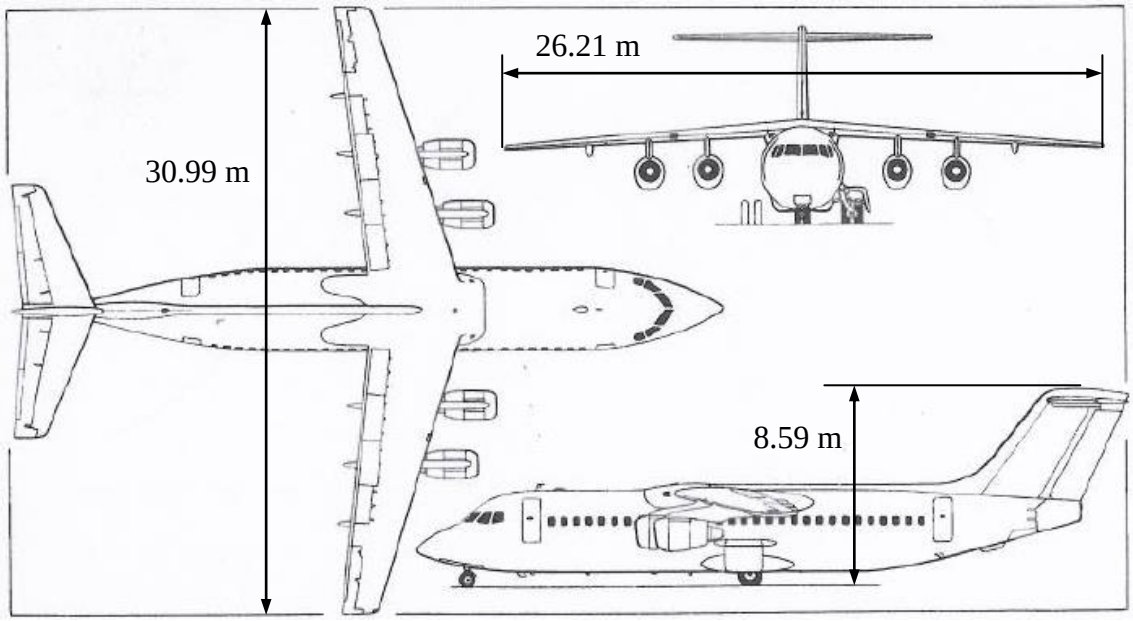

Figure H.1: Drawing of a general BAe 146 Series 300 aircraft (adapted from Jane's All The World's Aircraft, 1993, p. 384)

Table H.1: Some BAe 146 Series 300 characteristics (data taken from Jane's All The World's Aircraft, 1993, p. 385)

Length overall	30.99 m
Height overall	8.59 m
Wing span	26.21 m
Wind aspect ratio	8.57
Maximum take-off weight	44225 kg
Maximum landing weight	38328 kg
Maximum zero-fuel weight	35607 kg
Operating weight empty	24835 kg
Take-off distance to 10.7 m with max take-off weight (standard conditions at mean sea level)	1509 m
Landing distance from 15m with max landing weight (standard conditions at mean sea level)	1228 m

Figure H.2: Erected baffles at the Runway End Safety Area (RESA) of Runway 21 at Cranfield Airport, photo by Bennett (2012)

Figure H.3: Lidar vehicle used for plume dispersion measurements during the field trials at Cranfield Airport

Figure H.4: Satellite image of Runway 21, including the locations of some of the measurement equipment, as planned before the field trials (taken from Christie, 2011)

The Osiris particle counters are shown to be arranged symmetrically with respect to the runway centre line. During the actual field trials, the arrangement was changed to account for the prevailing west-south-westerly wind

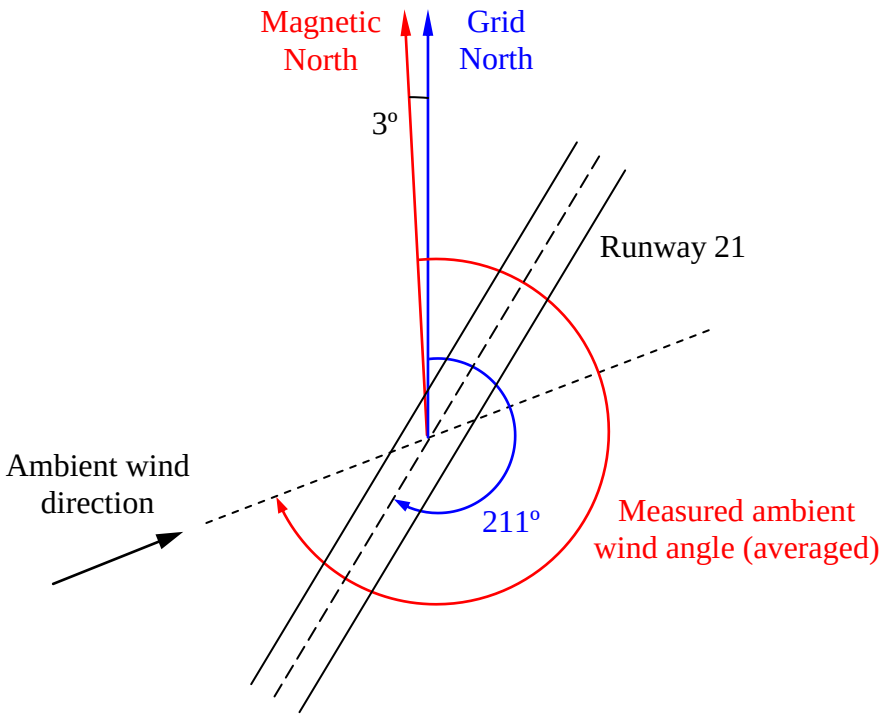

Figure H.5: Schematic illustration showing the relationship between measured ambient wind direction, magnetic north, grid north and the Runway 21 centre line

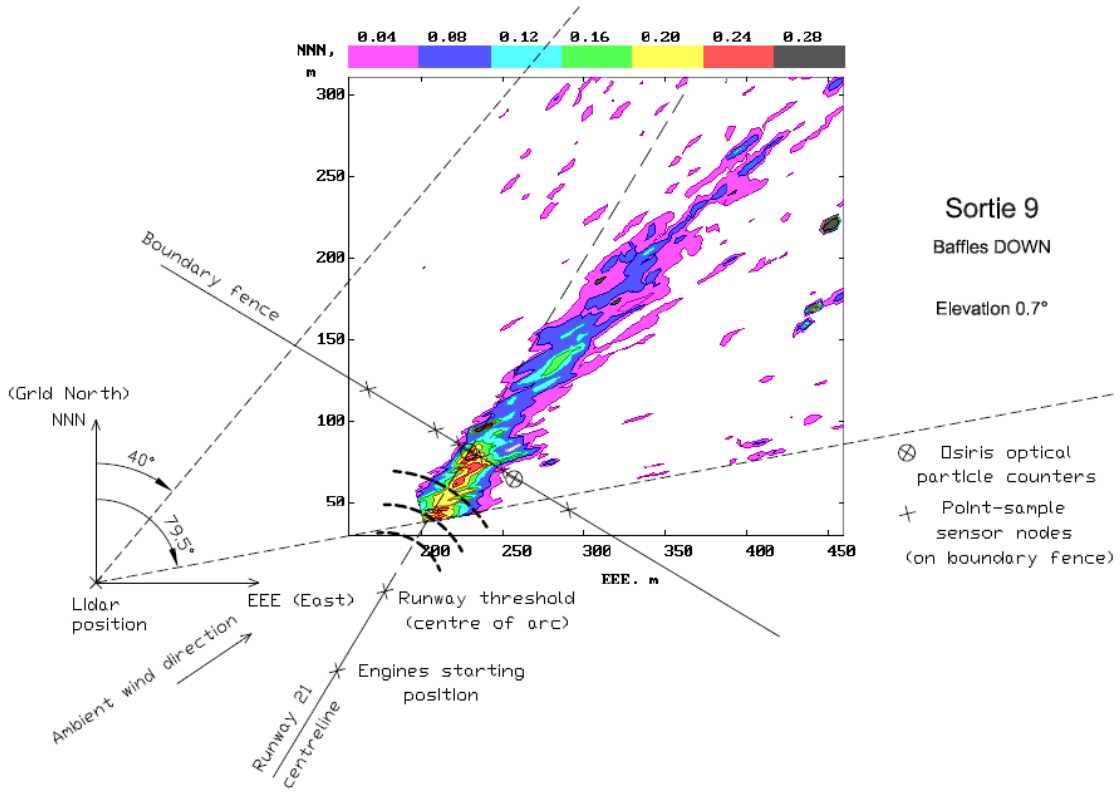

(a)

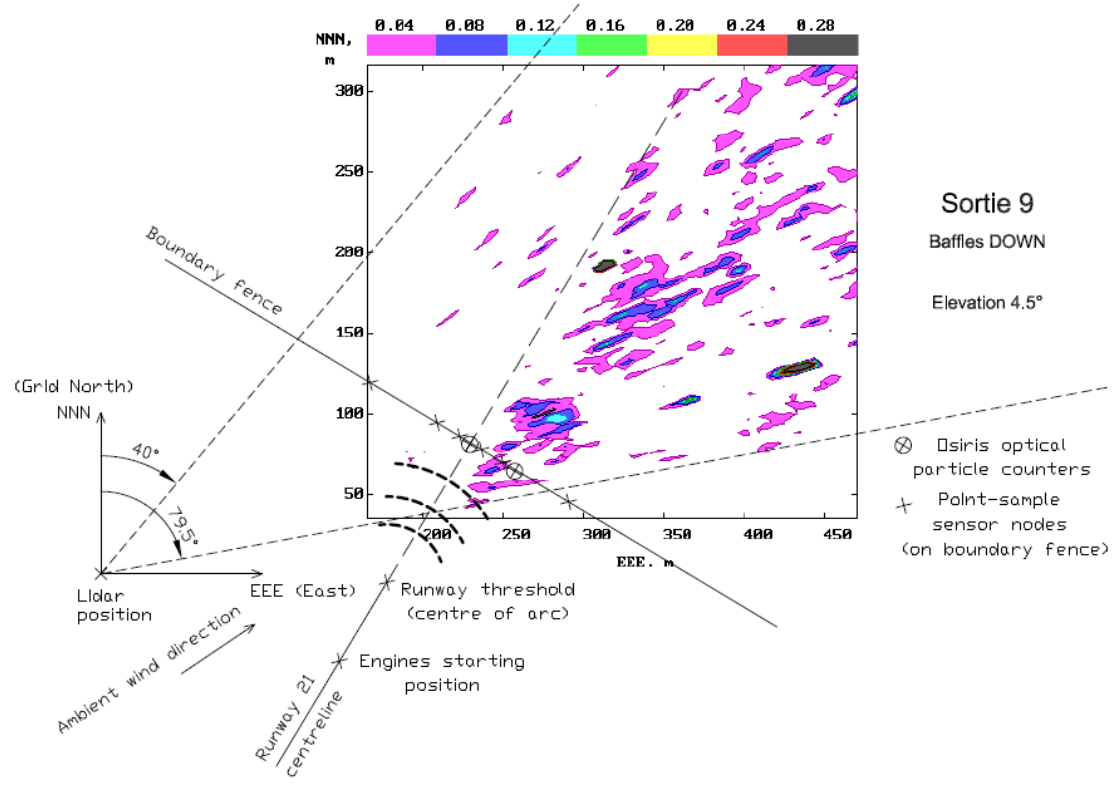

(b)

Figure H.6: Lidar data for Sortie 9: (a) 0.7º elevation, (b) 4.5º elevation (data by Bennett, 2012) Plot contours are given as excess concentration relative to the measured ambient concentration

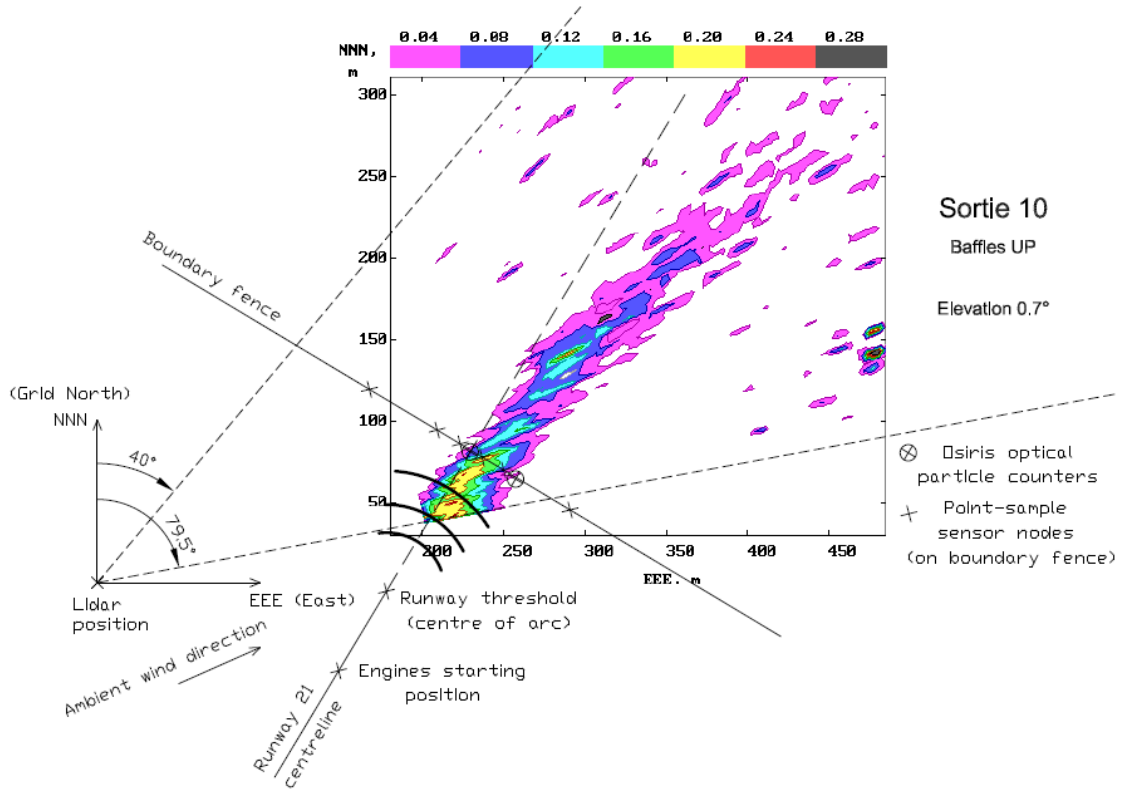

(a)

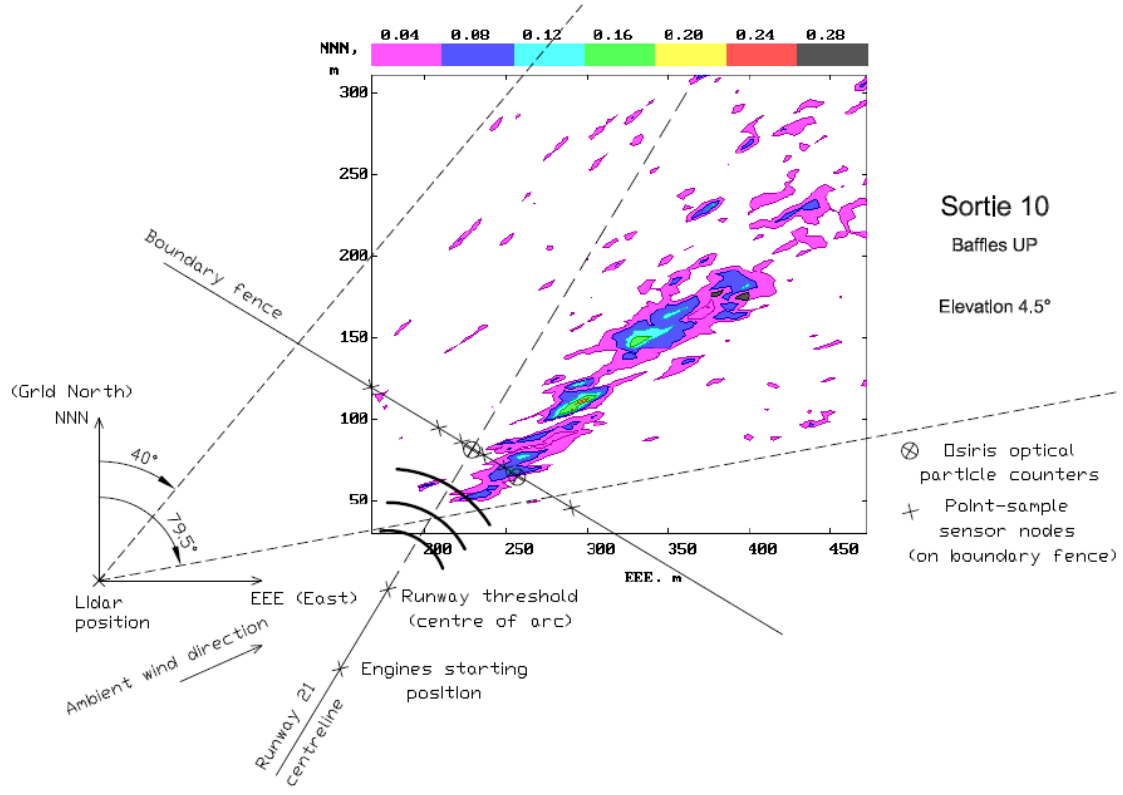

(b)

Figure H.7: Lidar data for Sortie 10: (a) 0.7º elevation, (b) 4.5º elevation (data by Bennett, 2012) Plot contours are given as excess concentration relative to the measured ambient concentration

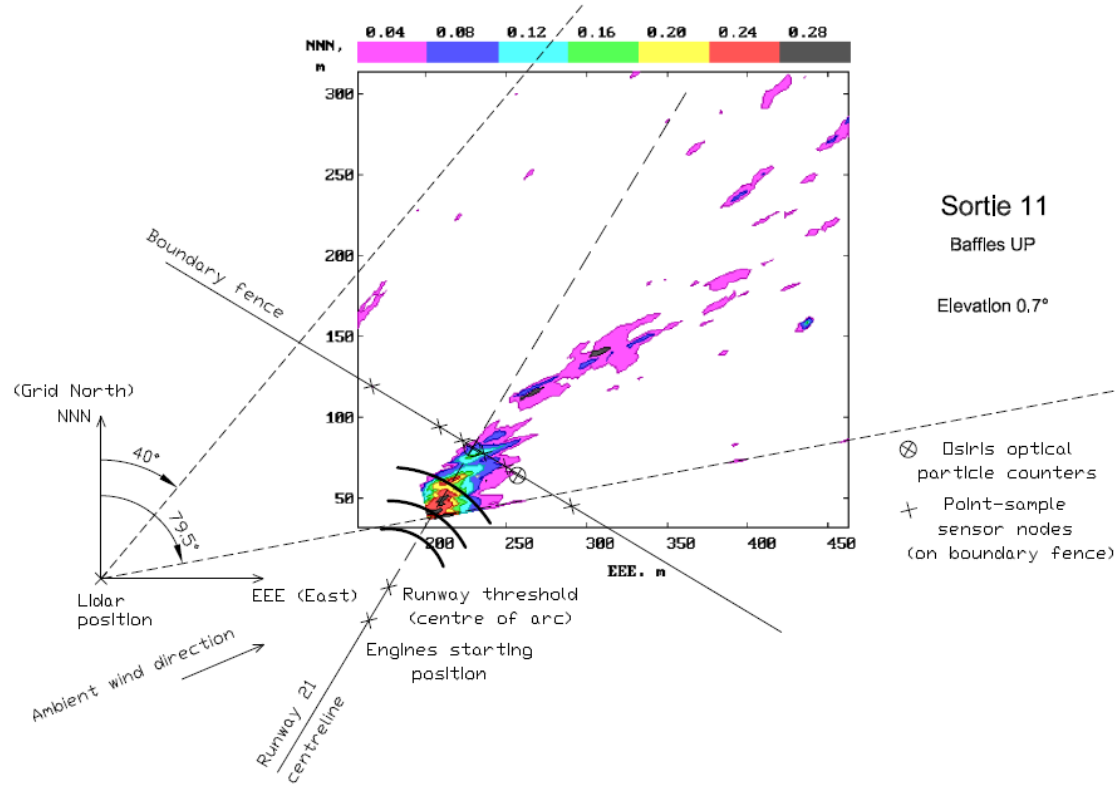

(a)

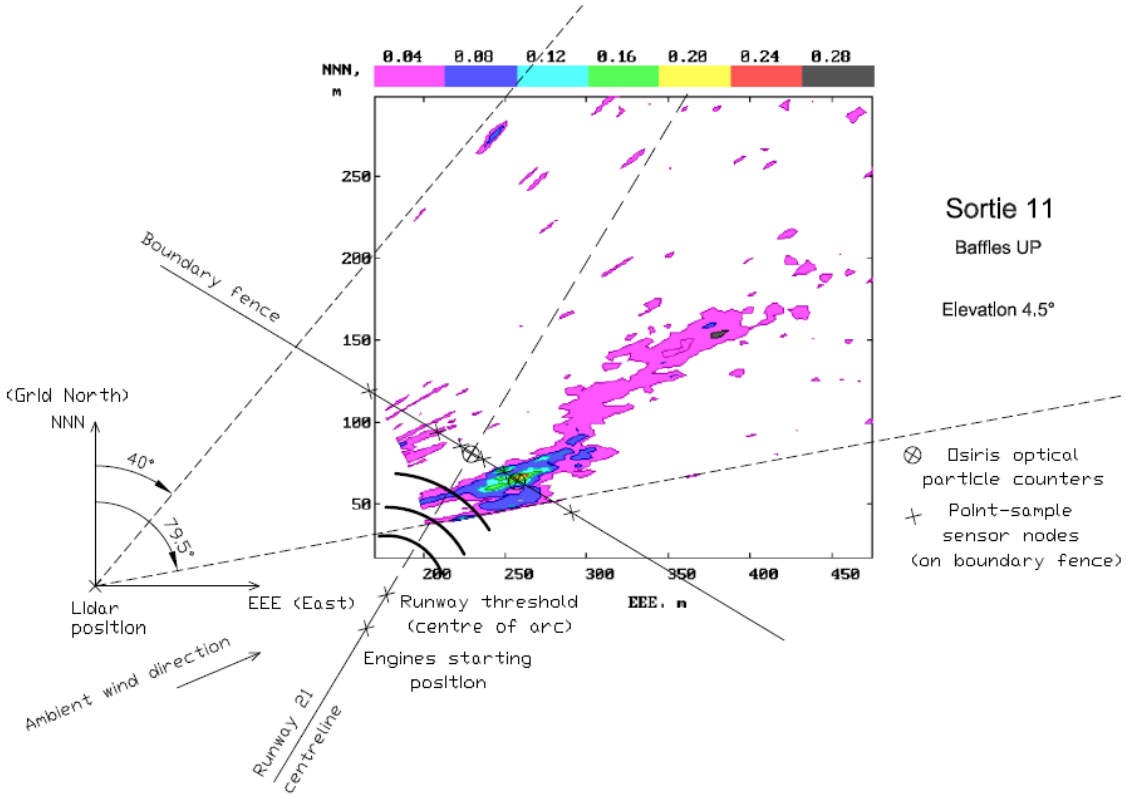

(b)

Figure H.8: Lidar data for Sortie 11: (a) 0.7º elevation, (b) 4.5º elevation (data by Bennett, 2012) Plot contours are given as excess concentration relative to the measured ambient concentration

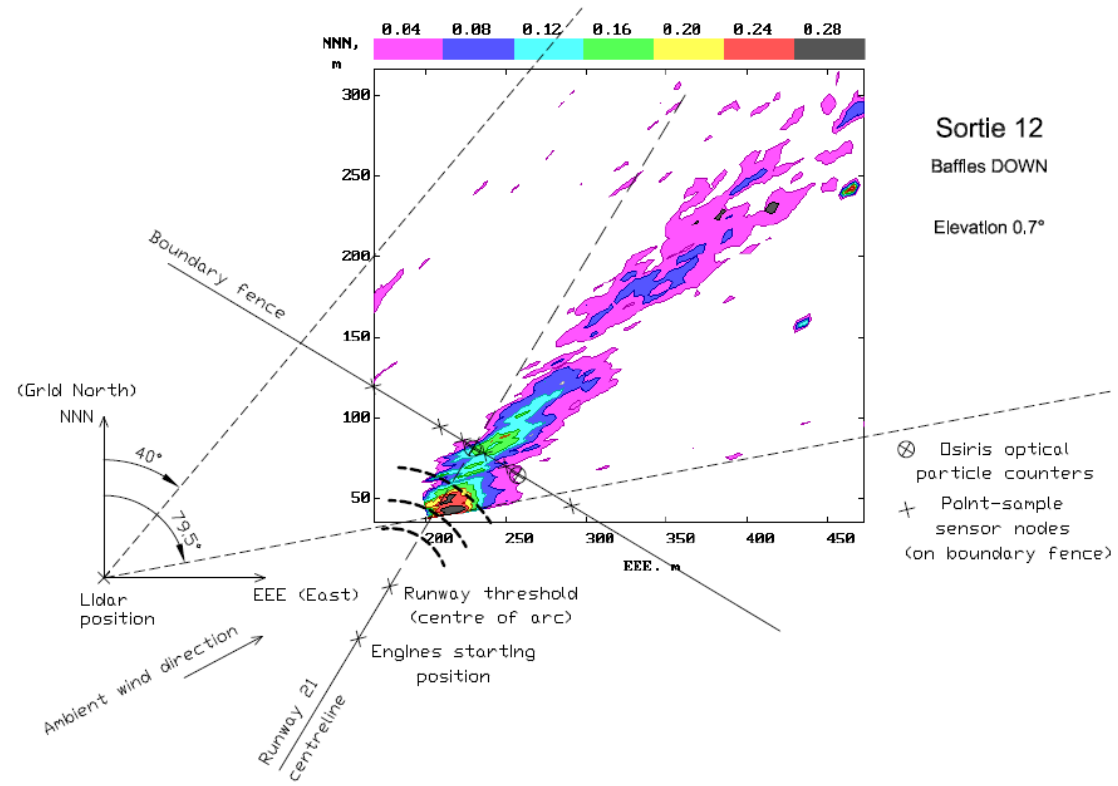

(a)

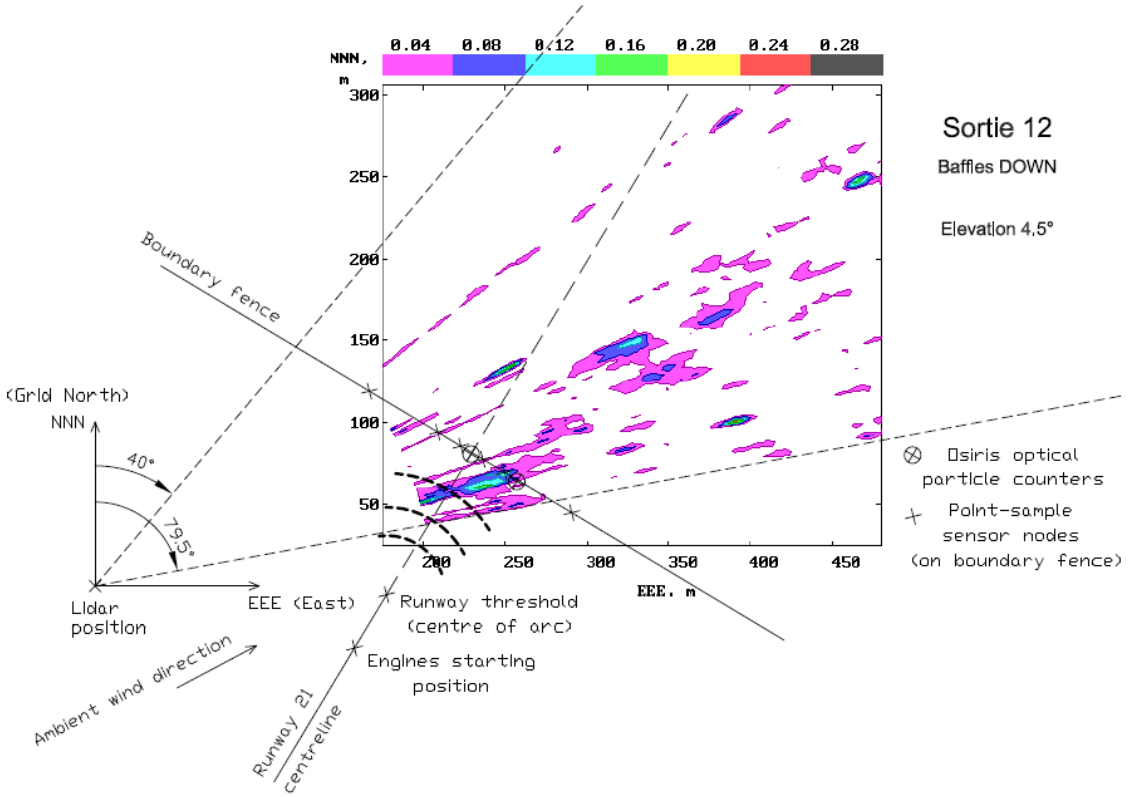

(b)

Figure H.9: Lidar data for Sortie 12: (a) 0.7º elevation, (b) 4.5º elevation (data by Bennett, 2012) Plot contours are given as excess concentration relative to the measured ambient concentration

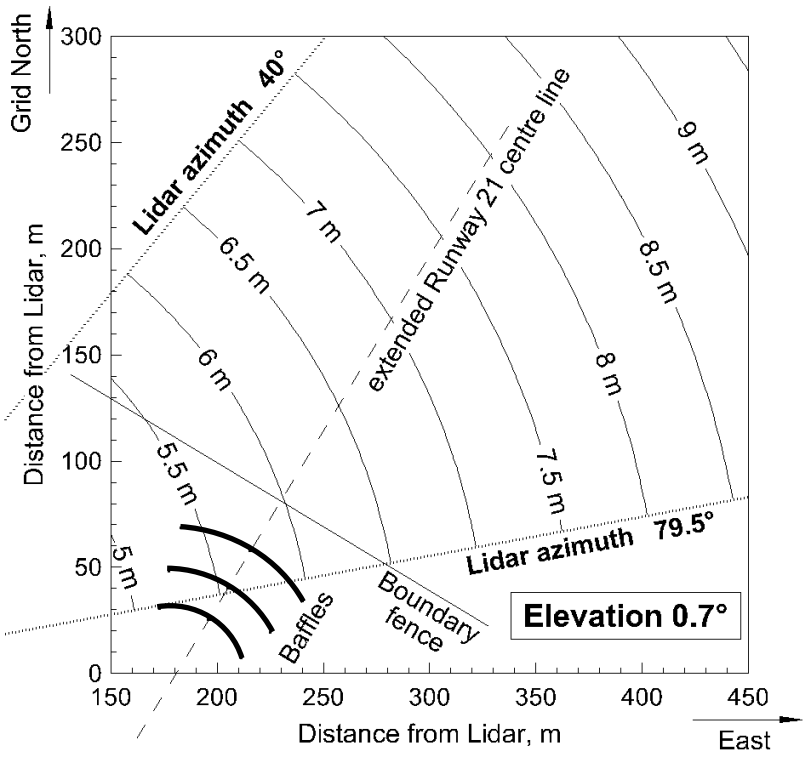

(a)

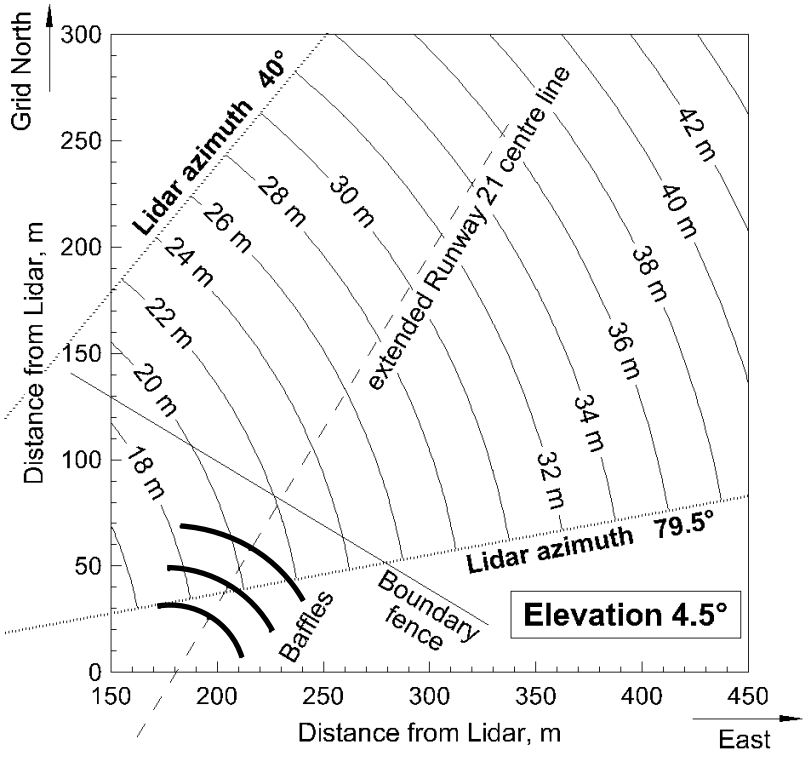

(b)

Figure H.10: Contours of Lidar scan height above the ground for elevation of: (a) 0.7º, (b) 4.5º

Appendix I: UAV turbine field trials

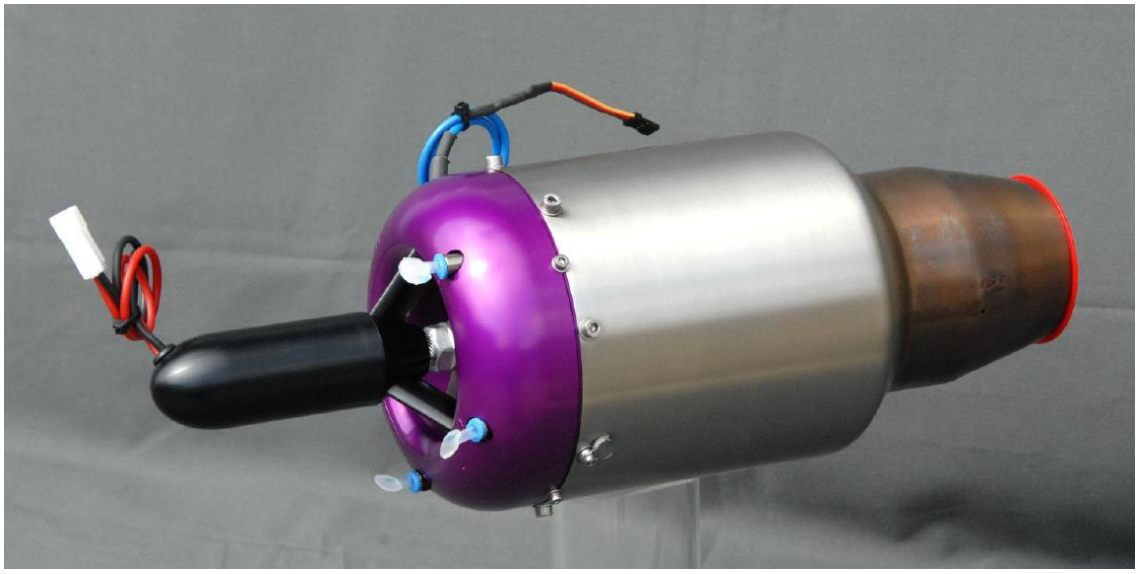

Figure I.1: Olympus HP gas turbine (image taken from AMT Netherlands, 2014)

Table I.1: Olympus HP gas turbine specifications (taken from AMT Netherlands, 2014)

Engine outer diameter	130 mm
Engine length	374 mm
Engine weight	2.9 kg
Maximum thrust (at standard pressure and temperature)	230 N
Maximum RPM	108 500
Pressure ratio	3.8:1
Mass flow rate at max thrust	0.45 kg/s
Fuel flow rate at max thrust	0.64 kg/min
Specific fuel consumption	46.4 g/(kNs)

Froude number scaling

This scaling method is based on Froude number equality, where the Froude number *Fr* is defined as

$$Fr = \frac{U}{\sqrt{gl}}$$

Equation I.1

For a scaling, defined as $\lambda = l_M / l_F$, the velocity ratio is expressed as

$$\frac{U_M}{U_F} = \sqrt{\lambda}$$

Equation I.2

The ratio of sub-scale and full-scale mass flow rates is then

$$\frac{\dot{m}_M}{\dot{m}_F} = \frac{(\rho UA)_M}{(\rho UA)_F} = \frac{\rho_M}{\rho_F}\lambda^{2.5}$$

Equation I.3

For $\rho_M \approx \rho_F$, the scaling is calculated as

$$\lambda \approx \left(\frac{\dot{m}_M}{\dot{m}_F}\right)^{0.4}$$

Equation I.4

With $\dot{m}_M$ = 0.45 kg/s (from *Table I.1*) and total mass flow rate of all four ALF502-R5 engines $\dot{m}_F$ = 349.5 kg/s (from *Table 8.1*), the scaling is equal to $\lambda \approx 0.07$, or $\lambda \approx 1{:}14.3$.

Accelerated source

For a full-scale and model source moving at a constant acceleration, the ratio of the accelerations is given by

$$\frac{a_M}{a_F} = \frac{\Delta U_M}{\Delta U_F}\frac{\Delta t_F}{\Delta t_M},$$

Equation I.5

where *a* is the linear acceleration, *U* is the speed and *t* is the time.

Similarly to *Equation I.2*, a relationship for the time at full scale and sub scale can be derived as follows:

$$\frac{t_F}{t_M} = \frac{1}{\sqrt{\lambda}}$$

Equation I.6

From *Equation I.2* and *Equation I.6*, the ratio of the accelerations from *Equation I.5* equals unity or

$$a_M = a_F$$

Equation I.7

Table I.2: Parameters of the baffle array for the planned UAV turbine field trials (by Bennett, 2012)

Row label	Distance to trailer [m]	Slope angle [°]	Slope height [m]	Vertical height [m]	Row length [m]	Estimated plume width [m]
A	4.00	60	8.0	6.9	2.1	0.98
B	4.96	60	9.9	8.6	2.6	1.21
C	6.15	60	12.3	10.6	3.2	1.50
D	7.63	60	15.2	13.2	4.0	1.86

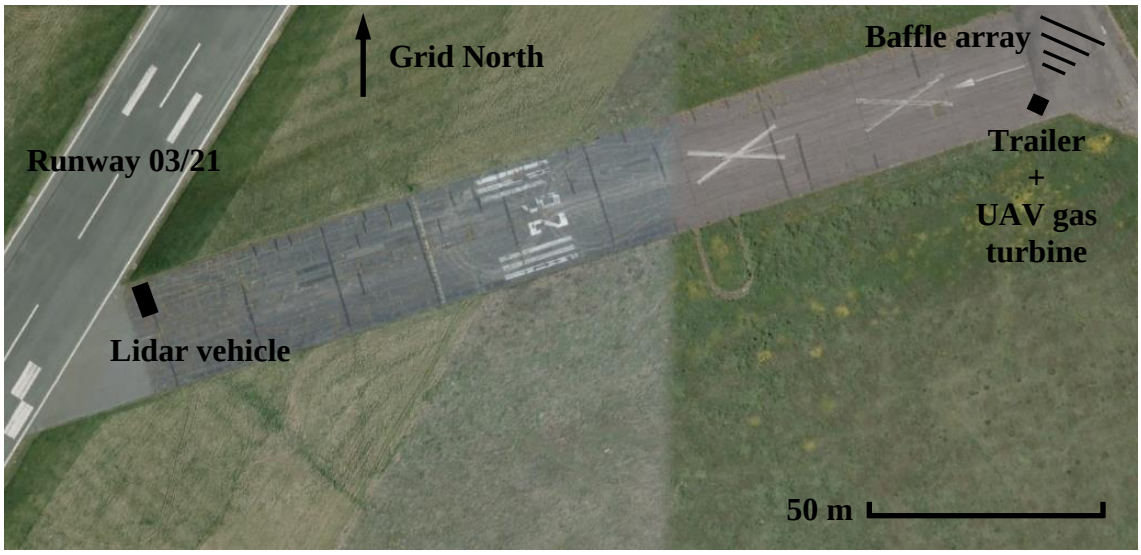

Figure I.2: Test location at Cranfield Airport, chosen the for UAV gas turbine trials; (satellite image produced with Google Maps, 2014)

The size, location and orientation of the Lidar vehicle, trailer and baffle array are approximate and not to scale

Figure I.3: Test arrangement of the field trials of November 2013 at Cranfield Airport